Investigation into vibration assisted micro milling: theory, modelling and applications

Lu Zheng

School of Engineering

Newcastle University

A thesis submitted for the degree of

Doctor of Philosophy

May 2020

Abstract

Precision micro components are increasingly in demand for various engineering industries, such as biomedical engineering, MEMS, electro-optics, aerospace and communications. The proposed requirements of these components are not only in high accuracy, but also in good surface performance, such as drag reduction, wear resistance and noise reduction, which has become one of the main bottlenecks in the development of these industries. However, processing these difficult-to-machine materials efficiently and economically is always a challenging task, which stimulates the development and subsequent application of vibration assisted machining (VAM) over the past few decades. Vibration assisted machining employs additional external energy sources to generate high frequency vibration in the conventional machining process, changing the machining (cutting) mechanism, thus reducing cutting force and cutting heat and improving machining quality. The current awareness on VAM technology is incomplete and effective implementation of the VAM process depends on a wide range of technical issues, including vibration device design and setup, process parameters optimization and performance evaluation. In this research, a 2D non-resonant vibration assisted system is developed and evaluated. Cutting mechanism and relevant applications, such as functional surface generation and microfluidic chips manufacturing is studies through both experimental and finite element analysis (FEA) method.

A new two-dimensional piezoelectric actuator driven vibration stage is proposed and prototyped. A double parallel four-bar linkage structure with double layer flexible hinges is designed to guide the motion and reduce the displacement coupling effect between the two directions. The compliance modelling and dynamic analysis are carried out based on the matrix method and lagrangian principle, and the results are verified by finite element analysis. A closed loop control system is developed and proposed based on LabVIEW program consisting of data acquisition (DAQ) devices and capacitive sensors. Machining experiments have been carried out to evaluate the performance of the vibration stage and the results show a good agreement with the tool tip trajectory simulation results, which demonstrates the feasibility and effectiveness of the vibration stage for vibration assisted micro milling.

The textured surface generation mechanism is investigated through both modelling and experimental methods. A surface generation model based on homogenous matrices transformation is proposed by considering micro cutter geometry and kinematics of vibration

assisted milling. On this basis, series of simulations are performed to provide insights into the effects of various vibration parameters (frequency, amplitude and phase difference) on the generation mechanism of typical textured surfaces in 1D and 2D vibration-assisted micro milling. Furthermore, the wettability tests are performed on the machined surfaces with various surface texture topographies. A new contact model, which considers both liquid infiltration effects and air trapped in the microstructure, is proposed for predicting the wettability of the fish scales surface texture. The following surface textures are used for T-shaped and Y-shaped microchannels manufacturing to achieve liquid one-way flow and micro mixer applications, respectively. The liquid flow experiments have been carried out and the results indicate that liquid flow can be controlled effectively in the proposed microchannels at proper inlet flow rates.

Burr formation and tool wear suppression mechanisms are studied by using both finite element simulation and experiment methods. A finite element model of vibration assisted micro milling using ABAQUS is developed based on the Johnson-Cook material and damage models. The tool-workpiece separation conditions are studied by considering the tool tip trajectories. The machining experiments are carried out on Ti-6Al-4V with coated micro milling tool (fine-grain tungsten carbides substrate with ZrO_2-$BaCrO_4$ (ZB) coating) under different vibration frequencies (high, medium and low) and cutting states (tool-workpiece separation or non-separation). The results show that tool wear can be reduced effectively in vibration assisted micro milling due to different wear suppression mechanisms. The relationship between tool wear and cutting performance is studied, and the results indicate that besides tool wear reduction, better surface finish, lower burrs and smaller chips can also be obtained as vibration assistance is added.

Acknowledgements

First and foremost, I would like to express my sincere appreciation to my supervisor Dr. Dehong Huo, for the continuous support and valuable guidance received throughout my PhD studies. Without his generous support, encouragement and patience the completion of the PhD project would not have been possible. My appreciation also goes to my second supervisor Dr. Michele Pozzi at the Heriot-Watt University and Dr. John Hedley at the Newcastle University, for the helpful guidance on the knowledge of mechatronics and control system. I must thank them for answering any questions I had and spending time reviewing the manuscripts.

I am also grateful to Dr. Wanqun Chen for his encouragement and help during difficult periods. His valuable suggestions always help me to solve the problems I met and give me insights to think through research problems from different perspectives.

Last, special thanks to my parents Jiguang Zheng and Hongyan Gao. Their unconditional love and consistent support have continuously encouraged me throughout this crucial time of my life.

Contents

List of Figures

List of Tables

Nomenclature

A	Vibration amplitude [μm]
C	Strain rate sensitivity coefficient
C_o^{in}	Output compliance of structure III [μm/N]
C_{out}	Stage output compliance [μm/N]
C_i^r	Compliance of micro beam at o_r-$x_r y_r z_r$ [μm/N]
C_r^e	Compliance at o_e-$x_e y_e z_e$ [μm/N]
C_{out}	Output compliance of the vibration stage [μm/N]
C_{P_A}	Output compliance of structure II [μm/N]
d_i	Infiltration depth [μm]
E	Modulus of elasticity [MPa]
$F_{i\ (i=x,y,z)}$	The corresponding force acting on the flexible hinge
f	Vibration frequency [Hz]
fz	Feed per tooth [μm]
f_s	Fraction of area occupied by solids on rough surfaces
G	Modulus of rigidity [MPa]
h	Tool mark height [μm]
h_d	Depth of fish scales surface structure [μm]
h_{dv}	Uncut chip thickness in vibration assisted machining [μm]
I_z	Moment of inertia of the flexible hinges around the z-axis [g/μm^2]
k	Structural correction factor of the flexure hinges
k'	Angle of minor cutting edge
k_o^{in}	Stiffness of structure III [N/μm]
k_{out}	Stage output stiffness [N/μm]
K_a	Stiffness of the piezoelectric actuators [N/μm]
k_{P_A}	Stiffness of structure II [N/μm]

L	Length of the micro Euler–Bernoulli beam [μm]
ΔL	Displacement of end executor [μm]
ΔL_o	Stroke of the piezoelectric actuators [μm]
m	Thermal softening coefficient
M_1	Equivalent mass of flexible hinges [g]
M_2	Equivalent mass of the end executor [g]
$M_{i\ (i=x,y,z)}$	Corresponding moment of inertia acting on the flexible hinge
n	Hardening coefficient
R	Tool radius [μm]
r_e	Cutting edge radius [μm]
R_d	Ratio of the flowing distance between outlet 1 and 2
$R_r(\delta)$	Rotation matrix of the local coordinate o_r-$x_r y_r z_r$ transferring to the global coordinate o_e-$x_e y_e z_e$
r_r	Position vector of the point o_r in the global coordinate o-xyz
$S_r(r_r)$	Skew-symmetric operator for the position vector r_r
T_k	Kinetic energy [kJ]
T_r^e	Compliance transformation matrix [μm/N]
U_k	Potential energy [kJ]
V_v	Vibration speed [μm/s]
V_n	Cutting speed [μm/s]
Vc	Critical velocity [μm/s]
V_f	Feed velocity [μm/s]
$\delta i\ (i = x, y, z)$	Deformation of the flexible hinge in the direction of x, y and z
$\delta\theta_{i(i=x,y,z)}$	The rotation angle of the flexible hinge along axis of x, y and z
ν	Poisson's ratio
ω	Angular velocity of the cutter [rad/s]
ϕ_x	Phase angles [°]

ϕ_y	Phase angles [°]
α_s	Shear coefficient of the material
ϵ	Natural frequency [Hz]
α	Tool edge clearance angle [°]
β	Tool edge rake angle [°]
Υ_{SL}	Solid-liquid interfacial tension [N/µm]]
Υ_{SV}	Solid-vapour interfacial tension [N/µm]]
Υ_{LV}	Liquid-vapour interfacial tension [N/µm]]
θ_w	Wenzel contact angle [°]
θ_c	Cassie contact angle [°]
θ_i	New model contact angle [°]
μ	Coefficient of friction

Abbreviations

AFM	Atomic force microscope
ALE	Arbitrary Lagrangian–Eulerian
DAQ	Data acquisition
EDS	Energy-dispersive X-ray spectroscopy
FE	Finite element
FEA	Finite element analysis
HMT	Homogenous matrices transformation
IKM	Inverse kinematic modelling
JC	Johnson cook
MCM	Matrix-based compliance modelling
PCD	Poly-Crystalline Diamond
PETA	Piezoelectric tool actuator
PID	Proportion Integration Differentiation
PRB	Pseudo rigid body
PZT	Piezoelectric ceramic material
SEM	Scanning electron microscope
VAM	Vibration assisted machining
VAMM	Vibration assisted micro milling
WEDM	Wire electrical discharge machining
ZB	ZrO_2 -$BaCrO_4$

Chapter 1 Introduction

1.1 Background and motivation

Precision components are increasingly in demand in various engineering fields such as MEMS, electro-optics, aerospace, automotive, biomedical engineering, and ICT hardware. In addition to the aims of achieving tight tolerances and high-quality surface finishes, many applications also require the use of hard and brittle materials such as optical glass and technical ceramics owing to their superior physical, mechanical, optical, and electronic properties. However, due to their high hardness and usually low fracture toughness, the processing and fabrication of those hard-to-machine materials have always been challenging. Furthermore, the delicate heat treatment required and composite materials in aeronautic or aerospace alloys have caused similar challenges for precision machining.

It has been reported that excessive tool wear and fracture damage are the main failure modes during the processing of such materials, leading to low surface quality and machining accuracy. Efforts to optimize conventional machining process to achieve better cutting performance with these materials have never been stopped and these optimizations including the cutting parameters, tool materials and geometry, and cutting cooling systems in the past decades (Ezugwu, Bonney and Yamane, 2003; Ulutan and Ozel, 2011; Silva *et al.*, 2013; Sutter and List, 2013; Sharman, Hughes and Ridgway, 2015; Sadik *et al.*, 2016). Generally, harder materials or wear-resistant coatings are applied and tool geometry is optimized to prevent tool cracking and to reduce wear on wearable positions such as the flank face (Jawaid, Sharif and Koksal, 2000; Ribeiro, Moreira and Ferreira, 2003; Basturk *et al.*, 2010; Ulutan and Ozel, 2011; Hatt, Crawforth and Jackson, 2017). Cryogenic coolants are used in the machining process and their input pressure has been optimized to achieve better cooling performance (MacHai and Biermann, 2011; Silva *et al.*, 2013; Sadik *et al.*, 2016). However, although cutting performance can be improved, the results are often still unsatisfactory.

Efforts to enhance machining performance have revealed that machining quality can be improved using the high frequency vibration of the tool or workpiece. Vibration assisted machining (VAM) was first introduced in the late 1950s, and has been applied in various machining processes, including both traditional machining (turning, drilling, grinding and, more recently milling) and non-traditional machining (laser machining, electro-discharge machining, and electro-chemical machining), and it is now widely used in the precision

manufacturing of components made of various materials. Vibration assisted machining adds external energy to the conventional machining process and generating high frequency, low amplitude vibration in the tool or workpiece, a periodic separation between the uncut workpiece and the tool can be achieved. This can decrease the average machining forces and generate thinner chips, which in turn leads to high processing efficiency, longer tool life, better surface quality and form accuracy, and reduced burr generation (Brehl and Dow 2008; W. Chen, Zheng, and Huo 2018; Chern and Chang 2006; Janghorbanian, Razfar, and Zarchi 2013; Lian et al. 2013; Li et al. 2012). Moreover, when hard and brittle materials, such as titanium alloy, ceramic and optical glass are involved, the cutting depth in the ductile-regime cutting mode can be increased (Zheng, Chen and Huo, 2018). As a result, cutting performance can be improved and unnecessary post-processing can be avoided, which allows the production of components with more complex shape features (Brehl and Dow, 2008). Nevertheless, there are still many opportunities for technological improvement and ample scope exists for better scientific understanding and exploration.

As an important part of vibration assisted machining process, vibration assisted micro milling is proposed to satisfy the increasing high demand on micro parts with complex 3D geometry. Due to the well-known size effect, the cutting edge radius of micro milling tool can be no longer ignored in micro milling process, which leads to a different cutting mechanism to its conventional scale counterpart (Teng *et al.*, 2018). The machining performance can be influenced by the tool edge radius when uncut chip thickness is small enough. It has been reported that the ratio of uncut chip thickness to cutting edge radius is closely linked with machining surface ploughing effect, effective rake angle and specific cutting energy, which in turn impacts the cutting performance (Huo, Lin and Dalgarno, 2014; Huo *et al.*, 2015; Dadgari, Huo and Swailes, 2018). Besides the merits above, size effect and ploughing effect can be suppressed effectively in vibration assisted micro milling process. As a result, better cutting performance can be obtained.

1.2 History and development of vibration assisted machining

The history of vibration technology in vibration assisted machining can be traced back to the 1940s. During the period of World War Two, the high demand for the electrically controlled four-way spool valves mainly used in the control of aircraft and gunnery circuits, and this stimulated the development of servo valve technology (Ashley and Millst, 1966). Due to their

wide frequency response and high flow capacity, electro-hydraulic vibrators were successfully developed and applied in vibration assisted machining in the 1960s with positive effects in enhanced processing quality and efficiency (Skelton, 1969). With the further development of technology, electromagnetic vibrators featuring higher accuracy and a wider range of frequency and amplitude generation were developed based on electromagnetic technology and these were successfully applied to various vibration assisted machining processes (Lenkiewicz, 1969). The need for complex hydraulic lines was eliminated and greater tolerance for the application environment was allowed, which also lead to smaller devices. As a result, a transmission line or connecting body can be attached to the vibrator to achieve a wide range of vibration frequency and amplitude adjustment (Balamuth, 1964). In the 1980s, the maturity of PZT piezoelectric ceramic technology had brought a new choice for the vibrator. A piezoelectric ceramic stack could be sandwiched under compressive strain between metal plates, and this has advantages including compactness, high precision and resolution, high frequency response and large output force (Xu *et al.*, 1998). Various shapes of piezoelectric ceramic elements can be used to make different types of vibration actuators, which means that the limitations of traditional vibrators were overcome and the application of vibration assisted machining technology for precision machining was broadened. In addition, it helped in the development of multi-dimensional vibration assisted machining equipment. Elliptical vibration assisted machining has received extensive attention since it was first proposed in the 1990s. Although this process has many advantages compared to its 1D counterpart in terms of reductions in cutting force and prolongation of tool life, it requires higher performance in the vibrator, producing a more accurate tool tip trajectory (Kumar et al. 2014; Negishi 2003; E. Shamoto, Suzuki, and Hino 2008; Eiji Shamoto and Moriwaki 1994; Xu and Zhang 2015). Piezoelectric actuators with high sensitivity can fulfil the requirements of vibration devices and promote the development of elliptical vibration assisted machining technology.

1.3 Aim and objectives of this research

This research aims to obtain a scientific understanding on the vibration assisted micro milling process, including vibration system development, functional surface texture generation and application, and cutting performance evaluation.

The specific objectives are set for achieving the overall aim of this PhD research:

1. To critically review the previous research on the vibration assisted machining and establish a body of systemic knowledge and the state-of-the-art research status.

2. To develop a decoupled 2D non-resonant vibration system with high motion accuracy, including structure design, control strategy determination and estalishment, and performance evaluation.

3. To investigate the unique surface texture generation principle by considering the tool tip geomerty and trajectory, and its subsequent applications on solid surface wettability modulation and liquid control in microfluidic channels.

4. To obtain a comprehensive understanding regarding the change of cutting mechanism under tool-workpiece separation or non-separation with the tool wear progression, as well as the influence of vibration frequency and amplitude variation on tool wear progression under the same tool-workpiece separation conditions.

5. To study the influence of vibration parameters on burr formantion through both experiments and simulation.

1.4 Scope of this dessertation

This thesis is categorised into seven chapters as shown in Fig. 1-1, and the methodology of this research is shown in Fig. 1-2. The brief synopsis of reminder chapters is listed in the following:

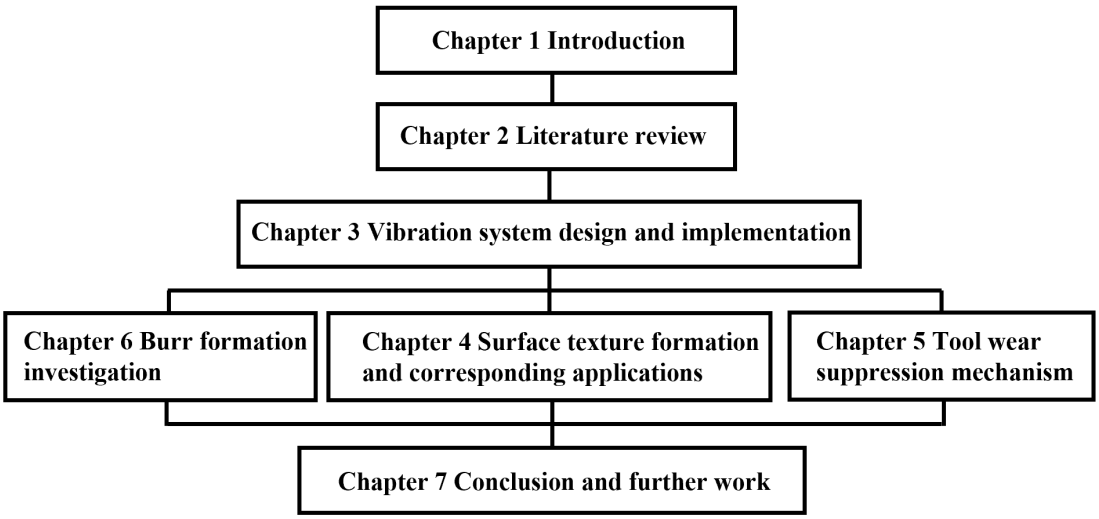

Figure 1-1 Structure of the thesis

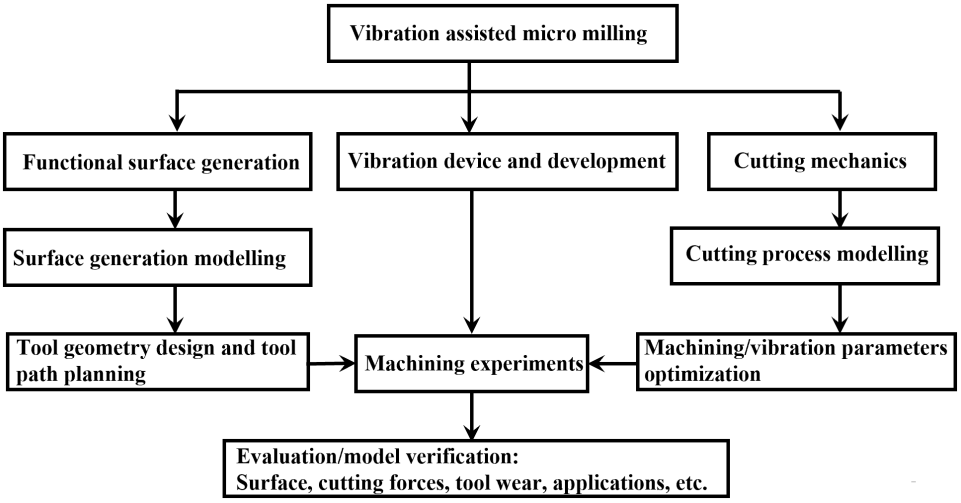

Figure 1-2 Methodology of this research

Chapter 2 explains the research background and critical reviews on the vibration assisted machining technology. It mainly includes the vibration system design, vibration assisted machining process, applications and benefits, and further trend.

Chapter 3 presents the design and implementation of the vibration system, which mainly contains mechanical structure determination and control system design. The key dimension parameters of the vibration stage are obtained through the analytical model and verified by the finite element model. The control system is developed through the combination of LabView software and DAQ devices. Moreover, the motion accuracy and the working bandwidth of vibration frequency and amplitude of the vibration system is also experimentally studied.

Chapter 4 investigates the surface texture formation mechanism and potential applications. A surface texture formation model is established by considering tool tip geometry and tool trajectories and verified through machining experiments. A contact model is proposed for describing the wettability variation of fish scale textured surface. The surface texture is used in the microfluidic chip manufacturing and the experiments result show liquid flow can be controlled successfully.

Chapter 5 comprehensively studies the tool wear suppression mechanism in non-resonant vibration assisted micro milling. The wear mechanisms and the influence of vibration parameters on flank wear, reduction in tool diameter, and tool edge radius, as well as the relationship between tool wear and cutting performance variation, are discussed.

Chapter 6 reports the burr formation investigation in non-resonant vibration assisted micro milling. Burr formation mechanism and the effect of vibration parameters on burr formation is studied quantitatively and qualitatively.

Chapter 7 highlights the conclusions and proposes the recommendations for the future work.

Chapter 2 Literature review

2.1 Overview of vibration assisted machining technology

As one of the most important unconventional machining methods, vibration assisted machining applies external energy to conventional machining process and generates high frequency small amplitude vibration on cutting tool or workpiece. It produces a periodic separation between uncut workpiece and the tool when the cutting velocity, vibration amplitude and frequency is set properly, which reduces cutting forces and generates small pieces of chips. As a result, surface finishes, tool life and form accuracy can be improved, and burr formation can be suppressed effectively.

Vibration assisted machining may be classified in two ways. The first is according to the dimensions in which vibration occurs: 1D, 2D or 3D vibration assisted machining. The other classification is based on the vibration frequency range; for example, in ultrasonic vibration assisted machining and non-ultrasonic vibration assisted machining. Ultrasonic vibration assisted machining is the most common type of VAM. It works at high vibration frequency (usually above 20 kHz) and a resonance vibration device maintains the desired vibration amplitude. Most of its applications are concentrated in the machining of hard and brittle materials due to the fact that high vibration frequency dramatically improves the cutting performance of difficult-to-machine materials. Meanwhile non-ultrasonic vibration assisted machining uses a mechanical linkage to transmit power to make the device expand and contract, and this can obtain lower but variable vibration frequencies (usually less than 10 kHz). It is easier to achieve closed-loop control due to the low range of operating frequency, which makes it uniquely advantageous in applications such as the generation of textured surface.

2.2 Review of vibration systems

A well-designed vibration system is quite important in vibration assisted machining. A typical vibration system consists of vibration sources (actuators), a vibration transmission/amplification mechanism and a control system. Generally, the actuators and transmission/amplification mechanisms selected to be complementary. Given that certain demands such as required vibration frequency and amplitude range are proposed in the design phase, the optimal overall device structure to match those demands is determined first. Then, the key structural parameters are optimized using the finite element analysis (FEA) method and

the corresponding dynamic and static characteristics can be obtained. As a result, these key values in turn influence the choice of the vibration actuators. According to the system's operating frequencies, these proposed vibration devices can be divided to two groups: the non-resonant mode and the resonant mode. In a non-resonant vibration system, the vibration actuators usually vibrate below its first natural frequency. In order to increase stability and reduce the dynamic error in the vibration stage, flexible hinge structures are widely used due to their superior dynamic response, low friction and ease of control. For a resonant system, a sonotrode (also called a horn or concentrator) vibrates at its natural frequency, transferring and amplifying a given vibration from a vibration source, which is usually a magnetostrictive or piezoelectric transducer. This system can achieve a higher operating frequency and greater energy-efficiency compared with a non-resonant system. However, its vibration trajectory cannot be controlled precisely owing to the nature of resonant vibrations and the phase lag between excitation and the mechanical response. Compared with resonant systems, non-resonant systems tend to achieve higher vibration accuracy, and it is easier to achieve closed-loop control of the vibration trajectories under low frequency conditions.

This chapter provides a general understanding of vibration systems, including actuator types and their selection, transmission/amplification mechanisms and control system design. By analysing design theories and principles, the advantages and disadvantages of various types of vibration devices are discussed. Moreover, future trends in vibration devices are also mentioned.

2.2.1 Actuators

As power output devices, actuators convert other types of energy into mechanical energy to drive the vibration stage. This not only contributes to the bandwidth of the vibration frequency and amplitude, but also to the accuracy of the motion of the vibration stage. Currently, two types of actuators, namely piezoelectric and megnetostrictive actuators are mainly selected for vibration systems. This section provides a general understanding information about these actuators, including their strengths and weaknesses.

2.2.2 Piezoelectric actuators

Piezoelectric actuators apply the unique piezoelectric properties of piezoelectric ceramics to convert high-voltage electrical energy into mechanical energy for high-frequency vibration.

Compared with other types of actuators, they have the characteristics of low cost, simple structure, small size, fast response, high control precision, the lack of magnetic field and electrical fields and no electromagnetic interference or electromagnetic noise, improving system stability and leading to more flexible designs of vibration devices. Various types of piezoelectric actuators, including stacked, thin plate, tubular and bimorph types, have been developed for different applications (Crawley and Luis, 1987; Bansevicius and Tolocka, 2002). Considering factors such as displacement output, stiffness, and frequency response, stack-type piezoelectric actuators made of multiple pieces of piezoelectric ceramic plates mechanically connected in series and electrically connected in parallel are usually chosen in actual vibration systems.

2.2.3 Magnetostrictive actuators

In the 1960/70s, the technology of PZT was not yet fully understood. And magnetostrictive actuators were the best choice for vibration devices. It applies a ripple voltage to the electromagnetic coil and its electromagnetic force is used to cause the moving core to vibrate. Although electromagnetic vibrators are reliable source of vibration, the major drawback is low energy efficiency caused by high electrical eddy current losses. These electrical losses are transformed into heat and may damage the vibrator (Geoffrey and Winston, 1989). Therefore, with electromagnetic vibrators the cooling issue always needs to be considered, leading to bulky size (Thoe, 1998). Currently, magnetostrictive actuators are usually applied in vibration systems which require low vibration frequency and large vibration amplitude.

2.2.4 Transmission mechanisms

Two mechanisms using either flexible hinges or an ultrasonic horn are mainly chosen in the design of a vibration system. The history of flexible hinge structures can be traced to the 1960s. With the development of the aerospace and aviation sectors, the resolution and size of the support in order to achieve small deflection ranges no longer met the requirements. After exploring various types of elastic support tests, engineers gradually developed flexible hinges which were characterised by high resolution, small volume, and no mechanical friction or gaps. Currently, many types of flexible hinges, including circular, elliptical, square fillet and single notch profiles have been developed and are widely used to guide the displacement of vibration in the non-resonant vibration assisted systems. In addition, they are often integrated into a

double parallel or parallel four bar linkage so as to reduce coupling motion, because the non-resonant vibration stage is usually designed to work in two or more dimensions (Wang et al. 2018). The ultrasonic horn is an important component of a resonant vibration system. It is used to transmit the mechanical energy converted from electrical energy into the workpiece by the transducer. It is a stage of the mechanical amplification of the power ultrasonic amplitude to improve the ultrasonic processing efficiency.

2.2.5 Drive and control

Besides accuracy in the processing and assembly of mechanical components, the control strategy used also has a great influence on the motion accuracy of the vibration system. Generally, these control systems can be divided as open or closed loop systems. Due to the high working frequency involved, an open loop system is the first choice for a resonant vibration system. To build a proper open loop control system for a piezoelectric actuator, a mathematical model of the piezo-driven stage needs to be built first due to its hysteresis, and non-linear and creep properties. Many methods taking into account the intrinsic mechanism and dynamic properties of piezoelectric actuators have been developed in recent decades, including the Preisach, Maxwell and Prandtl-Ishinskii models (Kuhnen, 2003; Bender, Lampaert and Swevers, 2005; Moheimani and Vautier, 2005). The reference is calculated from the corresponding control signal according to the reference input value and it is sent to the piezoelectric actuator through a piezoelectric amplifier to generate a corresponding displacement. The features of open loop control system include a simple structure and ease of implementation; however, when the object or control device is disturbed or the characteristic parameters change during the working process, error cannot be compensated for this affects the accuracy of control. To overcome this drawback, closed loop control systems are used. Close loop control systems are mainly used in non-resonant vibration systems and an industry standard controller is required. The traditional PID control method and algorithm have high control precision, but it is not suitable for uncertain time-varying systems. In contrast, fuzzy adaptive PID control can effectively identify the mathematical model of the controlled object, adjust the parameters and structure of the controller in real time according to given performance indicators, and reduce output error at this stage.

2.2.6 Vibration assisted machining systems

2.2.6.1 Resonant vibration systems

As a technology that has been successfully applied commercially, resonant vibration assisted machining systems work at the natural frequency of the system and apply the excitation vibration principle to increase the amplitude of vibration. A typical design for an ultrasonic vibration assisted machining system is the resonant rod type, which consists of three parts; namely, an ultrasonic transducer, acoustic waveguide booster and horn (see Fig. 2-1). In some research, the acoustic waveguide booster and horn are also called a sonotrode because the functions of the two components are quite similar (Brehl and Dow, 2008). The ultrasonic transducer is the source of vibration for the whole system and converts electrical energy into mechanical motion in longitudinal or compressive mode under self-excited vibration (Kumar *et al.*, 2017). Two types of electromagnetic and piezoelectric transducers are widely used and were introduced in the previous section. The high frequency low amplitude reciprocating harmonic vibration is generated by the ultrasonic transducer and amplified by the sonotrode to the desired location of a tool or workpiece. The sonotrode works by resonating with the transducer and there are strict requirements for its design and manufacturing. Poor design or fabrication will decrease the energy efficiency, reduce the cutting performance and vibration system durability, and may even cause serious damage to the transducer (Amin, Ahmed and Youssef, 1995; Sinn *et al.*, 2005; Adnan and Subbiah, 2010; Shen *et al.*, 2010). The cutting tool or workpiece is attached to the end of the horn to obtain the desired vibration. Moreover, the hold point of the whole system is usually set at node point with zero displacement in order to maintain its stability and reduce energy loss. According to the direction of movement, a resonant vibration system can be divided into three groups: 1D, 2D and 3D systems.

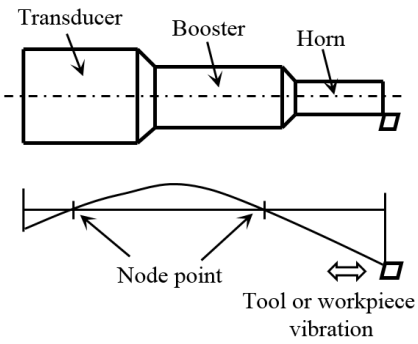

Figure 2-1 Typical design of a resonant vibrator

2.2.6.1.1 1D system

1D ultrasonic vibration assisted machining systems are the most common type due to their simple structure and ease of implementation. They can be divided into resonant rod and resonant tool types. Many researchers have proposed their own rod type vibrators. Zhong et al. (Zhong and Lin, 2006) improved the typical resonant rod type system and applied it to the turning process, as shown in Fig. 2-2 (a). A tool holder with a notch structure is introduced into the design to hold the tool firmly in place and to reduce its moving in the other degrees of freedom. During the machining process, bending occurs at the notch point to prevent deformation in the rest of the tool holder. Otherwise, the tool holder in proximity to a parabolic shape will affect machining performance. To obtain a more accurate measurement of cutting force during the vibration assisted milling process, a special clamp system was designed by Shen et al. (Shen et al. 2012) by integrating the clamping system and a dynamometer, as shown in Fig. 2-2 (b). The results showed that the impact of ultrasonic vibrations on measurement results are reduced effectively. Similarly, Liu et al. (Liu *et al.*, 2012; Nath and Rahman, 2008) studied ductile mode cutting with tungsten carbide, as shown in Fig. 2-2 (d). The new clamping system fixes the vibrator using four bolts, which simplifies the installation procedure of the vibrator and improves its accuracy.

The resonant rod type 1D resonant vibration system has a simple structure and high reliability; however, the resonance frequency of the system can be easily influenced when a workpiece or large mass is attached to the horn. Meanwhile, the issue of the installation of oversized part is also difficult to solve. Therefore, another type of resonant vibration system named resonant tool was developed by integrating the resources of vibration into the tool holder. A typical design was proposed by Ostasevicius et al. (Ostasevicius *et al.*, 2013). The milling cutter assembly is driven by piezo ceramic rings which are fixed into a standard Weldon tool holder and generate resonant tool movement in the vertical direction. Similarly, Alam et al. (Alam, Mitrofanov and Silberschmidt, 2011) improved the tool cutting assembly design and obtained a seven-fold increase in vibration amplitude by using a stepped shape of horn structure (Fig. 2-2 (c)).

As discussed in the previous sections, the vibration parameters for an ultrasonic vibration system largely depend on the dimensions and cross-sectional shape of the designed vibration transmission mechanism consisting of the booster and horn. However, the traditional approach

is based on the application of differential equations where the equilibrium of an infinitesimal element is taken into consideration under the influence of elastic and interia forces. This is time-consuming and inaccurate. To overcome these drawbacks, FEA is introduced at the design stage of the ultrasonic vibration system and its use can increase the accuracy of the vibration system, such as in natural frequency and the dimensions of the mechanism, which speeds up the development of vibration devices. Kuo (Kuo, 2008) proposed a milling cutter assembly design where the process of harmonic piezoelectric vibrations was simulated by an FEA dynamic simulation which optimized the key dimensions, reduced the influence of stress concentration on the system and increased its system efficiency. However, the simulation did not consider a situation where a tool is attached to the horn and this leads to a deviation in the system's natural frequency and vibration amplitude between the simulation results and operational results. Roy et al. (Roy, 2017) developed a circular hollow ultrasonic horn for milling cutter assembly and optimized its outline and cross-sectional shape by using FEA. Compared with conventional ultrasonic horn designs, such as those with stepped, conical and exponential shapes, the circular hollow ultrasonic horn achieved a higher magnification factor and lower axial, radial and shear stress, hence improving system performance and reducing the influence of stress concentration.

A different type of vibration drilling tool assembly design was proposed by Babitsky et al. (Fig. 2-3 (a)). In order to accomplish vibration assisted drilling, one side of the assembly was clamped in the three-jaw chunk of the lathe through the intermediate bush and energized by means of a slip-ring assembly fitted to the hollow shaft of the lathe at the end remote from the chuck (Babitsky, Astashev and Meadows, 2007). A further 1D ultrasonic vibration system was developed by Hsu et al. (Huang and Wu, 2007) and its working principle is quite similar to the ultrasonic bath. As shown in Fig. 2-3 (b), three commercial Langevin ultrasonic transducers were fixed underneath the vibration stage and were controlled by the same type of signals, generating vibrations at the same frequency and phase. As a result, resonance vibration can be obtained in the vibration stage.

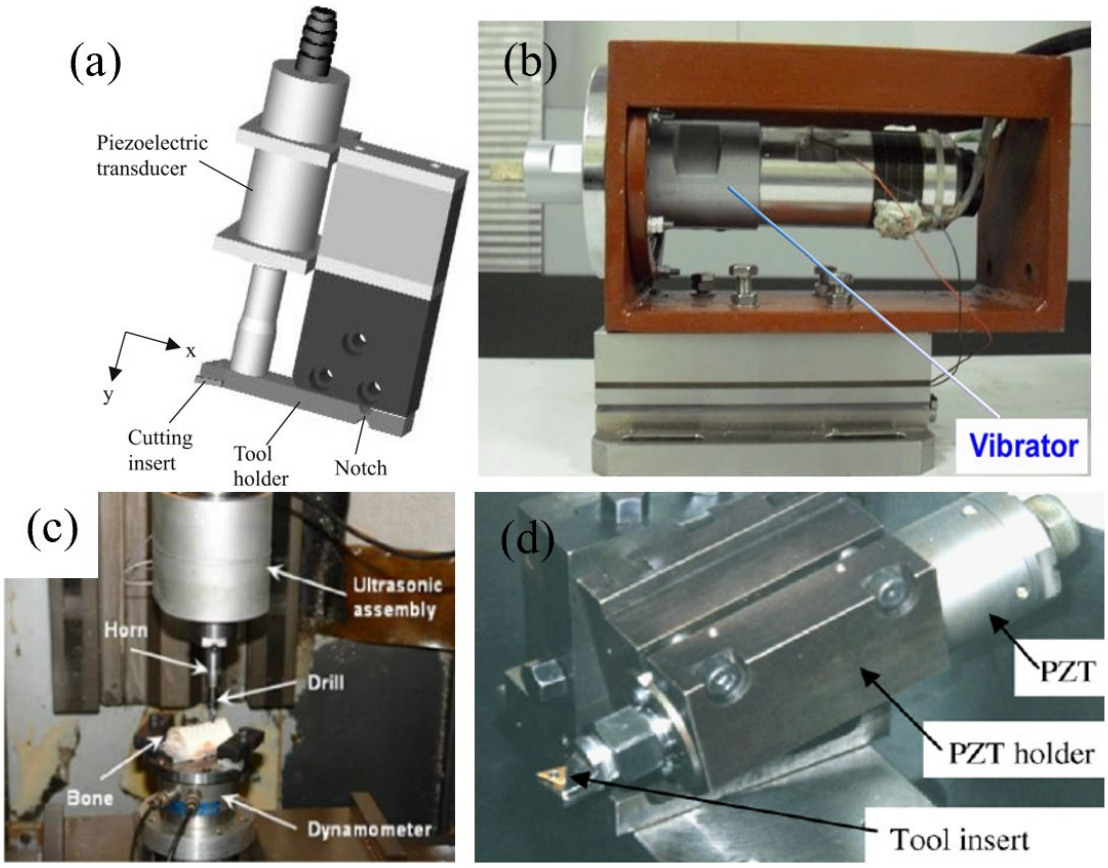

Figure 2-2 Vibrators, (a) Resonant rod type vibrator(Zhong and Lin, 2006); (b) Vibrator proposed by Shen et al. (Shen *et al.*, 2012); (c) Vibrator proposed by Alam et al. (Alam, Mitrofanov and Silberschmidt, 2011); (d) Vibrator proposed by Liu et al. (Liu *et al.*, 2012; Nath and Rahman, 2008)

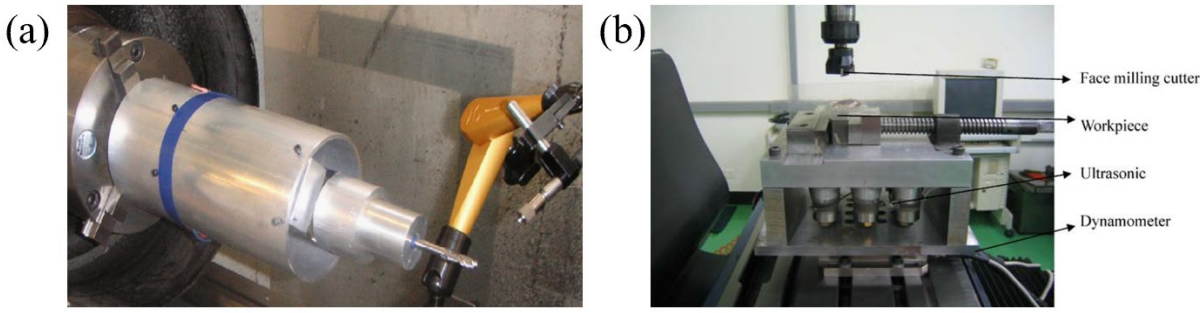

Figure 2-3 Vibrators, (a) Vibrator proposed by Babitsky (Babitsky, Astashev and Meadows, 2007); (b) Vibrator proposed by Hsu et al. (Hsu, Huang and Wu, 2007)

2.2.6.1.2 2D and 3D systems

Ultrasonic elliptical vibration assisted machining is also named 2D ultrasonic vibration assisted machining and has received widespread attention since it was first proposed in 1993. Compared with 1D systems, 2D systems can obtain better cutting performance and also require a higher standard of vibration devices. Due to its simple structure and ease of implementation, the

integrated resonant rod device is the most popular in proposed 2D vibration devices. There are two main designs: patch and sandwich types. For the patch type of integrated resonant rod, two sets of piezoelectric plates are attached to the outer wall of the resonant rod to achieve the same or different modes of resonance. In the sandwich type, two modes of resonance moment can be obtained by adding another set of piezoelectric rings to the 1D resonant rod. Moriwaki et al. (Moriwaki, 1995) developed a 2D patch-type ultrasonic vibration assisted turning system (Fig. 2-4 (a)) by attaching two pairs of piezoelectric actuators symmetrically in the centre of the four sides of a stepped horn. When two sinusoidal signals with different phases and the same frequency are applied to the piezoelectric actuators, a bending resonance state can be obtained in the vibrator in two mutually perpendicular directions simultaneously and the cutting tool attached at the end of the vibrator vibrates in elliptical mode. The coupling effect cannot be avoided, as the piezoelectric plates are placed in parallel. Shamoto et al. (Shamoto and Moriwaki, 1999; Shamoto *et al.*, 2002) optimized the dimensions and shape of the vibration rod and developed a control system to achieve more accurate tool trajectory. Experiments were conducted on hardened stainless steel and the machining accuracy and machined surface quality improved. A combination of bending and longitudinal vibration modes was also achieved in a different 2D patch-type ultrasonic vibrator designed by Liang et al. (Liang *et al.*, 2010; Peng *et al.*, 2012), as shown in Fig. 2-4 (b). The piezoelectric plates are bonded at the same side of the metal elastic body and the workpiece is fixed to the top of the vibrator. However, the vibration amplitudes involved are quite small only up to 0.4 μm due to mass issues with the vibrator, and an effect of workpiece mass on the vibration's amplitude and frequency is unavoidable.

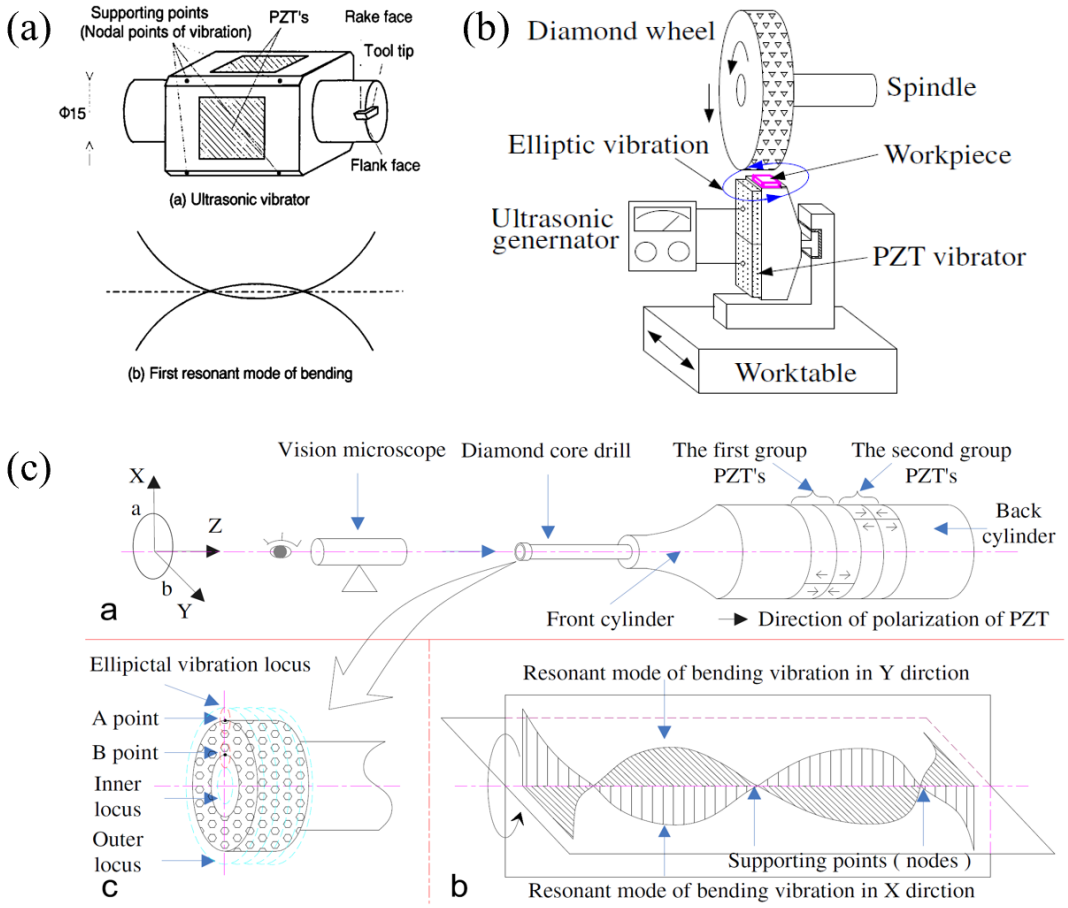

Figure 2-4 Vibrators, (a) vibrator proposed by Moriwaki et al. (Moriwaki, 1995); (b) Vibrator proposed by Liang et al. (Liang *et al.*, 2010; Peng *et al.*, 2012); (c) Vibrator proposed by Liu et al. (Liu *et al.*, 2012)

A typical sandwich type elliptical ultrasonic vibrator is shown in Fig. 2-4 (c) (Liu *et al.*, 2012; Geng *et al.*, 2015). The two groups of piezoelectric rings are sandwiched together in the drilling cutter assembly, and each group works at a different resonant mode to generate an elliptical tool tip trajectory. It should be noted that the installation point of this type of vibration device should be set at the coincidence point of the two resonance modes. Meanwhile, vibrators for mounting workpiece or non-rotating tools such as for turning and polishing have also been proposed using the same design principle (Li and Zhang, 2006; Suzuki *et al.*, 2006; Suzuki *et al.*, 2007, 2010; Yin *et al.*, 2017; Yin *et al.*, 2017). To achieve better performance, Börner et al. (Börner *et al.*, 2018) developed a cross-shaped converter for a 2D ultrasonic vibration assisted vibrator (Fig.2-5 (a)) and applied it to the milling process. As the high frequency vibration is transmitted to the cross-converter, the extension in horizontal direction will lead to a compression in the vertical direction. However, only small specimens can be used because those large of mass may influence the resonance frequency of the vibrator. Tan et al. (Tan *et*

al., 2018) built a symmetrically structured ultrasonic elliptical vibration assisted device (Fig. 2-5 (b)) using four pairs of piezoelectric rings. The node point of the device is naturally set at the centre of the flange, which is easy to locate. The device is fixed by two pair of grip holes displaced on both sides of the flange to reduce energy loss and improve cooling performance. Compared with the conventional design, the symmetrical structure can completely balance the internal force, which dramatically reduces error in the vibrator's motion. By changing the piezoelectric actuator to a magnetostrictive actuator, Suzuki et al. (J. Guo *et al.*, 2012; Jiang Guo *et al.*, 2012; Guo, Suzuki and Higuchi, 2013) developed an elliptical vibrating polisher (Fig. 2-5 (c)) and applied successfully it to process micro-aspheric lenses and tungsten carbide die/mold. The vibrator is based on a giant magnetostrictive material and with coils wound around it. It has four legs and each leg can be independently controlled for expansion or contraction. The elliptical tool trajectory can be obtained by appropriately setting the phase difference of the two pairs of opposing coils. To obtain the highest vibration amplitude, the vibrator is designed to work at a frequency of 9.2 kHz, which limits its processing performance.

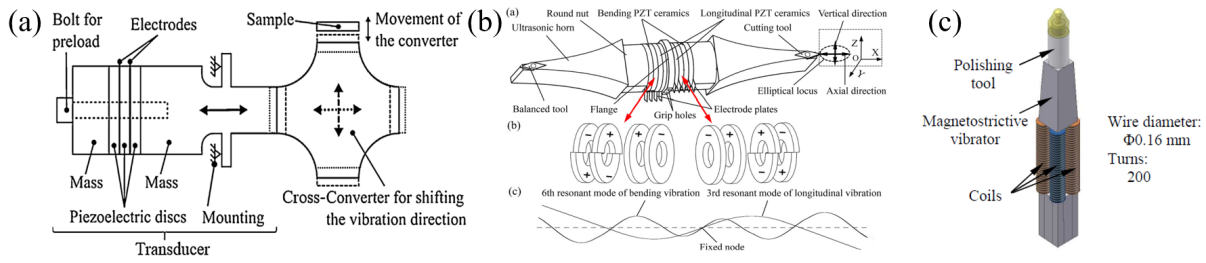

Figure 2-5 Vibrators, (a) Vibrator proposed by Börner et al. (Börner *et al.*, 2018); (b) Vibrator proposed by Tan et al. (Tan *et al.*, 2018); (c) Vibrator proposed by Suzuki et al. (J. Guo *et al.*, 2012; Jiang Guo *et al.*, 2012; Guo, Suzuki and Higuchi, 2013)

Different from integrated resonant mode vibration devices, a separate type of 2D resonant vibrators uses two independent Langevin vibrators placed in a V or L shape to obtain a two-dimensional vibration of the tool or workpiece (Kurosawa *et al.*, 1998; Zhang *et al.*, 2005; Asumi *et al.*, 2009). Fig. 2-6 (a) shows a typical separate 2D V-shaped vibrator proposed by Guo et al. (Guo and Ehmann, 2013). The two Langevin vibrators are set at an angle of 60 degrees to generate a unique tool tip trajectory. The head block is a flexure structure applied at the end of each vibrator to guide motion and reduce movement error. Each individual vibrator has an added end mass to preload the piezoelectric rings and adjust the natural frequency of the vibrators. A similar design was also applied in a vibration assisted polishing process (Song *et al.*, 2016). Yan et al. (Yanyan, Bo and Junli, 2009) developed a 2D 'L'-shaped resonant vibrator

for grinding, as shown in Fig. 2-6 (b). Two independent 1D resonant vibrators are placed perpendicularly on the sides of the vibrating stage. However, this type of 2D resonant vibrator is almost impossible to integrate into a rotating tool such as in a milling cutter assembly, which limits its application.

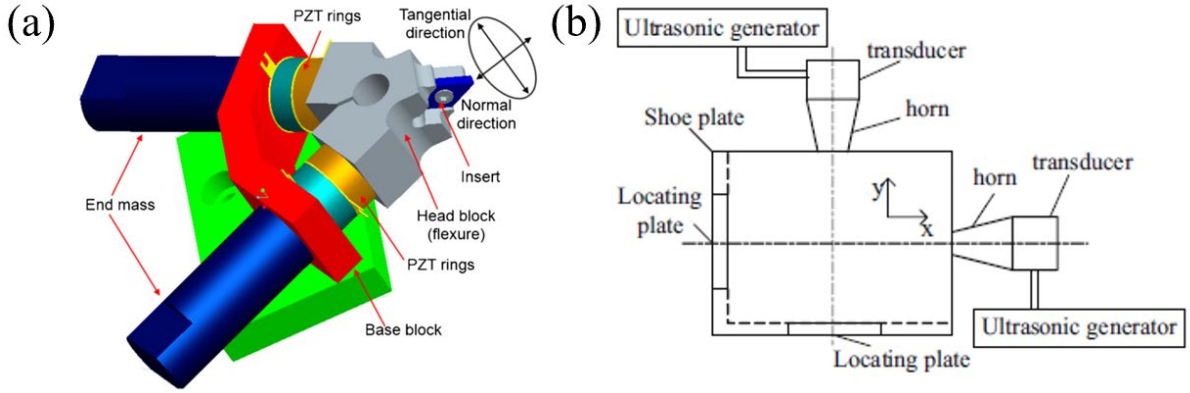

Figure 2-6 Vibrators, (a) Vibrator proposed by Guo et al. (Guo and Ehmann, 2013); (b) Vibrator proposed Yan et al. (Yanyan, Bo and Junli, 2009)

In order to obtain complex geometrical shapes, the milling process requires a feed vector in arbitrary directions with both vertical and horizontal components of feed vector necessary for 3D end milling. Hence there is a need for three-dimensional vibration assistance. Fig. 2-7 shows a three degrees of freedom resonant vibration tool which can generate longitudinal and two bending resonance mode vibrations by adding three sets of piezoelectric actuators to a resonance rod (E. Shamoto *et al.*, 2005; Eiji Shamoto *et al.*, 2005; Suzuki, Hino and Shamoto, 2007). The difficulty associated with this design is to accurately locate the node point of the vibration rod and to achieve three modes of resonance frequencies which are as close as possible to obtain sufficient vibration amplitude. Moreover, the crosstalk between the three resonance modes is much more prominent than that in a 2D resonant system. In order to reduce the motion coupling effect, stepped and the tapered portions are added to the resonant rod and the overall shape and dimensions are optimized so as to obtaining optimal performance.

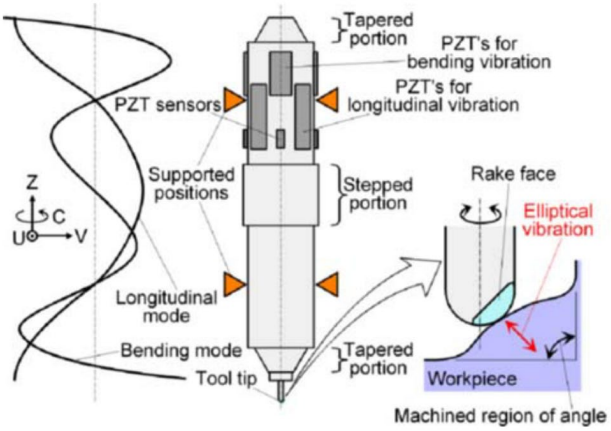

Figure 2-7 Layout of the 3D vibrator (E. Shamoto *et al.*, 2005; Eiji Shamoto *et al.*, 2005; Suzuki, Hino and Shamoto, 2007)

2.2.6.2 Non-resonant vibration system

Generally, resonant vibration systems are capable of achieving extremely high operating frequencies, and most of them can even reach ultrasonic vibration frequency levels (≥ 20 kHz). However, their limitations of fixed working frequency and vibration motion parameters, heat dissipation, open loop control and poor dynamic accuracy are also quite obvious. In addition, the performance of the vibrator heavily relies on the dynamic characteristic of the vibration horn, which increases the difficulty of vibrator design. To overcome those shortcomings in the resonant vibrator, much more attention has been paid to non-resonant vibration systems. Non-resonant systems apply forced vibration rather than excitation vibration as the design principle and produce variable vibration frequencies. However, it is hard to achieve a high working frequency, which is always less than the natural frequency, due to the issue of structural stiffness. Many of these designs are inspired by high precision micro/nano positioning stages (Lee *et al.*, 2007; Syahputra, Ko and Chung, 2014), and are discussed below.

The working principle of non-resonant vibration system can be explained by the schematic diagram in Fig. 2-8 (a). The whole system is driven directly by the preloaded piezoelectric actuator. In order to accurately transmit motion and reduce parasitic movement, flexible mechanisms (flexure hinges), which can be simplified into a set of spring-damper mechanisms, as shown in Fig. 2-8 (a), are always chosen as the linkage between the actuators and end executor. A displacement amplifying mechanism can be integrated into the flexure hinges if the amplitude is required larger than the displacement generated by the piezoelectric actuator. Moreover, decoupling issues also need to be considered in the design phase of the flexible mechanism when multidimensional motions are required.

Compared with resonant vibration systems, higher motion accuracy can usually be achieved with a non-resonant vibration system due to its inherent merits. This makes it more suitable for the manufacturing of micro-structured surfaces. Therefore, 1D non-resonant vibration systems are quite rare due to the complex tool trajectories required in producing unique surface microstructures. A typical design of a 1D non-resonant vibration system uses a combination of a parallel four-bar flexure hinge structure and a piezoelectric actuator (Kurniawan *et al.*, 2017). Fig. 2-8 (b) shows a 1D non-resonant vibration system design proposed by Long et. al. (Hong and Ehmann, 1995; Greco *et al.*, 2009). A single piezoelectric actuator is positioned at the parallel four-bar flexure hinge structure, which also includes a vibration displacement amplification function. The structural layout and closed-loop control system ensure high motion precision. A different design was proposed by Suzuki et al. (Suzuki *et al.*, 2017) with a complex mechanical structure. To ensure cutting accuracy, this vibrator aims to achieve high axial mechanical stiffness so as to reduce elastic deflection during the machining process. A cylindrical roller bearing is set between the cutting tool and piezoelectric actuators to guide the vibration and support the bending force acting on the cutter insert, and the twisting force in the machining process is supported by the pin. Moreover, bending stress is further reduced due to the flexible tip. Consequently, the shear stress which could damage them cannot be transmitted to the piezoelectric actuators. Because the output voltage for the control of the vibrator may reach up to 1000V, an air-cooling system is also integrated into the vibrator to prevent overheating.

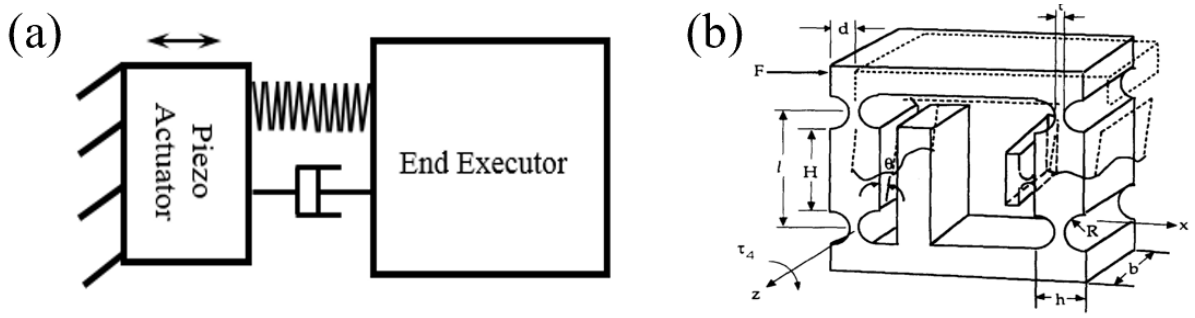

Figure 2-8 (a)Working diagram of non-resonant vibrator; (b) Vibrator proposed by Greco et al. (Greco *et al.*, 2009)

2.2.6.2.1 2D system

Compared with 1D systems, the application of 2D systems is more flexible. However, the coupling effect between the two vibration directions has a great impact on its accuracy. Two

configurations exist among the proposed designs, a vibration tool mainly for turning, and a vibration stage mainly for milling. A flexible hinge structure is often used to guide motion, and to reduce motion error and the coupling effect, although some other designs have also been reported. Brehl et al. (Brehl et al. 2006; Wang 2001) developed two types of non-resonant elliptical vibration assisted machining devices at two different working frequencies. One of these vibrators (Fig.2-10 (a)) works at a high vibration frequency up to 4.5 kHz but low vibration amplitude of less than 2 µm and requires a cooling chamber to prevent the vibrator from overheating. The other design (Fig. 2-10 (b)) operates at a low vibration frequency of 400 Hz but high vibration amplitude up to 22 µm and does not need an extra cooling system. The design principles of the two vibrators are almost the same. Two piezoelectric actuators are placed in parallel and generate two sinusoidal vibrations with a specific phase difference. Then, two sets of parallel high-frequency vibration motions are converted by the "T" shape tool holder into the desired elliptical cutting tool trajectory. To simplify the structure and improve the working frequency band of the vibrators, the piezoelectric actuators are used to achieve cutting tool support and positioning in both vibrator designs. However, the drawback of this design is that the accuracy of the vibrators is hard to guarantee under the conditions of open loop control. Therefore, it is not suitable for the precision machining processes due to the non-linear hysteresis and creep behaviour of the piezoelectric actuators which is unavoidable.

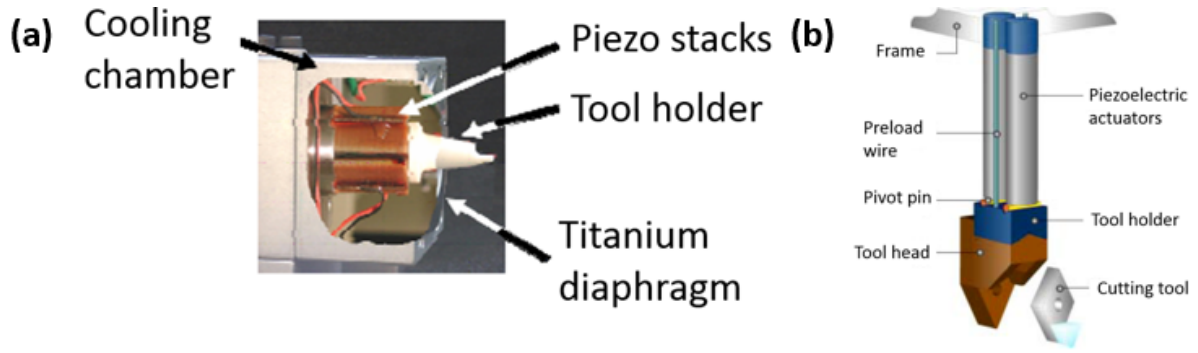

Figure 2-9 Vibrator proposed by Brehl et al. (Brehl et al. 2006; Wang 2001)

Another two design of 2D non-resonant vibration tool assembly (Fig. 2-11) were proposed by Kim et al. (Kim and Loh, 2007). Two stacked piezoelectric actuators are fixed/preloaded by a through-bolt on the tool holder and placed in parallel and perpendicular to each other respectively. A similar design proposed by Li et al. (Li *et al.*, 2018) uses four pairs of piezoelectric plates symmetrically placed at both side of the vibration platform. However, the major drawback of these designs is the motion coupling between the two motion directions,

which causes tangential shear stress inside the piezoelectric actuator and damages the vibrator. To overcome these drawbacks, many optimized design proposals have been proposed. Loh et al. (Loh and Kim, 2012) improved the current vibrator design and a better performance was obtained in their experiment results. Compared with the original design, the structure of the tool holder is optimized and a hemispherical structure is added at the junction of the piezoelectric actuator and tool holder, which changes the connection mode between them from surface contact to point contact. As a result, the motion coupling between the two piezoelectric actuators can be effectively avoided and potentially hazardous shear deformation of the piezoelectric actuators reduced. Another design adds cross-shaped voids to the tool vibrator, and the results show that the cross-interference of the vibration of each axis is effectively suppressed (Ahn, Lim and Son, 1999). Chern et al. (Chern and Chang, 2006) put forward a different vibration design employing a combination of piezoelectric actuators and linear guideways (see Fig. 2-12). However, the coupling effect cannot be reduced effectively because the end spring of the vibrating stage has no torsional stiffness.

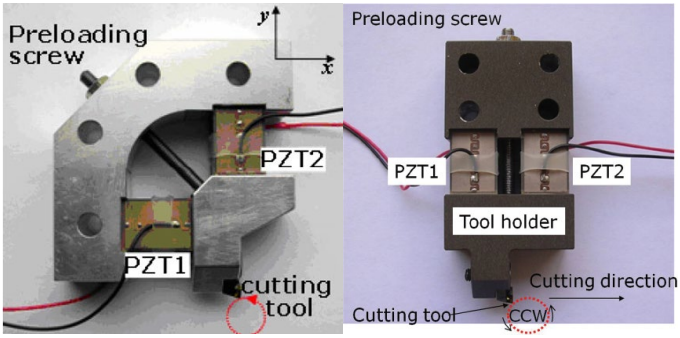

Figure 2-10 Vibrator proposed by Kim et al. (Kim and Loh, 2007)

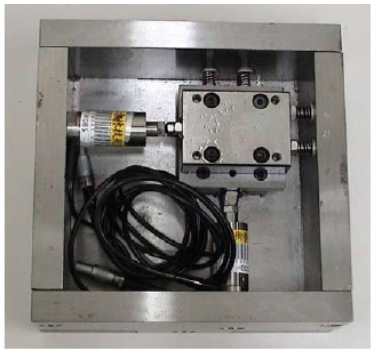

Figure 2-11 Vibrator proposed by Chern et al. (Chern and Chang, 2006)

To obtain better cutting performance and a more accurate tool tip trajectory, various non-resonant vibration stages with flexure joint based structures have been proposed. One of these designs uses independent driving, where each group of piezoelectric actuator drives one

direction of the vibrator and movement in each direction is independent of the others in order to minimize mutual coupling. A typical 2D non-resonant vibration stage based on the flexure joint based structure was developed by Jin et al. (Jin and Xie, 2015). The movable vibration table is connected to the piezoelectric actuators through flexible hinge structures in both directions. As the two piezoelectric actuators work together, the motion of the flexure hinges will be affected by coupling stiffness leading to an uneven displacement between the two directions, which makes it hard to control them precisely. Ding et al. (Ding, Chen and Cheng, 2010) built a non-resonant elliptical vibration stage using a parallel-kinematic double flexible hinges structure. The stage is driven by two independent piezoelectric actuators which are placed perpendicular to each other. The parallel-kinematic double flexible hinge structure has advantages such as compactness, high stiffness levels and no friction. In addition, it also reduces the coupling effect of the vibration stage. also a single flexure parallel four bar elliptical vibration stage has been developed using four flexible hinges supporting the movable stage (see Fig. 2-13) (Li *et al.,* 2012). However, a large stress concentration and parasitic movements cannot be eliminated due to structural defects. A planar integrated vibration stage with a symmetrical double flexible parallel four-bar structure was proposed by Zhang et al. (Zhang and Sun, 2006). It features a compact structure, zero clearance and no mechanical friction, which leads to better guidance properties. Compared with the single-parallel four-bar structure vibration stage, it not only eliminates the cross-coupling displacement, but also weakens the external interference to a certain extent. Another compact 2D non-resonant vibration stage design was proposed (Ibrahim, 2010; Ding *et al.*, 2011). Two pairs of piezoelectric actuators are placed symmetrical in flexible hinges around the oval mechanical structure. The circuit board is integrated into the vibration stage, which reduces the device's volume.

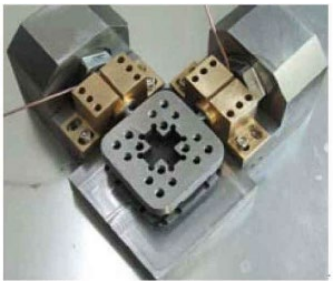

Figure 2-12 Vibrator proposed by Li et al. (Li *et al.,* 2012).

Another design applies two or more piezoelectric actuators in the same or multiple directions to produce a compound elliptical motion. A more complex tool trajectory can be obtained compared with an independently driven vibrating stage. In order to reduce the influence of

other factors on the vibration amplitude and frequency, it is usually integrated with the machine tool (Liu *et al.*, 2015). A flexible hinge structure based 2D vibration turning tool was also proposed as shown in Fig. 2-14 (a) (Kim *et al.*, 2009) . The design principle of the vibrator uses a set of vertically connected biaxial flexible hinges to support and guide the tool holder. When the tool holder is driven by two piezoelectric actuators, the elastic deformation of the flexible hinges in different directions can be employed to synthesize the motion of elliptical tool tip. Lin et al. (Lin *et al.*, 2017) reported a piezoelectric tool actuator (PETA) for elliptical vibration turning based on a hybrid flexure hinge connection (see Fig. 2-14 (b)). It consists two parallel four-bar linkage mechanisms and two right circular flexure hinges and effectively improves vibration accuracy and reduces the coupling effect between the two motion axes. The step responses, motion strokes, vibration resolutions, parasitic motions and natural frequencies of the PETA along the two input directions were analysed and the results show that the vibrator is capable of precision machining. A 2D low frequency vibration assisted polishing tool assembly is proposed by Chee et al. (Chee *et al.*, 2011). It consists of four mechanical amplitude magnified actuators screwed together on a centre piece which generates a planetary elliptical tool tip trajectory. Although the non-integral structure reduces the design and manufacturing difficulty of the vibrator, higher installation accuracy is also required due to the fact that the assembly accuracy has a great influence on the vibrator motion trajectory. To solve this problem and achieve higher tool motion accuracy, another 2D low frequency vibrator is shown in Fig. 2-14 (c) (Chee *et al.*, 2013). Three mechanical amplitude magnified actuators are arranged in a triangle around the centrepiece, and a highly repeatable and stable polishing trajectory can be obtained. In addition, the 2D low frequency vibrator is attached to a low contact force loader, which further reduces the polishing force and prevents damage to the surface layer of the workpiece. Compared with the previous system, this vibration system has advantages such as higher vibration accuracy, and lower grinding force and energy consumption, and the resolution of the vibration is also improved to 0.1 μm.

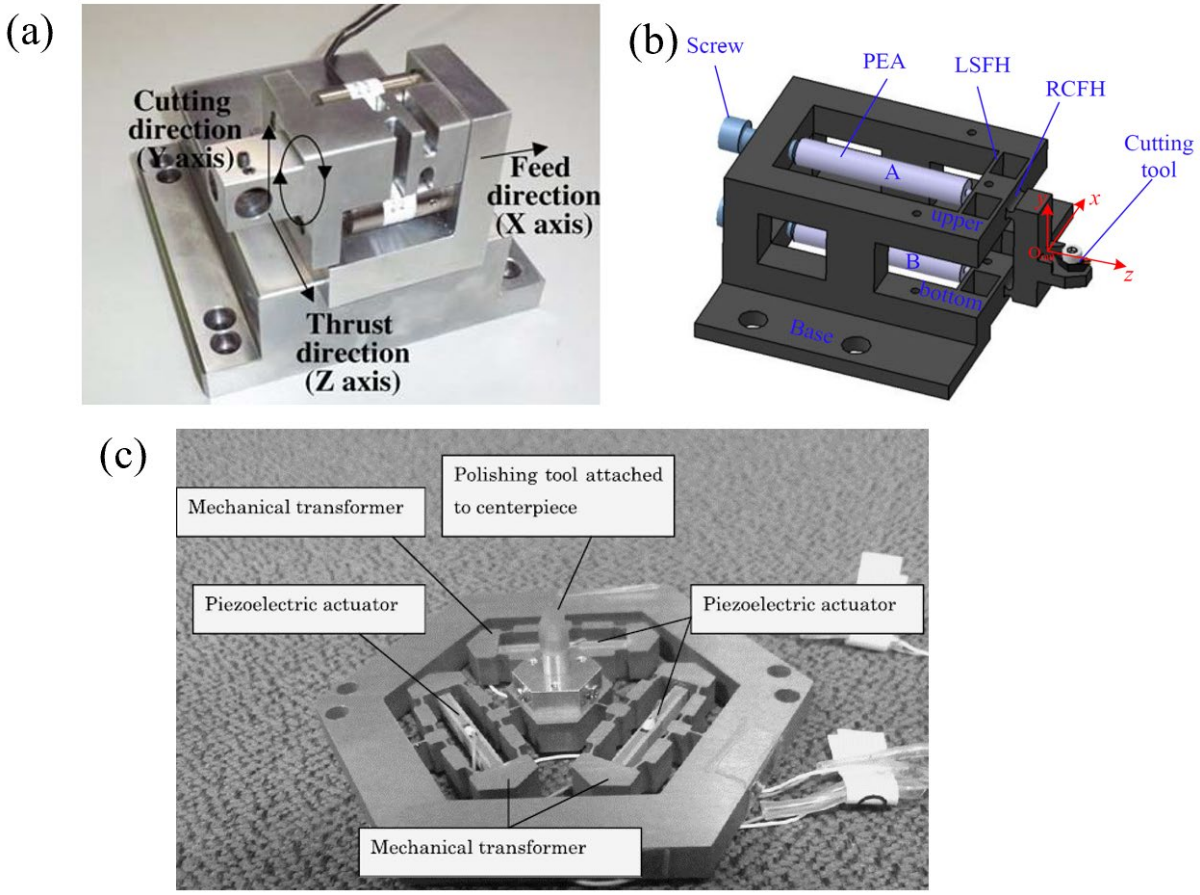

Figure 2-13 Vibrators, (a) Vibrator proposed by Kim et al. (Kim *et al.*, 2009); (b) Vibrator proposed by Lin et al. (Lin *et al.*, 2017); (c) Vibrator proposed by Chee et al. (Chee *et al.*, 2013)

2.2.6.2.2 3D systems

As an important part of non-resonant systems, the 3D vibration system can generate a more complex tool trajectory which is suitable for special applications such as the production of optical freeform surfaces on hard and brittle materials (Jieqiong, Yingchun and Xiaoqin, 2014). Similar to the design of the 2D non-resonant vibrator, the 3D non-resonant vibrator can also be divided into compound motion and independent drive types. For the latter 3D non-resonant vibrator, the coupling can seriously influence the accuracy of motion due to the motion of the vibration device which is composed of individual movements in three axes. In addition, the totally decoupled motions always require a large number of linkages with special structures needed for motion isolation, causing relatively low response rates (Li and Xu, 2011). Wang et al. and liu et. al. proposed two similar 3D non-resonant vibration devices (Wang, 2012; Liu *et al.,* 2013). However, their complex flexure joint based structures result in low bandwidth and response speeds. To overcome these drawbacks, a different type of independent drive 3D non-

resonant vibration device has been developed which is shown in Fig. 2-15 (a) (Zhu *et al.*, 2017). In this design, low coupling and high motion accuracy and response rates can be obtained by employing a compact and rotationally symmetrical structure and special flexure hinges with multiple DoFs. Fig. 2-15 (b) shows a representative design of the compound motion type 3D of non-resonant vibration device (Lu, 2014; Lin, Lu and Zhou, 2016). The vibration device is driven by four piezoelectric actuators and the different 3D motion planes and trajectory can be obtained by changing the acting locations of the piezoelectric stacks or parameters of the signals. By installing displacement sensors, this vibration device achieves closed-loop control and better motion accuracy.

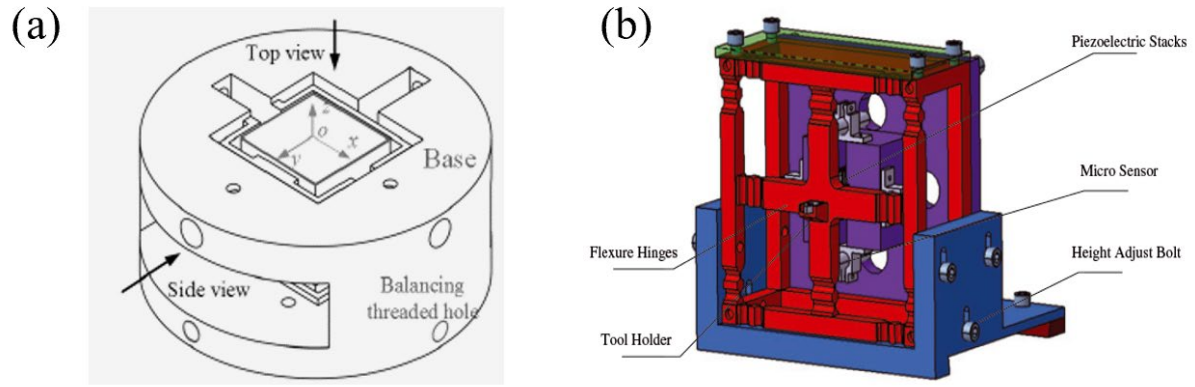

Figure 2-14 (a) Layout of a 3D non-resonant vibrator (Zhu *et al.*, 2017); (b) Compound motion type 3D vibrator (Lu, 2014; Lin, Lu and Zhou, 2016)

2.2.7 Future perspectives

With a deeper understanding of the cutting mechanisms in vibration assisted machining technology, its potential for processing hard and brittle material is gradually being explored. However, this also leads to stricter requirements for stability and real-time frequency tracking technology in vibration assisted machining systems due to the high loads involved in the machining process. Therefore, an inevitable trend has been to improve resonant vibration systems to adapt to large loads and frequency drift. At present, ultrasonic resonance devices are basically set at the cutter side because of the unpredictable mass and size of workpieces, which further affects amplitude and frequency of the resonant vibration. Nevertheless, the resonant state of the ultrasonic system is greatly influenced by the factors such as tool materials and clamping mode. Meanwhile, besides high frequency ultrasonic vibration, high cutting loads are also applied directly to the cutter, which leads to high standards requirement of cutting

tool (Zhang *et al.*, 2017). Accordingly, one of the most important trends in resonant vibration assisted machining systems is improvement in the system and the development of special tools. By taking into account the characteristics of ultrasonic vibration cutting and the integration of cutting tool and ultrasonic vibration system from the perspective of integrated collaborative design, tools can be adapted to the vibration system while meeting the processing requirements, which further ensures the stability of the resonant vibration system. In addition, the issue of overheating in ultrasonic vibration systems operating for long periods is also a problem which needs on urgent solution. Designing a dedicated vibration system with an internal cooling function will help to solve this problem. Due to the characteristic of the piezoelectric materials, nonlinear hysteresis nonlinear creep is unavoidable, which is one of the important factors affecting the motion accuracy of the vibration device. Therefore, the development on the field of precision drive and control system is also a critical trend.

As reviewed in the previous section, 2D vibration assisted machining systems are the most common type of non-resonant vibration system, and these systems are always built using piezoelectric actuators to drive the flexible hinges directly. In addition, most flexible hinge structures are designed to be symmetrical and the current effort in performance improvement of non-resonant vibration assisted machining systems is mainly focused on the optimization of shape, which limits improvements in performance. For serial flexible hinge structures in non-resonant vibration system, the main drawbacks are the accumulation of vibration error, low working frequency bandwidth and structural redundancy. For parallel flexible hinge structures in non-resonant vibration systems, the coupling effect between different axes is unavoidable, which seriously affects the motion accuracy of the system and can induce shear stress inside the piezoelectric actuators and damage them. Therefore, structural optimization of non-resonant vibration systems so as to improve vibration accuracy and reduce coupling effect is a major development trend.

Currently, vibration assisted machine tools for difficult-to-machine materials have not yet reached maturity. The reliability of the machine tool system and stability in long-term operation need to be evaluated and strengthened. Many sectors such as the aerospace and medical areas have high demand for stable ultrasonic-assisted machine tools. Hence, integrating current research results for ultrasonic vibration assisted technology and the development of special ultrasonic vibration auxiliary equipment will soon become an important research priorities.

2.3 Investigation on vibration assisted machining process

This section briefly introduces commonly used vibration assisted machining processes, including in milling, drilling, turning, grinding and polishing. Different vibration device layouts are required to implement these vibration assisted processes and to achieve advantages over the corresponding conventional machining processes.

2.3.1 Vibration assisted milling

Milling is one of the most common machining processes and is capable of fabricating parts with complex 3D geometry. However, uncontrollable vibration problems during the cutting process are quite serious and can affect processing stability, especially in the micro milling process, leading to excessive tolerance, increased surface roughness and higher cost. Vibration assisted milling is a processing method that combines the external excitation of periodic vibrations with the relative motion of the milling tool or workpiece to obtain better cutting performance. In addition to the same advantages as other vibration assisted machining processes, complex surface microstructures can also be obtained due to the combination of a unique tool path and external vibration. Currently, the application of vibration-assisted milling mainly focuses on the one-dimensional direction. The vibration may be applied in the feed direction, cross-feed direction or axial direction, and tool rotational vibrations may also be applied (Brehl and Dow, 2008). Little research has been carried out on 2D vibration-assisted milling due to the difficulty of developing two-dimensional vibration platforms (motion coupling, control difficulty), and the vibration mode of these 2D vibration devices mainly involves elliptical vibration and longitudinal torsional vibration.

2.3.2 Vibration assisted drilling

Problems such as large axial forces and poor surface quality are found in the process of drilling the hard and brittle materials. Vibration assisted drilling technology combines the vibration assisted machining mechanism with the traditional drilling process, and this can achieve more efficient drilling, especially for small bore diameters and deep holes. Compared with conventional drilling, the interaction between the tool and the workpiece is changed and the drilling tool edge cutting conditions are improved. Vibration assisted drilling has found applications in the high-efficiency and high-quality machining of various parts with difficult-to-machine holes (Baghlani *et al.*, 2016). Its main merits are as follows:

(1) Reductions in drilling power and drilling torque. The vibration changes the interaction between the drill tool and the workpiece and the cutting process changes from continuous cutting to intermittent cutting, leading to lower tool axial force. In addition, the friction factor between the tool and the workpiece/chips is reduced due to the pulse torque formed by the vibration. As a result, drilling torque is reduced (Alam, Mitrofanov and Silberschmidt, 2011; Ding *et al.*, 2014).

(2) Improvement in chip breaking and removal performance. The chip breaking mechanism is quite different when vibration is added. Fragmented chips can be obtained under certain vibration and machining parameters. Chip removal performance is much better compared with the continuous chips produced in conventional drilling (Chen *et al.*, 2019).

(3) Improvement in the surface quality of the walls of the drilled holes. In the vibration assisted drilling process, the reciprocal pressing action of the cutting edge on the inner hole surface is beneficial in reducing surface roughness. Moreover, the improved chip breaking performance also leads to smoother chip removal, which reduces the scratching of the drilled hole surface by chips and the surface roughness (Dvivedi and Kumar, 2007; Hsu and Tsao, 2009).

(4) Improvement in tool life. The intermittent cutting improves the drilling tool's cooling conditions, leading to lower cutting temperature and relieving the built-up edge and tool chipping effects. As a result, longer tool life can be obtained (Barani *et al.*, 2014; Pecat and Brinksmeier, 2014).

As shown in Fig. 2-16, according to the direction of vibration, vibration assisted drilling can be divided into axial, torsional and axial-torsional composite vibration drilling. The vibration direction in axial vibration drilling is consistent with the direction of the drilling tool axis, while in torsional vibration drilling, it is consistent with the direction of the drilling tool's rotation. Axial torsional composite vibration drilling combines the previous two types.

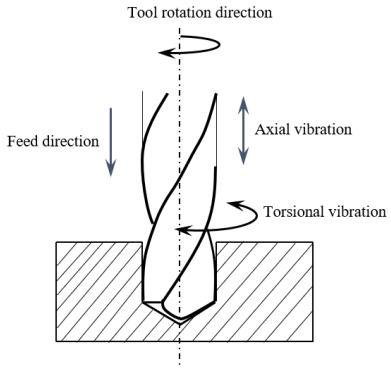

Figure 2-15 Schematic of vibration assisted drilling

2.3.3 Vibration assisted turning

Turning is a widely used machining method due to its high processing quality, metal removal rate, and productivity and efficient equipment utilization. However, drawbacks such as large cutting forces, difficulties in chip removal and serious tool wear can cause serious processing problems, such as low machined quality and efficiency and high cost. Vibration-assisted turning provides a new method for the efficient and high-quality machining of difficult materials. As shown in Fig. 2-17, vibration is applied to the turning tool mainly in the radial, tangential and feed directions. Multi-dimensional vibration assisted turning is generally referred as elliptical vibration assisted turning, where two of the above three vibration directions are chosen and applied to the turning tool. One-dimensional vibration assisted turning represents a large proportion of methods of vibration assisted turning proposed so far. Most apply vibration in the feed direction and experimental results have proven that this has a significant influence in reducing cutting forces, cutting temperature and improving the quality of processing. Currently, only a few studies have applied vibration in the other directions, and the effects and cutting mechanisms of involved in material processing need further research.

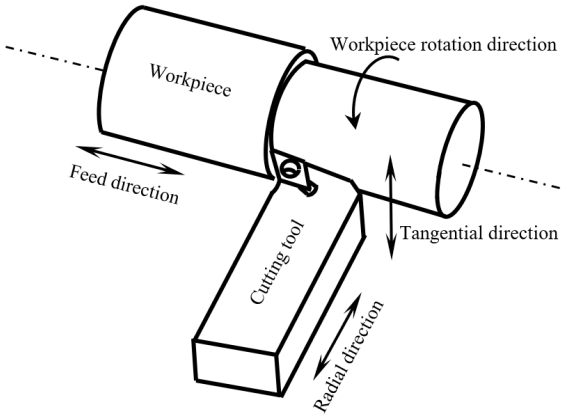

Figure 2-16 Schematic of vibration assisted turning

2.3.4 Vibration assisted grinding

Compared with other machining processes, grinding is increasingly used in the field of ultra-precision/precision machining due to its better machining accuracy and surface roughness. However, processing material with grinding wheels is a complex and stochastic process, where the ground surface may become damaged and low wheel life is caused by the high grinding forces and high surface cutting temperature (as the grinding wheel instantaneous temperature can reach 1000 °C). Vibration assisted grinding process applies vibration to the grinding wheel or workpiece during the grinding so as to improve the material removal performance. The vibration can be applied in the tangential, radial or axial directions along the grinding wheel, as is shown in Fig. 2-18. Vibration assisted grinding in the tangential and radial direction is similar to intermittent grinding, and tool-workpiece separation can be obtained during the machining process. Although vibration assisted grinding in the axial direction involves a continuous grinding process, the machining process is quite different in conventional grinding and features separation, impact and reciprocating ironing characteristics and lubrication effects, which can reduce grinding wheel blockage, cutting forces, workpiece residual stress and machined surface burn. As a result, better processing performance and longer tool life can be obtained. In addition, it also can effectively reduce the chipping of hard and brittle workpiece materials and surface or subsurface cracking as well as machined surface quality (Nik, Movahhedy and Akbari, 2012; Shen *et al.*, 2015; Chen *et al.*, 2016). Although similar to the mechanism of other vibration assisted machining processes, the randomness of the size, shape and distribution of abrasive grains on the grinding wheel surface and the complexity of the

grinding motion bring great challenges to the study of the mechanisms involved in the vibration assisted grinding.

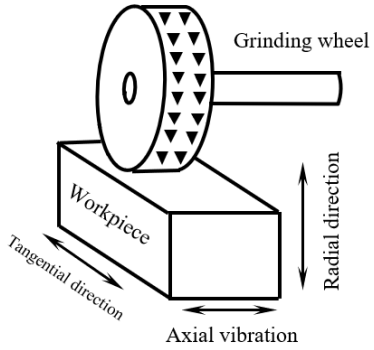

Figure 2-17 Schematic of vibration assisted grinding

2.3.5 Vibration assisted polishing

At present, various miniature optical lenses are generally fabricated by precision injection molding with silicon carbide or tungsten carbides molds, and these molds usually require polishing to achieve optical grade surface quality. However, small mold sizes and increasingly high precision requirements make the polishing process challenging. In the conventional polishing process, the high-speed rotation of soft polishing tools such as wool, rubber and asphalt polishing heads, are often used to process the workpiece surface. However, when the surface has complex curved shapes and a small curvature radius, the complicated polishing mechanism and uncontrollable polishing forces severely limit the processing results. Vibration assisted polishing can overcome some of the shortcomings in conventional polishing. Using this method, the polishing head does not need to be rotated at such high speeds, which helps in ensuring constant polishing force during the polishing process, which can also be used for smaller size molds. Current research shows that vibration assisted polishing can improve the surface roughness of the polished workpiece and the surface accuracy while achieving high polishing efficiency(Yin and Shinmura, 2004; Suzuki *et al.*, 2006; Shiou and Ciou, 2008).

2.3.6 Other vibration assisted machining processes

With the advantages of vibration assisted machining are gradually being demonstrated, more machining processes are being added to the vibration assisted machining family. Two examples of newly developed vibration assisted machining processes are vibration assisted boring and

vibration assisted electrical discharge machining. In order to solve the difficult machining problem of complex deep-hole parts with high-length-to-diameter ratios (>20) such as aero-engine fuel nozzles, vibration assisted boring has been developed. Compared with the conventional boring process, the tool can be prevented from colliding with the machined surface during the separation stage, the plastic critical cutting depth of the brittle material is increased, and cutting edge cracking and cutting tool flank face reverse bulges are avoided (Moraru, 2008; Zhang *et al.*, 2017). Its separation and reversal characteristics can greatly reduce the radial-thrust force and effectively improve the absolute stability of the cutting stiffness. As a result, the machined surface quality is improved and cutting flutter can be suppressed. Vibration assisted electrical discharge machining has also been successfully applied in processing micro-hole parts made of hard and brittle materials (Xu *et al.*, 2009; Shabgard *et al.*, 2013; Uhlmann and Domingos, 2016). In conventional electrical discharge machining, the discharge gap between the tool and the workpiece is usually only a few micrometers to several tens of micrometers, easily causes the deterioration due to the slag discharge effect and local concentration of processing debris, causing abnormal discharges and reducing processing efficiency. Compared with other processes, vibration assisted electrical discharge machining has better processing efficiency, and the results show that the slag removal effect is ameliorated and electrode wear reduced.

2.4 Applications and benefits of vibration assisted machining

2.4.1 Ductile mode cutting of brittle materials

When the cutting depth is less than a certain critical value (the critical depth of cut) in the processing of brittle materials, the cutting process will be transformed from brittle cutting mode into ductile cutting mode. This removes the workpiece materials by plastic flow instead of brittle fractures, leading to a crack-free surface. In ductile cutting mode, the critical cutting depth can be defined as the cutting depth at which a crack appears on the machined surface. If the undeformed chip thickness is less than the critical cutting depth, brittle cutting can be reduced in conventional cutting and a better surface finish can be obtained. However, in the actual processing of brittle materials, their critical cutting depth is usually in the range of microns or sub-micron, which reduces processing efficiency and increases the manufacturing time. Vibration assisted machining is an effective method used to increase the critical cutting depth in the ductile cutting mode and to improve the economics and feasibility of the processing

of brittle materials. It has been reported that smaller cutting forces can reduce microcrack propagation on the surface of the brittle parts and can increase the critical cutting depth for brittle materials under ductile cutting mode. In addition, a large enough plastic yielding force, but not large enough to cause material rupturing is also a necessary condition for the ductile cutting of brittle workpieces. Therefore, it is feasible to increase the brittle materials critical cutting depth within a reasonable stress range by using vibration assisted machining (Kim and Choi, 1997; Zhou *et al.*, 2002; Zhang *et al.*, 2014).

2.4.2 Cutting force reduction

A large number of cutting experiments and finite element analysis show that under the same cutting conditions, the average cutting force of vibration assisted machining is significantly lower than in the traditional cutting process and the cutting force in 2D vibration assisted machining process is less than that in 1D. Although the instantaneous peak cutting force of 1D vibration assisted machining is close to the steady state cutting force in conventional machining, a lower average cutting force can be obtained due to the periodic contact between the tool and workpiece during cutting (Zhou *et al.*, 2003; Babitsky, Mitrofanov and Silberschmidt, 2004; Zhang, Ehmann and Li, 2015). In 2D vibration assisted machining process, the shape of chips and interaction between them and the tool rake are quite different from in 1D due to the elliptical cutting tool trajectory, which leads to lower average cutting force and reduced instantaneous peak cutting force. The cutting force reduction is manifested in the following ways:

(1) The chip thickness in the 2D vibration assisted machining can be reduced due to the continuously overlapping of elliptical tool paths. As a result, the cutting forces in different directions can be reduced.

(2) Under certain conditions such as circular or narrowly elliptical tool paths, the cutting tool moves faster than the chip flow speed, causing reverse friction between the tool and the workpiece, and the back cutting force can be reduced or even reversed.

(3) The periodic contact between the cutting tool and workpiece improves the lubrication conditions during the cutting process and facilitates the dissipation of heat from the tool, resulting in a reduction in cutting force.

2.4.3 Burrs suppression

Burr formation, similar to chip generation, is a common and undesirable phenomenon in the machining process and one of the most important criteria in the evaluation of the machined surface. Vibration assisted machining can effectively suppress burr formation during processing and some researchers have proposed that burr height can be reduced up to 80% compared with conventional machining (Chang and Bone, 2005; Brehl *et al.*, 2006). Fig. 2-19 shows examples of burr reduction in vibration assisted machining. Almost no burrs can be found on the machined surface. This phenomenon is mainly due to the reduced cutting force, which leads to lower transient compressive stress and yield stress in the cutting deformation area. In addition, unique tool trajectories (such as elliptical trajectories) can result in discrete small of pieces of chips. As a result, burr formation can be suppressed.

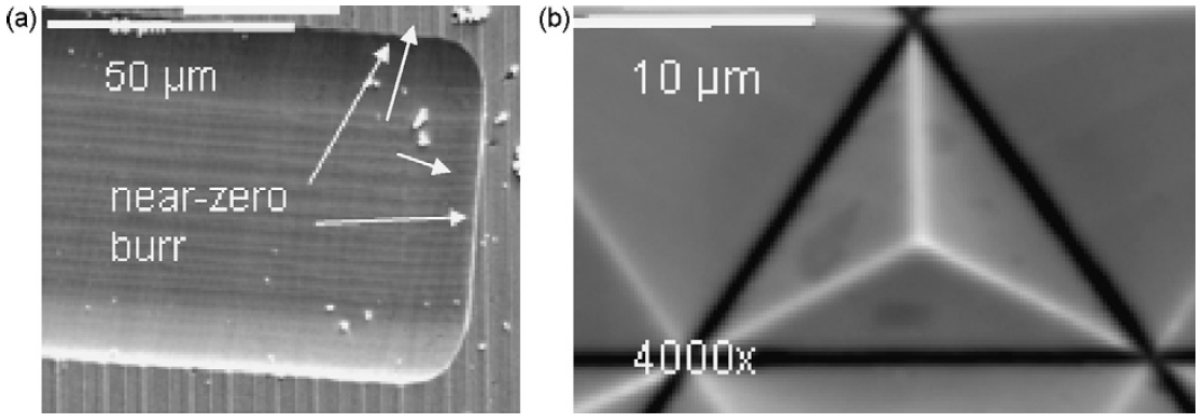

Figure 2-18 SEM images of burr-free structures made using 2D VAM. Single-crystal diamond tool in hard-plated copper. (a) Microchannel, 1.5µm deep; (b) 8µm tall regular trihedron made using dead-sharp tool with 70° nose angle (Brehl and Dow, 2008).

2.4.4 Tool life extension

Machining processes are inherently involved tool wear, which is usually evaluated in terms of average cutting force, machined surface roughness and cumulative cutting length. It has an important impact on surface quality and machining costs. Vibration assisted machining can effectively improve cutting tool life, especially in the processing of hard materials. Unlike the irregular wear caused by traditional machining tools, the tool wear in vibration assisted machining is smooth and inclined. At lower spindle speeds, due to the lower cutting temperatures, the dominant wear mechanism is abrasive wear. Because of the mechanical and impact contact between the workpiece and tool flank surface in VAM, tool life is less than that

in the conventional process. At higher cutting speeds, temperature activated wear mechanisms occur such as diffusion, chemical wear, and thermal wear. On the other hand, because of the intermittent separation of the workpiece and tool the temperature in the cutting zone in VAM is lower than that in conventional process, which tends to increase the tool life. Another reason for reduced the temperature in VAM is to the change in friction coefficient from semi-static to dynamic, which results in a reduced friction coefficient in the process and a change in the chip formation mechanism. As cutting speed increases, there is an increase in the degree of tool–workpiece engagement per tool revolution. As a result, the effect of vibration on the machining process decreases and the cutting forces in vibration assisted machining and conventional milling processes become closer to each other.

Generally, longer tool life can be achieved in 2D vibration assisted machining compared with 1D vibration assisted machining under the same cutting conditions. In order to fully understand the effect of vibration assisted machining on tool wear, it is necessary to discuss the reduction of tool wear according to different mechanisms since different wear mechanisms only appear in particular combinations of specific tools and workpiece materials.

2.4.4.1 Tool wear suppression in 1D vibration assisted machining

Mechanical wear occurs irrespective of tool and workpiece material and combinations, and it appears to be the main cause of tool wear for ferrous metal processing, regardless of tool types. In addition, due to the large cutting force, the most severe mechanical wear occurs when machining hard and brittle ferrous materials such as hardened steel, nickel or Inconel, which are also the most widely used in vibration assisted machining. Fig. 2-20 and 2-21 show SEM images of wear comparison results for PCD tools in conventional machining and 1D vibration assisted machining (Zhou *et al.*, 2003; Dong *et al.*, 2013). Scratches can be clearly seen, indicating abrasive wear as the dominant wear mechanism in these cutting experiments. Steel and SiC/Al composites were selected as the workpiece materials in these cases. The cutting and vibration parameters of vibration-assisted machining in both experiments are set to satisfy the periodically separation conditions of the tool and the workpiece, which reduce the average cutting force and temperature. As a result, a dramatic reduction of tool wear area can be found for these experiments as vibration added. Moreover, smoother wear can be found in the results of vibration assisted machining while irregular damage on the conventional machining tool. This also leads to a better surface finish results for vibration assisted machining.

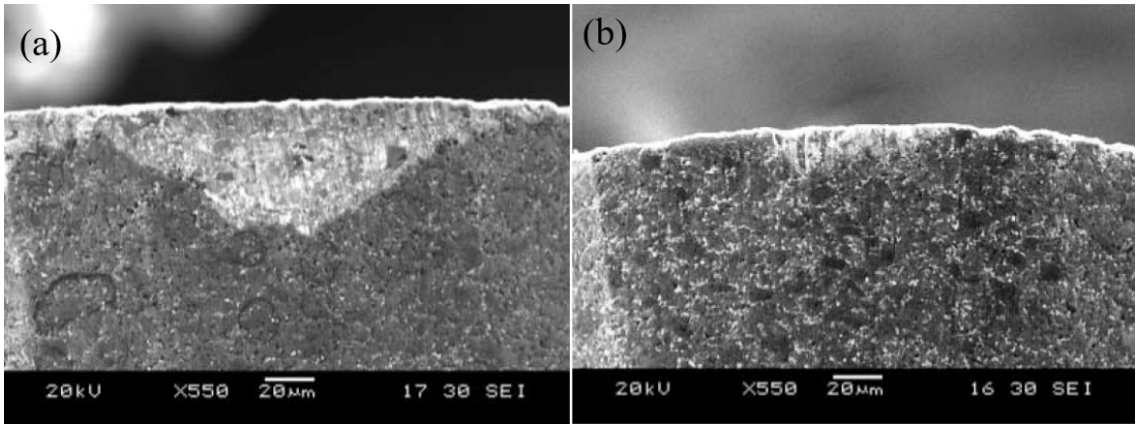

Figure 2-19 SEM photographs of worn-out tools, (a) Conventional machining; (b) Vibration assisted machining. (Zhou *et al.*, 2003)

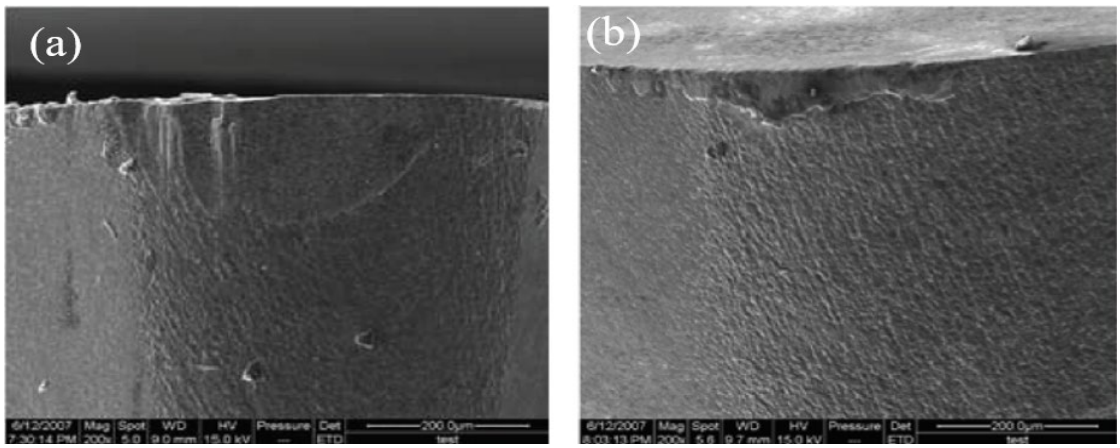

Figure 2-20 SEM micrograph of the tool flank wear patterns in (a) Conventional turning; (b) Vibration assisted turning (Dong *et al.*, 2013)

2.4.4.2 Tool wear suppression in 2D vibration assisted machining

Fig. 2-22 shows the results of a comparison tool wear in conventional machining and 2D vibration assisted machining on Inconel 718 (Lu *et al.*, 2015). Scratches can be observed from the worn parts of the two cutting tools, which indicates that the main wear mechanism is abrasive wear. It can be found that the flank wear in conventional machining is considerably heavier than that in 2D vibration assisted machining. In addition, the build-up of edge and boundary wear are effectively suppressed as 2D vibration is added. Similar results can also be found in Suárez's research (Suárez *et al.*, 2016). Tool life is significantly improved by adding elliptical vibrations to the face milling process of Ni-Alloy 718. Zhao et al. (Haidong *et al.*, 2016) studied the cutting mechanism of vibration assisted machining on Inconel 718 by comparing the tool wear and chip morphology in conventional and 2D vibration assisted

machining at different cutting lengths. The results indicate that the effective reduction of abrasive wear is one of the reasons for the longer tool life in 2D vibration assisted machining. Fig. 2-23 shows a comparison of the wear area of the steel processed by diamond tools in conventional machining, 1D vibration assisted machining and 2D vibration assisted machining (Zhang *et al.*, 2014). Smaller tool wear can be observed when vibration is added. Slight tool flank wear exists around the tool edge in 1D vibration assisted machining results, while the tool wear is almost unable to detect in 2D vibration assisted machining. In order to further study the tool wear mechanism, energy-dispersive X-ray spectroscopy (EDS) analysis is conducted on the worn area on the tool flank faces and the results indicate that the tool-workpiece separation in 2D vibration assisted machining promotes the generation of the oxide layer on the freshly machined surface, which in turn reduce the mechanical wear effect of tool edge.

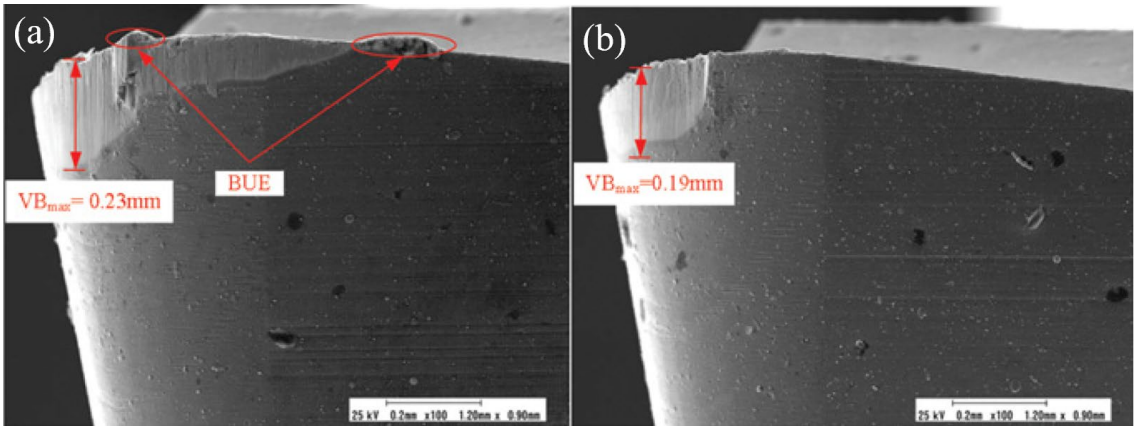

Figure 2-21 SEM micrographs of cutting tools used in (a) Conventional machining; (b) Elliptical vibration assisted machining (Lu *et al.*, 2015).

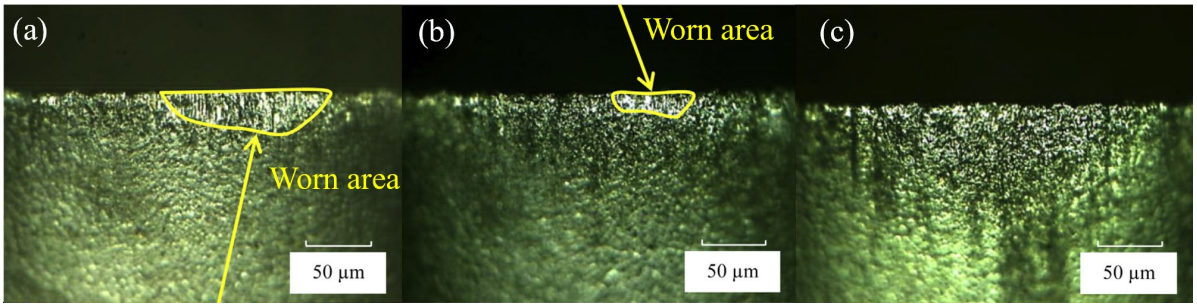

Figure 2-22 Microscope photographs (×1000) of the tool flank faces in the three machining processes: (a) Conventional machining; (b) 1D vibration assisted machining; (c) 2D vibration assisted machining (Zhang *et al.*, 2014).

The above experimental results indicate that the mechanical wear of the cutting tool in 2D vibration assisted machining can be further reduced compared with 1D vibration assisted

machining results. Besides the reasons given above, two merits, of lower cutting force and a unique elliptical tool trajectory are also contributed to this phenomenon. Fig. 2-24 shows cutting force variation in 1D vibration assisted machining and 2D vibration assisted machining respectively (Shamoto and Moriwaki, 1999). In can be found that the cutting force in 2D vibration assisted machining is significantly reduced compared with that in 1D vibration assisted machining. Other published results also indicate the positive effect on cutting force reduction of vibration assisted machining (Qin, Pei and Guo, 2009; Zhang, Senthil Kumar and Rahman, 2012; Kong *et al.*, 2015; Kong, Dong and Cohen, 2017; Ni *et al.*, 2019). On the other hand, the tool-workpiece contact area is not fixed during each elliptical cutting cycle. Fig. 2-25 shows the relative motion between the workpiece and the tool in 2D vibration assisted machining and three tool positions during machining are selected to vary the tool-workpiece contact area. It can be found that the flank wear area of the cutting tool decreases in each elliptical cutting cycle. In addition, the rake angle of the cutting tool gradually becomes more negative with the tool moving upward in its elliptical trajectory, leading to an inconstant shear angle for the processing material (Dautzenberg, Hijink and van der Wolf, 1982; Nakayama, Arai and Kanda, 1988). Moreover, cracks are generated in the cutting area of the hard and brittle workpiece due to the fluctuation in the cutting thickness and the impact of the cutting force. These are also reasons for the smaller cutting force in 2D vibration assisted machining than in1D vibration assisted machining. As a result, the uncut material is easier to remove and the tool life in 2D vibration assisted machining is further extended.

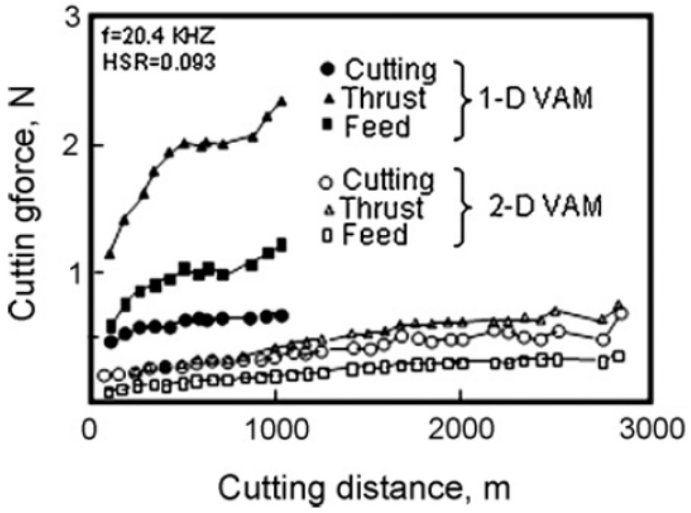

Figure 2-23 Comparison of average tool forces with distance (Shamoto and Moriwaki, 1999)

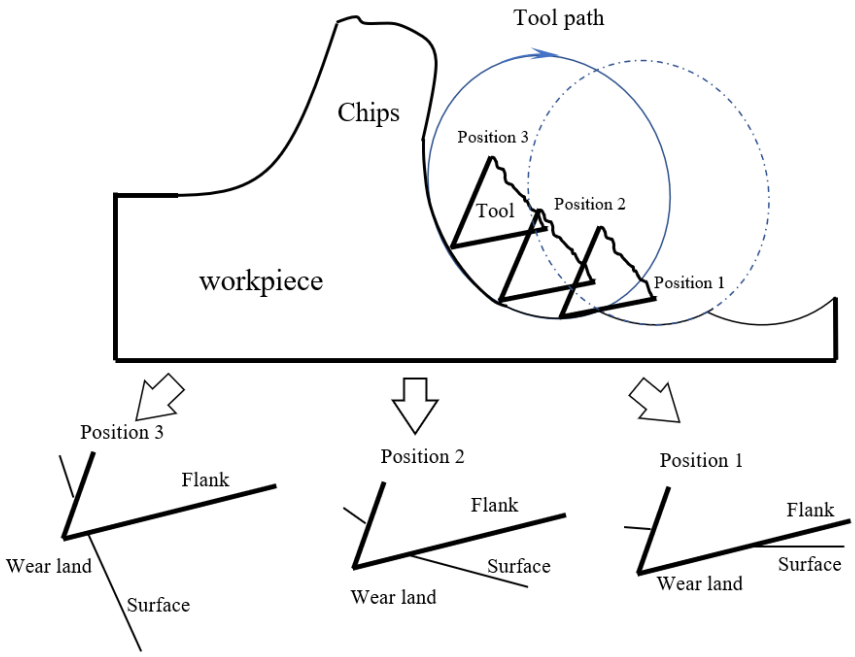

Figure 2-24 Relative motion between the workpiece and the tool in 2D vibration assisted machining

2.4.4.3 Tool wear suppression in vibration assisted micro machining

The increasing demand for micro parts and components has led to the development of micro machining technology. Micro machining involves higher technical requirements for the cutting tool and tool life is one of the most important factors restricting its application. Due to the well-known size effect, the cutting edge radius can be no longer ignored, and this leads to a different cutting mechanism in micro machining compared to its macro-scale counterpart process. Machining performance can be influenced by the tool edge radius when the undeformed chip thickness is small enough. It has been reported that the ratio of undeformed chip thickness to cutting edge radius is closely linked to the ploughing effect on the machining surface, effective rake angle and specific cutting energy, which in turn affects the cutting performance.

The mechanical and thermochemical wear mechanisms are still effective in explaining the wear of micro tools. Meanwhile, the ploughing effect is the main reason for micro tool wear when the feed rate is small enough. However, the effect of minimum chip thickness is unavoidable in a micro machining process. By applying vibration to the micro machining process, its stability can be improved because the instantaneous uncut chip thickness and cutting speed is changed significantly compared with in the conventional micro machining process, especially in the cutting in and cutting out area. As a result, the duration of the period of squeeze friction

between the tool and the workpiece can be reduced, resulting in longer tool life. Fig. 2-26 shows micro tool wear comparison results between conventional micro milling and vibration assisted milling (Ding *et al.*, 2010). The results show that the tool wear with vibration assistance can be reduced by approximately 5–20% compared to that in conventional micro milling. Moreover, the machined surface roughness and surface finish from vibration assisted processing is also better than in the conventional micro milling results, since the ploughing effect is effectively suppressed, which reduces the secondary damage from the worn cutting tool on the machined surface.

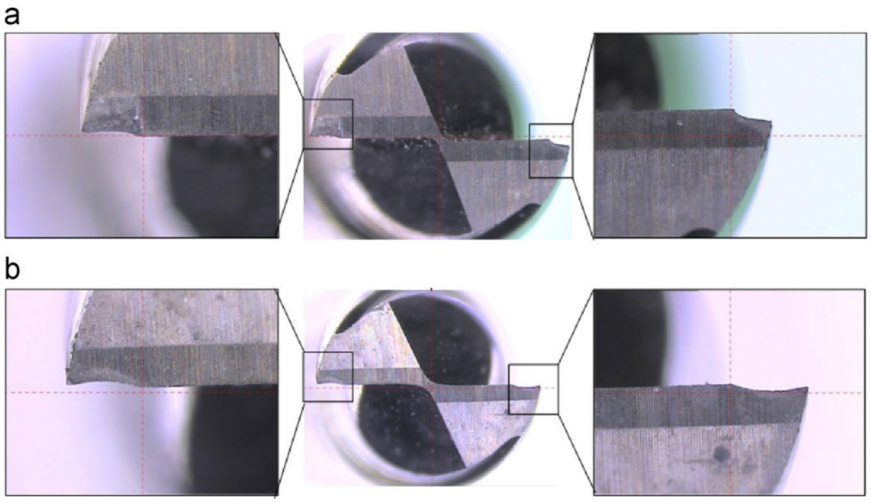

Figure 2-25 Photos of tool wear: (a) Without vibrations; (b) With vibrations. (Ding *et al.*, 2010)

2.4.4.4 Effect of vibration parameters on tool wear

Vibration parameters, such as vibration direction, amplitude and frequency have a great influence on tool life in vibration assisted machining. Changes in the vibration parameters will change the tool path, resulting in different cutting mechanisms, which in turn influence the tool life. Improperly set vibration parameters can shorten tool service life and reduce machined surface roughness and finish. Therefore, the optimization of vibration parameters in a vibration assisted machining process is necessary. Besides this, the relationship between the vibration parameters and other machining factors, such as the machining parameters and the size and geometry of the cutting tool, also need to be taken into account. Taking vibration assisted micro machining as an example, in order to effectively reduce the ploughing effect, elliptical vibration with high frequency and small amplitude as needed to meet the tool-workpiece separation conditions is usually applied. However, when the amplitude is too large, excessive fluctuations in cutting force will affect the tool, which increases tool wear. Javad et al. (Javad *et al.*, 2013)

experimentally studied the variation in tool life in elliptical vibration assisted milling at different cutting speeds. Fig. 2-27 shows the tool flank wear experiment results at low spindle speed (n = 500, 1000, and 2000 r/min). It can be found that tool wear is more serious when vibration is added. This is due to the unfavourable impacts of the workpiece on the tool flank surface and, subsequently, mechanical and wear mechanisms are the main factors leading to rapid tool failure in vibration assisted machining process. Lower spindle speeds lead to more effective impacts between the workpiece and tool flank surface. As spindle speed increases, the contact of tool on the workpiece also increases in each vibration cycle, and cutting approaches a continuous form, and consequently, the number of impacts on the tool flank surface is reduced. Moreover, the same results can also be obtained when vibration frequency is increased. Similar results have also been found elsewhere (Nath and Rahman, 2008; Zhang *et al.*, 2010; Li and Wang, 2014; Pecat and Brinksmeier, 2014).

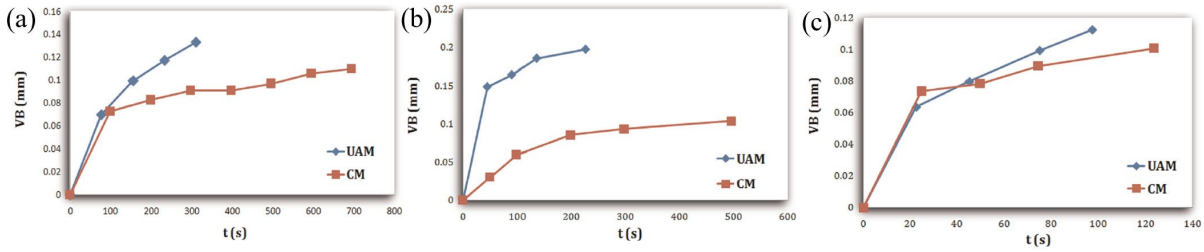

Figure 2-26 Time history of flank wear land width in conventional machining and vibration assisted machining (a) spindle speed 500 r/min; (b) spindle speed 1000 r/min; (c) spindle speed 2000 r/min (Janghorbanian, Razfar and Mohammad M.Abootorabi Zarchi, 2013).

2.4.5 Machining accuracy and surface quality improvement

Compared with the conventional machining process, vibration assisted machining can greatly improve machining accuracy and surface quality, and the improvements vary depending on the tool and workpiece materials, vibration conditions (vibration amplitude, vibration frequency and vibration dimensions), tool parameters and processing parameters such as feed rate, spindle speed and cutting depth. If the processing parameters are unchanged, the surface roughness in 1D and 2D vibration assisted machining can be reduced by approximately 40% and 85%, respectively (Brehl and Dow, 2008). There are many reasons for this. On the one hand, lower cutting forces can enhance the stability of the cutting process, which reduces tool run-out in the cutting depth direction and generates smaller chips. On the other hand, vibration assisted machining can reduce cutting tool wear and effectively avoid damage caused to the machined surface by worn tools. The tool's self-excited vibration is replaced with regular sine or cos

vibration, which reduces the residual height of the unremoved material. As a result, a better machined surface quality can be obtained.

2.4.6 Surface texture generation

Engineered textured surfaces have the characteristics of regular textural structures and high aspect ratio, enabling the component surface to serve specific functions such as reducing adhesion friction, improving lubricity, increasing wear resistance, changing hydrophilic performance and enhancing optical properties. Etching methods are commonly used to produce high precision surface microstructures, but these are costly and time-consuming. As a more flexible method, it has been proven that vibration assisted machining in either a single direction or two directions can form certain surface textures depending on the cutting-edge geometry and kinematics. Ping *et al.* (Ping *et al.*, 2013) studied the surface texture generation mechanism in two-dimensional vibration assisted turning process. A controllable surface texture can be generated by comparing the simulation and machining results. Chen *et al.* (Chen, Zheng and Huo, 2018) proposed a non-resonant vibration assisted micro milling system and produced two types of surface textures: wave and fish scale. By combining different vibration and machining parameters, the machined surface topography can be controlled. By changing the vibration and cutting parameters, Young *et al.* (Young *et al.*, 2015) generated different surface textures and the contact angle testing results showed machined surface hydrophilicity changes as processing and vibration parameters change. The same results were found by Ping *et al.* (Ping *et al.*, 2014) that anisotropic wetting surface can be generated in vibration assisted turning process. Currently, the proposed surface textures mainly include squamous, micro-dimple pattern and micro-convex pattern types, and their size ranges from a few microns to tens of microns, as shown in Fig. 2-28. There is an emerging trend to obtain certain surface performance using vibration assisted machining. For example, the size of the surface texture features can be controlled by changing the vibration and processing parameters, leading to variable surface wettability (Fig. 2-28) (Chen *et al.*, 2018). The process can also be used to create microchannels for the microfluidic control of the fluid flow, to name a few.

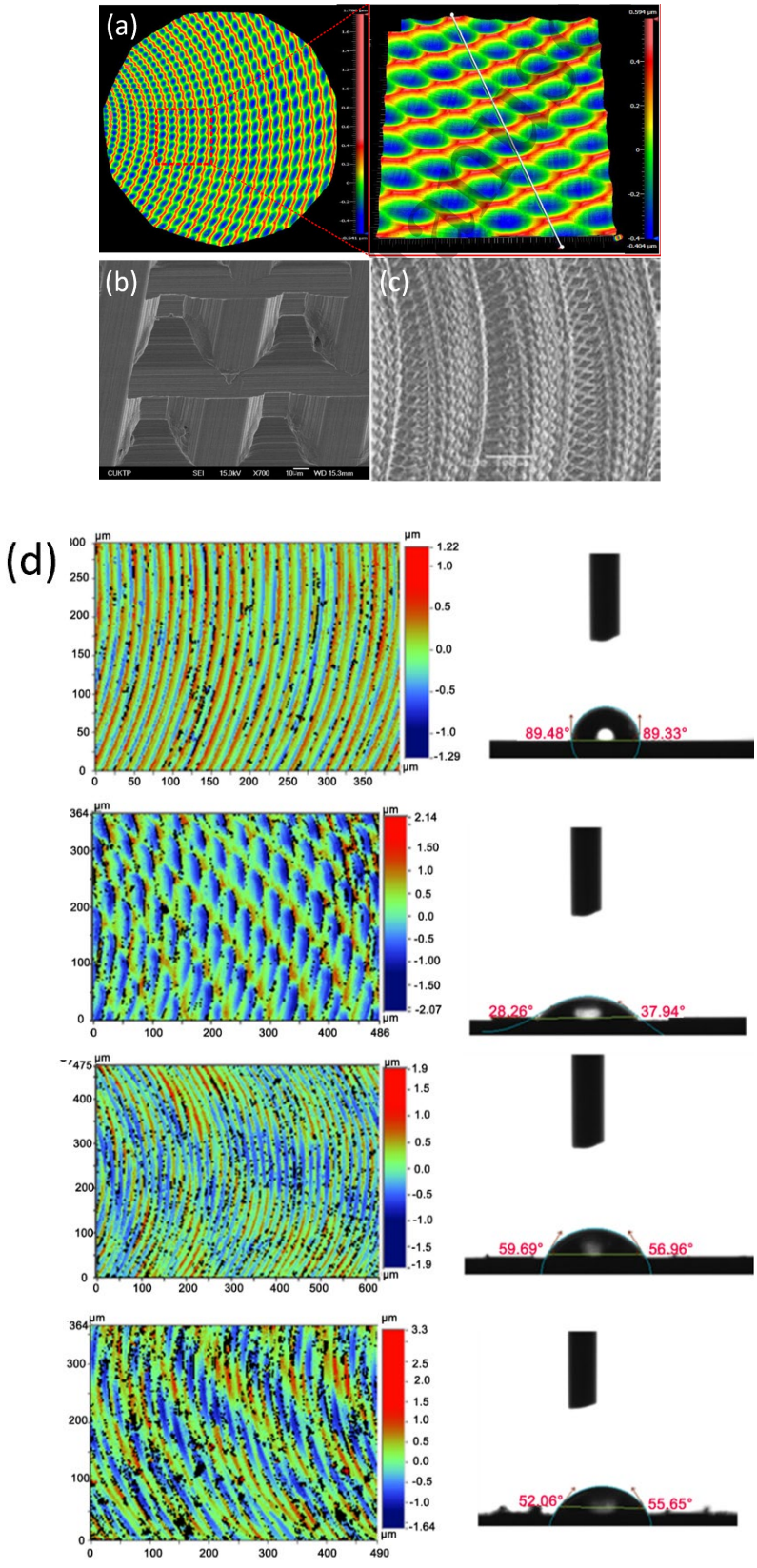

Figure 2-27 Surface texture produced by vibration assisted machining (a) Micro-dimple patterns (Lin *et al.*, 2017); (b) Micro-convex patterns (Kim and Loh, 2010); (c) Squamous patterns (Tao *et al.*, 2017); (d) Surface wettability variation with different surface texture (Chen *et al.*, 2018).

2.5 Summary

This chapter reviews the current state of vibration assisted machining technology including vibration system design, vibration assisted machining process and benefits and applications of the vibration assisted machining. The following conclusion can be obtained:

1) Vibration assisted machining has been in development for about 60 years since it was first proposed. It has been successfully applied to several machining processes, such as turning, milling, and grinding. Advantages such as extended tool life and better surface finishes have been discovered and have played an important role in improving the machining accuracy of hard and brittle materials and reducing costs. The sources of vibration have undergone on evolution from electro-hydraulic actuators to electromagnetic actuators to piezoelectric actuators and each evolution improves the motion accuracy of the vibration system.

2) Resonant vibration devices usually vibrate at their natural frequency and the vibration frequency and amplitude are fixed at certain values. Given the high demand for the precision machining of hard and brittle materials, high vibration frequency, low amplitude and the undertaking of large loads will be development trends for resonant vibration devices in the near future.

3) The applications of non-resonant vibration systems are more flexible compared with resonant systems due to the variable vibration amplitudes and frequencies. Besides pursuing a wider range of working frequencies and amplitudes, a reduction in the coupling effect is also a significant mainstream research aim with this type of vibration device.

Chapter 3 2D non-resonant vibration assisted micro milling system design and implementation

3.1 Introduction

According to the operating frequencies, the vibration devices can be divided into two groups: the resonant mode and the non-resonant mode. For a resonant system, a sonotrode (also called horn or concentrator) vibrates at its natural frequency transferring and amplifying a given vibration from a vibration source (usually by a magnetostrictive or piezoelectric transducer). It can achieve a higher operating frequency and more energy-efficient compared with non-resonant system. However, its the vibration trajectory cannot be controlled precisely owing to the nature of the resonant vibrations and the phase lag between the excitation and the mechanical response. Non-resonant vibration device applies forced vibration theory and can produce variable vibration frequencies which are always less than its natural frequency. Compared with resonant system, non-resonant system tends to achieve higher vibration accuracy, and it is easier to achieve closed-loop control of vibration trajectories under low frequency conditions. As one of the most promising ultra-precision motion mechanisms, Piezoelectric actuator driven flexible mechanism is widely applied in ultra-precision manufacturing, optical, biomedical and aerospace industries due to the merits such as fast response rate, high movement resolution, no friction and wear, compact structure and no lubrication required. 2D non-resonant vibration-assisted machining has received more and more attention due to its elliptical trajectories for generation unique surface topography and better processing performance. However, the full decoupling mechanism increases its design difficulty and sacrifices some of its performance. In addition, the piezoelectric actuator can only withstand compressive stress, the mechanism coupling motion will generate shear stress and cause damage.

Currently, two types of flexure joint based structure: serial and parallel, have been developed to reduce the coupling effect. Serial type flexure joint based structure features as easy to control and low motion coupling, but it also has the drawbacks: (a) the complex structure leads to a low structure stiffness, working bandwidth and response rate; (b) Motion errors at various levels in the kinematic chain are transmitted step by step and form a large error accumulation at the end; (c) It is difficult to achieve consistent dynamic performance for each axis of motion. On the contrast, the benefits of the parallel type flexure joint based structure are compact

structure, which leads to high stiffness, bandwidth and motion accuracy. However, the coupling effect between different motion axes cannot be suppressed effectively and a double symmetric structure is always required. In order to overcome the shortcomings of the above flexure joint based structures, a new 2D non-resonance vibration assisted micro milling system based on both serial and parallel type flexure structure is developed to achieve low coupling movement, high working bandwidth and high accuracy.

3.2 Structural design of the vibration device

Fig. 3-1 shows the mechanical structure of the vibration stage which is driven by two piezoelectric actuators. It aims to achieve superb processing performance including high vibration frequency bandwidth, wide range of vibration amplitude, high movement resolution and accuracy with low coupling displacement. To satisfy above requirements, a double parallel four-bar linkages with double layer flexible hinges structure is chosen for this stage. Parallel four-bar linkages mechanisms are widely used in the applications where the motion direction is fixed and the angular motion needs to be eliminated. However, large stress concentration and parasitic movements cannot be eliminated and these drawbacks can be overcome by using double parallel four-bar linkages structure (Lin *et al.*, 2017). Under the same stress conditions, the cross-coupling displacement occurs on both sides of the flexible hinges due to the influence of structural symmetry, which theoretically solves the problem and keeps the stage motion linearity. Four flexible hinges with two sizes (R_1 and R_2) are center-symmetrically placed on each side of the parallel four-bar linkage (see Fig. 3-1). The value of R_1 is designed as large as possible to ensure a large vibration displacement of the vibration stage. While the value of R_2 is designed as small as possible to ensure the rigidity of the entire mechanism. To further reduce vibration stage coupling effect between the two directions, an inner layer flexible hinges structure is proposed, which is made by a single rod flexible mechanism. To simplify design and reduce manufacturing costs, all the flexure joint based structures are set by right circle hinges, although other types of flexible hinges, such as elliptical-arc-fillet flexure hinges and corner-filleted hinges are also suitable for the vibration stage. Considering working environment, the material of the vibration device needs to meet the requirements such as good mechanical and elastic properties, high thermal conductivity and low thermal expansion. Spring steel (080A67) with high fatigue strength limit is chosen as the structural material. The stage is manufactured by using wire electrical discharge machining (WEDM) to reduce contour

errors and residual stresses. Two preloaded piezo actuators (P-844.20 Physik Instrumente) are selected to drive the vibration stage.

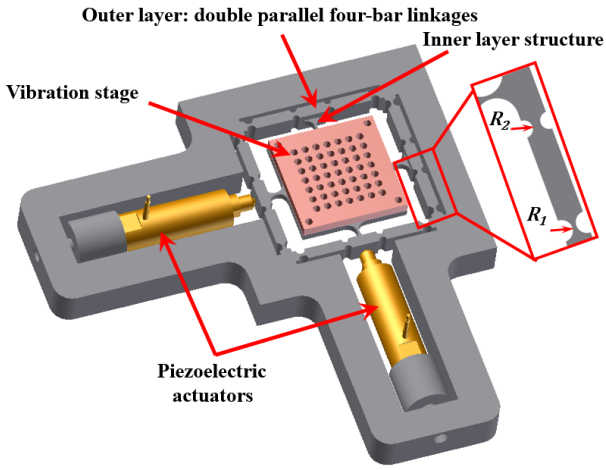

Figure 3-1 Layout of the designed vibration stage.

3.3 Modelling of compliant mechanism

Various methods have been developed for compliant mechanisms modelling including pseudo-rigid body (PRB) method, Castigliano's second theorem and inverse kinematic modelling (IKM). The pseudo-rigid body method equivalents the elastic rod (or hinge) model to the corresponding rigid rod model to achieve model simplification and more suitable for planar structure (Yangmin Li and Qingsong Xu, 2009; Zhu *et al.*, 2014). The Castigliano's second theorem expresses the strain energy of the flexure joint based structure as a function of the load. However, the calculation process is quite complicated involving partial differential equations, which is not conducive to the design optimization of the mechanism. The inverse kinematic modelling is the most accurate method compared with the previous two methods. However, the computational process can be time consuming. To overcome the abovementioned drawbacks, a method named matrix-based compliance modelling (MCM) is developed building from the linear Hooke's law for the material (Li and Xu, 2009). The working principles between the IKM and MCM are somewhat similar. They all apply the flexibility matrix of flexible hinge unit and spatial coordinate transformation to build the stiffness/compliance model for a complex flexible mechanism. However, compared with the IKM method, the MCM replaces the Lagrange equation to the position transformation matrix, which improves the computational efficiency and modelling accuracy.

3.3.1 Compliance modelling of Flexure hinges based on matrix method

In the modelling, each of flexure hinge in the stage is uniformly divided into N pieces and each of them can be treated as a micro Euler–Bernoulli beam. It is more suitable for modelling spatial compliant mechanisms with complex structures and shapes because higher calculation accuracy and efficiency can be easily obtained by using matrix operations. Therefore, the matrix-based method is chosen for modelling the proposed 2D vibration stage.

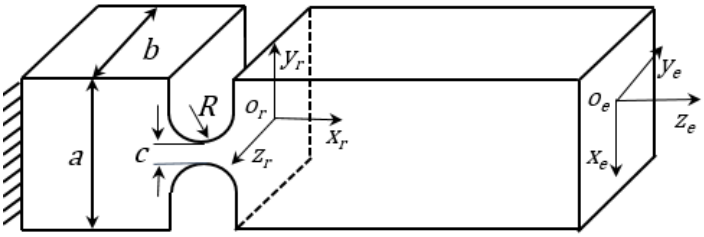

Figure 3-2 Schematic of flexure hinge.

The basic structure element in the 2D vibration stage is the right circular flexure hinge which is shown in Fig. 3-2 with its local Cartesian coordinate o_r-$x_ry_rz_r$. By considering the complicated shear and torsion effects, a 6×6 matrix for describing compliance C_i^r every micro beam at o_r-$x_ry_rz_r$ is proposed and can be expressed as:

$$C_i^r = \begin{pmatrix} C_{1,1} & 0 & 0 & 0 & 0 & 0 \\ 0 & C_{2,2} & 0 & 0 & 0 & C_{2,6} \\ 0 & 0 & C_{3,3} & 0 & C_{3,5} & 0 \\ 0 & 0 & 0 & C_{\theta_x M_x} & 0 & 0 \\ 0 & 0 & C_{5,3} & 0 & C_{5,5} & 0 \\ 0 & C_{6,2} & 0 & 0 & 0 & C_{6,6} \end{pmatrix} \quad (3\text{-}1)$$

Where:

$$C_{1,1} = \frac{\delta x}{F_x} = \frac{1}{Eb}\left[\frac{2(2s+1)}{\sqrt{4s+1}} arctan\sqrt{4s+1} - \frac{\pi}{2}\right] \quad (3\text{-}2)$$

$$C_{2,2} = \frac{\delta y}{F_y} = \left(\frac{\delta y}{F_y}\right) + \left(\frac{\delta y}{F_y}\right)_\tau \tag{3-3}$$

$$\left(\frac{\delta y}{F_y}\right) = \frac{12}{Eb}\left[\frac{s(24s^4+24s^3+22s^2+8s+1)}{2(2s+1)(4s+1)^2} + \frac{(2s+1)(24s^4+8s^3-14s^2-8s-1)}{2(4s+1)^{\frac{2}{5}}} arctan\sqrt{4s+1} + \frac{\pi}{8}\right] \tag{3-4}$$

$$\left(\frac{\delta y}{F_y}\right)_\tau = \frac{1}{Gb}\left[\frac{2(2s+1)}{\sqrt{4s+1}} arctan\sqrt{4s+1} - \frac{\pi}{2}\right] \tag{3-5}$$

$$C_{2,6} = \frac{\delta y}{M_z} = -\frac{12}{EbR}\left[\frac{2s^3(6s^2+4s+1)}{(2s+1)(4s+1)^2} + \frac{12s^4(2s+1)}{(4s+1)^{\frac{2}{5}}} arctan\sqrt{4s+1}\right] \tag{3-6}$$

$$C_{3,3} = \frac{\delta z}{F_z} = \left(\frac{\delta z}{F_z}\right) + \left(\frac{\delta z}{F_z}\right)_\tau \tag{3-7}$$

$$\left(\frac{\delta z}{F_z}\right) = \frac{12R^2}{Eb^3}\left[\frac{2s+1}{2s} + \frac{(2s+1)(4s^2-4s-1)}{2s^2\sqrt{4s+1}} arctan\sqrt{4s+1} - \frac{(2s^2-4s-1)\pi}{8s^2}\right] \tag{3-8}$$

$$\left(\frac{\delta z}{F_z}\right)_\tau = \frac{1}{Gb}\left[\frac{2(2s+1)}{\sqrt{4s+1}} arctan\sqrt{4s+1} - \frac{\pi}{2}\right] \tag{3-9}$$

$$C_{3,5} = \frac{\delta z}{M_y} = \frac{12R}{Eb^3}\left[\frac{2(2s+1)}{\sqrt{4s+1}} arctan\sqrt{4s+1} - \frac{\pi}{2}\right] \tag{3-10}$$

$$C_{5,3} = \frac{\delta \theta_y}{F_z} = \frac{R\delta \theta_y}{M_z} = \frac{12R}{Eb^3}\left[\frac{2(2s+1)}{\sqrt{4s+1}} arctan\sqrt{4s+1} - \frac{\pi}{2}\right] \tag{3-11}$$

$$C_{5,5} = \frac{\delta \theta_y}{M_y} = \frac{12}{Eb^3}\left[\frac{2(2s+1)}{\sqrt{4s+1}} arctan\sqrt{4s+1} - \frac{\pi}{2}\right] \tag{3-12}$$

$$C_{6,2} = \frac{\delta \theta_z}{F_y} = -\frac{R\delta \theta_y}{M_z} = -\frac{12}{EbR}\left[\frac{2s^3(6s^2+4s+1)}{(2s+1)(4s+1)^2} + \frac{12s^4(2s+1)}{(4s+1)^{\frac{2}{5}}} arctan\sqrt{4s+1}\right] \tag{3-13}$$

$$C_{6,6} = \frac{\delta \theta_z}{M_z} = \frac{12}{EbR^2}\left[\frac{2s^3(6s^2+4s+1)}{(2s+1)(4s+1)^2} + \frac{12s^4(2s+1)}{(4s+1)^{\frac{2}{5}}} arctan\sqrt{4s+1}\right] \tag{3-14}$$

Where $\left(\frac{\delta}{F}\right)_\tau$ is the linear deformation of the flexible hinge caused by the shear force under the action of the load *F*. $\delta i\ (i = x, y, z)$ are the deformation of the flexible hinge in the direction of *x*, *y* and *z* and $F_{i\ (i=x,y,z)}$ are the corresponding force. $\delta\theta_{i(i=x,y,z)}$ are the rotation angle of the flexible hinge along the axis of *x*, *y* and *z* and $M_{i\ (i=x,y,z)}$ are the corresponding moment of inertia. *R, b* and *c* are the key dimensions of the flexure hinge, as shown in Fig. 3-2. And *s*

= *c/R, G* and *E* are the modulus of rigidity and modulus of elasticity, respectively. By arranging the above equations, a widely accepted flexible matrix is represented as (Ryu *et al.*, 1999; Lobontiu *et al.*, 2001):

$$C_i^r = \begin{pmatrix} \frac{L}{Ea_ib_i} & 0 & 0 & 0 & 0 & 0 \\ 0 & \frac{4L^3}{Eb_ia_i^3}+\frac{\alpha_sL}{Gb_ia_i} & 0 & 0 & 0 & \frac{6L^2}{Eb_ia_i^3} \\ 0 & 0 & \frac{4L^3}{Eb_ia_i^3}+\frac{\alpha_sL}{Gb_ia_i} & 0 & -\frac{6L^2}{Eb_i^3a_i} & 0 \\ 0 & 0 & 0 & \frac{\Delta\theta_x}{\Delta M_x} & 0 & 0 \\ 0 & 0 & -\frac{6L^2}{Eb_i^3a_i} & 0 & \frac{12L}{Eb_i^3a_i} & 0 \\ 0 & -\frac{6L^2}{Eb_i^3a_i} & 0 & 0 & 0 & \frac{12L}{Eb_i^3a_i} \end{pmatrix} \quad (3\text{-}15)$$

where L is the length of the micro Euler–Bernoulli beam. a_i and b_i are the cross-section dimensions of the i-th micro Euler–Bernoulli beam. ν is the Poisson's ratio, α_s is the shear coefficient of the material and can be expressed as (Cowper, 1966):

$$\alpha_s = \frac{12+11\nu}{10(1+\nu)} \quad (3\text{-}16)$$

The torsional model of the flexure hinge is developed considering thickness-to-width ratio ($\tau = a_i/b_i$) and its equation being expressed by (Chen and Howell, 2009):

$$C_{\theta_x M_x} = \frac{7L}{2G}\left(\frac{1}{a_ib_i^3}+\frac{1}{a_i^3b_i}\right)\frac{\tau^2+2.609\tau+1}{1.17\tau^2+2.191\tau+1.17} \quad (3\text{-}17)$$

k is the structural correction factor of the flexure hinges, which is defined by b/c and relationships are showing in Table 3-1.

Table 3-1 Relationship between structural correction factors and structure parameters

b/c	1	2	10	∞
k	0.141	0.229	0.312	0.333

In general, the proposed vibration stage is composed of many flexure hinges connected in parallel and series. Additionally, each flexure hinge can be considered as a series connection of all the micro beams when neglecting the effects of stress distributions on elastic deformations of the flexure hinges. In order to develop the compliance of the vibration stage, the compliance of flexure hinges need to be transferred from the local coordinate o_r-$x_ry_rz_r$ to the global coordinate o_e-$x_ey_ez_e$ (see Fig. 3-2):

$$C_r^e = \sum_{i=1}^{N} T_r^e C_i^r (T_r^e)^T \tag{3-18}$$

Where C_r^e is the compliance at o_e-$x_ey_ez_e$. T_r^e is the compliance transformation matrix (CTM) and can be expressed as (Koseki *et al.*, 2002; Pham and Chen, 2005; Tang and Li, 2013):

$$T_r^e = \begin{bmatrix} R_r(\delta) & S_r(r_r)R_r(\delta) \\ O & R_r(\delta) \end{bmatrix} \tag{3-19}$$

Where $R_r(\delta)$ is the rotation matrix of the local coordinate o_r-$x_ry_rz_r$ transferring to the global coordinate o_e-$x_ey_ez_e$, given by:

$$R_r(\delta) = \begin{bmatrix} cos\delta & sin\delta & 0 \\ -sin\delta & cos\delta & 0 \\ 0 & 0 & 0 \end{bmatrix} \tag{3-20}$$

$r_r = [x_r, y_r, z_r]$ is the position vector of the point o_r in the global coordinate o-xyz. $S_r(r_r)$ is the skew-symmetric operator for the position vector r_r and can be defined as:

$$S_r = \begin{bmatrix} 0 & -z_r & y_r \\ z_r & 0 & -x_r \\ -y_r & x_r & 0 \end{bmatrix} \tag{3-21}$$

3.3.2 Compliance modelling of flexure mechanism

Fig. 3-3 shows a typical flexible mechanism including both series and parallel structures. The Flexible mechanism end executor O - xyz is supported by several flexible chains (Ch_i) in parallel and each flexible chain consists of several flexible hinges connected in series. O_i - $x_iy_iz_i$ is the Cartesian coordinate system of the output point O_i for the i-th flexible chain (Ch_i), $O_{k,i}$ - $x_{k,i}^L y_{k,i}^L z_{k,i}^L$ is the Cartesian coordinate system for the k-th flexible hinge on the i-th flexible

chain. Assume the compliance of the flexible hinge $O_{k,i}$ in local coordinate system $O_{k,i}$ - $x_{k,i}^L y_{k,i}^L z_{k,i}^L$ is $C_{k,i}$, as it transfer to the coordinate system O_i - $x_i y_i z_i$:

$$C_{k,i}^{o_i} = T_{k,i}^{o_i} C_{k,i} (T_{k,i}^{o_i})^T \tag{3-22}$$

Where $C_{k,i}^{o_i}$ is the compliance for flexure hinge $O_{k,i}$ in the coordinate $O_{k,i}$ - $x_{k,i}^L y_{k,i}^L z_{k,i}^L$, $T_{k,i}^{o_i}$ is the compliance transformation matrix and can be expressed as:

$$T_{k,i}^{o_i} = \begin{bmatrix} R_{k,i}^{o_i}(\alpha) & S_{k,i}^{o_i}(r_i) R_{k,i}^{o_i}(\alpha) \\ O & R_{k,i}^{o_i}(\alpha) \end{bmatrix} \tag{3-23}$$

Where $R_{k,i}^{o_i}(\alpha)$ and $S_{k,i}^{o_i}(r_i)$ is the rotation matrix and position transformation matrix (under the position vector $r_i = [x_i, y_i, z_i]$) for the flexure hinge $O_{k,i}$ to the flexible chain (Ch_i) coordinate O_i - $x_i y_i z_i$, respectively. Which can be expressed as:

$$R_r(\alpha) = \begin{bmatrix} cos\alpha & sin\alpha & 0 \\ -sin\alpha & cos\alpha & 0 \\ 0 & 0 & 0 \end{bmatrix} \tag{3-24}$$

$$S_{k,i}^{o_i} = \begin{bmatrix} 0 & -z_i & y_i \\ z_i & 0 & -x_i \\ -y_i & x_i & 0 \end{bmatrix} \tag{3-25}$$

For the flexible chain (Ch_i) with k flexible hinges connected in series, the compliance C_{o_i} for the output point O_i relative to the fixed end (B_i) is:

$$C_{o_i} = \sum_{k=1}^{k} T_{k,i}^{o_i} C_{k,i} (T_{k,i}^{o_i})^T \tag{3-26}$$

Therefore, the compliance for the end executor C_o can be expressed as:

$$C_o = \left[\sum_{i=1}^{N} \left(T_{o_i}^{o} C_{o_i} (T_{o_i}^{o})^T \right)^{-1} \right]^{-1} \tag{3-27}$$

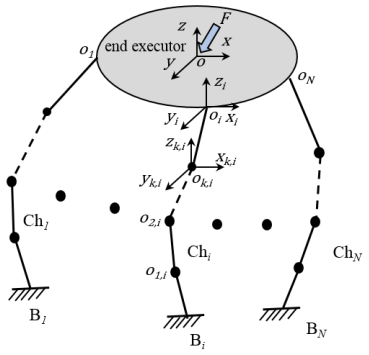

Figure 3-3 Working principles for the typical flexure mechanism

3.3.3 Compliance modelling of the 2 DOF vibration stage

Due to the structure symmetric design, the output compliance C_{out} which is defined as the compliance of the point o when external force F_A is applied, is same in both directions of the vibration stage. Moreover, high accuracy examination of the output compliance is always required to guarantee the accuracy. Fig. 3-4 (I) shows the simplified vibration stage structural features and the main dimensional parameters. It consists of double layer structures, with the outer layer constructed by the parallel connection of four bars and inner layer constructed by normal right circle flexure hinges. Fig. 3-4 (II) shows the one quarter of the parallel connection of four bars structure for outer layer structure including two right circle flexure hinges. Based on the matrix method, its output compliance C_{P_A} with respect to the global coordinate can be expressed as:

$$C_{P_A} = (k_{P_A})^{-1} = C_{a_1}^{o} + C_{b_1}^{o} + C_{b_2}^{o} = T_{P_A}^{o} C_{a_1}^{P_A} (T_{P_A}^{o})^T + T_{P_A}^{o} C_{b_1}^{P_A} (T_{P_A}^{o})^T + T_{P_A}^{o} C_{b_2}^{P_A} (T_{P_A}^{o})^T \quad (3\text{-}28)$$

Where the local compliances $C_{a_1}^{P_A}$, $C_{b_1}^{P_A}$ and $C_{b_2}^{P_A}$ are the compliance at p_A-$x_A y_A$ and the corresponding global compliances are $C_{a_1}^{o}$, $C_{b_1}^{o}$ and $C_{b_2}^{o}$, k_{P_A} is the output stiffness, $T_{P_A}^{o}$ are the transformation matrices.

In order to further reduce the coupling motion, the compression/tensile stiffness of flexure hinges in inner layer is set much higher than their rotational stiffness. Therefore, the compression/tensile stiffness (belongs to level direction flexure hinges) can be ignored when calculating the inner structure compliance. Due to the symmetry design, the half inner layer structure only contains one flexure hinge as shown in Fig. 3-4 (III) and the relevant compliance C_o^{in} is:

$$C_o^{in} = (k_o^{in})^{-1} = C_{m_1}^o \tag{3-29}$$

Where k_o^{in} is the stiffness of structure III, the global compliances $C_{m_1}^o$ do not need to be transferred.

Overall, the vibration stage contains three individual limbs connected at the canter point *o* in parallel including both out layer and inner layer structure. Therefore, the stage output compliance C_{out} can be calculated by considering the total compliance of the three limbs:

$$C_{out} = (k_{out})^{-1} = [2(2C_{P_A})^{-1} + (2C_{m_1}^o)^{-1}]^{-1} \tag{3-30}$$

where k_{out} is the stage output stiffness.

Due to the symmetric design and the piezoelectric actuators placement locations, the actuation forces are applied on the end executor directly. As the end executor is assumed to be rigid, the input and output points and relevant compliances are coincident and can be expressed as:

$$C_{in} = C_{out} \tag{3-31}$$

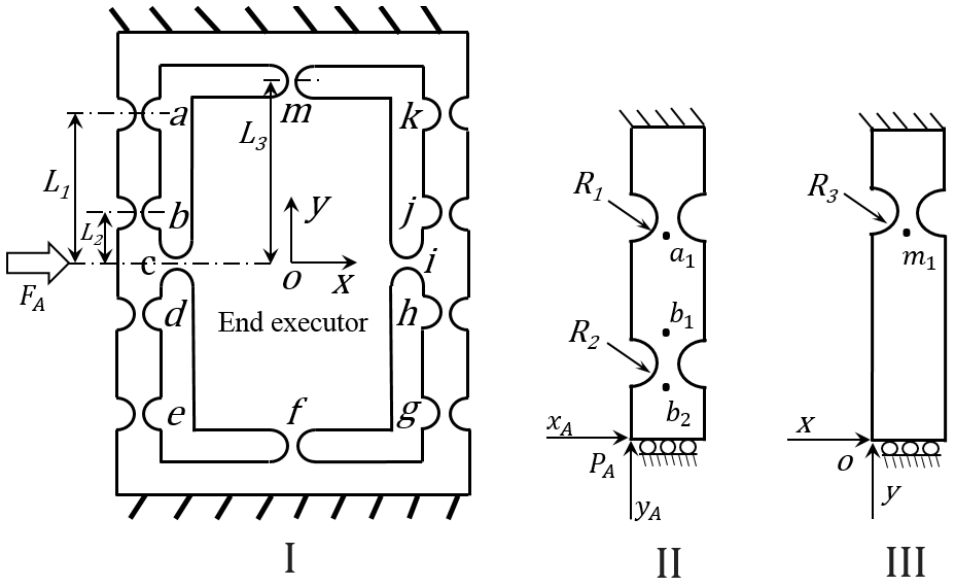

Figure 3-4 Compliances model of vibration stage.

3.3.4 Dynamic analysis of the vibration stage

As shown in section 3.2.3, the structure in each DOF of the vibration stage is the same. Therefore, only unidirectional dynamics is discussed and the dynamic model of the vibration stage is shown in Fig. 3-5. Assume that the end executor obtains a displacement of **s**= $[x, 0, 0]^T$

under the action force F and the corresponding kinetic energy T_k and potential energy U_k can be expressed as:

$$T_k = \frac{1}{2}\dot{x}^2 M_2 + 2\dot{x}^2 M_1 + 2I_z\theta_z^2 \tag{3-32}$$

$$U_k = \frac{x^2}{2C_{out}} \tag{3-33}$$

Where M_1 and M_2 donate the equivalent mass of flexible hinges and the equivalent mass of the end executor, respectively. I_z and $\theta_z = \frac{x}{l}$ are the moment of inertia of the flexible hinges around the z-axis and the corresponding turning angles, respectively.

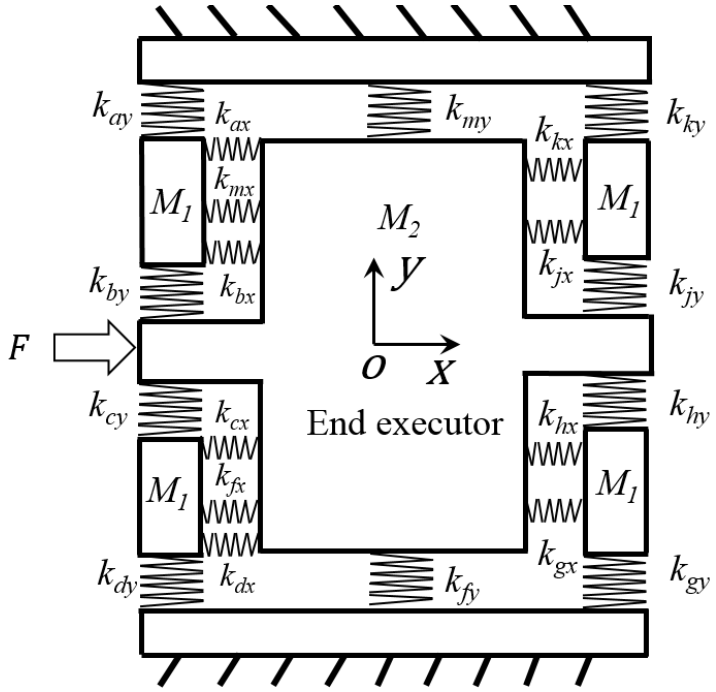

Figure 3-5 Dynamic model of the vibration stage.

The dynamics of the vibration stage can be obtained by substituting the kinetic and potential energies into the Lagrangian equation:

$$\frac{d}{dt}\left(\frac{\partial T_k}{\partial \dot{s}}\right) - \frac{\partial T_k}{\partial \dot{s}} + \frac{\partial U_k}{\partial s} = F \tag{3-34}$$

Overall, the dynamic equations for describing free motion of vibration stage can be expressed as:

$$(M_2 + 4M_1 + \frac{4I_z}{l^2})\ddot{x} + \frac{x}{C_{out}} = F \tag{3-35}$$

Then, the natural frequency of the vibration stage can be obtained as:

$$\epsilon = \sqrt{\frac{1}{(M_2+4M_1+\frac{4I_z}{l^2})C_{out}}} \tag{3-36}$$

3.3.5 Finite element analysis of the mechanism

3.3.5.1 Structural optimization

In order to achieve the best performance of the developed vibration stage under the condition of mutually restrictive, the vibration stage structure dimensional parameters are optimized by importing the analytical model to the ANSYS mechanical APDL software. It aims to achieve both as large as possible natural frequency and compliance. According to the overall structure design, the range of R_1, R_2, R_3 are shown below:

$$\begin{cases} 0.5 < R_1 < 2.9 \\ 0.5 < R_2 < 2.9 \\ 2 < R_3 < 5 \end{cases} \tag{3-37}$$

And the mathematical model can be expressed as:

$$\begin{cases} f_{max} = f(R_1, R_2, R_3) \\ C_{max} = C(R_1, R_2, R_3) \end{cases} \tag{3-38}$$

As a result, the optimized structural parameters and the material properties are listed in Table 3-2.

Table 3-2 Vibration stage structural parameters and the material properties used in the FEA model

Structural parameters								
R_1/mm	R_2/mm	R_3/mm	L_1/mm	L_2/mm	L_3/mm	a/mm	b/mm	c/mm
1.71	1.14	4.96	34	9.5	31	9	6	2
Material properties								
Density		Young's modulus		Poisson's ratio		Yield strength		
7850kg/m^3		197.5Gpa		0.3		430Mpa		

3.3.5.2 Static and dynamic performance analysis

In order to evaluate the new analytical model, the output compliance and natural frequency of the vibration stage are validated by using FEA method through ANSYS mechanical APDL. The meshing of the vibration stage is based on the hexahedron-dominated method, while approximate and curvature control method in the advanced dimension control is selected for meshing the curve structure.

FE static analysis is first performed where a 1N constant force is applied to the vibration stage and the setup of the FE model is shown in Fig. 3-6. And the results are shown in Fig. 3-7. It can be seen in Fig. 3-7 (a) that a maximum deformation of 0.02 μm occurs at the flexible hinges. This corresponds to the structural stiffness of the vibration stage of 50N/μm or structural compliance of 0.02 μm/N. As shown in Table 3-2, the discrepancy between the analytical model and FEA model is 3.5%, which indicates a high accuracy of the analytical model. The error may be attributed to the complex shear effects and stress concentration effects in the connections of the flexible hinges and it can be compensated by close-loop control of the vibration stage. Fig. 3-7 (b) shows the stress distribution of the vibration stage and it can be noticed that the maximum stress value is 106.3MPa that is well below the yield strength of the material (430Mpa).

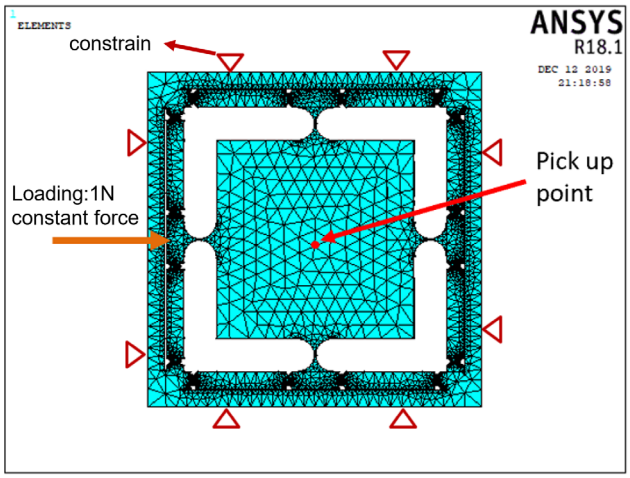

Figure 3-6 Setup of FE model

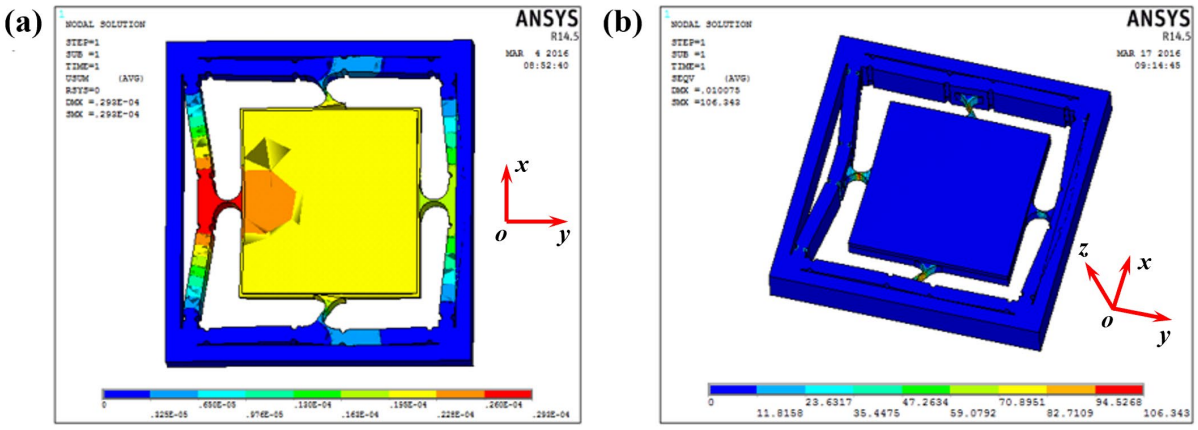

Figure 3-7 Static FEA simulation of the vibration stage (a) Displacement distribution; (b) Stress distribution

FE Modal analysis is performed to evaluate the dynamic performance of the developed vibration stage. Fig. 3-8 (a) and 3-8 (b) show the first two vibrational mode shapes and the responding natural frequencies are 2760.4Hz and 10661.7Hz, respectively. In the first vibration mode shape, it can be found that the vibration stage moves up and down along the z-axis (out of the plane). For the second vibration mode shape, the vibration stage moves back and front along the y-axis. The deviations (see Table 3-3) between analytical and FEA modal for first and second natural frequencies are 1.78% and 2.2%, respectively. It shows that the developed analytical model can predict the dynamic performance of the vibration stage accurately.

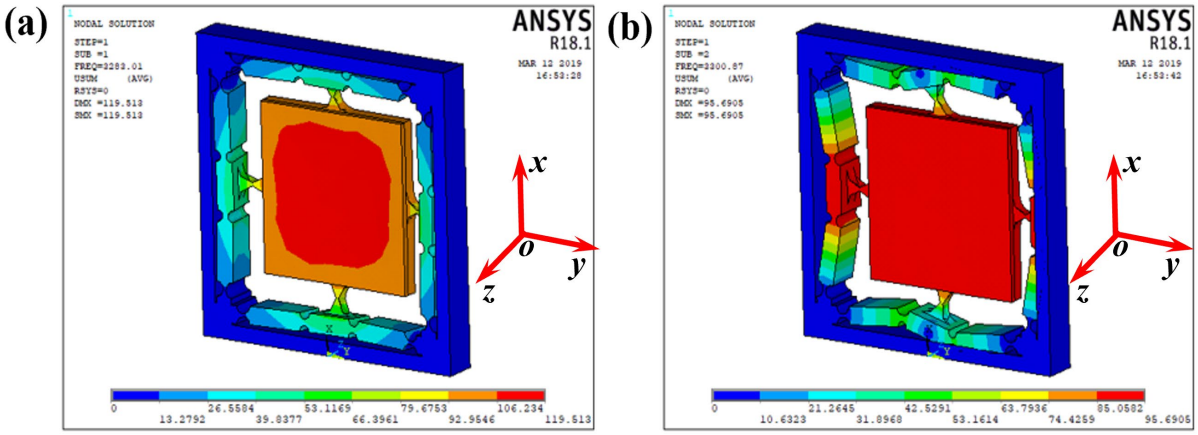

Figure 3-8 The first two modes of the vibration stage, (a) The first mode of deformation along z-axis (2760.4 Hz); (b) The second mode of deformation along y-axis (10661.7 Hz).

Table 3-3 Comparisons of static and dynamic results

	Compliance	First resonance frequency	Second resonance frequency
FEA	0.02 μm/N	2760.4 Hz	10661.7 Hz
Analytical model	0.0193μm/N	2809.5 Hz	10896.3 Hz
Deviation (%)	3.5%	1.78%	2.2%

3.3.5.3 Piezoelectric actuators selection

Two preloaded piezoelectric actuators (P-844.20 Physik Instrumente) are selected to drive the proposed vibration stage by considering the working frequency and amplitude range. The specifications are given in Table 3-4.

Table 3-4 The Specification of P-844.20 piezo actuators

Travel range	30μm	Electrical capacitance	12μF
Resolution	0.3nm	Resonant frequency	12 KHz
Stiffness	107 N/μm	Mass without cable	108g
Push/Pull force	3000N	Length	65mm

The actually achievable displacement of the vibration stage can be expressed as:

$$\Delta L = \Delta L_o \frac{K_a}{K_a + K_{out}} \tag{3-39}$$

Where ΔL and ΔL_o are the displacement of end executor and stroke of the piezoelectric actuators, respectively. K_a is the stiffness of the piezoelectric actuators, which is 107 N/μm, K_{out} represents to the stiffness of the vibration stage. Therefore, the maximum displacement of the vibration stage is almost 20 μm, which is big enough for the further application.

3.4 Control system design

3.4.1 Control program construction

The control system is developed based on the LabVIEW platform (2014 SP1) due to its friendly graphical user interface, powerful data acquisition and analysis capabilities and highly integrated control of system-related equipment. As the vibration stage is driven by two separate

piezoelectric actuators, two individual continuous control signals are needed, and the data of real-time stage vibration displacements also needs to be collected and recorded. Therefore, the developed control system consists two part: control signal generation part (signal generator) and data collection part (oscilloscope). Fig. 3-9 shows the architecture of the control signal generation part. The output signals and their sample rate, which is mainly affected by the output hardware, need to be defined first. Due to LabVIEW software does not support infinite generation sample function, then a certain number of samples should be defined. In order to obtain continuous output signals, a structure named "for loop" is applied here and the program will cycle the function infinitely until press "stop" button. Other functions like generating sweep signal are also added into the program. Fig. 3-10 shows the architecture of data collection program part. Similarly, the data collection channels and sample rate need to be set first. The "for loop" function is utilized to collect the data infinitely. After a series of mathematical operations and filtering processes, the vibration displacement data can be obtained.

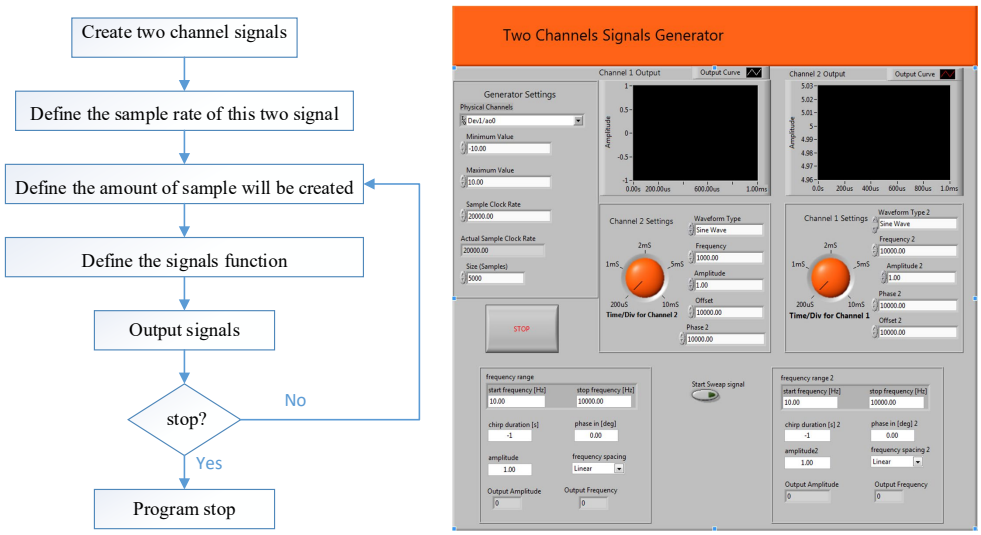

Figure 3-9 The architecture and LabVIEW control panel of the control signal generation part

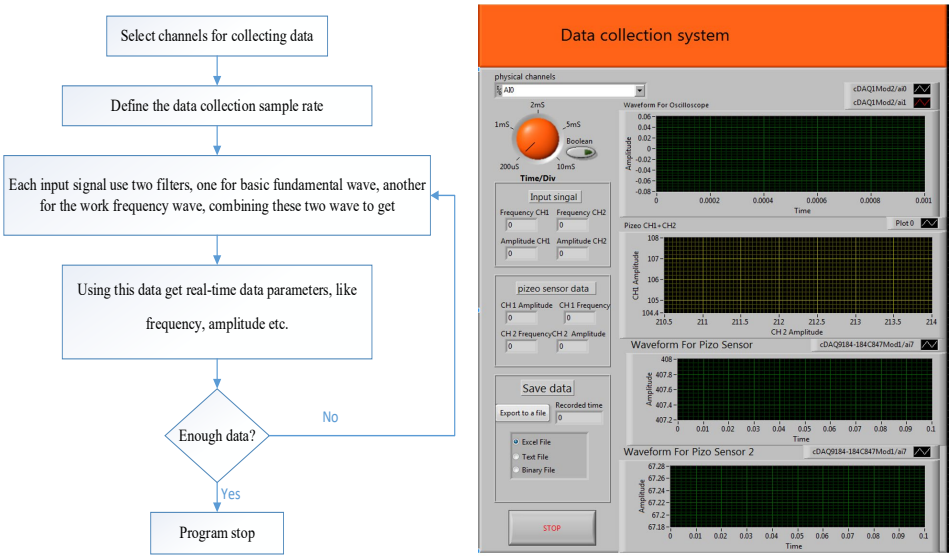

Figure 3-10 The architecture and LabVIEW control panel of the data collection part

3.4.2 Hardware selection

As the corresponding hardware system, DAQ device acts as the interface between the program and signals from the outside world. Two types of DAQ devices are widely used, data output module for generating signals and data input module for digitizing incoming signals so that a computer can interpret them. Due to the proposed vibration system aims to work under thousands of vibration frequency, the DAQ devices with low sample rate will not be able to truly restore the input or output signals and unable to generate or receive the desired vibration amplitude and frequency. By considering sample rate and resolution issues, the DAQ card selection results show in Table 3-5. Moreover, the two cards were mounted on to the cDAQ-9178, which is an Eight-Slot USB Chassis. It is designed for small, portable sensor measurement systems. The chassis provides the plug-and-play simplicity of USB to sensor and electrical measurements, optimize the data transfer between the cards and the computer.

Table 3-5 The specification of selected DAQ devices

Production name	Module type	Signal ranges	Channels	Sample rate	Resolution	Isolation	Connectively
NI 9221	Voltage input	± 60 V	8 Single-ended	800kS/s	12-Bit	250Vrms Ch-Earth (Screw Terminal) 60 VCD Ch-Earth (D-SUB)	Screw Terminal 25-Pin D-SUB
NI 9263	Voltage output	± 10V	4	100kS/s/ch	16-bit	250 Vrms Ch-Earth	screw-Terminal

To monitor the vibration displacement effectively, a modular capacitive sensor system (DL6220, Micro-epsilon) with two capacitive sensors (CS005, Micro-epsilon) is selected and the technical parameters are shown in Table 3-6.

Table 3-6 The Specification of selected Capacitance sensors and controller

Demodulator DL6200					
Resolution dynamic	Bandwidth	Data rate digital output	Sensitivity deviation	Analog output	No. of channels
0.02% FSO	5 kHz (-3 dB)	3.906 kSa/s	≤ ± 0.1 % FSO	0 ~10 V	Max. 4
Capacitance sensor CS005					
Measuring range	Linearity		Resolution (nm)		Dimensions
0.05mm	≤ ± 0.15 µm	≤ ± 0.3 % FSO	0.0375 (static)	1 (dynamic)	Ø6 × 12 mm

3.4.3 Layout of the control system

The schematic of the whole system is shown in Fig. 3-11. Both machine tool and vibration stage are controlled by the same host computer. For the vibration stage, the parameters of control signals set in the LabVIEW program and sent from an NI 9263 output DAQ (data acquisition) card. They can be used to drive the piezo actuators by going through a high voltage piezo amplifier. At the same time, the vibration displacement is monitored by a modular capacitive sensor system (DL6220, Micro-epsilon) with two capacitive sensors (CS005, Micro-epsilon) in each direction. A NI 9221 input DAQ card is selected for collecting the stage displacement data from the capacitive sensors.

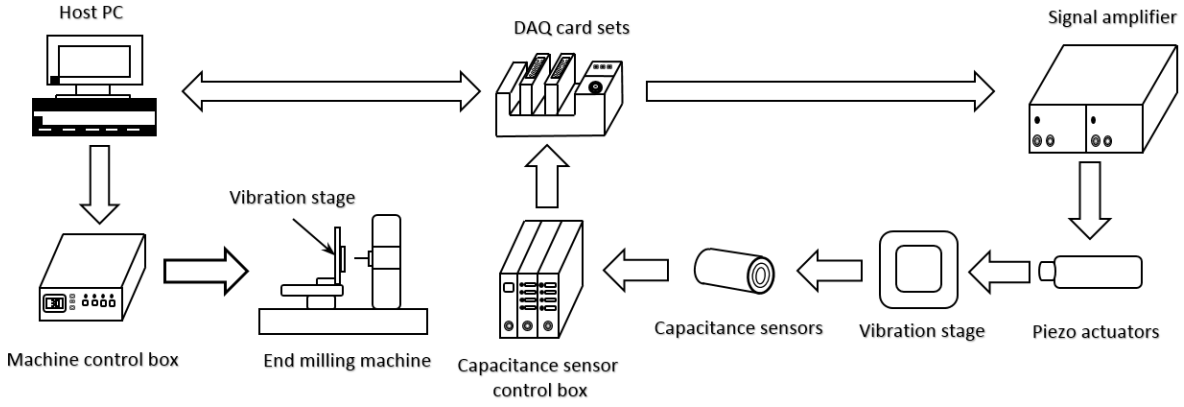

Figure 3-11 Layout of the control system

3.4.4 Closed loop control system

Piezo actuators are chosen for vibration generation resources. However, the linearity of the piezo actuators can be influenced by many factors, including nonlinear hysteresis caused by internal friction of piezoelectric materials and nonlinear creep caused by bipolar progressive rearrangement, which adversely affects the motion accuracy of the vibration stage. On the other hand, the structural coupling and the interaction between the machine tool and the work piece during machining will also reduce its motion accuracy. Therefore, a closed-loop servo control system is integrated into the developed LabVIEW program. PID algorithm is an important method for closed-loop control due to its simple algorithm and high reliability. However, drawbacks such as insufficient parameters tuning, poor control performance and adaptability result in its inability to perform high-performance control of systems with strong nonlinear and time-varying uncertainties (Leang and Devasia, 2007; Fleming, 2010). To overcome these shortcomings, a fuzzy adaptive PID control system is proposed for the vibration stage control system. Fig. 3-12 shows the block diagram of the fuzzy adaptive PID control system. The two-dimensional displacements of the vibration stage are measured by the capacitance sensors and sent back to the DAQ device as the feedback signals. *E* (error) and *EC* (error rate of change) of the vibration displacements are chosen as the inputs to the fuzzy controller and the output three parameters (K_P, K_I, K_D) of the PID controller are obtained according to the edited fuzzy control rules. In order to ensure the control accuracy, the fuzzy sets for the vibration displacement error *E* and error rate *EC* are set six and four levels respectively, which are *E* = {PB, PM, PS, NS, NM,NB} and *EC* = {PB, PM, PS, NS}, and the fuzzy sets of output controller is set seven levels, which is K_P, K_I, K_D = {PB, PM, PS, ZE, NS, NM, NB}. The fuzzy language variables of the vibration displacement error and the error rate are quantized to the integer domain for [−6, 6]. Compared with the traditional PID controller, fuzzy adaptive PID control system is extremely flexible and adaptable and effectively avoids accurate mathematical modelling process. However, the developed fuzzy adaptive PID control system can only work effectively when the vibration frequency is lower than 200 Hz due to the hardware limitations (DAQ devices and capacitance sensors).

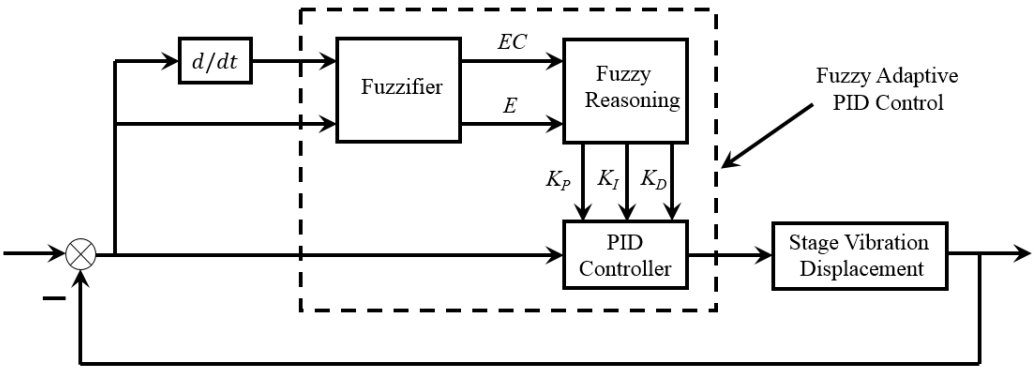

Figure 3-12 Block diagram of fuzzy adaptive PID control system

Fig. 3-13 shows the stage vibration trajectories error comparison results with and without the fuzzy adaptive PID control system under the condition of 100 Hz input signal frequency. Two channels sinusoidal signals are sent to the two piezo actuators with a 0° (see Fig. 3-13 (a) and (d)) 90° (see Fig. 3-13 (b) and (e)) and 180° (see Fig. (c) and (f)) phase difference, respectively. It can be found that input signal phase difference nearly has no influence on the vibration stage total trajectory errors with and without close-loop control conditions, which indicates that the designed vibration stage has a good movement precision retaining ability. Furthermore, the total vibration trajectory error (including the inherent noise of the capacitive sensors) is reduced from 0.25 μm to 0.15 μm when fuzzy adaptive PID control system was adapted, which is almost 40% increase on the vibration trajectory accuracy. Considering the noise effect, the vibration trajectory error is as small as 0.05 μm and only 2.17% of the total vibration displacement for both directions. The results show that the developed fuzzy adaptive PID control system can decrease the vibration trajectory error dramatically at low vibration frequencies.

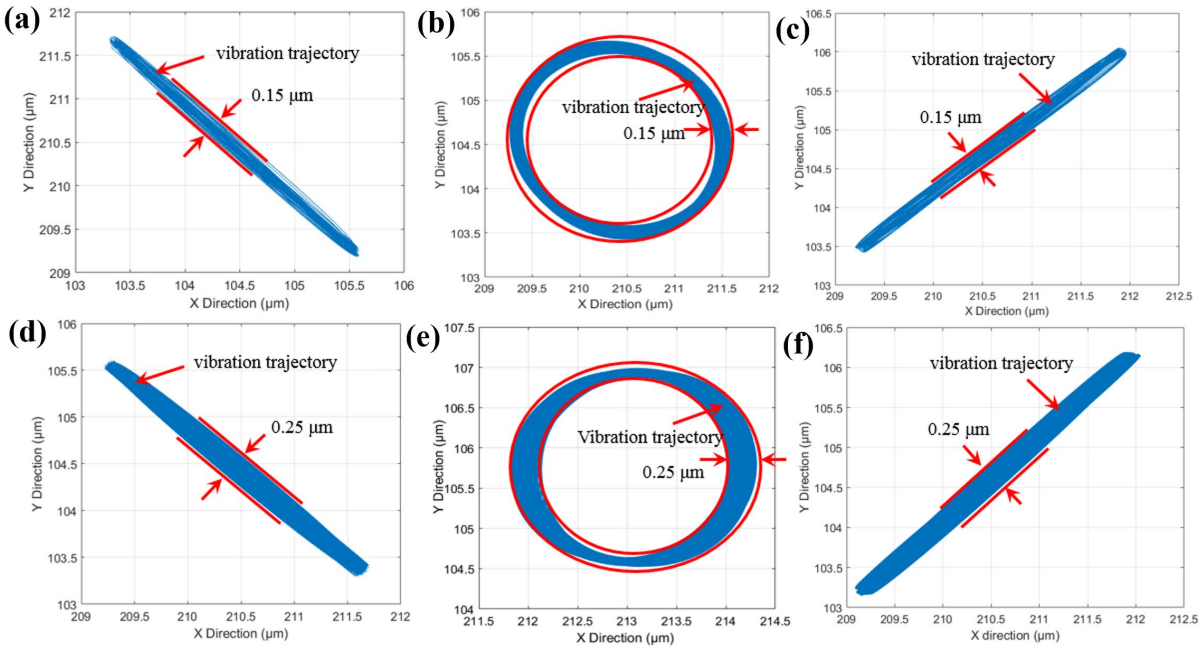

Figure 3-13 Stage vibration trajectories error comparison results, (a) 0° phase difference with fuzzy adaptive PID control system; (b) 90° phase difference with fuzzy adaptive PID control system; (c) 180° phase difference with fuzzy adaptive PID control system; (d) 0° phase difference without fuzzy adaptive PID control system; (e) 90° phase difference without fuzzy adaptive PID control system; (d) 180° phase difference without fuzzy adaptive PID control system;

3.5 Performance evaluation of the vibration stage

3.5.1 Relationship between the input signal and vibration displacement

Under the static condition, the control signal voltage and the corresponding displacement of the vibrating stage end executor are fixed linear relationship. However, when it refers to dynamic, the relationship will be changed as the vibration frequency variation due to the strength of structural resonance effect. Therefore, experiments for getting the accuracy relationship is necessary for the vibration system further application. Fig. 3-14 shows the layout of the testing devices. Vibration stage was fixed on the testing bench to get more space for capacitance sensor installing. A little cubic mounted at the centre of the stage for measuring vibration displacement and all the results are put in the appendix section.

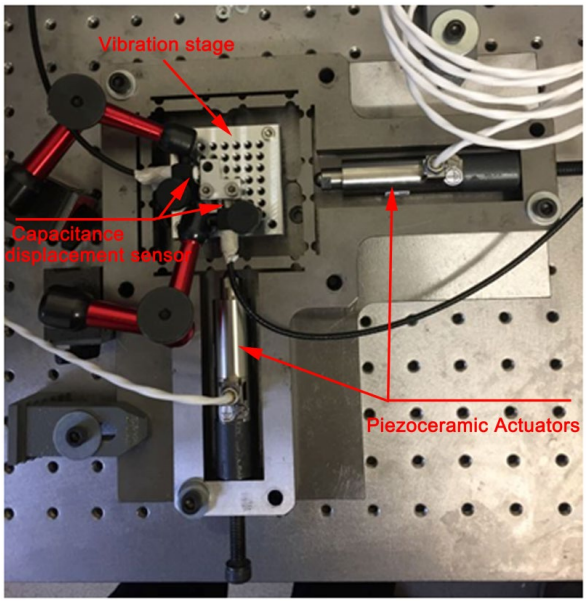

Figure 3-14 Layout of testing devices

3.5.2 Dynamic performance and decoupling evaluation

To experimentally investigate the dynamic characteristic of the developed vibration stage, frequency-response experiments were conducted in the condition of single-direction excitation. 0.8V sinusoidal discrete sweep voltage signals are sent to the piezo actuator at an interval of 500Hz over the frequency range 0 Hz to 12000 Hz. The corresponding vibration displacements are collected by the capacitive sensors and the frequency-amplitude results are shown in Fig. 3-15. It indicates that the first-order resonance frequency is between 2500 Hz and 3000 Hz and the second-order resonance frequency is between 10500Hz and 11000 Hz. The testing results show a good agreement with the results obtained from analytical (2809.5 Hz and 10896.3 Hz) and FEA (2760.4 Hz and 10661.7 Hz) models.

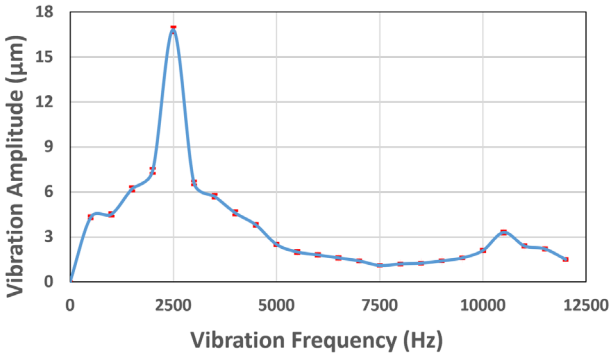

Figure 3-15 Frequency-amplitude results under control signal voltage at 0.8V

As discussed in Section 3.1, the coupling effect is one of the factors that have significant influence on the motion accuracy of the vibration stage. To investigate the working stability of the closed-loop control system, two variable sinusoidal signals (0.3V and under 200Hz) with a 90° phase difference are sent into the control system. The total vibration trajectory error is measured by using the method in Fig. 3-13. The total stage vibration trajectories error variation results under 200 Hz is illustrated in Fig. 3-16 (a). It can be found that when fuzzy adaptive PID control system operates, the total error is reduced by about 0.1 μm during the working frequency range, which indicates that it is an efficient method to further increase the working accuracy of the vibration stage. To further investigate the full working vibration frequencies total vibration trajectory error, the frequency-response experiments were conducted. The two variable sinusoidal signals (0.3V) are set at a 90° phase difference with an interval of 500 Hz over the frequency range 0 Hz to 12000 Hz. It can be observed from Fig. 3-16 (b) that the fluctuations in vibration trajectory error with frequency are acceptable and increases slightly as the vibration frequency increases. It reaches the peak points at the frequencies of 2500 Hz and 11000 Hz, respectively, due to the stage resonant effect. Generally, the proposed double parallel four-bar linkages with double layer flexible hinges structure can eliminate coupling errors completely. However, the testing vibration trajectory errors are influenced by many factors, such as the manufacturing and testing environment issues.

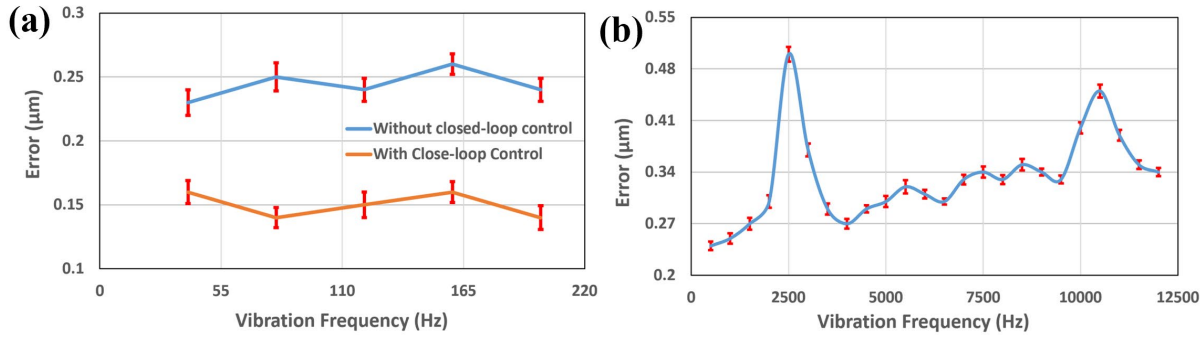

Figure 3-16 (a) Total stage vibration trajectories error variation results under 200 Hz, (b) Total vibration trajectory errors variation for full working frequency range.

3.6 Conclusion

This chapter details design, analysis, control and test of a new non-resonant vibration device for vibration assisted micro milling. To achieve high motion accuracy and reduce the coupling effect between the two vibration directions, the vibration stage is designed to be completely symmetrical based on the double parallel four-bar linkages with double layer flexible hinges

structure. The compliance of the flexure mechanisms is modelled by using matrix-based compliance modelling method. The dynamic characteristics and complete compliance are carried out by using the Lagrangian principle and considering the stage structure, respectively. Acceptable deviations (3.5% for compliance, 1.78% for first resonance frequency and 2.2% for second resonance frequency) can be obtained by comparing the analytical results with the FEA results, which indicate the feasibility of the proposed analytical model.

A close-loop control system is developed by using fuzzy adaptive PID control method based on LabVIEW program. The stage frequency-response tests confirm the resonant vibration frequencies and a relatively low tool tip coupling error (2.6% of the vibration amplitude).

Chapter 4 Investigation on surface texture formation and corresponding applications

4.1 Introduction

The microstructures have the characteristics of rules texture structure, high aspect ratio. These surface microstructures make the component has certain specific functions, such as reducing adhesion friction, improving lubricity and wear resistance and have specific optical properties (Kanemitsu *et al.*, 1993; Alpas and Zhang, 1994; Maboudian and Howe, 1997; Liao, Normand and Coddet, 2000; Jung and Bhushan, 2006). Such advantages are widely used for lots application, such as sliding contact elements, magnetic storage disk surfaces, machine tools guide-ways, hydrodynamic bearings, cam followers, rolls of forming processes, and mechanical face seals (Hadad and Ramezani, 2016).

Therefore, it is of great significance to investigate and manufacture the surface texturing. This chapter presents a novel method to obtain the unique surface textures by non-resonant vibration assisted milling. The kinematics analysis of the vibration assisted micro milling is firstly introduced and a surface generation model based on homogenous matrices transformation (HMT) is proposed. On this basis, series of simulations are performed to provide insights into the effects of various vibration parameters (frequency, amplitude and phase difference) on the generation mechanism of typical textured surfaces in 1D and 2D vibration assisted micro milling. The wettability tests are performed on the machined surfaces with various surface texture topographies. A new contact model, which considers both liquid infiltration effects and air trapped in the microstructure, is proposed for predicting the wettability of the fish scales surface texture. In addition, the fish scale surface textures are applied to the microfluidic channels and the liquid flow experiments have been carried out, the results indicate that liquid flow can be controlled effectively in the proposed microchannels at proper inlet flow rates.

4.2 Surface texture modelling

The generation process of textured surface can be recognized as the result of the interactions between a cutter with a specific shape and workpiece. In the machining process, the cutter is fed at specified machining path, and surface microstructures could be formed on the machined surface due to the cutting edge overlap trajectories. Thus, the surface generation in vibration-assisted milling is easily affected by various factors, including the kinematics of machining systems, the real geometry of cutting edge, machining and vibration parameters, etc. To

accurately model the vibration-assisted milling surface generation process, the cutting edge detection and modelling, the kinematics modeling and analysis, and the coordinate transformation from cutting edge to workpiece surface, are the key steps.

As illustrated in Fig. 4-1, one HMT-based calculation algorithm for the surface generation is proposed and it mainly consists of the following steps:

Firstly, the geometry of the cutting edge is detected by scanning electron microscope (SEM) and atomic force microscope (AFM), and it can be described with a numerical function. Secondly, the cutting edge and workpiece are discretized into series of points. Thirdly, all points on the cutting edge are transferred from tool coordinate system to workpiece coordinate system by HMT, which forms the simulated surface in a point cloud. Then the Z-map technology, which means plot the minimum z as a function of x and y in the workpiece coordinate system, is applied to generate the final machined surface.

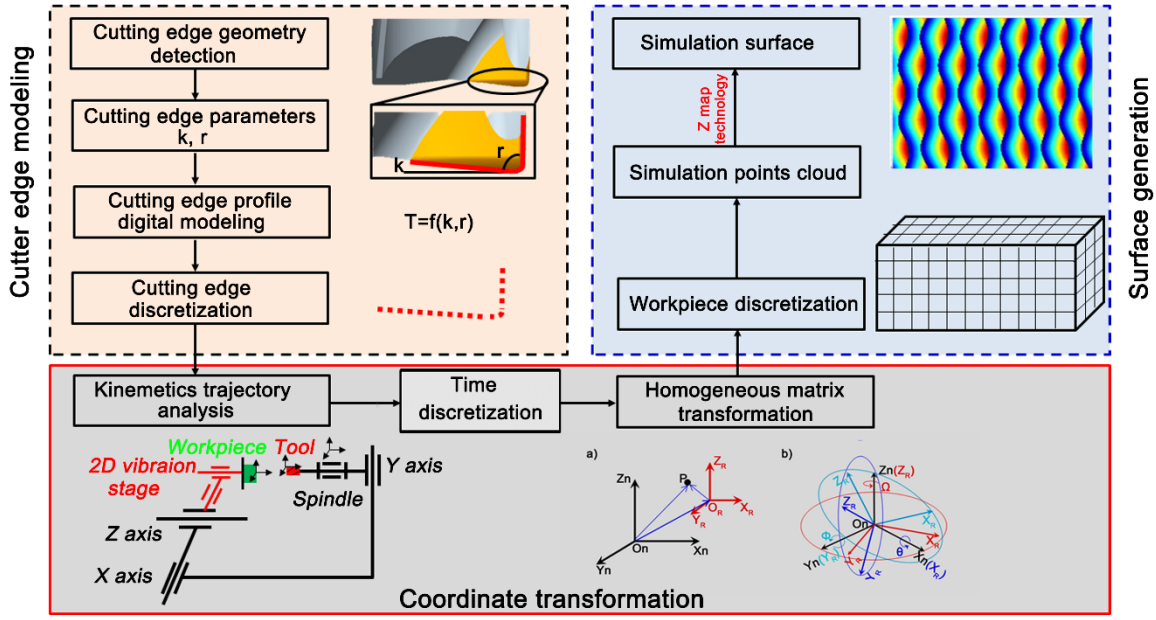

Figure 4-1 Flow chart of the surface simulation process

4.2.1 Cutter edge modelling

To accurately predict the surface topography in the vibration assisted milling process, the real contour of the cutter edge should first be described. Thus, the micro end mills were first detected by SEM and AFM before machining experiments to obtain the cutter geometry parameters. Fig. 4-2 a) show the SEM images for the two flutes micro milling tool. And the

minor cutter edge angle r_e and angle of minor cutting edge k' are measured in image analysis software ImageJ®, which are 3 μm and 5°, respectively.

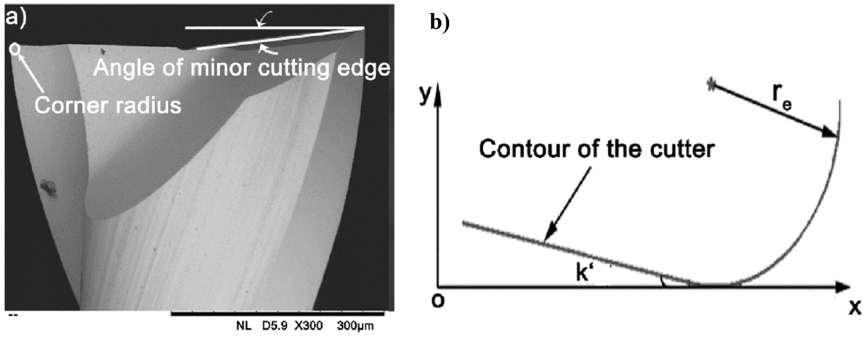

Figure 4-2 Tool geometry. a) side view; b) end cutting edge profile.

The profile of cutter edge, which is shown in Fig. 4-2 b), can be described as:

$$z = f(x) = \begin{cases} -xtank + (R - r_e - r_e sink)tank + r(1 - cosk), & 0 < x < R - r_e - r_e sink \\ -\sqrt{{r_e}^2 - [x - (R - r_e)]^2} + r_e, & x \geq R - r_e - r_e sink \end{cases} \quad (4\text{-}1)$$

where r_e, k', and R denote the tool edge radius, angle of minor cutting edge, and tool radius, respectively. The tool center, as shown in Fig. 4-2 b) is set to the origin of coordinate system, Z axis is aligned with the tool axis, and XY-plane is aligned with the tool rake face of one cutting flute.

4.2.2 Kinematics analysis

In order to realize the oscillating motion between the tool and workpiece, high frequency vibration with small amplitude could be superimposed to tool or workpiece. In this research, vibration is applied to the workpiece. As shown in Fig. 4-3, workpiece is simultaneously fed in the x- and y-direction, and the axial depth of cut is in the z direction.

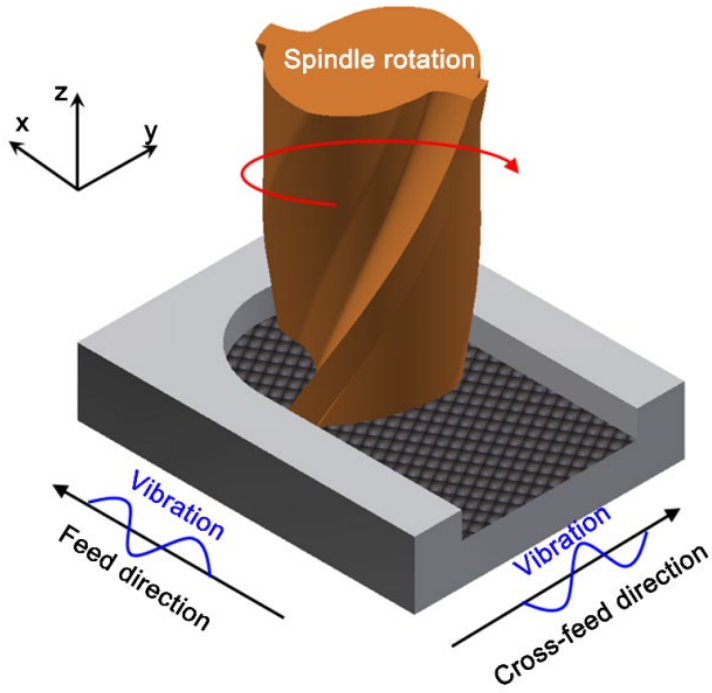

Figure 4-3 Schematic diagram of vibration assisted milling

The relative displacement (x_i, y_i) of tool tip to workpiece in vibration assisted micro milling process can be depicted by Eq. (4-2):

$$\begin{cases} x_i = V_f t + Rsin\left[\omega t - \frac{2\pi(Z_i-1)}{Z}\right] + Asin(f_x t + \emptyset_x) \\ y_i = Rcos\left[\omega t - \frac{2\pi(Z_i-1)}{Z}\right] + Bsin(f_y t + \emptyset_y) \end{cases} \quad (4\text{-}2)$$

where R and ω are the radius and angular velocity of the cutter, z_i is the i^{th} cutter tooth, and Z is the number of flutes. V_f is the feed velocity. A and B are the vibration amplitudes, f_x and f_y are the vibration frequencies, ϕ_x and ϕ_y are the phase angles, in x- and y-directions.

4.2.3 Homogeneous matrix transformation

From Eq. (4-2), it can be noted that, apart from t, 10 independent parameters are required to determine the tool tip trajectory in the 2D vibration-assisted milling. Owing to the effects of so many parameters, the tool tip trajectory in vibration assisted micro milling process is much more complex. In order to accurately describe the tool tip trajectory, the homogeneous matrix transformation (HMT) method is adopted and the detailed HMT process in vibration assisted micro milling process is introduced in the following section.

4.2.3.1 Basic theory of HMT

To represent the position of a rigid body in a three-dimensional space with a given coordinate system, a 4×4 matrix, ${}^{j}T_i$, is needed. This matrix represents the coordination transformation from the rigid body frame (o_i-x_i y_i z_i) to the reference coordinate frame (o_j-x_j y_j z_j) i.e. homogeneous matrix transformation. The first three columns of the homogeneous transformation matrix (HTM) refer to the direction cosines (unit vectors i, j, k). They represent the orientations of x_i, y_i and z_i axes of the rigid body in the reference coordinate frame, respectively, all having scale factors which are zero. The last column represents the relative position of the coordinate system of the rigid body to the reference coordinate frame (Chen, Zheng and Huo, 2018).

Fig. 4-4 shows the typical coordinate transformations from (o_i-x_i y_i z_i) to (o_j-x_j y_j z_j) including the translation transformation along x, y and z, and the rotation transformation with α, β and γ. The corresponding HTM are given in Table 4-1.

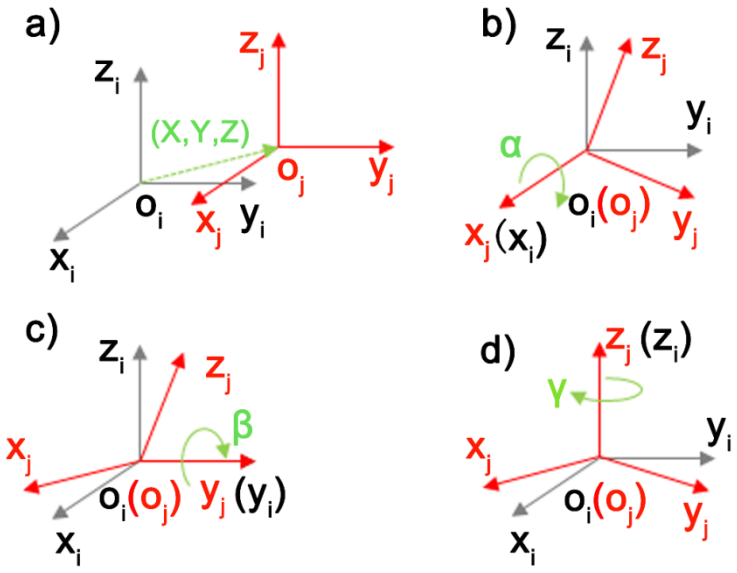

Figure 4-4 Coordinate transformations: a) translational transformation, b-d) rotational transformation with α, β and γ.

Table 4-1 HTM from (o_i-x_i y_i z_i) to (o_j-x_j y_j z_j)

Translation transformation	X, Y, Z	$^{j}T_i = \begin{bmatrix} 100 & x_{ij} \\ 010 & y_{ij} \\ 001 & z_{ij} \\ 000 & 1 \end{bmatrix}$
Rotation transformation	α	$^{j}T_i(\alpha) = \begin{bmatrix} 1 & 0 & 0 & 0 \\ 0 & cos\theta & -sin\theta & 0 \\ 0 & sin\theta & cos\theta & 0 \\ 0 & 0 & 0 & 1 \end{bmatrix}$
	β	$^{j}T_i(\beta) = \begin{bmatrix} cos\phi & 0 & -sin\phi & 0 \\ 0 & 1 & 0 & 0 \\ sin\phi & 0 & cos\phi & 0 \\ 0 & 0 & 0 & 1 \end{bmatrix}$
	γ	$^{j}T_i(\gamma) = \begin{bmatrix} cos\Omega & -sin\Omega & 0 & 0 \\ sin\Omega & cos\Omega & 0 & 0 \\ 0 & 0 & 0 & 0 \\ 0 & 0 & 0 & 1 \end{bmatrix}$

4.2.3.2 Establishment of HTM in the end milling process

To determine the effect of the error for each machine component on the relative position of tool tip to workpiece, the tool-workpiece spatial relationship should be pre-defined. To illustrate the relative position of a rigid body with respect to a given coordinate system, a 4×4 homogeneous transformation matrix (HTM, $^{R}T_n$) is needed. this also indicates the coordinate transformation from the rigid body frame (O_n-X_n Y_n Z_n) to reference coordinate system (O_R-X_R Y_R Z_R).

In the HTM, the first three columns are direction cosines (unit vectors i, j, k). They represent the orientations of X_n, Y_n and Z_n axes of the rigid body with respect to the (O_n-X_n Y_n Z_n), and their scale factors are zero. The last column in the HTM represents the relative position between the origins (O_n, O_R) of (O_n-X_n Y_n Z_n) and (O_R-X_R Y_R Z_R). Besides this, for clarity, P_s (a scale factor) is usually set to unit length.

As shown in Fig. 4-5a), the transformation of the coordinate of point $P(x, y, z)$ from (O_n-X_n Y_n Z_n) to (O_R-X_R Y_R Z_R) can be expressed as:

$$\overrightarrow{O_nP} = \overrightarrow{O_nO_R} + \overrightarrow{O_RP} = (x, y, z) + (x_{Rn}, y_{Rn}, z_{Rn}) = (x + x_{Rn}, y + y_{Rn}, z + z_{Rn}) \quad (4\text{-}3)$$

Where (x_{Rn}, y_{Rn}, z_{Rn}) refers to the coordinates of O_n *in* (O_R-X_R Y_R Z_R).

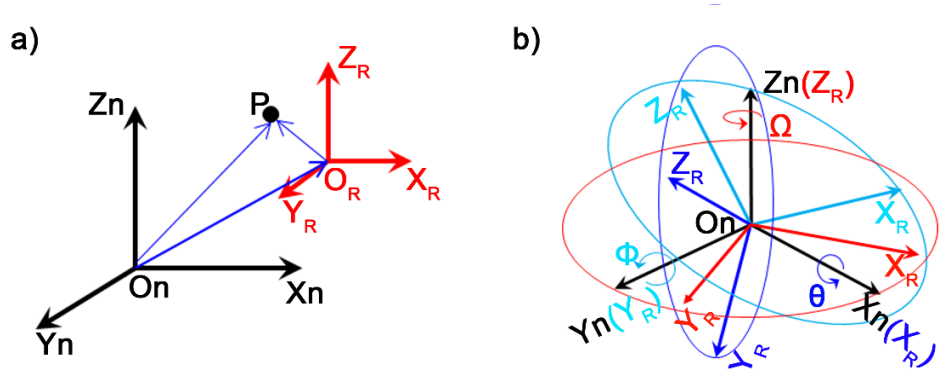

Figure 4-5 The coordinate transformations, a) Translational transformation; b) Rotational transformation

The pre-superscript and post-subscript are applied to represent the reference frame and the reference frame after transformation, respectively. The transfer matrix is expressed as:

$$^{R}T_n = \begin{bmatrix} 1 & 0 & 0 & x_{Rn} \\ 0 & 1 & 0 & y_{Rn} \\ 0 & 0 & 1 & z_{Rn} \\ 0 & 0 & 0 & 1 \end{bmatrix} \quad (4\text{-}4)$$

Thus, the coordinate transformation process of any point in a coordinate frame (n) to a reference frame (R) can be depicted via equation (4-3):

$$\begin{bmatrix} X_R \\ Y_R \\ Z_R \\ 1 \end{bmatrix} = {}^{R}T_n \begin{bmatrix} X_n \\ Y_n \\ Z_n \\ 1 \end{bmatrix} \quad (4\text{-}5)$$

In Fig. 4-5b), it can be seen that $O_n(x, y, z)$ has been transformed to $O_R(x, y, z)$ after the rotation around x-, y- and z-axis. The rotation angles have been labelled to be θ, ϕ and Ω, respectively. To describe the transformation process from (O_n-X_n Y_n Z_n) to (O_R-X_R Y_R Z_R), which is realized by the rotation around x-axis with a rotation angle θ, the following equation established.

$$\begin{cases} x_R = x_n \\ y_R = y_n cos\theta - z_n sin\theta \\ z_R = y_n sin\theta + z_n cos\theta \end{cases} \quad (4\text{-}6)$$

Thus, the corresponding homogeneous matrix could be expressed as:

$$\begin{bmatrix} 1 & 0 & 0 & 0 \\ 0 & cos\theta & -sin\theta & 0 \\ 0 & sin\theta & cos\theta & 0 \\ 0 & 0 & 0 & 1 \end{bmatrix} \tag{4-7}$$

Similarly, the matrixes used to depict the rotation around *y*-axis with a rotation angle ϕ, and the rotation around *z*-axis with a rotation angle Ω can be also expressed as:

$$\begin{bmatrix} cos\phi & 0 & -sin\phi & 0 \\ 0 & 1 & 0 & 0 \\ sin\phi & 0 & cos\phi & 0 \\ 0 & 0 & 0 & 1 \end{bmatrix} \tag{4-8}$$

And

$$\begin{bmatrix} cos\Omega & -sin\Omega & 0 & 0 \\ sin\Omega & cos\Omega & 0 & 0 \\ 0 & 0 & 0 & 0 \\ 0 & 0 & 0 & 1 \end{bmatrix} \tag{4-9}$$

The homogeneous matrix transformation method has been explained in detail in (Börner *et al.*, 2018) and it has been proved to be an effective tool for error analysis of machine tools (Weinert *et al.*, 2008; Klimant, Witt and Kuhl, 2014). In the previous HMT model, it is recognized that the cutting trajectory of the machine tool can be generated by using one point, e.g. tool tip. In this research, the whole cutting edge profile is discretized into numerous points. Then, by combining with the Z-map technology, the 3D machined surface topography can be simulated.

4.2.3.3 HMT in vibration assisted micro milling process

It is widely recognized that the surface topography of a machined surface can be generated by the cutting of the cutter edge on the workpiece. To obtain the machined surface, the HMT of the vibration assisted micro milling process should be conducted for the whole cutter edge. The HMT of a single point transformation from (o_i-x_i y_i z_i) to (o_j-x_j y_j z_j), is illustrated in Fig. 4-4, and the tool tip trajectory can be obtained using this method.

Fig. 4-6 shows a schematic diagram of the vibration-assisted milling equipment setup. The removal of workpiece material is performed by the cutter with high rotation speed. The vibration is applied to the workpiece, which is fed along the *x*-direction. Also, it can be seen that the local coordinate system of the cutter (O_t-$X_tY_tZ_t$) and the rotation coordinate system (O_T-

$X_TY_TZ_T$) are applied to describe the tool profile and the spindle rotation. Besides this, the translation coordinate systems, i.e. O_V-$X_VY_VZ_V$ and O_W-$X_WY_WZ_W$ are used to depict the vibration on the workpiece and the feed of the control system. The detailed transformation or rotation values of each coordinate system in the vibration assisted micro milling process process are given in Table 4-2.

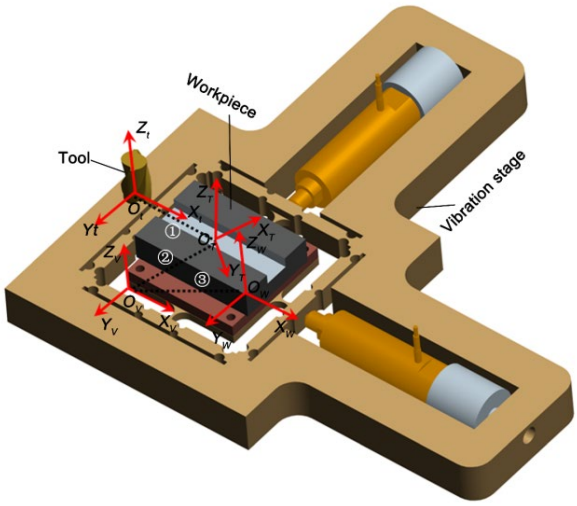

Figure 4-6 The coordinate systems in vibration assisted milling

Table 4-2 State value for each HMT

HMT	x	y	z	α	β	γ
${}^{T}T_t$	0	0	0	0	0	$\varphi - \omega t$
${}^{V}T_T$	$A\sin(2\pi f_x t + \emptyset_x)$	$B\sin(2\pi f_y t + \emptyset_y)$	0	0	0	0
${}^{W}T_V$	$x_0 + (i-1)a_e$	$y_0 + v_f t$	0	0	0	0

The homogeneous coordinates of the cutter edge in O_t-$X_tY_tZ_t$ are given as:

$$\begin{bmatrix} x_t \\ y_t \\ z_t \\ 1 \end{bmatrix} = {}^{R}T_n \begin{bmatrix} x \\ 0 \\ f(x) \\ 1 \end{bmatrix} \tag{4-10}$$

The O_T-$X_TY_TZ_T$ only considers the rotation speed of the cutter. The X_T and Y_T axes are aligned with the cutter feed and cross-feed directions, respectively. And the Z_T axis is parallel to Z_t. The origin of the tool coordinate system is same as that of the local tool coordinate system. The angular velocity of O_t-$X_tY_tZ_t$ relative to O_T-$X_TY_TZ_T$ is therefore the spindle angular velocity. As shown in Fig. 4-7, the relative rotational angle (θ) of two coordinate systems change with time. When the points of the cutter edge are changed from O_t-$X_tY_tZ_t$ to O_T-$X_TY_TZ_T$, the rotational effect is considered.

$$\theta = \varphi - \omega t \tag{4-11}$$

where φ is the initial angle between X_t and X_T axes. In this research, it is set to 0°. ω is the tool rotation angular velocity *(rad/s)* and t is cutting time *(s)*.

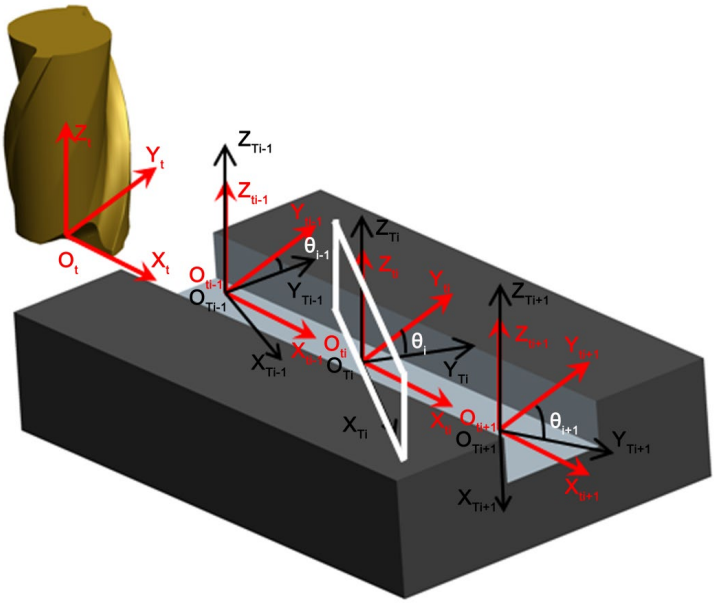

Figure 4-7 Tool instantaneous attitude position

The HTM from O_t-$X_tY_tZ_t$ to O_T-$X_TY_TZ_T$ can be expressed as:

$${}^{T}T_{t} = \begin{bmatrix} cos\theta & -sin\theta & 0 & 0 \\ sin\theta & cos\theta & 0 & 0 \\ 0 & 0 & 1 & 0 \\ 0 & 0 & 0 & 1 \end{bmatrix} \tag{4-12}$$

In the workpiece coordinate system (O_W-$X_WY_WZ_W$), X_W, and Y_W, refer to the feed direction and cross-feed direction, respectively. And Z_W represents the direction of the axial depth of cut, which is parallel to Z_t. In 3-axis milling process, only the translation between O_W-$X_WY_WZ_W$ and

O_T-$X_TY_TZ_T$ occurs. The initial position of O_W-$X_WY_WZ_W$ relative to O_T-$X_TY_TZ_T$ could be determined according to the actual machining situation.

By transforming the coordinates of the tool cutter edge from O_t-$X_tY_tZ_t$ to O_W-$X_WY_WZ_W$, the position of each point on the cutter edge relative to the workpiece can be obtained, and the height of the cutter edge at any point could also be recorded through the Z_W coordinate.

The original coordinate of O_T-$X_TY_TZ_T$ for each feed in cross-feed direction relative to O_W-$X_WY_WZ_W$ is obtained by:

$$\begin{cases} x_{oT} = x_o + (i-1)a_e \\ y_{oT} = y_o + v_f t \\ z_{oT} = z_o \end{cases} \tag{4-13}$$

where (x_0,y_0,z_0) is the initial position of the origin of O_T-$X_TY_TZ_T$ in the O_W-$X_WY_WZ_W$, which is set as $(0,-R,0)$ in this research. a_e is the radial cutting depth (mm). i is the number of feed in cross-feed direction; v_f is the feed speed in Y_w direction (mm/s).

As shown in Fig. 4-7, owing to the effect of the vibration applied on the workpiece, the relative displacement between tool and workpiece is changed. Thus, the origin coordinates of O_T-$X_TY_TZ_T$ for each feed in radial direction relative to the origin of O_W-$X_WY_WZ_W$ can be calculated as:

$$\begin{cases} x_{oT} = x_o + (i-1)a_e + Asin(f_x t + \emptyset_x) \\ y_{oT} = y_o + v_f t + Bsin(f_y t + \emptyset_y) \\ z_{oT} = z_o \end{cases} \tag{4-14}$$

where $x(t)$ and $y(t)$ denote the components of the dynamic instantaneous displacement between tool and workpiece in x-and y-direction, respectively.

Thus, the HTM from O_T-$X_TY_TZ_T$ to O_W-$X_WY_WZ_W$ can be expressed as:

$$^{W}T_T = \begin{bmatrix} 1 & 0 & 0 & x_o + (i-1)a_e + Asin(f_x t + \emptyset_x) \\ 0 & 1 & 0 & y_o + v_f t + Bsin(f_y t + \emptyset_y) \\ 0 & 0 & 1 & z_o \\ 0 & 0 & 0 & 1 \end{bmatrix} \tag{4-15}$$

The cutter edge in the workpiece coordinate system O_W-$X_WY_WZ_W$ can be expressed as:

$$\begin{bmatrix} x_W \\ y_w \\ z_w \\ 1 \end{bmatrix} = {}^{W}T_{T}\ {}^{T}T_{t} \begin{bmatrix} x_t \\ y_t \\ z_t \\ 1 \end{bmatrix} = \begin{bmatrix} xcos\theta + x_o + (i-1)a_e + Asin(f_x t + \emptyset_x) \\ xsin\theta + y_o + v_f t + Bsin(f_y t + \emptyset_y) \\ f(x) + z_o \\ 1 \end{bmatrix} \tag{4-16}$$

Fig. 4-8 illustrates two typical tool tip trajectories in vibration assisted micro milling process based on the HMT. When the vibration is an odd multiple of the spindle rotation frequency, a complex surface texture is generation by the overlapping between the adjacent cutter teeth. And when the vibration is an even multiple of spindle rotation frequency, a wave surface is generated. It can be noted that the ratio between the vibration frequency and the spindle rotation speed has a significant influence on the texture generation.

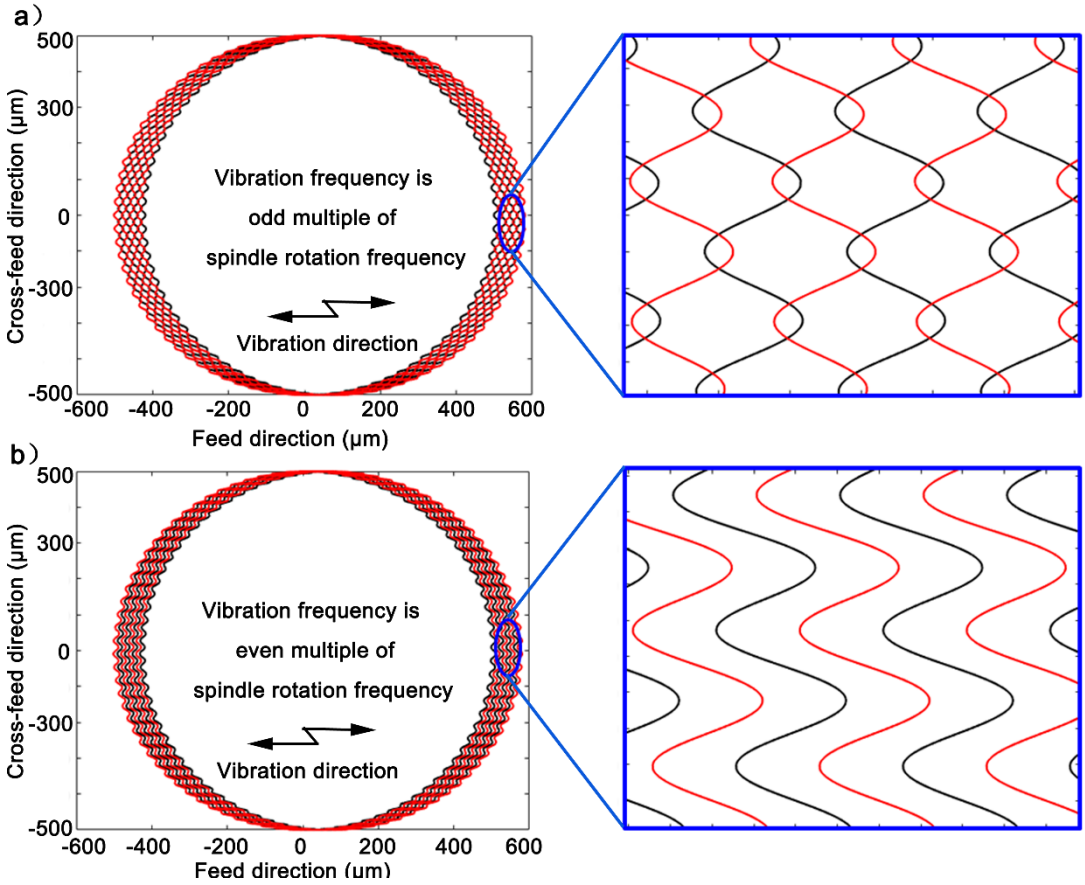

Figure 4-8 Tool tip trajectories of vibration assisted micro milling process with different RVS. a) Odd multiple, b) Even multiple

4.2.4 Surface generation

According to the copy principle of tool contours, the workpiece surface topography is formed by sweeping the cutter edge profile along the tool path.

In order to model the surface generation through numerical simulations, cutter edge and workpiece are discretized into a series of elements. The machined surface topography could be formed by mapping the cutter edge contour onto workpiece surface. Fig. 4-9 illustrates the schematic diagram of the simulation of surface generation. Firstly, the cutter edge is discretized into numerous elements, and workpiece is evenly divided into *n* columns and *m* rows. The intersection of each row and column forms a grid point. The height of each point on the machined workpiece surface can be obtained by calculating the tool cutting depth (*z*-coordinate) at grid point. To obtain one complete surface, the height of the middle position between two grid points can be obtained using a curve fitting algorithm.

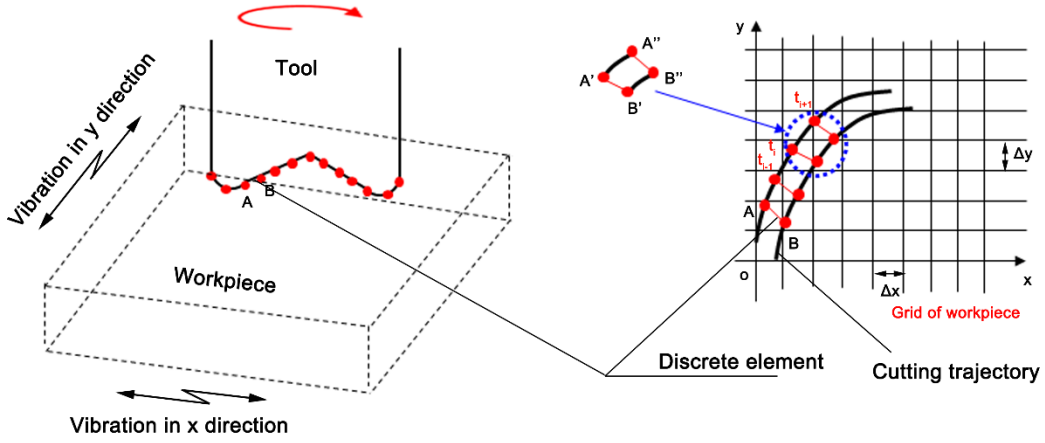

Figure 4-9 Schematic of surface generation simulation algorithm

4.2.5 Surface generation simulation

In-depth understanding of the machining process of structured surface in vibration assisted milling, especially when the relationship between machining and vibration parameters, surface texture and its wettability are known, means that surface simulation is an effective way to realize the deterministic manufacturing of functional surfaces.

In order to investigate the influence of vibration parameters on surface generation, the machining and cutter parameters, such as spindle rotation speed, number of tooth and the feed per teeth, are pre-defined, as shown in Table 4-3. In a previous investigation (Tao *et al.*, 2017), the ratio of vibration frequency to spindle rotation speed, as well as vibration amplitude significantly influence on the texture generation. To clearly indicate the influence of vibration parameters on the surface topography, eight typical sets of vibration parameters are selected in

this study. The spindle speed is kept at 6,000 rpm (rotation frequency is 100Hz). The vibration frequency is set to 8300 Hz (odd multiple of spindle rotation frequency) and 8400 Hz (even multiple of spindle rotation frequency). Meanwhile， three typical vibration amplitudes, that is, 2, 5 and 7μm, are employed. They are less, equal and larger than the half of the feed per tooth (10 μm), respectively. In addition, to investigate the influence of a phase difference between the two vibration directions on the surface generation, the phase difference is set to 0, π/4 and π/2, respectively.

Table 4-3 Machining and vibration assisted parameters

Set No.	Spindle speed (rpm)	Feed per tooth (μm)	*x*-direction		*y*-direction		Phase difference (rad)
			vibration amplitude (μm)	vibration frequency (Hz)	vibration amplitude (μm)	vibration frequency (Hz)	
1	6000	10	2	8300	0	0	0
2	6000	10	5	8300	0	0	0
3	6000	10	7	8300	0	0	0
4	6000	10	7	8400	0	0	0
5	6000	10	5	8400	5	8400	π/2
6	6000	10	5	8400	5	8400	0
7	6000	10	5	8300	5	8300	0
8	6000	10	5	8300	5	8300	π/4

From set 1-3 (see Table 4-3), it can be found that the frequency of the vibration applied in *x*-direction is odd multiple of the spindle rotation frequency. Since the applied vibration trajectory is a sinusoidal curve, the valleys (crests) of the current cutter trajectory are intersected with the crests (valleys) of the following cutter trajectory. As a result, three types of surface topographies are obtained, as shown in Fig. 4-10 a-c). It can be found that different kinds of fish squamous structures are generated on the machined surface, corresponding to the vibration amplitudes of less, equal and larger than half of the feed per tooth.

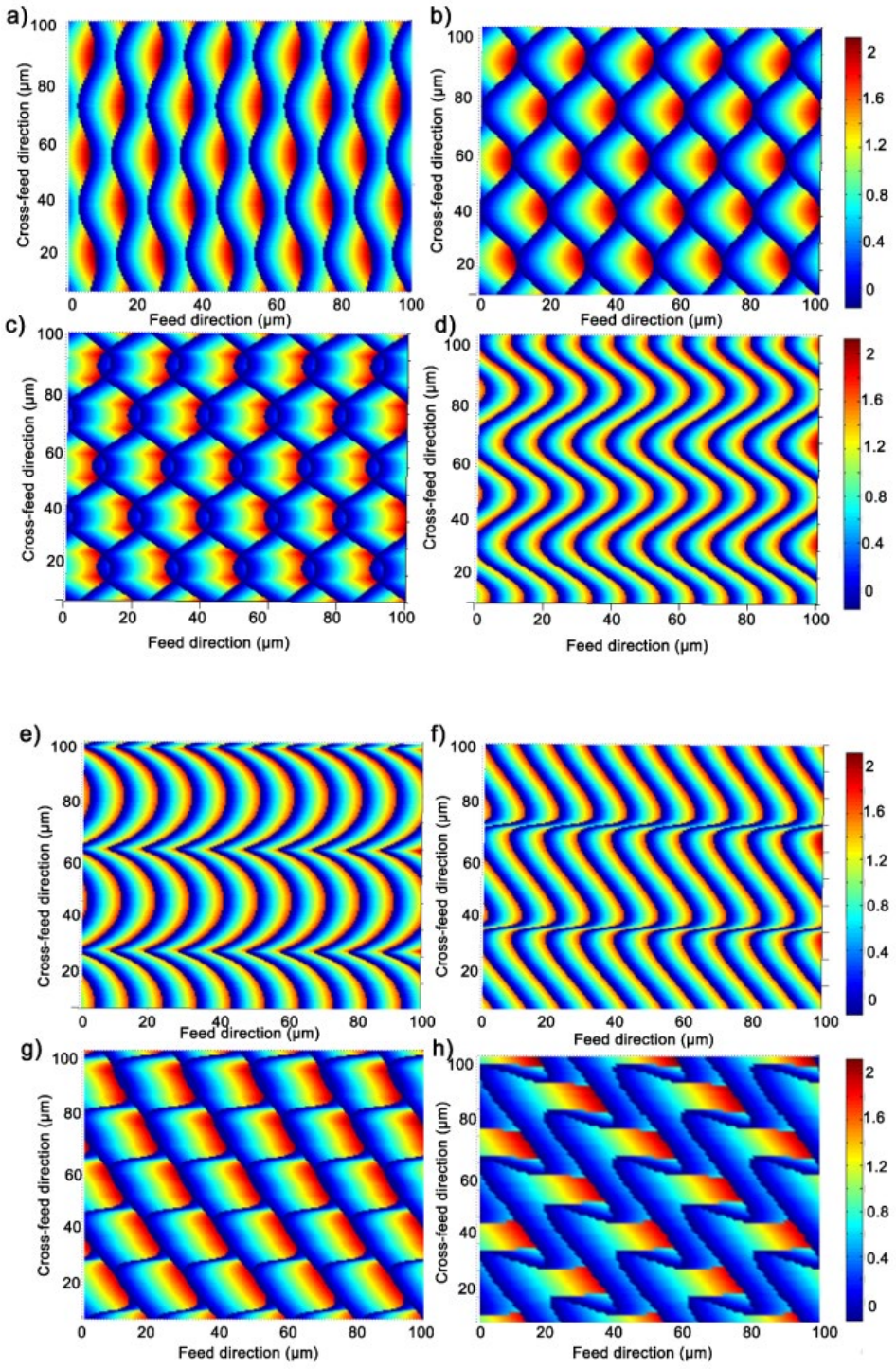

Figure 4-10 Simulation results of the VAM surface. a-h) Surface generated with the machining and vibration parameters of set 1-8.

In the vibration-assisted milling experiments of Set 4, since the vibration frequency applied in *x*-direction is an even multiple of the spindle rotation frequency, the crests (valleys) of the current cutter trajectory are intersected with those of the following cutter trajectory, thereby leading to the formation of a wavy surface, as shown in Fig. 4-10 d).

In the milling experiments of Sets 5 and 6, the vibration is applied to both the *x*- and *y*-directions. Moreover, the vibration frequencies are an even multiple of the spindle rotation frequency, and the phase differences between two vibration signals are pi/2 and zero, respectively. Under the effects of the *x*- and *y*-direction vibrations, it can be seen in Fig. 4-10 e) and f) that the crests (valleys) of the current cutter trajectory also meets the crests (valleys) of the following cutter trajectory. Meanwhile, the spatial distribution of wavy surface is changed, due to the phase difference between two vibration signals, as shown in Fig. 4-10 e) and f).

Finally, similar to those of Sets 5 and 6, vibrations are also applied in *x*- and *y*-directions in the milling experiments of Set 7 and 8. However, the vibration frequencies (odd multiple of spindle rotation frequency) and the phase differences of zero and pi/2 between two vibration signals are adopted. From the results (see Fig. 4-10 g) and h), it can be noted that the valleys (crests) of the current cutter trajectory also meet the crests (valleys) of the following cutter trajectory. Finally, two evidently different surfaces topographies are finally obtained, which can be attributed to the effects of different phase differences between the two vibration signals.

4.2.6 Experiments and results

In the present work, uncoated two-flutes micro cutting tool with the diameter of 0.5 mm is used. The workpiece material is Al-6061. In order to verify above simulation results, the machining parameters used in the experiments are the same as those adopted in the simulation.

The surface topography of each machined surface was tested using a white light interferometer surface profilometer (Vecco NT1100), as shown in Fig. 4-11. It can be clearly seen that Figs. 4-11 a), b), and d) agree well with the simulation results (see Fig. 4-10 a), b) and c)), respectively. However, other experimental results are not consistent with the simulation results in Fig. 4-10. This could be ascribed to the effects of different kinds of vibrations. In the milling experiments corresponding to Fig. 4-11 a), b) and d), the vibration is only applied in one direction. The control of vibration amplitude is easy. However, in the milling experiments corresponding to Fig. 4-11 e-h), vibration is applied in both of *x*-and *y*-directions. Owing to the stiffness coupling effect of 2D-vibration stage, due to the interaction of the vibrations in the *x*- and *y*-direction, vibration amplitude and the phase difference between *x*- and *y*-direction vibration signals do not reach the expected value. As for the milling corresponding to Fig. 4-11 c), due to the elastic recovery effect of the material, the overlap of two adjacent cutter edges is too small to be reflected on the machined surface.

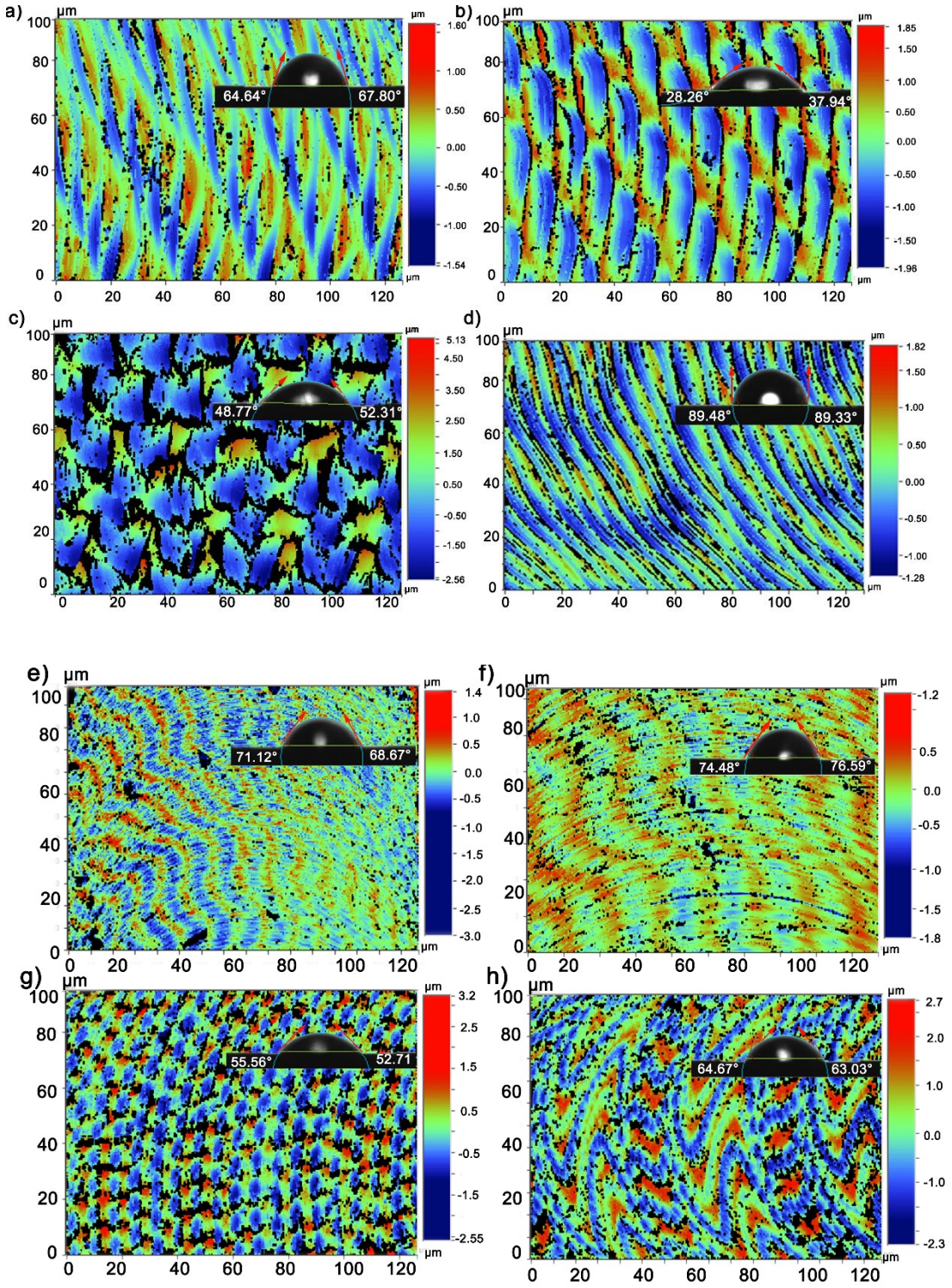

Figure 4-11 Experiment results of the VAM surface. a-h) Surface generated with the machining and vibration parameters of set 1-8.

Overall, the surface texture model proposed in the present work can accurately describe the surface generation in 1D vibration-assisted milling process. However, due to the coupling

effect of the *x*- and *y*-direction vibration, it is still hard to accurately predict the surface generation in the 2D vibration assisted milling process.

The water contact angle on each machined surface is also measured and the results show that the workpiece surface generated at different vibration parameters exhibit different wettability (see Fig. 4-11). According to the measured water contact angles, the contact angles of these textured surfaces vary from 30° to 89°, which shows a great potential in surface wettability controlling.

4.3 Modulation of textured surface wettability

Wettability is one of the most important characteristics inherent to a surface, which has a significant effect on the flow of a liquid over a solid substrate (Firincioglu, Blunt and Zhou, 1999). It is the result of the interfacial tensions interaction of three phases (vapour, solid surface and liquid) and can be expressed by the surface contact angle (Young, 1805). Benefits such as superior lubrication and wear resistance can be obtained by modifying a solid surface wettability to an appropriate value, which results in wide applications such as in the bio-medical field and oil industry (Buckley, Takamura and Morrow, 1989; Borruto, Crivellone and Marani, 1998; Zhou, Morrow and Ma, 2000; Li and Chen, 2006). Surface wettability can be affected by many factors, such as material types, surface roughness and surface microstructure. Accordingly, research on creating particularly hydrophilic surfaces and the relevant theories, such as contact models and the influence of surface free energy variation on contact angle have been carried out in the past decades. Li *et al.* (Li and Amirfazli, 2005) found that solid surface hydrophilicities with distinct surface textures can be quite different even if they have similar surface roughness. To explain this phenomenon, an analytical method was proposed to calculate the contact angle based on a typical pillar surface microstructure by considering the surface energy variation in the Wenzel and Cassie's contact model. A different theory is proposed by Shi *et al.* (Shi *et al.*, 2016): they fabricated a parallel-channels surface microstructure by using high speed micro milling machine and built a relationship between the droplets' Gibbs free energy on the surface and the contact angle. To improve the hydrophilicity of a polymer membrane and extend its life, Yang *et al.* (Yang *et al.*, 2015) fabricated a mineral coating to cover it. Results showed that both wettability and structural stability of the polymer membrane were improved. However, this method cannot produce a controllable wettability of the surface. Fuat *et al.* (Topuz, Möller and Groll, 2015) solved this problem by developing a

multilayers coating. Through changing the terminal layer, the contact angle varies between 37° and 45°. However, its application is limited by the complexity of the process, its high cost and the coating's susceptibility to ageing. Producing surface textures is another way to change surface drop impact characteristics, and many techniques such as high speed micro machining, laser cutting and etching have been applied in the manufacturing process. A pillars-array microstructure fabricated with a CNC machine is proposed by Lee *et al.* (Lee *et al.*, 2010). It is found that the pillars-array micro-structure can effectively improve the material hydrophobic properties and the surface wetting state changes (from Cassie state to Wenzel state) as pillars' spacing increases. Laser cutting is another efficient way to manufacture unique surface patterns with different surface wettability. However, special equipment is required for the process (Rukosuyev *et al.*, 2014; Razi, Mollabashi and Madanipour, 2015). Andrew *et al.* (Sommers and Jacobi, 2006) developed a parallel-grooves surface structure by using etching. According to the contact angle measurement results, the etched surface hydrophobicity is increased and can be controlled within a certain range; furthermore, an anisotropic wettability is obtained. the surface textures obtained by using non-traditional machining techniques also suffer from problems such as hard to control production process and hence inaccuracy in reproduction. Although non-traditional machining techniques permit tailoring wettability via surface textures, they involve complex production processes and are difficult to reproduce accurately (Burgers *et al.*, 2000).

The machine results in section 4.3 show a different wettability of the machined surface with different surface texture. This section will focus on the wettability modulation of the fish scale surface textures. A new contact model is proposed and verified through sessile drop method.

4.3.1 Kinematic analysis of surface topography generation

4.3.1.1 Tool tip trajectories analysis

The principle of fish scale surface texture modification during vibration assisted micro milling is investigated first. According to equation (4-2), as the vibration is only applied on X axis direction (feed direction), the relative trajectories of the tool tips and the workpiece can be expressed as:

$$X_i = V_f t + R\sin\left(\frac{n\pi t}{30} + i\pi\right) + A_x \sin\left(2\pi f_x t + \varphi_x\right)$$
$$Y_i = R\cos\left(\frac{n\pi t}{30} + i\pi\right) \quad (4\text{-}17)$$

Where f_x (Hz) and A_x (μm) are the vibration frequency and amplitude, respectively, and φ_x is the initial vibration phase angle.

According to Eq. (4-17), two unique adjacent tool paths can be generated, as shown in Fig. 4-12. With proper phase differences, a closed area (fish scales) can be produced, with the crests or troughs of the one tool tip corresponding to the troughs or crests respectively of the following tool tip. To describe this situation, the ratio between vibration frequency and spindle rotational frequency is defined as the frequency ratio (δ) and the condition to achieve this regular pattern for a two-flute cutter is:

$$Frequency\ ratio\ (\delta) = {}^{60\ f_x}/_{n} = odd\ numbers \quad (4\text{-}18)$$

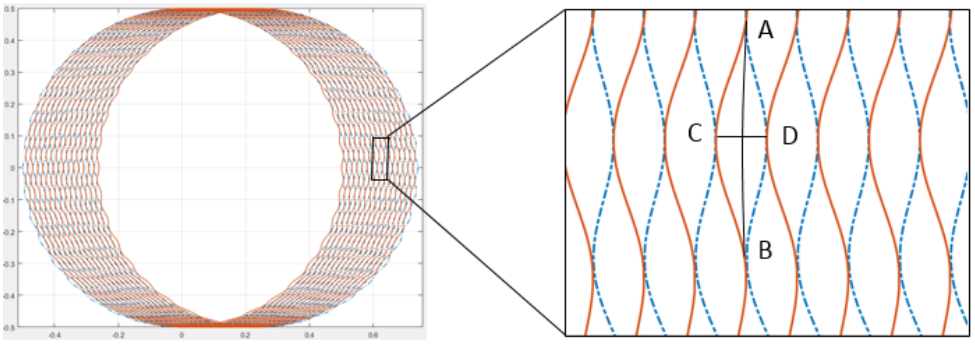

Figure 4-12 Tool tip trajectories for vibration assisted milling

By considering the relationship between vibration amplitude and feed rate f_z (μm/tooth), three types of fish scales surface textures can be fabricated, each with specific characteristic dimensions (*AB*, *CD* in Fig. 4-13).

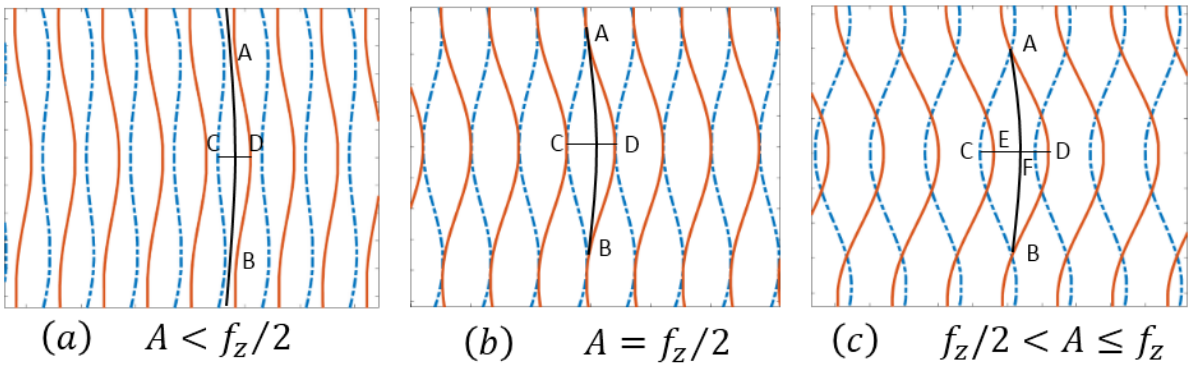

Figure 4-13 Different topography on fish scales surface structure

When the vibration amplitude is less than half of the feed rate, there is no intersection and a gap can be found between one and the following tool tips trajectories, see Fig. 4-13(a). The area of the fish scales decreases as the vibration amplitude is reduced. The characteristic dimensions can be expressed as:

$$\begin{cases} \widehat{AB} = \pi Rn/60f_x \\ CD = 2A_x \end{cases} \tag{4-19}$$

Fig. 4-13(b) illustrates the second type of fish scales surface structure on the condition of $A = f_z/2$. Intersection points can be found in the tool tips trajectories and the characteristic dimensions can be expressed again using Eq. (4-19).

Fig. 4-13(c) shows the third type of fish scales surface structure, obtained when $\frac{f_z}{2} < A < f_z$. The crest, or trough, of the former tool tooth overlaps with the trough, or crest, of the following tool, so the characteristic dimensions can be expressed as:

$$\begin{cases} \widehat{AB} = \pi Rn/60f_x \\ CE = FD = A_x - f_z/2 \\ EF = 2f_z \\ CD = 2A_x + f_z \end{cases} \tag{4-20}$$

It can be noted that the length $\widehat{AB}$ of the surface texture is in proportion to the tool radius and the spindle speed, and in inverse proportion to the vibration frequency. The width *CD* of the surface texture increases with the increase of the feed per tooth and the amplitude of the vibration.

4.3.1.2 Depth prediction in fish scales surface textures

The analysis of the depth profile of fish scales surface structures requires understanding of the surface generation mechanism. In the conventional micro-milling process, the cutter path has a great effect on the formation of tool marks and affects the surface topography. Depending on cutter tooth profile and cutting parameters, the feed marks assume one of two configurations, as shown in Fig. 4-14.

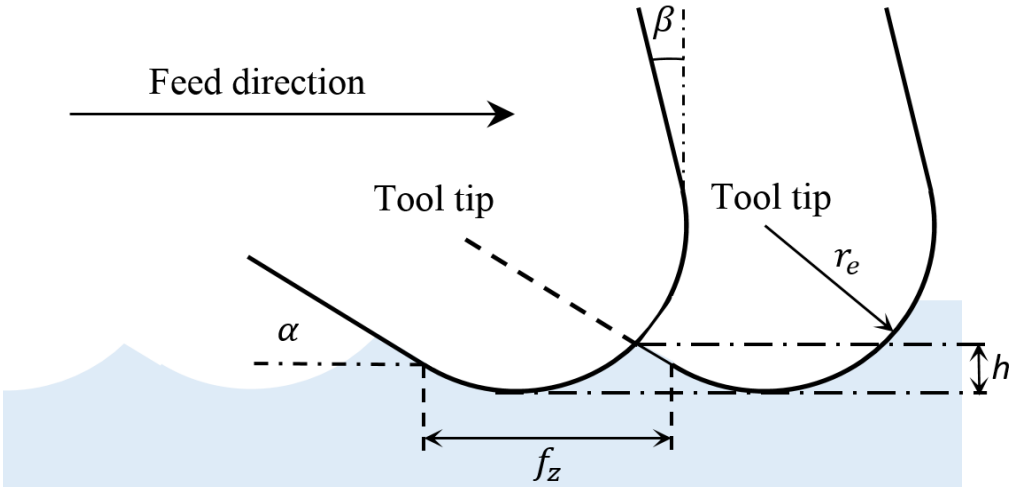

(a)

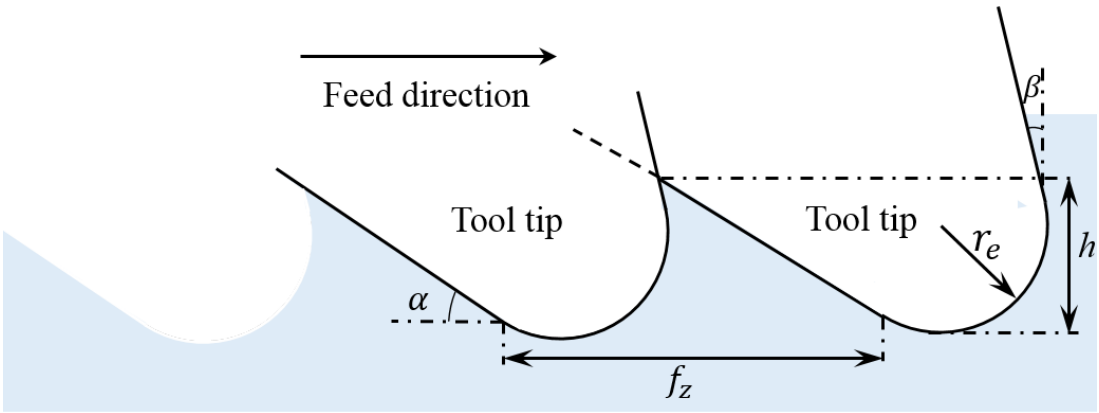

(b)

Figure 4-14 Tool mark generation process

Fig. 4-14(a) shows the successive positions of the tool tip when $f_z \leq r_e\cos\beta + \frac{r_e\sin\beta}{\tan\alpha} + \frac{r_e\cos^2\alpha}{\sin\alpha} + r_e\sin\alpha$: the current tool edge and the flank face of the following tool tooth intersect in a point that determines the height of the structure. The feed mark height h can be expressed as:

$$h = \frac{4r_e + {r_e}^2 - \left((f_z - \frac{r_e \cos^2\alpha}{\sin\alpha} - r_e \sin\alpha)^2 - \sqrt{-4(f_z - \frac{r_e \cos^2\alpha}{\sin\alpha} - r_e \sin\alpha)^2 - 2r_e \left(f_z - \frac{r_e \cos^2\alpha}{\sin\alpha} - r_e \sin\alpha \right) + 8{r_e}^2} \right)}{4} \quad (4\text{-}21)$$

Where r_e is the cutting edge radius, α and β are the tool edge clearance angle and tool edge rake angle, respectively.

Fig. 4-14(b) shows the condition when $f_z > r_e \cos\beta + \frac{r_e \sin\beta}{\tan\alpha} + \frac{r_e \cos^2\alpha}{\sin\alpha} + r_e \sin\alpha$, the intersection point can be found between the current tool rake face and the flank face of the following tool. The feed mark high h can be expressed as:

$$h = \frac{f_z \tan\alpha - \frac{r_e \sin^2\beta \tan\alpha}{\cos\beta} - r_e \cos\beta \tan\alpha - r_e \cos\alpha - r_e \sin^2\alpha / \cos\alpha}{1 - \tan\alpha \tan\beta} + r_e \quad (4\text{-}22)$$

As a sinusoidal vibration is applied in the feed direction, the depth of fish scales surface structure h_d is described by two different expressions depending on the amplitude of vibration A_x, as follows:

when $2A_x \leq r_e cos\beta + \frac{r_e \sin\beta}{\tan\alpha} + \frac{r_e \cos^2\alpha}{\sin\alpha} + r_e \sin\alpha$:

$$h_d = \frac{4r + {r_e}^2 - \left((2A_x - \frac{r_e \cos^2\alpha}{\sin\alpha} - r_e \sin\alpha)^2 - \sqrt{-4(2A_x - \frac{r_e \cos^2\alpha}{\sin\alpha} - r_e \sin\alpha)^2 - 2r_e \left(2A_x - \frac{r_e \cos^2\alpha}{\sin\alpha} - r_e \sin\alpha \right) + 8{r_e}^2} \right)}{4} \quad (4\text{-}23)$$

when $2A_x > r_e cos\beta + \frac{r_e \sin\beta}{\tan\alpha} + \frac{r_e \cos^2\alpha}{\sin\alpha} + r_e \sin\alpha$:

$$h_d = \frac{2A_x \tan\alpha - \frac{r_e \sin^2\beta \tan\alpha}{\cos\beta} - r_e \cos\beta \tan\alpha - r_e \cos\alpha - r_e \sin^2\alpha / \cos\alpha}{1 - \tan\alpha \tan\beta} + r_e \quad (4\text{-}24)$$

4.3.2 Wettability modelling

The well-known Young's contact model describes a solid surface wetting state by considering the interaction among the three phases present, see Fig. 4-15. The contact angle θ can be expressed by:

$$\cos\theta = \frac{\gamma_{SV} - \gamma_{SL}}{\gamma_{LV}} \quad (4\text{-}25)$$

where γ_{SL}, γ_{SV} and γ_{LV} are the solid-liquid, solid-vapour and liquid-vapour interfacial tensions, respectively.

Figure 4-15 Young's Contact Model

However, this equation only applies to ideally smooth, uniform and rigid surfaces. The experimental value of surface contact angle is observed to differ from θ. To explain this disagreement, two different theories have been put forward. Wenzel (Wenzel, 1936) developed his own liquid-surface fully contact model by considering the effect of solid surface roughness. The contact area between liquid and solid surface increases if one assumes that the liquid fills all the surface micro grooves (Fig. 4-16). As a result, solid-liquid and solid vapour energy will correspondingly change. The model predicts the Wenzel contact angle θ_w as:

$$\cos\theta_w = r\cos\theta \tag{4-26}$$

Where r is the roughness factor (the ratio between real area and the rough surface area)

On the other hand, after investigating the surface physical and chemical properties, Cassie (Cassie and Baxter, 1944) attributed the contact angle difference to surface Gibbs free energy changing due to inhomogeneity of surface structure. He proposed a contact model where all the micro pits on the rough surface are filled with air (Fig. 4-17). With this assumption, the Cassie contact angle, θ_c is calculated as:

$$\cos\theta_c = -1 + f_s(\cos\theta + 1) \tag{4-27}$$

where f_s is the fraction of area occupied by solids on rough surfaces.

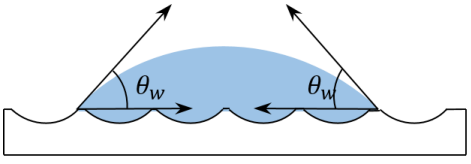

Figure 4-16 Wenzel Contact Model

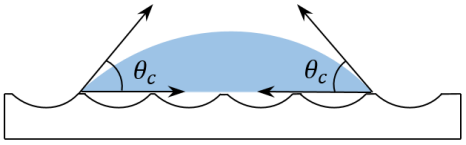

Figure 4-17 Cassie Contact Model

According to these two contact models, for solid substrates of a given roughness, there exist two distinct contact angles. In fact, the wetting state can transit from Cassie model to Wenzel model for solid surfaces with pits open to the atmosphere: the droplet spreads out and fills the micro pits naturally due to its own weight and infiltration (Feng and Jiang, 2006; Park *et al.*, 2009). However, when the pits are closed, pockets of air can be trapped inside and cannot easily escape, which is suitable for the surface texture created by the vibration assisted micro milling. After an appropriate time, a state of equilibrium (stable or metastable) will be reached (Fig. 4-18).

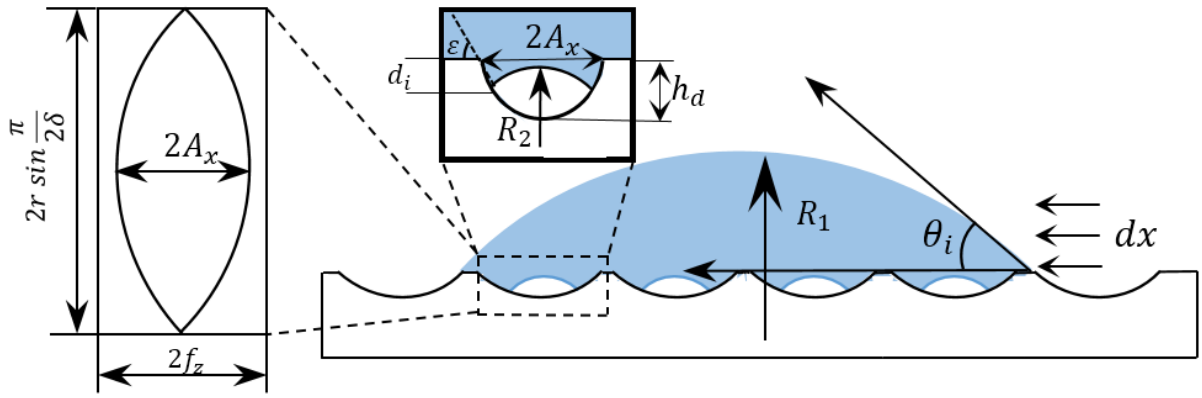

Figure 4-18 Illustration of the intermediate contact model

If an external disturbance causes an overall displacement *dx* (see Fig. 4-18) of the water droplet, perturbing the equilibrium reached in the intermediate contact model, an increment *dG* of the total Gibbs free energy is observed, resulting from variations in the energy of the three interfaces present:

$$dG = dG_{SL} + dG_{SV} + dG_{LV} \tag{4-28}$$

where dG_{SL}, dG_{SV} and dG_{LV} are the energy increment of the solid-liquid, solid-vapour and liquid-vapour interfaces, respectively.

By considering the fish scales surface texture in Fig. 4-18, Eq. (4-28) can be expressed as:

$$dG = (1 - f_s)\Upsilon_{LV}dx + \frac{2d_i \int_0^{\frac{\pi rn}{60f_x}} \sqrt{1+(\frac{60f_xA_x}{rn}\cos\frac{60f_xt}{rn})^2}dt}{2f_z r \sin\varepsilon \sin\frac{n\pi}{120f_x}}(\Upsilon_{SL} - \Upsilon_{SV})dx + \Upsilon_{LV}dx\cos\theta_i + f_s(\Upsilon_{SL} - \Upsilon_{SV})dx \quad (4\text{-}29)$$

where f_s is the percentage of area occupied by solids on rough surface, given by:

$$f_s = 1 - \frac{nA_x}{60f_x f_z \sin\frac{\pi}{2\delta}} \quad (4\text{-}30)$$

And ε is the critical angle between fish scales and surface and depends on the vibration amplitude A_x and depth of fish scales h_d.

Since the Gibbs energy is stationary at equilibrium, its derivative with respect to a perturbed parameter is zero:

$$\lim_{dx\to 0}\frac{dG}{dx} = 0 \quad (4\text{-}31)$$

By combining Eq. (4-29) and (4-31), and the expression for *fs*, a new equation for describing the contact angle in this model can be presented:

$$\cos\theta_i = \left(f_s + \frac{d_i \int_0^{\frac{\pi rn}{60f_x}} \sqrt{1+(\frac{60f_xA_x}{rn}\cos\frac{60f_xt}{rn})^2}dt}{rf_z \sin\varepsilon \sin\frac{n\pi}{120f_x}}\right)\cos\theta + f_s - 1 \quad (4\text{-}32)$$

From Eq. (4-32), the static contact angle θ_i is determined by both vibration parameters (frequency, amplitude) and cutting parameters (spindle speed, tool geometry and feed rate).

By introducing the frequency ratio δ (defined in Eq. (4-18)), Eq. (4-32) can be simplified to:

$$\cos\theta_i = \left(1 - \frac{A_x}{\delta f_z \sin\frac{\pi}{2\delta}} + \frac{d_i \int_0^{\frac{\pi r}{\delta}} \sqrt{1+(\frac{\delta A_x}{r}\cos\frac{\delta t}{r})^2}dt}{f_z r \sin\varepsilon \sin\frac{\pi}{2\delta}}\right)\cos\theta - \frac{A_x}{\delta f_z \sin\frac{\pi}{2\delta}} \quad (4\text{-}33)$$

The value of $\sin\varepsilon$ can be calculated via trigonometry. On the other hand, the value of infiltration depth d_i can be obtained by considering the pressure change of the air in the micro-pits caused by the droplet contacting the substrate. The original air pressure in the micro pits is equal to atmospheric pressure (P_0), whereas a pressure P_2 is reached after the liquid contacts the surface and a new equilibrium is established. The pressure within the droplets (P_1) is determined by the liquid surface tension. These quantities are related by:

$$P_1 - P_0 = \frac{2\gamma}{R_1} \tag{4-34}$$

$$P_2 - P_1 = \frac{2\gamma}{R_2} = \frac{2\gamma \mathrm{COS}\theta}{A_x} \tag{4-35}$$

$$P_2 = P_0 + \frac{2\gamma}{R_1} + \frac{2\gamma \mathrm{COS}\theta}{A_x} \tag{4-36}$$

where γ is the liquid surface tension, θ is the contact angle, R_1 is the radius of the droplet and R_2 is the radius of the liquid in the micro pits, as shown in Fig. 4-18.

According to the ideal gas law, the product of air pressure and volume remains unchanged during this isothermal process. Moreover, the volume of the two states can be calculated geometrically. Consequently, the two states can be expressed as:

$$\frac{P_0 \pi^2 A_x h_d rn}{180 f_x} = \frac{P_2 \pi^2 A_x rn (h_d - d_i)^3}{135 f_x {h_d}^2} \tag{4-37}$$

$$d_i = h_d - \sqrt[3]{\frac{3P_0 {h_d}^3}{4P_2}} \tag{4-38}$$

By substituting Eq. (4-37) into Eq. (4-33), the solid surface contact angle can be obtained.

According to the developed wettability model, it can be found that the machined surface wettability is the result of a combination of multiple parameters, such as vibration amplitude, vibration frequency, spindle speed, feed rate and tool diameter. This study will only focus on the effect of frequency ratio and vibration amplitude on the surface wettability.

4.3.3 Experimental setup

4.3.3.1 Surface texture generation

The experiments are conducted through the proposed vibration assisted micro milling device proposed in Chapter 3. Slots milling experiments are conducted on Al6061 alloys with vibration in the feed direction. 1 mm diameter uncoated carbide end mills are used. The slot cross-section dimensions are 5mm wide and 50 μm deep. The machining and vibration parameters are listed in Table 4-4.

Table 4-4: Machining and vibration parameters used in the experiments

No	Amplitude (μm)	Frequency (Hz)	Spindle speed (rpm)	Feed rate (μm/tooth)	Frequency ratio
1	0	0	3000	8	0
2	4	1950	3000	8	39
3	4	1750	3000	8	35
4	4	1450	3000	8	29
5	4	1250	3000	8	25
6	4	950	3000	8	19
7	2	1250	3000	8	25
8	6	1250	3000	8	25
9	8	1250	3000	8	25

4.3.3.2 Surface wettability measurement

The machined specimens are cleaned with ethanol solution in an ultrasonic cleaner. The machined surface textures are verified by an optical surface profiler and the corresponding surface contact angles are measured by using a contact angle meter (OneAttension with Theta Lite, LT100) through the sessile droplet method. The whole testing process is performed at room temperature. Three measurements were carried out at each measurement point with the amount of 5 μL±0.1μL water droplets to increase the measurement accuracy.

4.3.4 Results and discussion

4.3.4.1 Machining results

The machined surface texture is observed using white light interferometer (Zygo NewView 5200) according to the ISO 25178: Geometric Product Specifications (GPS) standard. And the testing results are shown in Fig. 4-19 and 4-20. Fig. 4-19 shows the surface generated by the conventional micro milling without vibration assistance and clear regular circular tool marks can be observed. The results obtained from vibration assisted micro milling are shown in Fig. 4-20. The results obtained from different frequency ratios ranging from 19 to 39 with fixed vibration amplitude of 4 μm (half of the feed per tooth) are shown in Fig. 4-20(a-e). It can be observed that the locus of the tool vibration are along with the cutting path, the crest (valley) of one tooth exactly overlaps with the valley (crest) of another tooth which leads to the finish scale surface textures. When the frequency ratio increases, the area of the fish scales decreases

as predicted from the simulation. Fig.(b), (f), (g), (h) illustrate the surface texture with the No.2, 7, 8, 9 experiments, *i.e.* the vibration amplitude varying from 2 to 8 μm while the frequency ratio is fixed at 25. When the vibration amplitude increases, the relationship of one tooth crest (valley) to another's valley (crest) changes from no contact to overlap, which in turn influences the size of the fish scales unit. This agrees well with the simulation results.

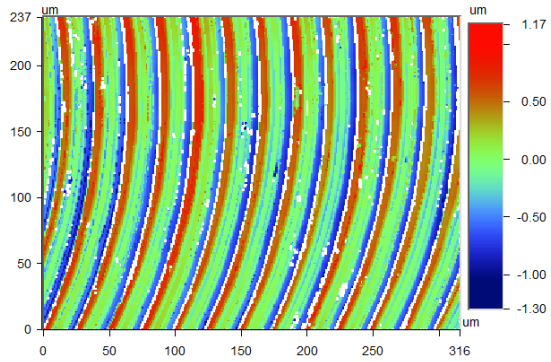

Figure 4-19 Surface texture of conventional micro milling

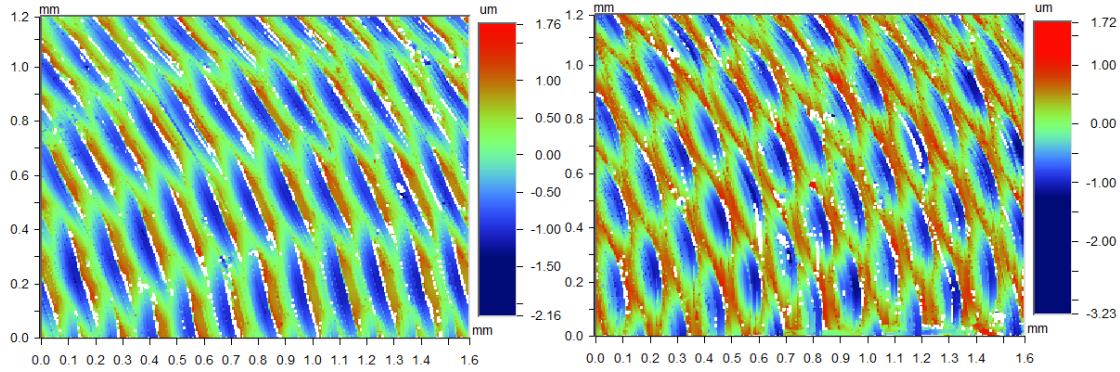

(a) (b)

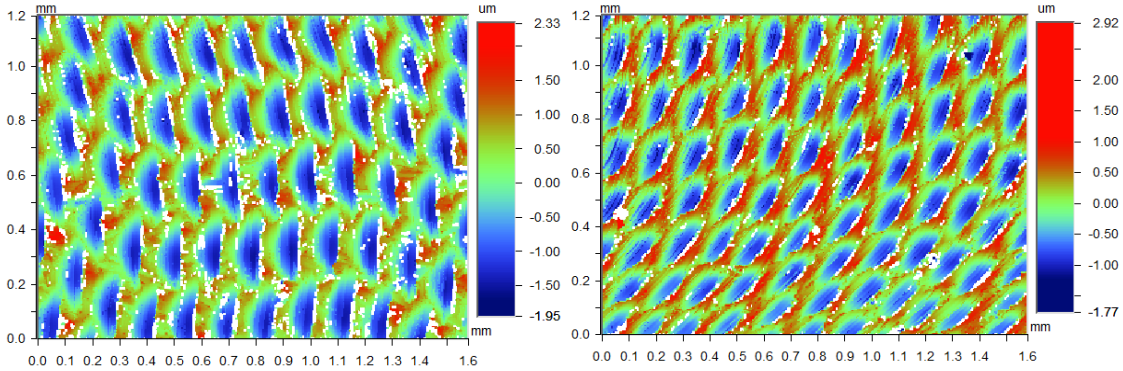

(c) (d)

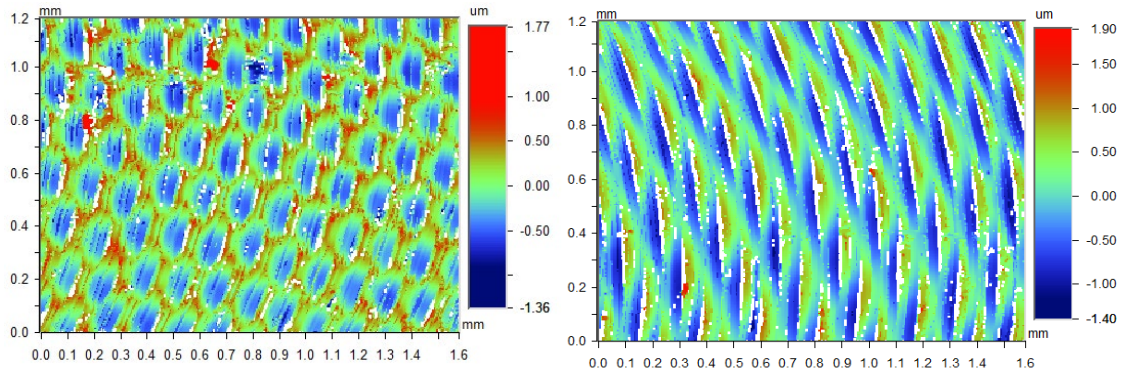

(e) (f)

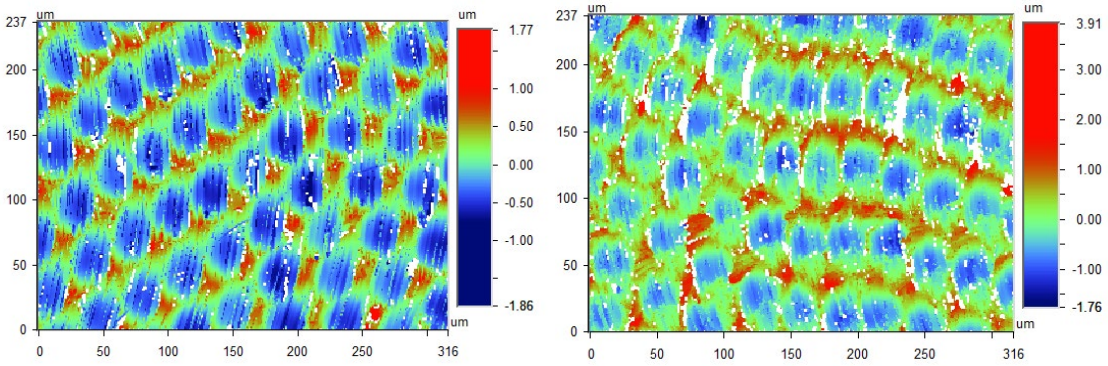

(g) (h)

Figure 4-20 Fish scales surface textures with different vibration parameters: (a) Vibration amplitude 4 μm with frequency ratio 19; (b) Vibration amplitude 4 μm with frequency ratio 25; (c) Vibration amplitude 4 μm with frequency ratio 29; (d) Vibration amplitude 4 μm with frequency ratio 35; (e) Vibration amplitude 4 μm with frequency ratio 39; (f) Vibration amplitude 2 μm with frequency ratio 25; (g) Vibration amplitude 6 μm with frequency ratio 25; (h) Vibration amplitude 8 μm with frequency ratio 25.

4.3.4.2 Wettability testing results

As discussed in the previous sections, the surface wettability can be quantitatively measured and compared through contact angles. Fig. 4-21 illustrates contact angle results with different vibration parameters. Generally, the size of the fish scale unit has a great influence on the surface wettability. With the size of the fish scale unit increasing, the hydrophilicity of the surface will be enhanced. It can be found that the two dimensions of the fish scale unit are controlled by the frequency ratio and vibration amplitude, which agrees well with the simulation results. The contact angle results show a higher changing rate in the frequency ratio domain data due to the size of the fish scale unit changes more obviously compared with the

vibration amplitude parameters. It can be observed that the contact angle in the conventionally machined surface was measured as 89˚, whereas all the surfaces machined by vibration assisted micro milling have lower contact angle values ranging from 33˚ to 57˚, which indicates that a more hydrophilic surface has been produced by vibration assisted milling.

The contact angle obtained from machining experiments was compared with simulation results obtained from the proposed contact model, as well as both Wenzel's and Cassie's contact models (see Fig. 4-22). Compared with the results of Wenzel's and Cassie's contact models, the proposed contact model provides more accurate contact angle prediction in both frequency ratio domain and vibration amplitude domain. In Fig. 4-22 (a), as frequency ratio increases from 19 to 39, the variation of corresponding experimental contact angle shows a linear increase from 33˚ to 57˚. Although the theoretical prediction shows the same trend as the experimental data, the predictive accuracy is different for different frequency ratios. Some of the prediction values are in good agreement with the experimental data, such as when the frequency ratios are 25, 29 and 35. However, the prediction values have large errors compared with the experimental data when the frequency ratio are 39 and 19, with prediction contact angle value 62˚ and the testing result 57˚± 2.4˚ and prediction contact angle value 30˚ and the testing result 33.3 ˚± 2.2 ˚, respectively. This is due to the errors of actual vibration amplitude produced by the piezo-actuator driven stage is different at different vibration frequencies. Future effort will be made to overcome the mechanical limitation of vibration stage and reduce vibration amplitude errors.

As shown in the tool tip trajectories simulation results (see Fig. 4-12), the area of the micro unit reduces when the frequency ratio increases, which changes the percentage of area occupied by solids on rough surface and the filtration area in the fish scales structure. According to Eqs. (4-29 to 39), when the value of contact angle increases, the surface wettability turns to be more hydrophobic. In addition, it is reported that the contact angle is one of the important factors indicating the surface free energy, where smaller surface free energy corresponds to higher contact angles (Zhenyu *et al.*, 2016). This implies that increasing the frequency ratio will decrease the surface free energy. Fig. 4-22 (b) shows the effect of vibration amplitude for both testing and theoretical data when the frequency ratio is 25. Generally, the contact angle decreases with the vibration amplitude and reaches the lowest value (around 33˚) at 8 μm and the highest value (around 45˚) at 2 μm, which agrees well with the theoretical data. This is due to higher vibration amplitude causing a larger size of fish scales unit, which affects the

infiltration area and the air pressure in the microstructure. As a result, a lower contact angle and an increased surface free energy can be obtained.

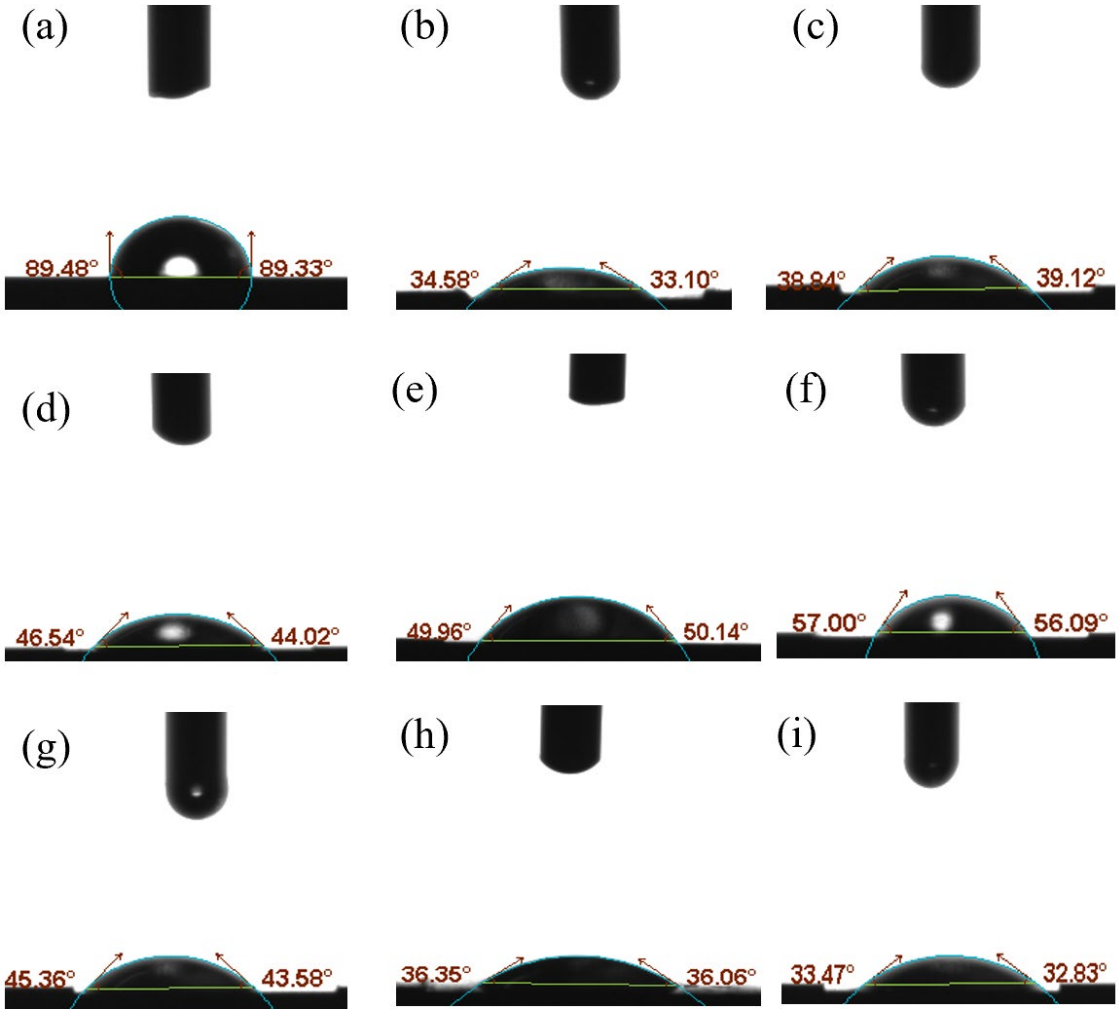

Figure 4-21 Contact angle measurement results: (a) Conventional micro milling (b) Vibration amplitude 4 µm with frequency ratio 19; (c) Vibration amplitude 4 µm with frequency ratio 25; (d) Vibration amplitude 4 µm with frequency ratio 29; (e) Vibration amplitude 4 µm with frequency ratio 35; (f) Vibration amplitude 4 µm with frequency ratio 39; (g) Vibration amplitude 2 µm with frequency ratio 25; (h) Vibration amplitude 6 µm with frequency ratio 25; (i) Vibration amplitude 8 µm with frequency ratio 25;

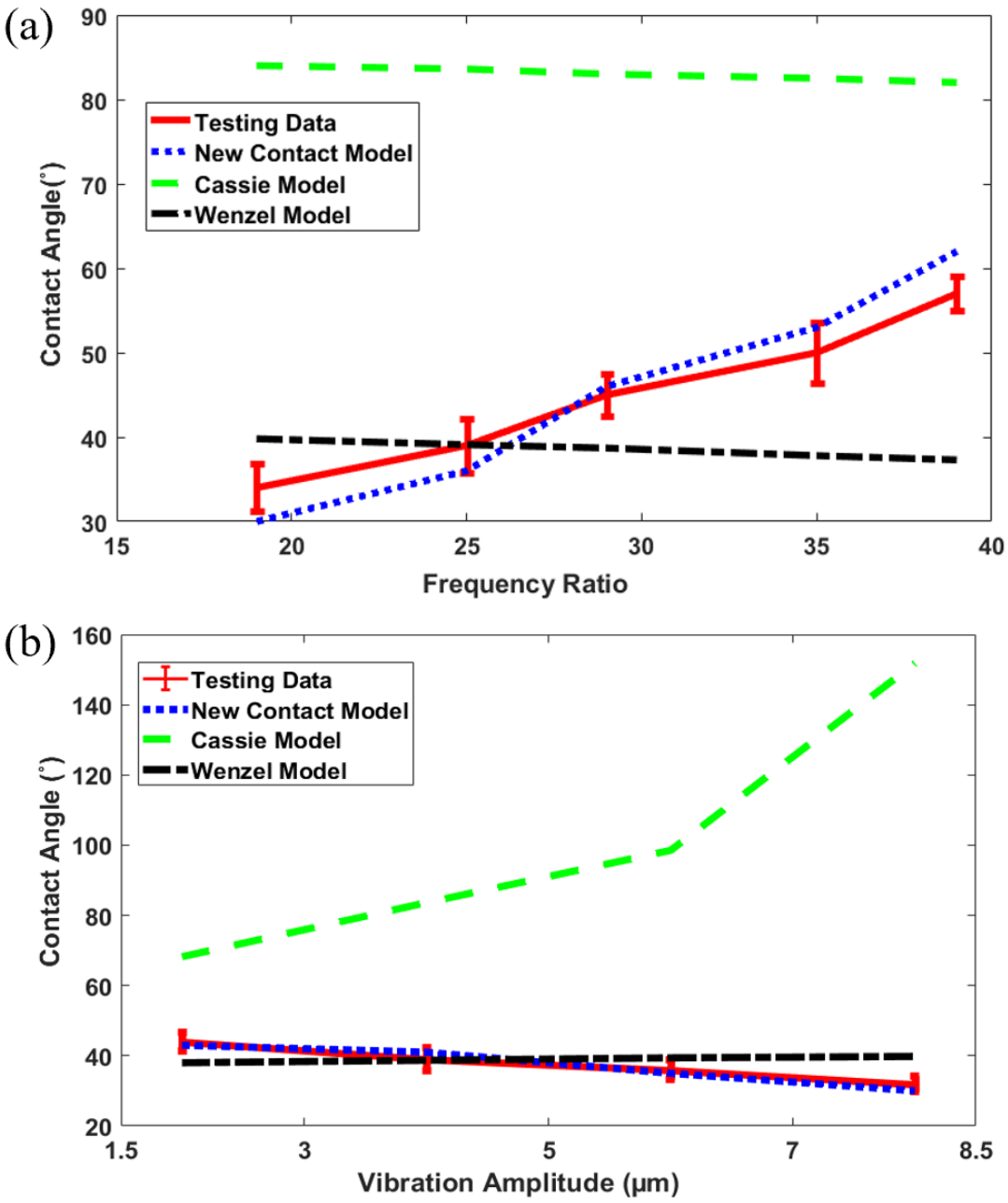

Figure 4-22 Contact angle results between experimental and theoretical data, (a) Data of frequency ratio domain with the vibration amplitude fixed at 4 μm; (b) Data of vibration amplitude domain with frequency ratio fixed at 25.

4.4 Liquid flow control in microfluidic channels

Microfluidic devices play an important role in the chemical, pharmaceutical, energy and aerospace industries because they integrate basic operations such as sample preparation, reaction, separation and detection onto a single chip, offering unique advantages such as small amounts of sample and reagent, less time consumption, lower cost and high throughput (Nguyen and Wu, 2005; Wang *et al.*, 2015; Yen, Ando and Shen, 2016). Fluid flow in

microchannels is different from that in the macro channels due to the lower Reynolds number caused by the low flow scale (the geometry size of microchannel), leading to the motion control of the liquid in the microfluidic a challenging task. Accordingly, research on liquid flow control in microchannels, such as flow regulation and mix, on/off switching and sealing of liquids, gases or vacuum have been carried out in the past decades (Hessel, Löwe and Schönfeld, 2005; Volker, Holger and Friedhelm, 2005; Capretto *et al.*, 2011). In order to achieve these purposes, micromixer and microvalve are usually required in microchannels.

Currently, the proposed microvalves can be divided into two groups, mechanical material-based and nonmechanical material-based valves. Magnetic, mechanical, and pneumatic mechanisms are usually used in the design of mechanical material-based microvalves (Hartshorne, Backhouse and Lee, 2004; Studer *et al.*, 2004; Oh *et al.*, 2005, 2012; Yamahata *et al.*, 2005; Grover *et al.*, 2006). However, moving and sealing components are usually required in these micro valves, which increases the cost and difficulty of manufacture. The other type is the nonmechanical material-based microvalves, such as paraffin, ice and hydrogel-based microvalves (Gui and Liu, 2004; Pal *et al.*, 2004; Wang *et al.*, 2005; Satarkar *et al.*, 2009). However, the requirements, such as temperature, pH, solvent composition, and ionic strength limit their applications. Similarly, micromixers also can be categorized as passive and active micromixers. Passive micromixers rely on diffusion or chaotic advection mechanisms and usually requires long or complex geometry mixing channels for the mixing process (Burns *et al.*, 1998; Stroock *et al.*, 2002; Jen *et al.*, 2003; Niu and Lee, 2003). While, external disturbances such as pressure, temperature, electrohydrodynamic, dielectrophoretic, electro kinetics, magnetohydrodynamics and acoustics, are usually required in active micromixers (Deshmukh, 2000; Fujii *et al.*, 2003; Moctar, Aubry and Batton, 2003). However, the requirement of corresponding components or external power in these micromixers limit their application. Therefore, it is strongly desired to develop alternative microvalves and micromixers with widely applications and cost-efficient.

It has been reported that fluid flow in microchannels is highly influenced by the properties of surrounding walls due to the large surface-to-volume ratio. Hence, modifying microstructure and wettability of these walls is another strategy for the design of microvalves and micromixers, and several examples have shown the feasibility of manipulating liquid flow using this method. Surface textures with certain wettability, such as stooped nanohair, grandient and micro elliptical pillars surface, is usually built in microchannels to control the flow in a particular

direction. Wang et al. (Wang *et al.*, 2014) proposed a one-way valve design using Janus Si elliptical pillar arrays with anisotropic wettability in a T-shaped microchannel. It can work at different flow rates and pressures and gas-liquid separation was also successfully performed. Kim et al. (Kim and Suh, 2009) applied directionally bent nanohairs on microchannels to control fluid motion and the fluid velocity along the stooped direction was about 6 times faster than that in the reversed direction. Bae et al. (Bae *et al.*, 2014) fabricated asymmetric Lucius prism array surface texture in microfluidic channels to control the fluid speed. In addition, textured surfaces, such as slanted wells, ridges or grooves can also be used in the design of passive micromixers. Johnson et al. (Johnson, Ross and Locascio, 2002) developed a passive mixer using slanted wells along a prefabricated polycarbonate microchannel. Stroock et al. (Stroock *et al.*, 2002) incorporated patterned grooves on the floor of microchannels to generate chaotic flow and decrease the mixing distance. However, complex fabrication processes or membranes with unique materials are required in these proposed researches, which limits its applications.

Conventional microchannel manufacturing usually uses lithography and etching methods, which are in high precision but are only economic for high volume production. Recently, micro milling has been proved an effective way to fabricate microfluidic devices due to low cost and high efficiency (Guckenberger *et al.*, 2015). In section 4.4, the utilization of vibration assisted micro milling on unique fish scale surface texture fabrication to modify the solid surface wettability has been studied. In this section, the application of these surface texture as a liquid flow controlling strategy in microchannels is studies. Liquid flow experiments in designed microchannels have been carried out and the results show that liquid flow can be controlled successfully in both T-shaped and Y-shaped microfluidic chips.

4.4.1 Fabrication of microchannels and chips

Fig. 4-23 shows the schematic diagram of the microchannel fabrication process, which are the T-shaped and Y-shaped microchannels for one-way valve and micromixer, respectively. All the microchannels are manufactured on PMMA material chips with 50 μm depth and other dimensions are shown in Fig. 4-23. Then, the machined plate is bonded with another same size plane PMMA plate using thermally-solvent assisted method (Bamshad, Nikfarjam and Khaleghi, 2016). For the one-way valve microchannel application, T-shaped microchannels are fabricated to explore the flow controlling application of the developed fish scale surface

textures. Different surface textures with different contact angles are set at microchannel inlet, outlet 1 and 2, as well as the corresponding dimensions of microchannels, as shown in Fig. 4-23 (a). Fig. 4-23 (b) shows the fabrication details of Y-shaped microchannel chips, the outlet and inlet channels are fabricated by conventional micro milling and different fish scale surface textures are set at the mixing channels to study the liquid mixing effect.

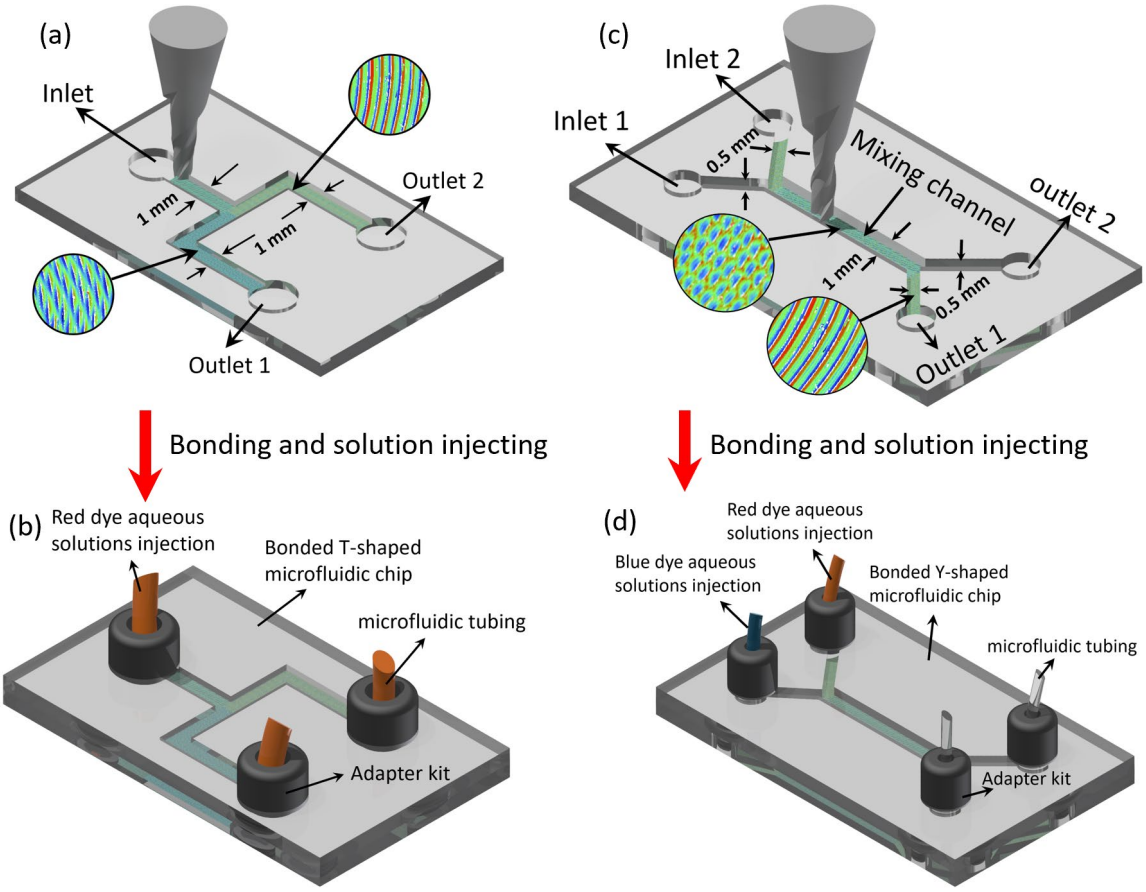

Figure 4-23 Fabrication process of microchannel chips and corresponding dimensions of microchannel (a) T-shaped microchannel, (c)Y-shaped microchannel

4.4.2 Results and discussion

4.4.2.1 Flowing behaviour in T-shaped microchannels

To study the flowing behaviour in T-shaped microchannels, microfluidic chips with T-shaped microchannels are manufactured and the corresponding surface texture arrangement are listed in Table 4-5. The No. x (x =1, 2, 5, 9) is the machining and vibration parameters as shown in Table 4-4, and the corresponding surface textures are shown in Fig. 4-20.

Table 4-5 Surface texture arrangement for T-shaped microchannels

Set	Inlet	Outlet 1	Outlet 2
1	No. 1	No. 1	No. 1
2	No. 1	No. 1	No. 9
3	No. 1	No. 1	No. 2
4	No. 1	No. 1	No. 5

To observe the liquid flow motion, the aqueous solutions containing red dye is injected from the inlet through a syringe pump and the other two outlets are connected with atmosphere to ensure the free motion of the liquid. Fig. 4-24 shows the flow behaviour of the Rhodamine aqueous solution in the designed T-shape microchannels of Set 2. And the ratio of the flowing distance between outlet 1 and 2 microchannels is defined as R_d to describe the one-way flowing behaviours. When the injected flow rate is set at 4.0 ml/h as shown in Fig. 4-24 (a), it shows that the liquid only flow through outlet 2 and one-way flowability can be obtained. Moreover, it can be found that the value of the ratio of flowing distance is zero because the hydrophilic of the bottom surface of outlet 2 is better than that in outlet 1. As the flow rate increases to 5.5 ml/h and 7ml/h (Fig. 4-24 (b) and (c)), the liquid start to enter to outlet 1 and the value of the ratio of flowing distance decreases from almost 5.2 to nearly 2.1. It turns out that as flow rate increase, the input pressure also increases and the effect of surface textures and their corresponding wettability on liquid flow is reduced. This is due to the gap between the driving force of liquid and the surface tension difference in the two outlet surfaces is gradually reduced. When the flow rate is above 8 ml/h as shown in Fig. 4-24 (d), both outlet 1 and outlet 2 are filled with Rhodamine solution. The one-way valve function failed at this flow rate and the value of the ratio of flowing distance is equal to 1.

To further investigate the influence of the proposed surface texture on the one-way flowing behaviours in microchannels, the results of the ratio R_d varying with the flow rates at different developed T-shaped microchannels are shown in Fig. 4-25. It can be found that the value of the ratio R_d in Set 1 microchannels is fixed at 1 for all flow rates, which indicates liquid flow cannot be controlled when the bottom surface of the two outlet microchannels are set with the same surface texture. As the textured surfaces are manufactured at the bottom surface of outlet 2 (Set 2, 3 and 4 microfluidic chips), the value of the ratio R_d varies with the input flow rates, indicating the liquid flow can be controlled effectively. Generally, liquid flow controlling in the microchannels can be promoted when increasing the difference of hydrophilicity between

the two outlet bottom surfaces. When the input flow rate is 4ml/h, the ratio R_d in both Set 2 and 3 is 0, which means no liquid enters outlet 1 and one-way flowability is achieved at this input flow rate. However, although one-way flowability also can be obtained at the input flow rate of 4ml/h for Set 4 microfluidic chips, the liquid starts to enter to outlet 1 and the ratio R_d almost 6.2. This is due to the contact angle of outlet 2 bottom surface in Set 4 microchannels is larger than that in Set 2 and 3 microfluidic chips, which decreases the difference of surface tension between outlet 1 and 2. As the input flow rate turns to 5.5ml/h and 7ml/h, the liquid driving forces increase and the fluid enters outlet 2 on all three microfluidic chips (Set 2, 3 and 4). The values of the ratio R_d in Set 2 microfluidic chips are always the biggest at that time, indicating the best liquid control ability can be obtained due to its highest hydrophilic on outlet 2 bottom surface. When the input flow rate comes to 8ml/h, fluid fills both outlets for all three microfluidic chips and the ratio R_d are all equal to 1. The one-way valve function is failed at this velocity. Overall, these results suggest that the fabricated microfluidic chips with the textured surface can be acted as a one-way valve and the working ranges of the flow rate of these proposed microfluidic chips are not the same due to the difference of surface tension between the two outlets surface in different microfluidic chips.

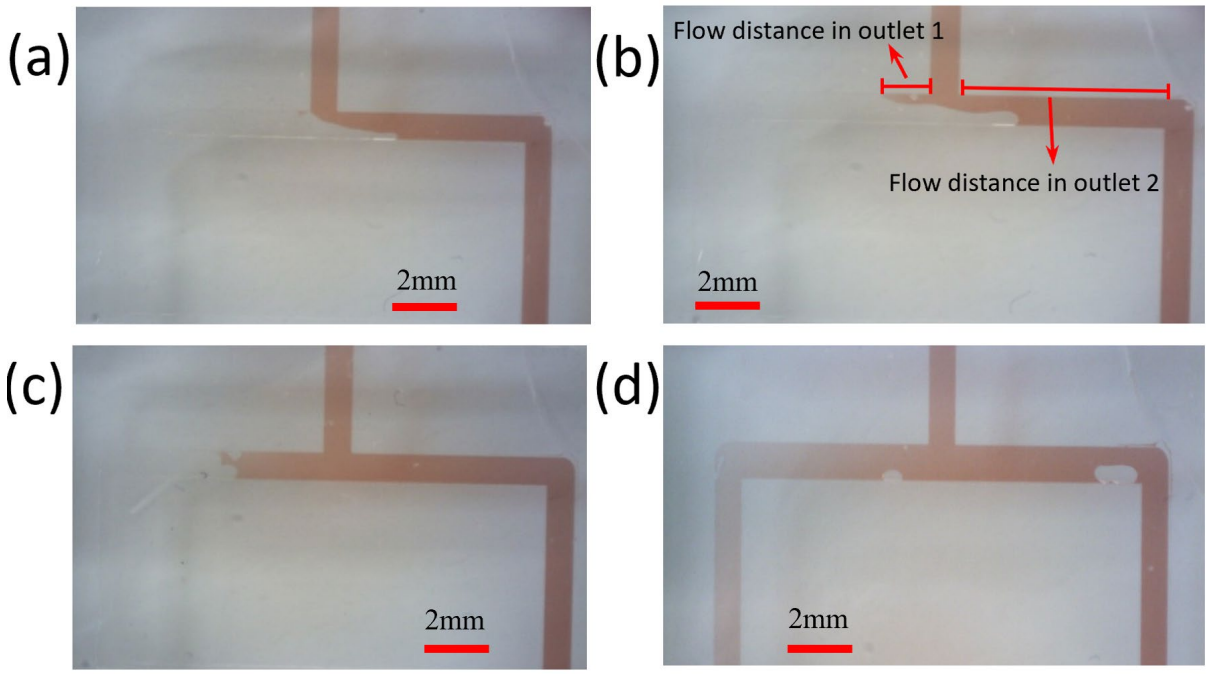

Figure 4-24 Flowing behaviours of the Rhodamine aqueous solution in T-shaped microchannels of Set 2 microfluidic chips; (a) flow rate is 4.0 ml/h, (b) flow rate is 5.5 ml/h, (c) flow rate is 7 ml/h, (d) flow rate is 8 ml/h.

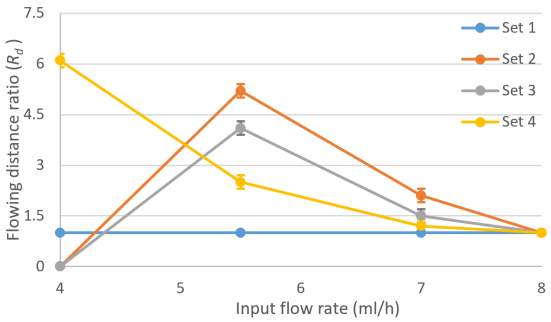

Figure 4-25 Flowing distance ratio variation for different manufactured microfluidic chips at different input flow rate.

4.4.2.2 Mixing behaviour in Y-shaped microchannels

Microfluidic chips with Y-shaped microchannels are manufactured to investigate liquid mixing effect and the corresponding surface texture arrangement are listed in Table 4-6. The No. x (x =1, 5, 9) is the machining and vibration parameters as shown in Table 4-4, and the corresponding surface textures are shown in Fig. 4-20.

Table 4-6 Surface texture arrangement for Y-shaped microchannels

Set	Inlet 1	inlet 2	Mixing channel
1	No. 1	No. 1	No. 1
2	No. 1	No. 1	No. 9
3	No. 1	No. 1	No. 5

To study the mixing ability of these developed microchannels, two different colour aqueous solutions (red and blue dyes) is injected from the two inlets with the same input flow rate through the syringe pump and the all the outlets are connected with atmosphere to ensure the free motion of the liquid (See Fig. 4-23 (d)). Fig. 4-26 shows the mixing behaviour of the Rhodamine aqueous solution in the designed Y-shape microchannels in all three manufactured microfluidic chips, the blue and red Rhodamine aqueous solution is injected from inlet 1 and 2 at the input flow rate of 4ml/h. And the mixing length L_m is measured to evaluate the mixing ability (see Fig. 4-26). It can be found from Fig. 4-26 (a) that the border of the two liquid in the mixing channel is quite clear and the two liquid do not mix in the mixing microchannel fabricated by conventional micro milling, which indicates laminar flow dominates the liquid flow in this mixing microchannel. And in this mixing channel, liquid mixing mainly relies on diffusion effect, resulting in a slower mixing process and long microchannel usually required to complete the mixing process. While the results in Fig. 4-26 (b) and (c) show that the liquid

mixing length is reduced as the fish scale surface textures are arranged to the mixing microchannel. This can be attributed to the chaotic advection effect of the fish scales surface texture on the liquid flow and many researches have been confirmed that the fluid flow in microchannels can be influenced as textured surface is built, generating chaos flow. As a result, the mixing length can be reduced. In addition, lower mixing length can be achieved by the microfluidic chip with better hydrophilic fish scale surface texture (Fig. 4-26 (b)), indicating the strength of chaotic advection can be influenced by the characteristic dimensions of fish scale surface texture in the microchannel. It has also been reported that the flow resistance will increase with the increase of hydrophilicity of the microchannel surface (Pit, Hervet and Léger, 2000; Tretheway and Meinhart, 2004), which enhances the diffusion effect, leading to a short mixing length.

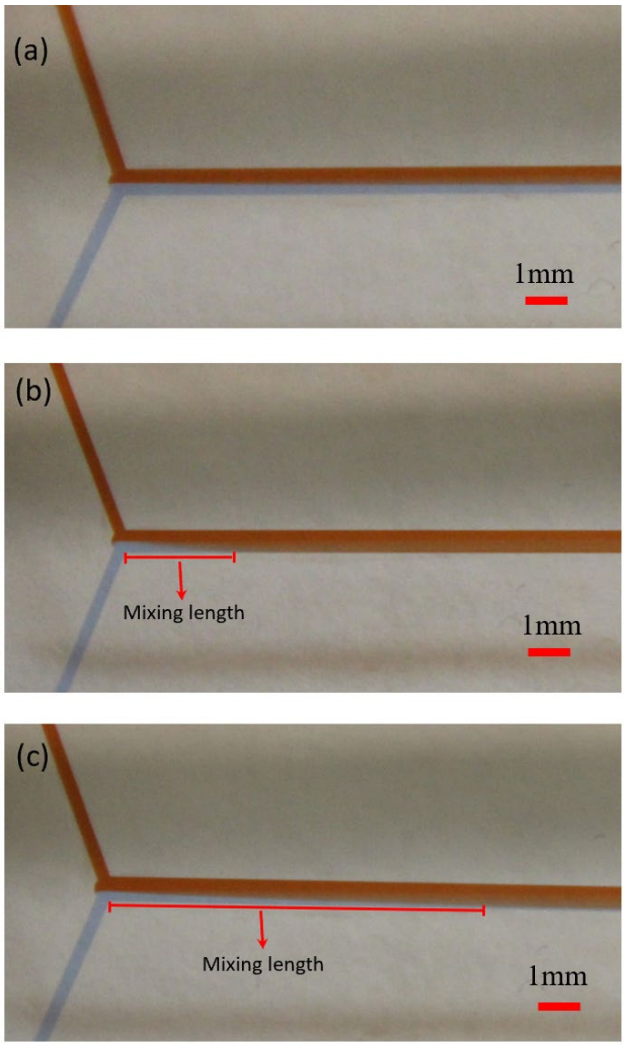

Figure 4-26 Flowing behaviours of the Rhodamine aqueous solution in Y-shaped microchannels at input rate of 4ml/h; (a) Set 1 microfluidic chips, (b) Set 2 microfluidic chips, (c) Set 3 microfluidic chips.

4.5 Conclusion

This chapter provides a comprehensive investigation on the surface texture formation mechanisms and corresponding applications. The surface textures are modelled based on the homogeneous matrix transformation and cutter edge sweeping technology, which is verified by a series of machining experiments. The wettability of the produced surface texture is studied, and a new contact model is established to describe the contact state and predict the contact angle of fish scale surface texture. In addition, the application of these surface texture as a liquid flow controlling strategy in microchannels is studies. Liquid flow experiments in designed microchannels have been carried out and the following conclusions can be drawn:

A simple and accurate surface generation model is proposed, emphatically focusing on the effects of vibration parameters on the surface generation mechanism. The proposed surface texture model could accurately depict the generation process of surface topography in 1D vibration-assisted milling.

Surfaces with fish scales textures can be produced by using appropriate machining and vibration parameters. The relationship between the machining and vibration parameters are established in the surface generation model. The size of the fish scales unit can be controlled by the frequency ratio and the vibration amplitude.

1) A contact model is developed to predict the hydrophilicity of fish scales textured surfaces by considering the effects of trapped air pressure in the surface microstructure, infiltration area and the percentage of area occupied by solids on a rough surface.

2) The wettability testing results on the machined surface show that the proposed contact model can predict the contact angle accurately.

3) The results also indicate that the fish scales textured surface turns to more hydrophilic and a surface with controllable wettability can be obtained by optimizing the machining and vibration parameters.

4) One-way valves in T-shaped microchannels is developed to achieve the purpose of the one-way flow of liquid in microchannels by considering the relationship between surface tension difference and liquid driving force caused by different microstructures and corresponding wettability.

5) Micro-mixers in the Y-shaped microchannel are developed by setting different fish scales surface textures in the mixing channel. The liquid flow results show that chaotic convection can be obtained by the fish scales surface textures and the strength of chaotic convection varies with the wettability and characteristic dimensions of the fish scales.

Chapter 5 Investigation on tool wear suppression mechanism in non-resonant vibration assisted micro milling

5.1 Introduction

Cutting tools are subjected to extremely severe friction due to the metal-to-metal contact between the cutting tool and workpiece during material processing, which causes high level of stress and temperature near the surface of the tool and hence leads to unavoidable tool wear. Worn tools can reduce machining accuracy and surface finish, which in turn leads to deteriorating cutting efficiency and increased machining costs. Increasing tool life and part quality are imperative in high value machining performance and productivity. Cutting parameter optimization is a common method for tool wear reduction and extending tool life in conventional machining, but its effect is limited. The reduction of tool wear is the main benefits of applying vibration assistance to the machining process, and the former is more relevant with hard-to-machine materials and the latter is applicable to all ductile materials. Numerous research efforts have focused on investigating the removal and deformation mechanisms of materials in vibration assisted machining from the perspective of tool wear. This chapter studies the effect of vibration assisted micro milling in reducing on tool wear through analysing the mechanisms and appearance of tool wear, as well as the characteristics of vibration assisted micro milling.

5.2 Classification of tool wear

Tool wear can be divided into two groups: abnormal and normal wear, as shown in Fig. 5-1. Abnormal wear is usually caused by impact or uneven heating during machining process, leading to the brittle damage of cutting tools such as chipping, fracture, spalling and cracking. Normal wear is a process in which tool wear gradually increases over time. It is caused by the friction and thermochemical effects during the machining process, leading to rake wear, flank wear, tool tip wear and boundary wear (Yan *et al.*, 2009).

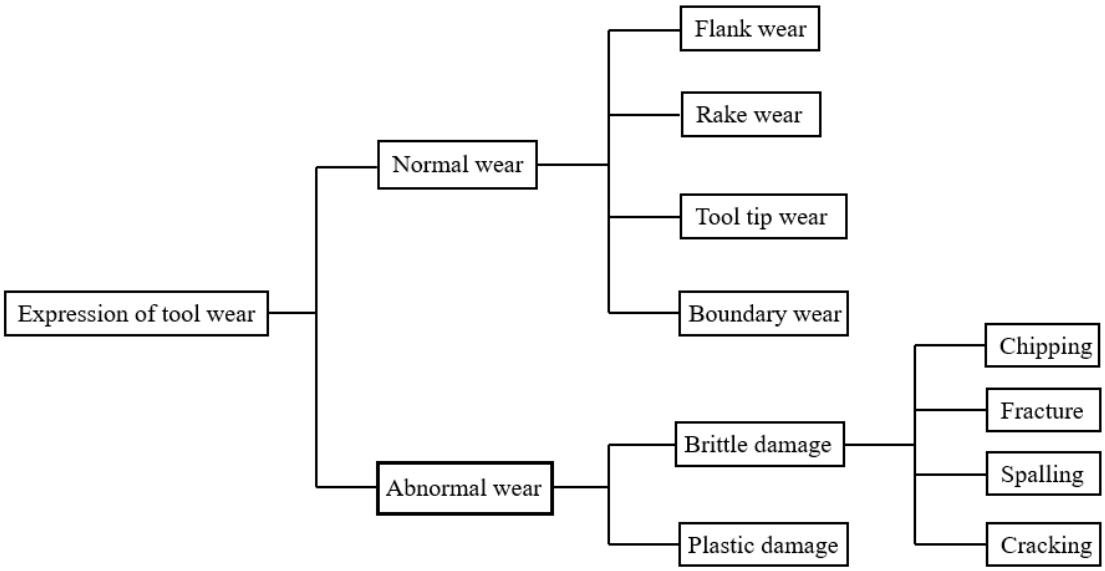

Figure 5-1 Classification of tool wear (Yan *et al.*, 2009)

Rake wear usually occurs when processing plastic materials, leading to a crater behind the cutting edge on the tool rake face due to high cutting speeds, as shown in Fig. 8-2. The position on the tool rake face which reaches highest temperature is usually where the wear starts, and the area and depth of the crater will expand and increase over time, leading to the increased rake angle of the cutting tool which in turn improves the cutting conditions and makes it easy for the chips to curl and break. However, the strength of the cutting tool will be weakened as the crater continues to grow, leading to the breakage and chipping of cutting tools.

Flank wear is caused by the strong friction between the machined surface and the tool flank face, and a uniform area with a zero clearance angle on the tool flank face eventually forms. This usually happens along with tool tip wear and boundary wear, as shown in Fig. 5-2. In addition, flank wear is usually used as the standard for tool wear since it can affect the dimensional accuracy and surface quality of the machined surface.

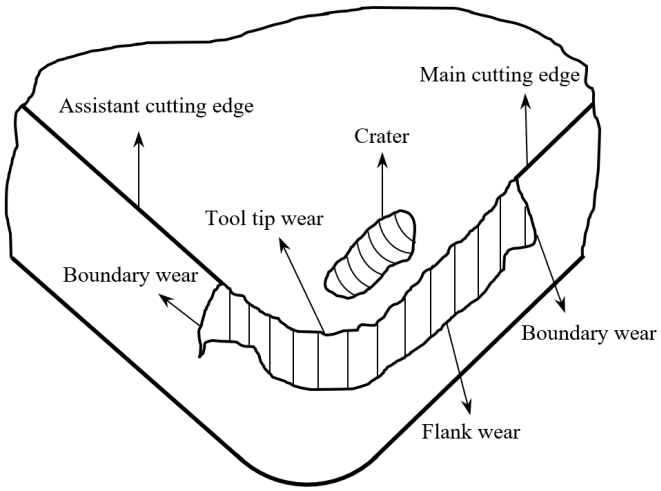

Figure 5-2 Layout of tool wear (Yan *et al.*, 2009)

5.3 Wear mechanism and influencing factors

Understanding the mechanisms and factors affecting tool wear during machining is very important in order to improve tool life and cutting performance. Mechanical and thermochemical wear mainly contribute to the normal wear process of cutting tools. Mechanical wear, including abrasive wear, is wear on the tool friction surface due to the intense friction occurring during processing. Meanwhile thermochemical wear is due to chemical reactions between the tool and the workpiece materials in high temperature conditions. Some wear mechanisms only occur in specific tool materials when processing certain workpiece materials, but multiple wear mechanisms usually work together during the tool wear process. These wear mechanisms include the following:

(1) Coating delamination only takes place on coated cutting tools and is believed to be the initial wear mechanism of the coated tool. A chemical reaction between the workpiece and coating material and crack propagation at the cutting tool substrate interface caused by differences in the thermal coefficient of expansion between the coating matrix and the tool substrate have been proposed as the main reasons for coating delamination. In addition, severe friction during processing also speeds up this phenomenon.

(2) Abrasive wear is one of the most common wear mechanisms and occurs in most metal cutting processes. It is caused by friction between the tool surface and the workpiece and leads to micro-grooves on the worn tool (especially on the tool rake face) due to

the high hardness particles contained in the workpiece. Abrasive wear can be reduced effectively using the cutting tools with higher material hardness.

(3) **Adhesion wear** also called "cold welding", is caused by the adsorption of atoms between the friction surfaces of cutting tool and workpiece (chips) at the specific pressure levels and high temperatures. The materials at the bonding points of the two friction surfaces (workpiece and cutting) become torn due to the relative motion in the machining process, and adhesion wear will occur when the particles on the tool cutting surface are taken away by the workpiece surface. The plasticity of the material to be processed and cutting conditions are the main factors affecting adhesion wear, and the effect of changing the cutting tool material used is quite limited in terms of reducing the adhesion wear.

(4) **Diffusion wear** is the results of a chemical reaction. Molecular activity between the tool and the workpiece contact surface is increased due to high temperature and pressure during processing, which leads to the diffusion and replacement of alloy elements such as titanium (Ti), tungsten (W) and cobalt (Co) from the cutting tool into the workpiece. Meanwhile, the element iron (Fe) in the workpiece diffuses into the cutting tool and reduces the mechanical properties of the tool material. As a consequence, diffusion wear occurs due to the severe friction effect during the machining process. It is greatly affected by the cutting temperature and speed, and higher speed and temperature will speed up diffusion wear.

(5) **Oxidation wear** is also caused by the high temperature and pressure in the machining process. Unlike diffusion wear, oxidation wear requires the intervention of oxygen. An oxidation reaction on the tool surface generates a layer of brittle oxide, such as CoO and WO_2, etc. As the machining process goes on, the brittle oxide on the tool surface is taken away by the workpiece or chip causing cutting tool wear. This usually occurs in the tool cutting edge area, which is in contact with the surrounding air.

Variables affecting tool wear mainly include the following four factors:

(1) **Workpiece materials:** Cutting force and cutting energy are highly dependent on the workpiece material and its physical and mechanical properties, including microstructure, hardness, mechanical and thermal properties, which in turn affect tool wear. The plasticity, hardness and thermal conductivity of the material have the greatest impact on tool wear.

(2) **Cutting parameters:** Parameters such as cutting speed, cutting depth and feed rate have a great influence on the heat of cutting and cutting forces during machining, which in turn affect tool wear.

(3) **Cutting tool:** To obtain the optimum cutting performance, suitable tool parameters such as tool material, coating, and geometry need to be considered for different cutting conditions (roughing or finishing).

(4) **Machine tool**: The dynamic characteristics of the machine tool which are determined by the machine structure have a great influence on the stability of the cutting process. Unstable cutting processes are usually accompanied by large flutter, leading to a high fluctuating load on the tool. As a result, tool failure occurs due to the excessive wear or chipping of the cutting tool.

5.4 Tool wear reduction in vibration assisted micro milling

The life of cutting tool can be significantly extended in vibration assisted micro milling and the effect of tool wear reduction under different tool-workpiece separation conditions are different due to the varying cutting mechanisms. Therefore, it is necessary to study the tool-workpiece separation conditions first.

5.4.1 Analysis of tool-workpiece separation conditions

According to the tool tip trajectory analysis in chapter 4, three different continuous tool-workpiece separation conditions can be obtained in the vibration assisted milling process. Fig. 5-3 (a) shows the first type separation state, it appears when relative speed between tool and workpiece in the cutting direction goes against the spindle speed direction and tool motion can be expressed as the following four steps: in step 1, cutting tool starts to contact with workpiece and the relative speed is positive. In step 2 cutting tool is about to break contact with workpiece and the relative speed is equal to zero. In step 3 the relative speed is reversed and cutting tool withdraws from workpiece. In step 4 the relative speed is positive again and another cutting cycle is started.

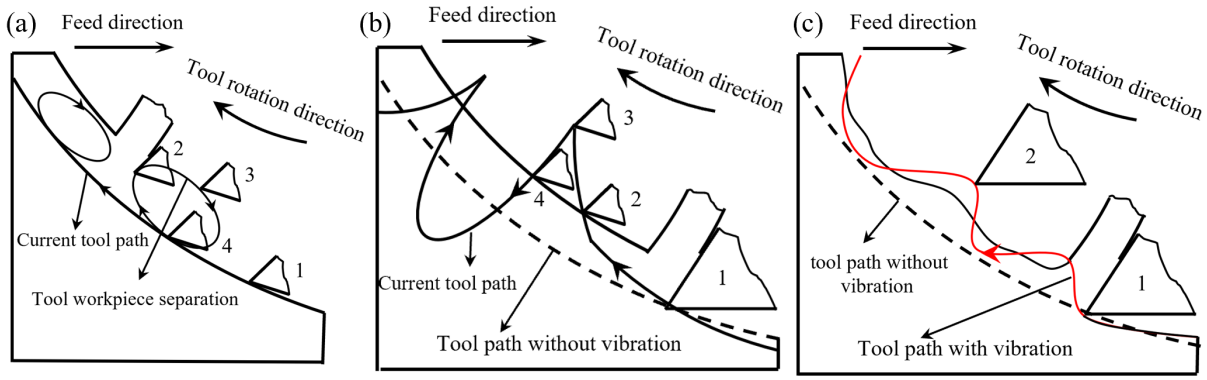

Figure 5-3 Three types of tool-workpiece separation conditions

Therefore, as the necessary condition for achieving the first type tool-workpiece separation, the tool or workpiece vibration speed (V_v) needs to be greater than the nominal cutting speed (V_n, the relative speed of the tool tip without vibration assistance), which can be expressed as:

$$[V_v = 2\pi f_x A_x \cos(2\pi f_x t + \varphi_x) cos\alpha] \geq [V_n = \frac{\pi r n}{30}] \tag{5-1}$$

Simplify Eq. (5-1)

$$\cos(2\pi f_x t + \varphi_x) cos\alpha \geq \frac{rn}{60 f_x A_x} \tag{5-2}$$

Eq. (5-2) is only valid when:

$$\frac{rn}{60 f_x A_x} \leq 1 \tag{5-3}$$

Fig. 5-3 (b) shows the second type separation state, it is determined by the relationship between the vibration amplitude and the instantaneous uncut chip thickness, and the separation process also can be expressed as the following four steps: in step 1, cutting tool starts to contact with workpiece, and at that time, the vibration amplitude is smaller than the instantaneous uncut chip thickness. In step 2, the instantaneous uncut chip thickness is zero and the cutting tool and workpiece are ready to separate. In step 3, the cutting tool lose contact with the workpiece and the value of vibration displacement is larger than the instantaneous uncut chip thickness. In step 4, the cutting tool recontact with the workpiece and another cutting cycle is started.

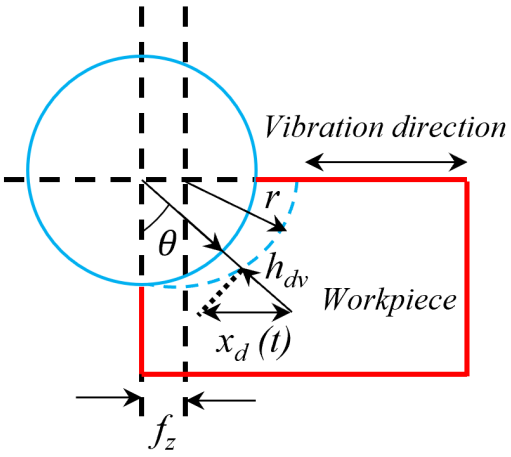

Figure 5-4 Schematic diagram of instantaneous uncut chip thickness

Fig. 5-4 shows the layout of instantaneous uncut chip thickness and uncut chip thickness in vibration assisted machining h_{dv} can be expressed as:

$$h_{dv} = f_z sin\theta + x_d sin\theta = (f_z + x_d) sin\theta \tag{5-4}$$

where f_z is the feed rate, and the second separation occurs when $f_z + x_d < 0$

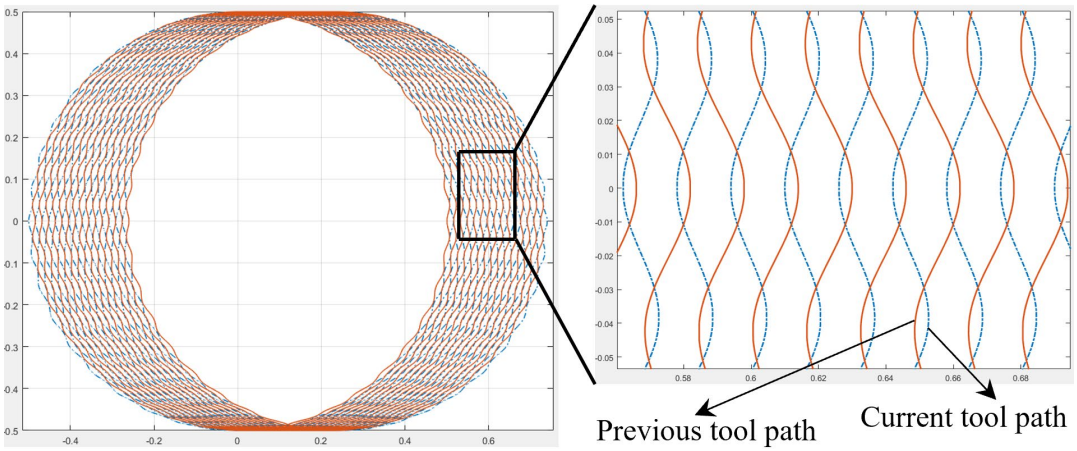

Figure 5-5 Tool trajectories for the third type separation condition.

Fig. 5-3 (c) shows the third type separation state by considering the interaction between the current and previous tool tip trajectories. Fig. 5-5 shows the tool trajectories simulation results and the trajectory interaction can be found between the current and previous tool trajectories. And this happens when applied vibration frequency is odd numbers of the spindle rotation frequency, and the vibration amplitude is greater than half of the feed per tooth.

5.5 Finite element simulations

Finite element simulations have been successfully utilized to investigate cutting mechanism over the past few decades. To further understand the relationships between tool wear and cutting performance, a finite element (FE) model is built using ABAQUS/Explicit commercial finite element software, as shown in Fig. 5-6. Different vibrations are applied to the Ti-6Al-4V workpiece and the cutting tool was set as an analytical rigid body with predefined cutting speed. The data of No. 1, 6 and 7 in the table 2 are selected as the vibration and machining parameters applied in the FE model. The workpiece material behaviour is described by Johnson cook (JC) material and damage models. In this model, the flow stress σ can be defined as (Yadav *et al.*, 2017):

$$\sigma = (A + B\bar{\varepsilon}^{n})\left[1 + C\ln\left(\frac{\dot{\bar{\varepsilon}}}{\dot{\bar{\varepsilon}}_0}\right)\right]\left[1 - \left(\frac{T - T_{room}}{T_M - T_{room}}\right)^{m}\right] \quad (5\text{-}5)$$

Where A, B and C are yield strength, hardening modulus, and strain rate sensitivity coefficient, respectively. m and n are the hardening coefficient and the thermal softening coefficient, respectively. T, T_{room} and T_M are the workpiece material temperature, room temperature and the melting temperature of the workpiece material. These parameters are shown in Table 5-1.

Cutting process usually involves large deformation and high deformation rate, therefore the workpiece is meshed with four-node quad-dominated element (CPE4R, 4-node bilinear element) with the average mesh size of 5 μm. To avoid excessive mesh distortion in every analysis increment, arbitrary Lagrangian–Eulerian (ALE) formulation with the advancing front algorithm is selected. To describe contact condition between cutting tool and workpiece, Coulomb friction model is used with the friction coefficient of 0.5.

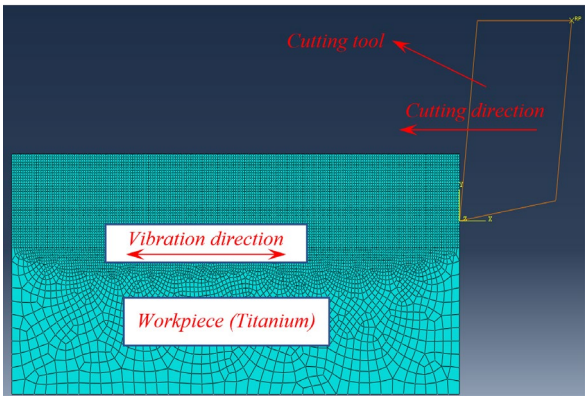

Figure 5-6 FE model of vibration assisted machining

Table 5-1 Mechanical properties and materials constant in J-C model for titanium alloy (Yadav *et al.*, 2017)

Properties	values
Density (g/cm^3)	0.0045
Young's Modulus (MPa)	96832.3
Poisson's Ratio	0.32
Yield stress (MPa)	825
A (MPa)	1098
B (MPa)	1092
n	0.93
m	1.1
C	0.014
d_1	-0.09
d_2	0.25
d_3	-0.5
d_4	0.014
d_5	3.87

5.6 Experimental setup

Slot milling experiments are carried out on Ti-6Al-4V using 1mm diameter two flutes coated end mills with helix angles of 45˚, whose substrates is the fine-grain tungsten carbides and coated with ZrO_2 -$BaCrO_4$ (ZB). The geometry of the brand-new micro end mills is checked using a scanning electron microscope (SEM), and their cutting-edge radius is measured to be 3.0 μm in average (Fig. 5-7 (e)). In order to monitor the tool wear accurately, cutting edge radius, flank wear and tool effective diameter reduction, which highly effect the processing performance, are selected as tool wear criteria. Cutting edge radius variation and tool effective diameter reduction are measured as shown in Fig. 5-7 (e) and Fig. 5-7 (f), respectively. Fig. 5-7 (c) shows measurement method of tool flank wear (*VB*), which is explained as the band width in the direction perpendicular to the cutting edge. And in this work, average value of flank wear is chosen for describing tool flank wear by measuring ten different positions on the worn tool flank face (Fig. 5-7 (c)). Moreover, each result is measured 10 times to reduce measurement error. All the micro cutters are selected from the same batch to eliminate the effects of tool manufacturing errors.

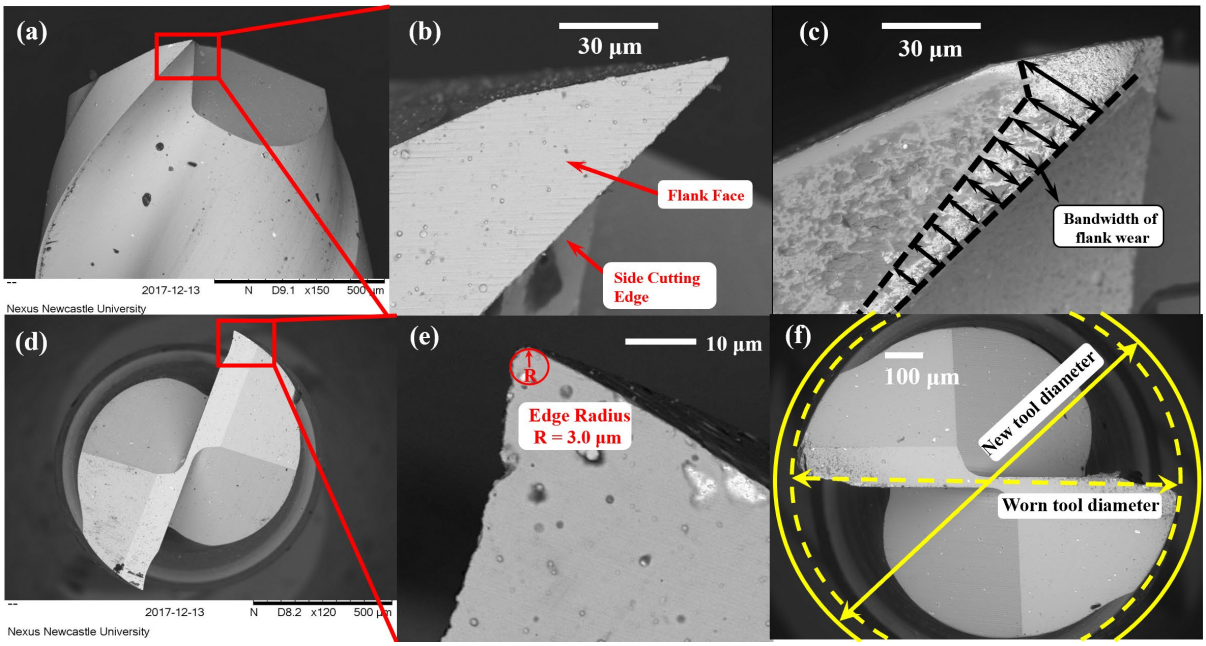

Figure 5-7 SEM results of cutting tools. (a) Side view of brand-new tool;(b) Flank face of brand new tool; (c) Measurement method of tool flank wear;(d) Top view of brand new tool; (e) Measurement method of tool edge radius; (f) Measurement method of worn tool diameter loss.

The machining and vibration parameters are shown in Table 5-2 and only feed direction vibration is applied in these experiments. In order to reduce the influence of ploughing effect on the whole experiments, the feed rate is set to 1.5µm/tooth, which is larger than the minimum chip thickness (0.3-0.4 times of the cutting edge radius). The vibration parameters are selected according to the analysis results on the tool-workpiece separation conditions in Section 5.4. It aims to achieve the tool-workpiece separation and non-separation under three (high, medium and low) different frequencies by changing the vibration amplitudes. In addition, a conventional machining with the same machining parameters is carried out as a control experiment to analyse the effect of vibration parameters on tool wear. The cutting tools are cleaned by the ultrasonic bath and checked by the SEM after every 100mm cutting length. The machining results, such as burrs, surface roughness and chips are checked by the SEM and a white light interferometer (Zygo NewView 5200), respectively.

Table 5-2 Machining and vibration parameters used in the experiments

No	Vibration amplitude (μm)	Vibration frequency (Hz)	Spindle speed (rpm)	Feed rate (μm/tooth)	Axial depth of cut (μm)	Tool-workpiece separation
1	0	0	30000	1.5	50	NO
2	0.5	1500	30000	1.5	50	NO
3	1	1500	30000	1.5	50	YES
4	0.5	3500	30000	1.5	50	NO
5	1	3500	30000	1.5	50	YES
6	0.5	5500	30000	1.5	50	NO
7	1	5500	30000	1.5	50	YES

5.7 Results and discussion

5.7.1 Tool wear results and wear mechanism

The results obtained from the machining experiments have shown that the tool wear is significantly affected by the vibration conditions and the results for tool flank wear, cutting edge radius variation and tool effective diameter reduction are shown in Fig. 5-9, 5-10 and 5-11, respectively. Fig. 5-9 illustrates the results of tool flank wear under different vibration conditions. The tool flank wear gradually increases with the increase of cutting length in all cutting experiments. Greater flank wear is observed in conventional micro milling at all cutting length, which means vibration assistance has a positive effect on reducing tool flank wear. When the vibration is added, the tool average flank wear length decreases by about 20% to 40% depending on the vibration conditions and the minimal wear is recorded at the vibration frequency of 5500 Hz and amplitude of 1 um. It can be observed that higher vibration frequency and tool-workpiece separation can effectively reduce the average tool flank wear. Generally, the tool wear behaviour can be divided into three stages. In the first wear stage, a cutting length from the start to approximately 200 mm in this experiment, a relatively high tool wear rate can be observed. During this stage, the contact area is comparatively small due to the brand new tool sharp cutting edge, which leads a high pressure and hence speed up the tool wear. With the progression of tool wear, the contact area between tool flank face and workpiece on the worn tool cutting edge becomes lager and smoother. As a result, the pressure is reduced and the tool wear rate slows down. The tool wear enters the third stage as the cutting length reaches 600 mm in this experiment and a higher tool wear rate is observed on average tool flank wear on the results of both conventional micro milling and vibration assisted micro milling without

tool-workpiece separation. This may be caused by the increase of the tool edge radius (Fig. 5-9) which exacerbates the influence of the size and ploughing effect and hence speeds up the tool wear. On the other hand, the rate of average tool flank wear in the condition of tool-workpiece separation is relatively stable beyond the cutting length of 600 mm. This can be attributed to the significant variation of instantaneous uncut chip thickness and cutting speed due to periodic contact between the tool and workpiece, which reduces the time of the squeeze friction between the tool and the workpiece as well as extends the cutting length of second stage.

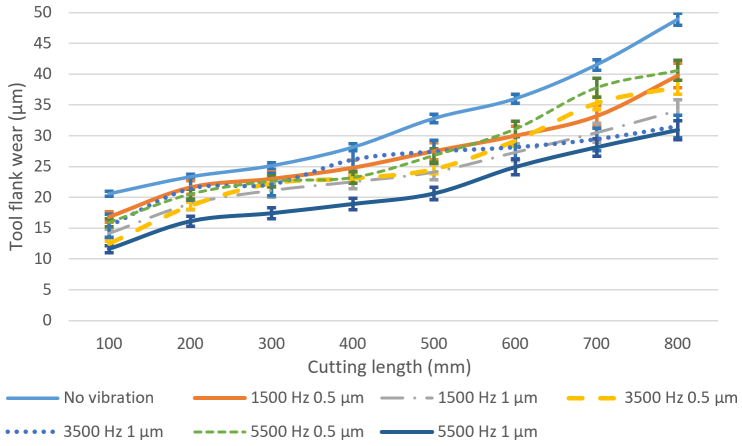

Figure 5-8 Tool flank wear under different vibration conditions and cutting length

Fig. 5-10 shows the results of tool cutting edge radius variation for different vibration conditions. It can be found that in conventional milling the tool cutting edge radius increases dramatically and reaches to almost 11.5 μm at 100 mm cutting length due to the sharp edge of the brand new tools and high cutting forces. When vibration is applied, the rate of cutting edge becoming blunt has decreased significantly. The lowest worn tool cutting edge radius can be observed at the vibration frequency of 5500 Hz and amplitude of 1 μm. Generally, when keeping the amplitude constant, the increase rate of cutting edge radius will decrease as the vibration frequency decreases at the same cutting length. Higher vibration amplitude can suppress cutting edge becoming blunt when the vibration frequency is constant, which agrees with the tool flank wear results.

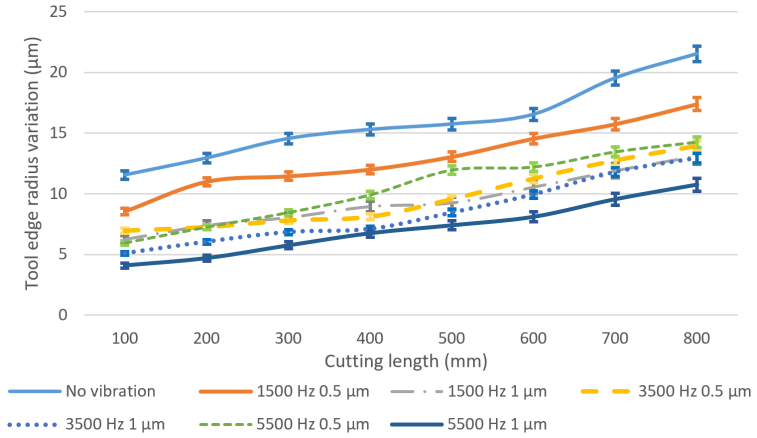

Figure 5-9 Tool edge radius variation under different vibration conditions and cutting length

The accuracy of the milling tool diameter has a great influence on the machining accuracy. Fig. 5-11 shows the worn tool diameter loss under different vibration conditions. It can be observed that the tool diameter loss under all vibration conditions increases as the cutting length increases, and the cutting tool in conventional milling has the highest tool diameter loss from 8 μm at the cutting length of 100 mm to the 28 μm at the cutting length of 800mm. When adding the vibration to the milling process and fixing the vibration amplitude at 0.5 μm, a 25% to 40% tool diameter loss reduction can be obtained through changing vibration frequencies (1500 Hz, 3500 Hz and 5500 Hz) compared with the conventional milling results at the cutting length of 100 mm. A further reduction, 33% to 50% for the three different frequencies, can be reached when vibration amplitude is fixed to 1 μm. Moreover, the tool diameter loss in higher vibration amplitude (1 μm) usually lower that in lower vibration amplitude at the same vibration frequency, which is contributed by the lesser contact time of the tool with the workpiece and hence lower tool abrasive wear at tool-workpiece separation condition.

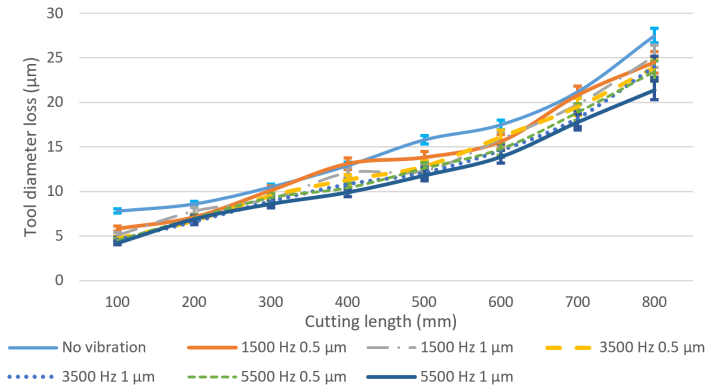

Figure 5-10 Tool diameter loss under different vibration conditions and cutting length

Fig. 5-12 shows the SEM results of flank face for the worn tools under different vibration conditions. SEM images of tool wear at cutting lengths of 100 mm, 400mm and 800 mm, are presented. It can be found that the tool wear varies with different vibration conditions at the same cutting length and the cutting tool in conventional milling is the most worn tools among these conditions. To further understand the reasons causing tool wear results differently in conventional micro milling and vibration assisted micro milling, wear mechanisms are studied. In these wear mechanisms, coating layer loss (in Fig. 5-12), which is reported causing by chemical reaction or crack propagation caused by the difference in thermal expansion coefficient between the coating and the substrate, is believed as the initial wear mechanism for coated tool (Jawaid, Sharif and Koksal, 2000). As an important indicator of coating layer loss, the area of coating layer loss is highly related to the properties of the coating layer material and the value of cutting force. And for the ZB coating, the friction coefficient will increase with temperature increasing at relatively low temperatures (Ouyang, Sasaki and Umeda, 2002). According to the tool wear results in Fig. 5-12, coating layer loss can be found in all experimental conditions. The cutting tool in conventional micro milling obtains the largest area of coating layer loss compared with that in vibration assisted micro milling. In addition, in the proposed experiment conditions, heat generation in the cutting zone is limited due to low the axial depth of cut, feed rate and relatively short cutting length per SEM checking cycle. As vibration is added, lower cutting force, which is verified by both machining and FE results (Fig. 5-13), and cutting temperature can be obtained, leading to a lower value of friction coefficient of ZB coating and reducing the coating galling effect. It also can be found that the coating layer loss area in the condition of tool-workpiece separation is smaller than that in tool-workpiece non-separation under the same vibration frequency and the same cutting length. This can be contributed by the periodic separation effect between the cutting tool and the workpiece, which not only promotes the cutting tool heat dissipation and reduces the cutting temperature, leading to a lower friction coefficient, but also further decreases the average cutting force due to the cyclical fluctuation of cutting forces (from 0 to almost 3.5N), which is shown in Fig. 5-13. As a result, smaller area of coating layer loss can be obtained.

Adhesive wear is believed to be one of the dominant wear mechanisms of coated carbide tool when processing titanium alloys, leading the cutting tool failure. It always happens as the coating layer loss takes place or worn out completely and large pressure, strong friction and high temperature can speed up the adhesive wear progress. In the Fig. 5-12, bonded workpiece materials can be observed at the flank face in all experimental conditions and the result of

energy dispersive spectrometer (EDS) analysis (see Fig. 5-14) reveals high concentrations of titanium, confirming the adhesive wear takes place. The results of conventional machining are studied first to investigate the progress of adhesive wear in conventional micro milling. In the early wear stage, the bonded workpiece material at the cutting edge gradually increases with the cutting length and finally form a built-up edge, which can be found in the Fig. 5-12 of conventional micro milling at cutting length of 100 mm. As the worn tool continues to impact and squash, the built-up edge begins to crack and eventually causes the substrate at the cutting edge breakage, forming craters, which can be found in Fig. 5-12 of conventional milling at cutting length of 400 mm. This wear process repeats as the cutting length increases causing the craters bigger and bigger until the cutting tool is failed, which is shown in Fig. 5-12 of conventional milling at cutting length of 800 mm. As the vibration is added to the conventional micro milling process, the tool wear results in Fig. 5-12 show that the adhesive wear progress is postponed backward. In the early wear stage (cutting length of 100 mm), smaller built-up edge on the cutting tool can be found in the results of vibration assisted micro milling. As the cutting length increases, the crater on the cutting tool of vibration assisted micro milling is also smaller than that on the conventional micro milling. In addition, the adhesive wear in vibration assisted micro milling also varies with the different vibration conditions. The amount of bonded workpiece material and the size of craters on the worn cutting tool will be reduced when increasing the vibration frequency and satisfying the condition of tool-workpiece separation. And the best result can be obtained on the cutting tool results of the vibration condition 5500 Hz and 1 μm. This benefits from its smaller cutting forces, processing time reduction and lower tool temperature.

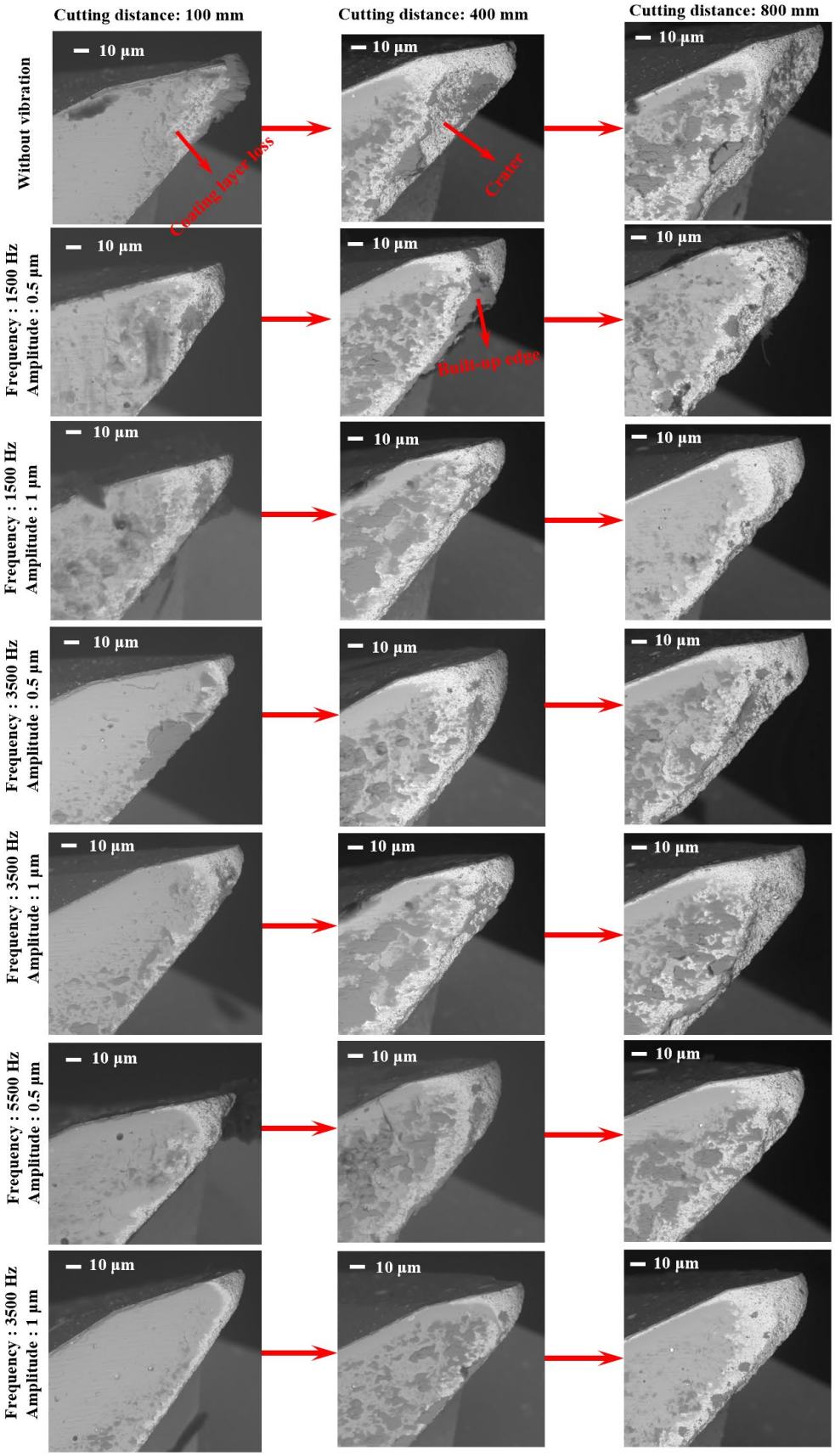

Figure 5-11 SEM results of flank face for the worn tools under different vibration conditions and different cutting length

Mechanical wear caused by the strong friction between the tool and workpiece is also one of the wear mechanisms in these experiments. The results also show that the mechanical wear can be reduced effectively under the conditions of higher vibration frequency and tool-workpiece separation, which is again contributed by the smaller friction force. Fig. 5-15 shows the layout of contact length between the workpiece and the tool in vibration assisted micro milling, and high frequency reciprocating motion can be obtained by the cutting tool.

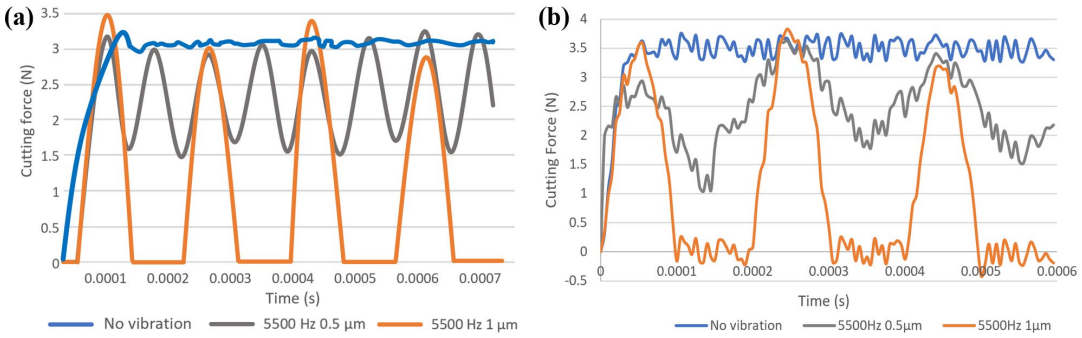

Figure 5-12 Results of cutting force, (a) FE model, (b) machining test

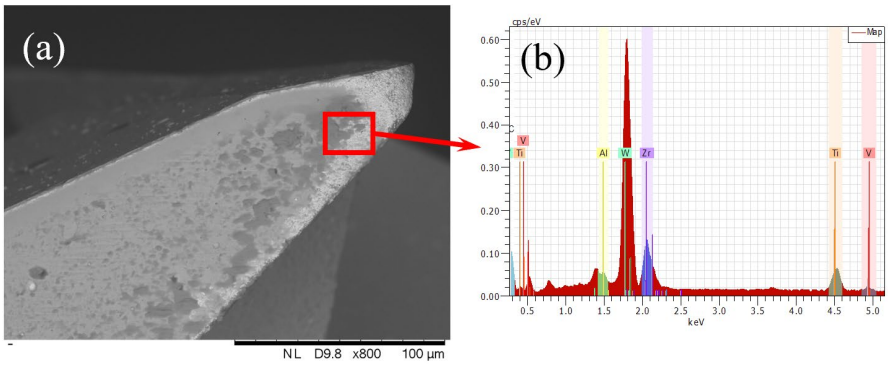

Figure 5-13 SEM image and EDS spectra of worn tool

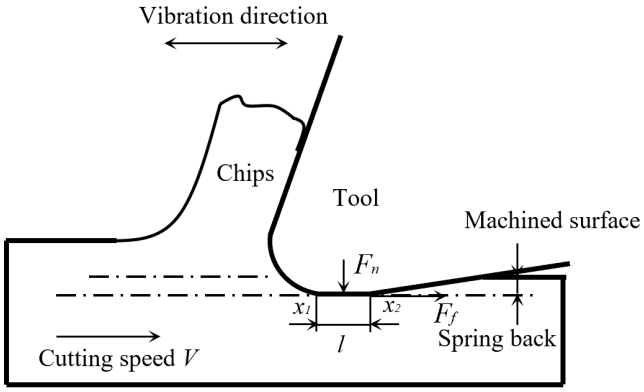

Figure 5-14 Layout of contact length between the workpiece and the tool in vibration assisted micro milling

In Fig. 5-15, the initial contact length between the tool flank face and workpiece is l, when vibration is added on the cutting tool, the actual contact length can be expressed as:

$$L = l + Asin2\pi ft \tag{5-6}$$

Where t is the cutting time, f and A are the vibration frequency and amplitude respectively.

Therefore, the relative position of two contact points x_1 and x_2 can be expressed as:

$$x_1 = Vt + \frac{L}{2} = Vt + \frac{l+Asin2\pi ft}{2} \tag{5-7}$$

$$x_2 = Vt - \frac{L}{2} = Vt - \frac{l+Asin2\pi ft}{2} \tag{5-8}$$

Where V is the cutting speed.

The relative speed of the two contact points, V_1 and V_2 can be expressed as:

$$V_1 = \dot{x}_1 = V + \pi fAcos2\pi ft = V + V_c cos2\pi ft \tag{5-9}$$

$$V_2 = \dot{x}_2 = V - \pi fAcos2\pi ft = V - V_c cos2\pi ft \tag{5-10}$$

Where $V_c = 2\pi fA$ is the critical velocity.

Then the instantaneous total friction force on the tool flank face $F_t(t)$ can be expressed as:

$$F_t(t) = \frac{\mu F_n}{2}[sgn(V + V_c cos2\pi ft) + sgn(V - V_c cos2\pi ft)] \tag{5-11}$$

Where F_n is the fixed normal force between the two contact points, μ is the coefficient of friction, t is the time.

And the average of the total friction force F_a during a vibration cycle can be expressed as:

$$F_a = \frac{1}{T}\int_0^T F_t(t)\,dt = \begin{cases} \frac{2\mu F_n}{\pi}\arcsin\left(\frac{V}{V_c}\right) & (V < V_c) \\ \mu F_n & (V \geq V_c) \end{cases} \tag{5-12}$$

According to Eq. (5-10), the friction force on the tool flank face is μF_n when cutting speed V is larger than or equal to the critical velocity V_c. And this process is similar to the normal machining process so the direction of the friction F_r does not change during the machining process. The friction force on the tool flank face is much less than μF_n when cutting speed V

is less to the critical velocity V_c. And the direction of the friction changes periodically with the separation of the tool from the workpiece, which in turn reduces tool mechanical wear.

5.7.2 Relationship between tool wear and cutting performance

Tool wear also has an important influence on the cutting performance such as surface finish and burr formation. It has been reported that size effect will be amplified when micro milling tool, especially worn micro milling tool, cuts in and cuts out the workpiece. The amplified side effect exacerbates the ploughing effect at the edges of machined slot and affects the surface finish and burr formation in that area (Aramcharoen and Mativenga, 2009). Fig. 5-16 shows the SEM measurement of burrs and the machined surface at the edge area of the up-milling side of conventional micro milling and vibration assisted micro milling. Large top burr formation, worse surface finish, surface cracks and large amount of uncut material can be observed on the machined result of conventional micro milling. While smaller size of burrs, better surface finish, and no uncut material can be found in the results of vibration assisted micro milling. The best result on burr and the surface finish can be observed at the vibration frequency of 5500 Hz and amplitude of 1 μm, which also agrees with the tool wear results. Generally, the burr size and surface crack will be decreased with the increase of vibration frequency and the condition of tool-workpiece separation. This mainly benefit from the low tool wear and the unique cutting mechanism. On one hand, the ploughing effect can be effectively reduced due to lesser wear of tool cutting edge radius and better tool geometry (smaller crater and less bonded workpiece materials on the tool), on the other hand, a bigger shear angle (Fig. 5-17) can be obtained when tool-workpiece separation conditions are satisfied, leading to a lower uncut chip thickness and smaller friction between the cutting tool and chips, improving the machining performance and further reducing tool wear (Chen *et al.*, 2018). As a result, better surface finish, smaller burr and lesser surface crack can be obtained by increasing vibration frequency and satisfying tool-workpiece separation condition in vibration assisted micro milling.

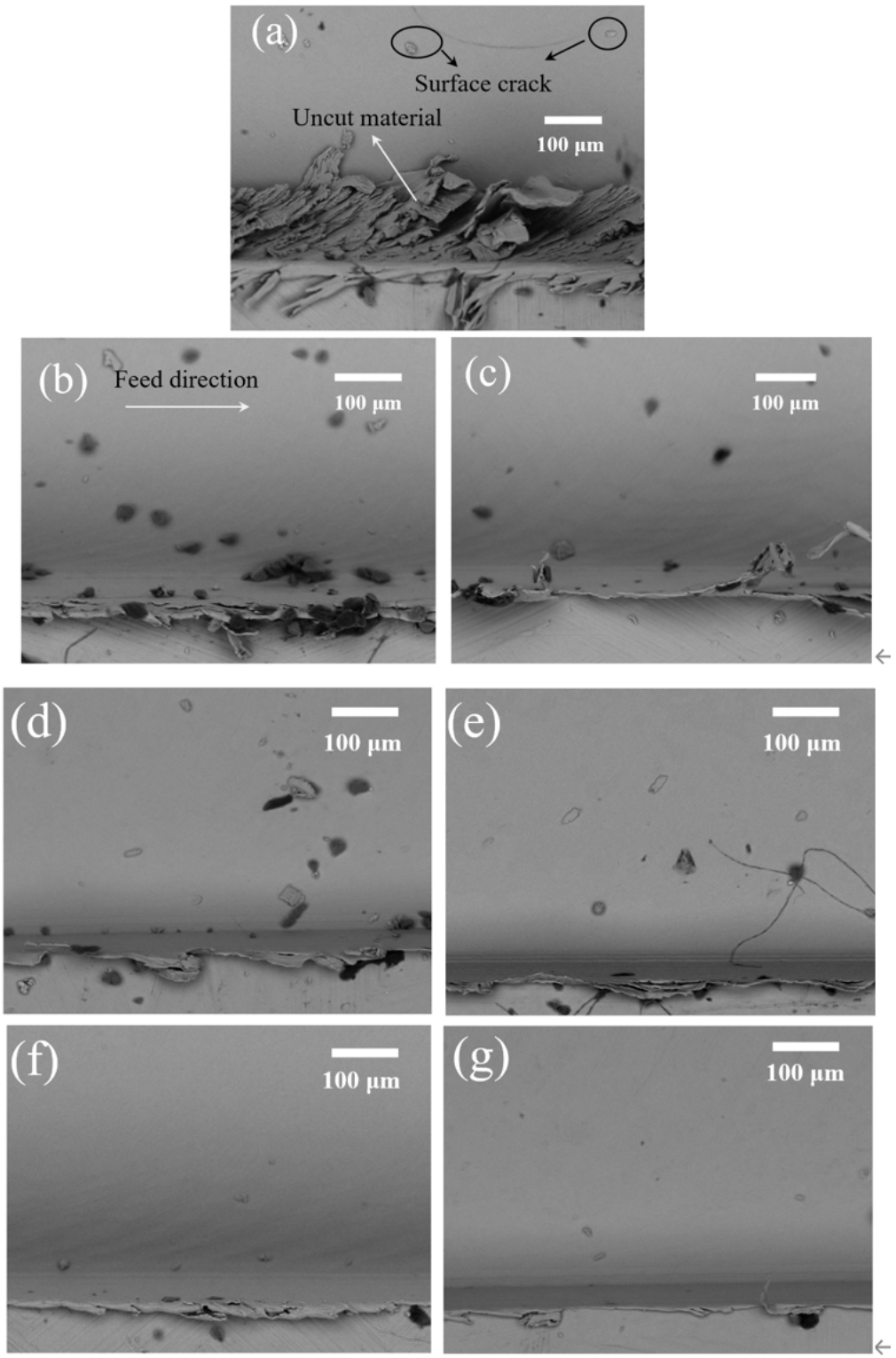

Figure 5-15 SEM measurement of burrs and the machined surface at the edge area of the up milling side of conventional micro milling and vibration assisted micro milling at the cutting length of 600mm. (a) Conventional micro milling; (b) Vibration amplitude 0.5 µm and vibration frequency 1500Hz; (c) Vibration amplitude 1µm and vibration frequency 1500Hz; (d) Vibration amplitude 0.5 µm and vibration frequency 3500Hz; (e) Vibration amplitude 1 µm and vibration frequency 3500Hz; (f) Vibration amplitude 0.5 µm and vibration frequency 5500Hz; (g) Vibration amplitude 1 µm and vibration frequency 5500Hz;

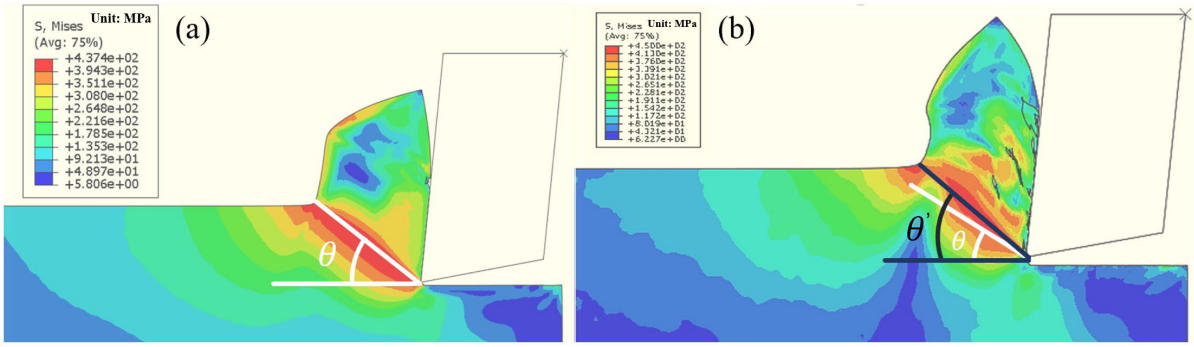

Figure 5-16 FE results of shear angle. (a) Conventional micro milling, (b) Vibration assisted micro milling with tool-workpiece separation

5.8 Conclusion

This chapter studied the tool wear suppression mechanisms in vibration assisted micro milling process. Machining experiments and finite element simulation are conducted by considering tool-workpiece separation conditions. The results show that the adhesive and mechanical wear of the micro tool can be effectively reduced as vibration is added, leading to an extended tool life and better cutting performance. The following conclusion can be drawn:

(1) Tool wear can be reduced effectively as vibration is added and the minimized tool wear can be obtained as tool-workpiece separation condition is satisfied due to the suppression of size and ploughing effect.

(2) Coating layer loss initiates wear mechanism for coated tool, and adhesive and mechanical wear are the main wear mechanisms for the substrate wear of the cutting tools. These wear mechanisms can be suppressed effectively in vibration assisted micro milling when tool-workpiece separation occurs, because the periodic separation between the cutting tool and workpiece enhances the cooling effect of the tool and reduces the cutting force as well as the generation of built-up edge.

(3) The relationship between tool wear and cutting performance is studied. Compared with conventional micro milling, the cutting performance in vibration assisted micro milling can be improved. The machining results also indicate that better surface finish, smaller burr and lesser surface crack can be obtained by increasing vibration frequency and satisfying tool-workpiece separation condition due to the low tool wear and the unique cutting mechanism.

Chapter 6 Burr formation investigation in non-resonant vibration assisted micro milling

6.1 Introduction

Similar to chip generation, Burr formation is a common phenomenon in the machining process and an important criterion in the evaluation of the machined surface. Burrs are caused by the plastic deformation of the material at the end of the cutting process and their generation is affected by many factors, including cutting parameters, tool geometry and material properties (Ton, Park and Ko, 2011). The presence of burrs affects the product life cycle and machining accuracy, and also poses a risk to operators. Therefore, an extra deburring or edge finishing process is usually needed, which is costly and inefficient. However, the deburring process may introduce unwanted residual stress and can even damage the parts. In addition, when it comes to micro-parts, the small size of the parts makes the deburring process more difficult, and these parts are easily damaged in the process and lead to scrap. This chapter aims to investigate the burr formation suppression mechanism in vibration assisted micro milling through both finite element (FE) and experimental methods.

6.2 Burr formation and classification

Burr formation is a complex process influenced by many factors such as material properties, manufacturing processes and shapes. The first study of burr formation in the machining process can be traced back to the 1970s (Gillespie and Blotter, 1976). It was found that the metal of the cutting layer will produce a large shear slip under the action of the tool, resulting in a large plastic deformation in the cutting process. A burr is formed if the material remains on the workpiece. Currently, two different approaches are commonly accepted by researchers for descriptions of burring in machining. In terms of burr formation, four types of machining burrs can be categorised: rollover burr, tear burr, cut-off burr and Poisson burr, as shown in Fig. 6-1. The rollover burr is a kind of bended chip which is also called an exit burr because it is usually formed at the end of processing. The tear burr is not the result of shearing clearing, rather it is caused by the result of material tearing loose from the workpiece, which is much like the burr formation found in the punching process. The cut-off burr is the consequence of workpiece falling apart from raw material before cutting process is finished. The Poisson burr is a result of the material's tendency to bulge to the sides when it is compressed until permanent plastic deformation occurs. Another type of burr description is according to the shapes,

locations and formation mechanisms of the burrs (Silva *et al.*, 2015). Fig. 6-2 shows the burrs types in the machining process which includes entrance burr, exit burr, side burr and top burr. The size and formation mechanisms of these four types of burrs are different. The top burr is the result of Poisson and tear burr and appears at the top surface of the workpiece. The exit burr is defined as a burr attached to machined edge at the end of milling and the side burr adheres to the transition surface (Piquard *et al.*, 2014).

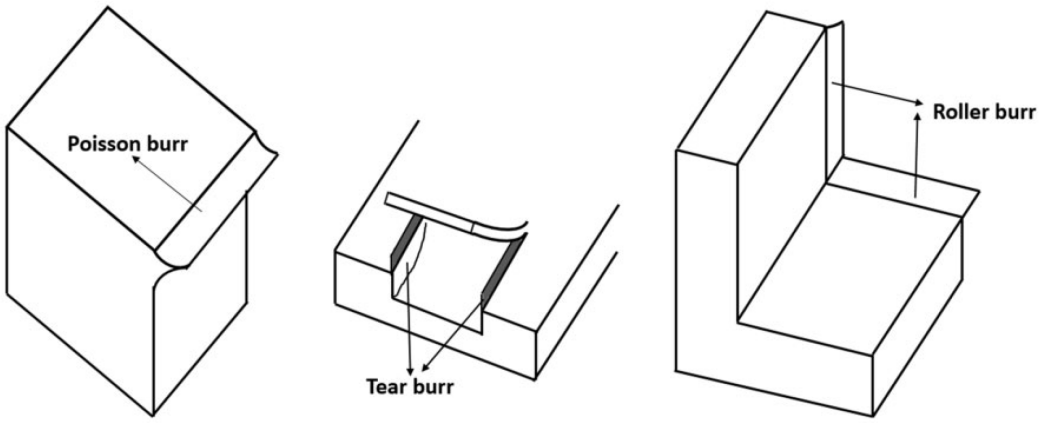

Figure 6-1 Schematics of Poisson burr, tear burr and rollover burr (International Organization for Standardization [ISO], 2013; Zheng, Chen and Huo, 2018).

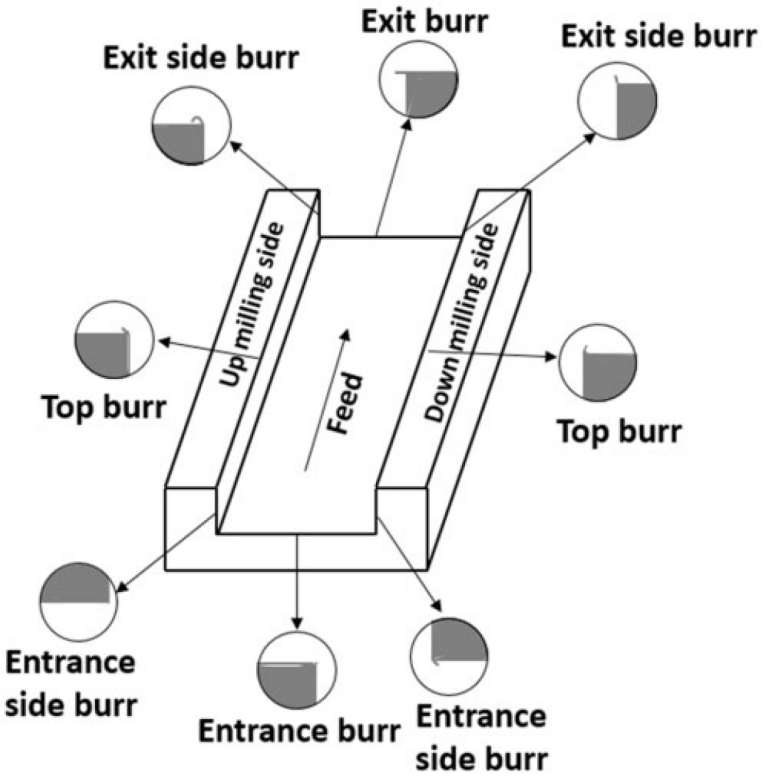

Figure 6-2 Types of burrs in micro-end milling (International Organization for Standardization [ISO], 2013; Zheng, Chen and Huo, 2018).

6.3 Burr reduction mechanism in vibration assisted micro machining

The removal of burrs is more difficult in micro machining due to the small size of the workpiece. The size effect in micro machining leads to a different cutting mechanism, and this influences burr formation. Fig. 6-3 shows the formation of the machined surface in micro machining. In the micro cutting process, compression shear deformation occurs when the workpiece material is compressed by the cutting tool, and chips are formed along the shear plane OM due to the shear slip effect. However, a layer of workpiece material Δs cannot form chips along the shear plane OM due to the size effect, and the machined surface can be obtained as that workpiece material is severely squeezed and rubbed by the cutting tool. As the micro cutting tool approaches the end of the workpiece, the plastically deformed layer of the workpiece material Δs will flow and form burrs at the edges of the workpiece. Burr size will increase with the increase in the ratio of undeformed chip thickness to the cutting edge radius (Aramcharoen and Mativenga, 2009). In addition, the point O will move up for a worn cutting tool due to the increase in cutting edge radius, which increases the thickness of Δs and the corresponding elastic-plastic deformation. As a result, the burr size will also be increased.

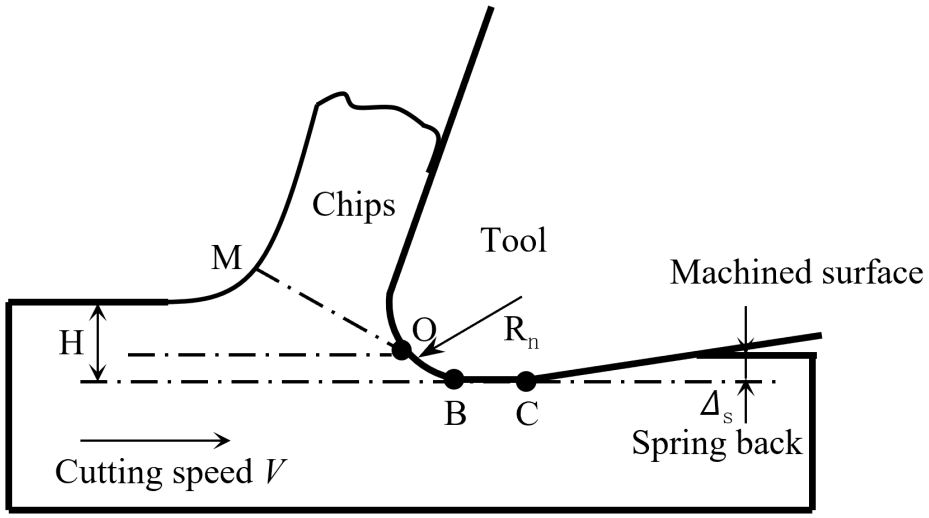

Figure 6-3 The formation of machined surface in micro machining

6.3.1 Experimental setup

To experimental study the burr formation in vibration assisted micro milling, slot milling experiments are carried out on Ti-6Al-4V using 1 mm diameter uncoated carbide end mills. The cutting-edge radius of the tools is measured approx. 3 μm on the effects of vibration

frequency and vibration direction are investigated. The experimental machining and vibration parameters are listed in Table 6-1.

Table 6-1 Vibration and cutting parameters

NO.	Amplitude (μm)	Frequency (Hz)	Spindle Speed (rpm)	Feed rate (mm/min)	Vibration direction
1	0	0	20000	50	NA
2	1	400	20000	50	Feed direction
3	1	4000	20000	50	Feed direction
4	1	9000	20000	50	Feed direction
5	1	400	20000	50	Feed and cross feed direction
6	1	4000	20000	50	Feed and cross feed direction
7	1	9000	20000	50	Feed and cross feed direction

6.3.2 Results and discussion

To investigate the machining burr formation under different vibration parameters, machining experiments are conducted with a left to right feed direction, and all machining surfaces are checked by a SEM (TM3030, Hitachi) and the testing results illustrate that burr is always smaller on up milling side for all vibration parameters. Fig. 6-4 shows a comparison between typical machined slots by conventional and vibration assisted micro milling respectively. Large top burrs can be found on the workpiece machined by conventional micro milling on both up milling and down milling sides. More machining tearing burrs appear on the down milling side compared with up milling side and this phenomenon can be explained through analyzing the slot milling process. As the cutter is engaged to the workpiece, the workpiece material is squeezed and pushed in up milling side first. As the process going on, the uncut chip thickness increases, which enhances support effect on the uncut materials and the shear action on material removal. However, on down milling side, the support effect of uncut material is smaller than that on up milling side, and hence the uncut materials are pushed out of the top of down milling side and large irregular tearing burrs are generated on this side. It can be hard to remove these burrs due to the small feature size and influence the accuracy of the milling slot. While in

vibration assisted micro milling, no large top burr can be found on both sides. Since vibration is superimposed to the process, the motion of tool tip becomes to reciprocating (one dimensional VAMM) or elliptical (two dimensional VAMM). This leads to a periodic separation between tool tip and the workpiece. As a result, the down milling and up milling can occur on both sides of the slot alternatively (Chen *et al.*, 2018). In addition, material removal mode changes from shear dominated deformation in conventional micro milling process to a mixed action that combines dynamic impact and shear deformation in VAMM, and the ploughing/rubbing between workpiece and cutter is also reduced. As a consequence, the cutting force and discontinued chips can be reduced, which in turn reduce the burr generation and improve machining accuracy. Fig. 6-4 (b) shows improved slot edge quality from VAMM.

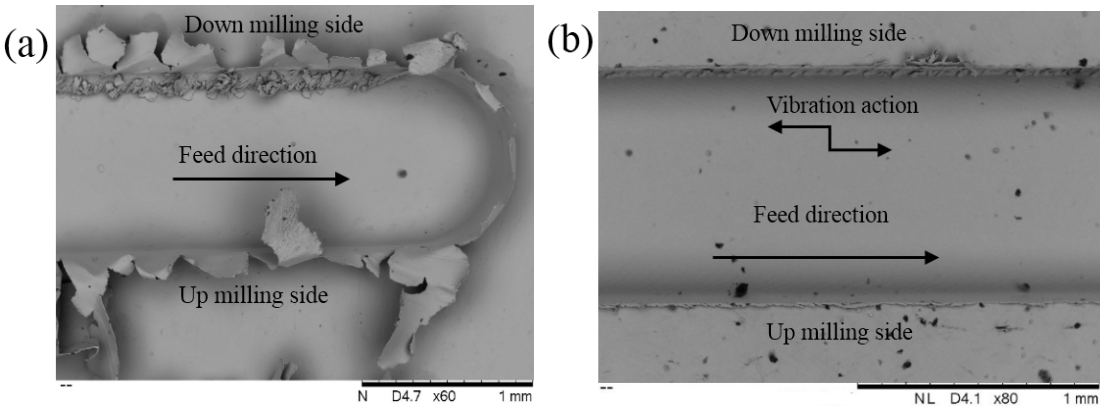

Figure 6-4 Machining results comparison between (a) Conventional micro end milling and (b) Vibration assisted micro end milling

Fig. 6-5 shows the enlarge images on down milling side for tear burr observation, by comparing the results of (a)(b), (c)(d) and (e)(f), it can be seen when vibration frequency is constant, the tear burr size is reduced as adding cross feed direction vibration to the process, that is due to tool tip cutting direction has been changed slightly and enhance material tearing loose from the workpiece (Brehl and Dow, 2008). In addition, a trend of reduced tear burr can be found when increasing vibration frequency under same vibration direction. As the tool vibration frequency increases from 400 Hz to 8000 Hz, the tool vibration speed is enhanced, this leads to an increase in reciprocating cutting on down milling side and large tear burr is removed. As a result, the tear burr size can be reduced.

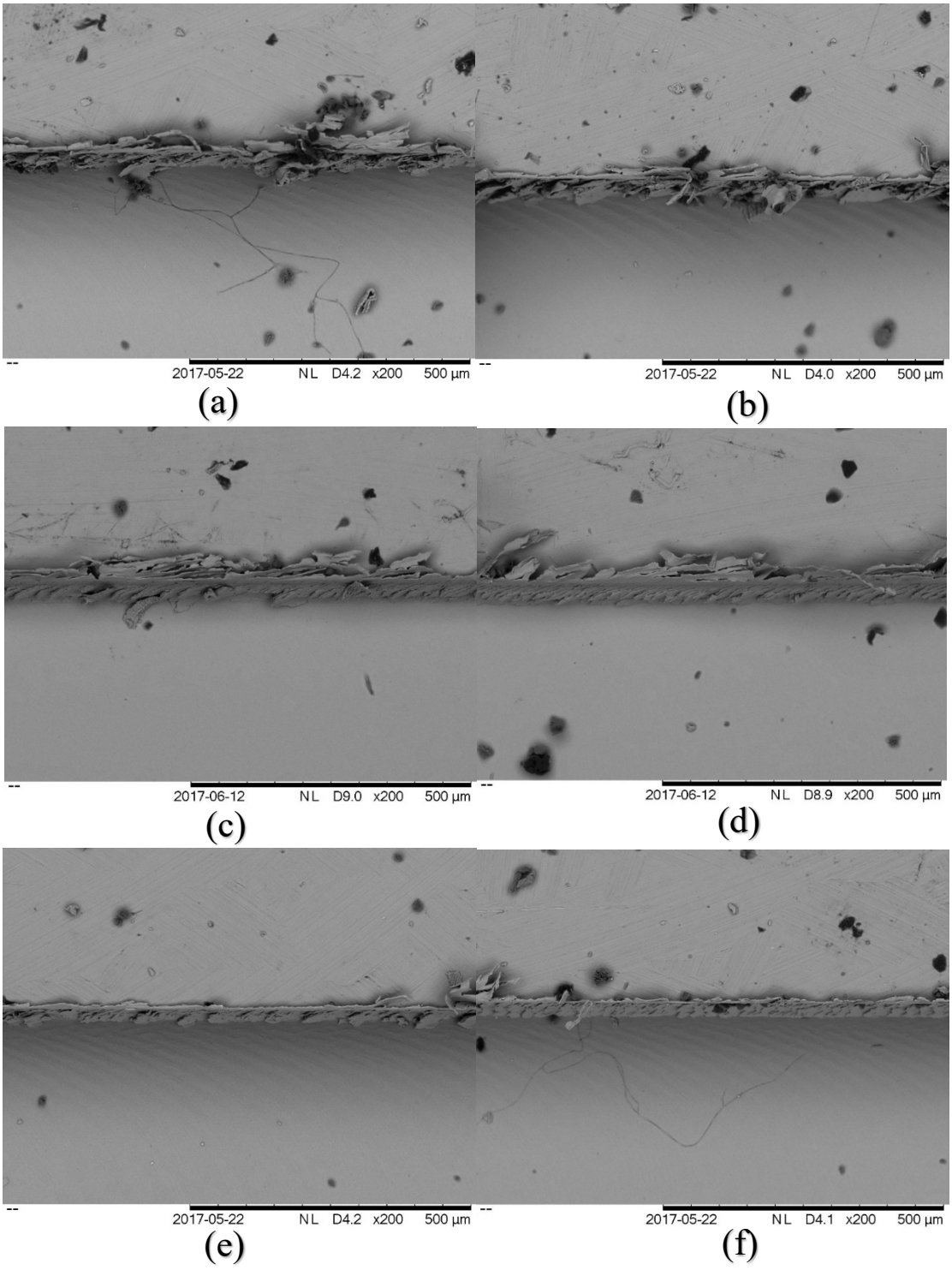

Figure 6-5 Down milling side tear burr results with different parameters: (a) Feed direction vibration with a frequency of 400Hz. (b) Feed and cross direction vibration with a frequency of 400Hz. (c) Feed direction vibration with a frequency of 4000Hz. (d) Feed and cross direction vibration with a frequency of 4000Hz. (e) Feed direction vibration with a frequency of 8000Hz. (f) Feed and cross direction vibration with a frequency of 8000Hz.

In order to assess the top burr height precisely, the maximum top burr height *h* was measured as shown in Fig. 6-6. The variation of top burr height results with the vibration frequency for two vibration modes (feed direction and feed and cross feed direction) are shown in Fig. 6-7.

It demonstrates that the top burr height in both vibration modes of VAMM is always smaller than that in the conventional micro milling, which indicates that the VAMM is an effective way to reduce top burr generation. Fig 6-7 (a) shows the top burr height variation for both up milling and down milling sides between conventional micro end milling and the feed direction VAMM. The maximum burr height in conventional micro milling is around 36 μm on the down milling side and 28 μm on the up-milling side. As vibration is applied to the process, the top burr height will be reduced by 58% to 82% on up milling side and nearly 50% on down milling side depending on the parameters. Moreover, higher vibration frequency has a positive effect on burr height reduction. The higher vibration frequency, the lower top burr height can be obtained. That is due to the intermittent cutting effect. As the vibration frequency increases, the critical velocity V_c (equation 5-8) can be larger than upfeed velocity of micro end milling, and a less average cutting force and less cutting heat can be generated. This reduces the instantaneous compressive and bending stresses in the cutting deformation zone and decreases the ploughing/rubbing effect between cutting tool and workpiece. As a result, top burr height is reduced.

Fig. 6-7 (b) shows the top burr height variation results for 2D VAMM. The burr height in 2D VAMM is also reduced but there is not much improvement compared to the 1D VAMM. There is no effect on the critical velocity V_c when cross-feed direction vibration is added to the cutting process and the top burr reduction is mainly contributed by feed direction vibration in the 2D VAMM process. It can be concluded that the vibration in cross-feed direction has little effects on the top burr height reduction in slot milling process. As the vibration in cross-feed direction not changes the cutting trajectory between the cutter and the workpiece during the material removal process, it almost has no positive effects on the top burr reduction. For some specific parameters the top burr height is even larger than that in 1D VAMM. The top burr height in down milling side increases almost 3 μm when vibration frequency changes from 400Hz to 4000Hz and both up milling and down milling side burr height reach the lowest value at the frequency of 8000Hz which is 6 μm and 13 μm, respectively.

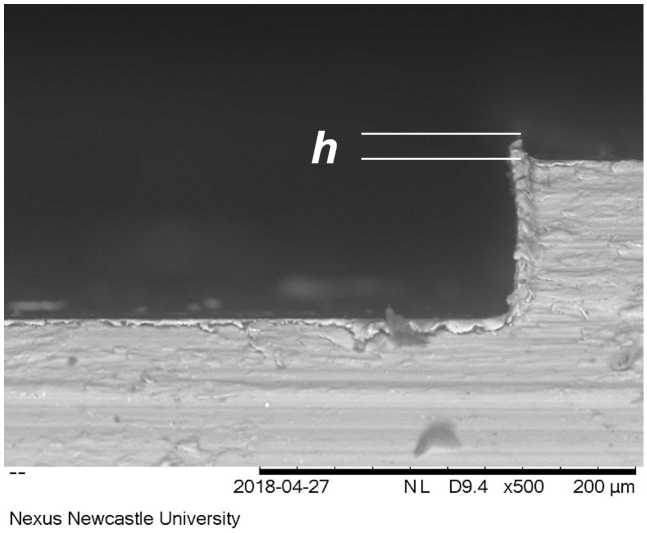

Figure 6-6 Top burr height measurement

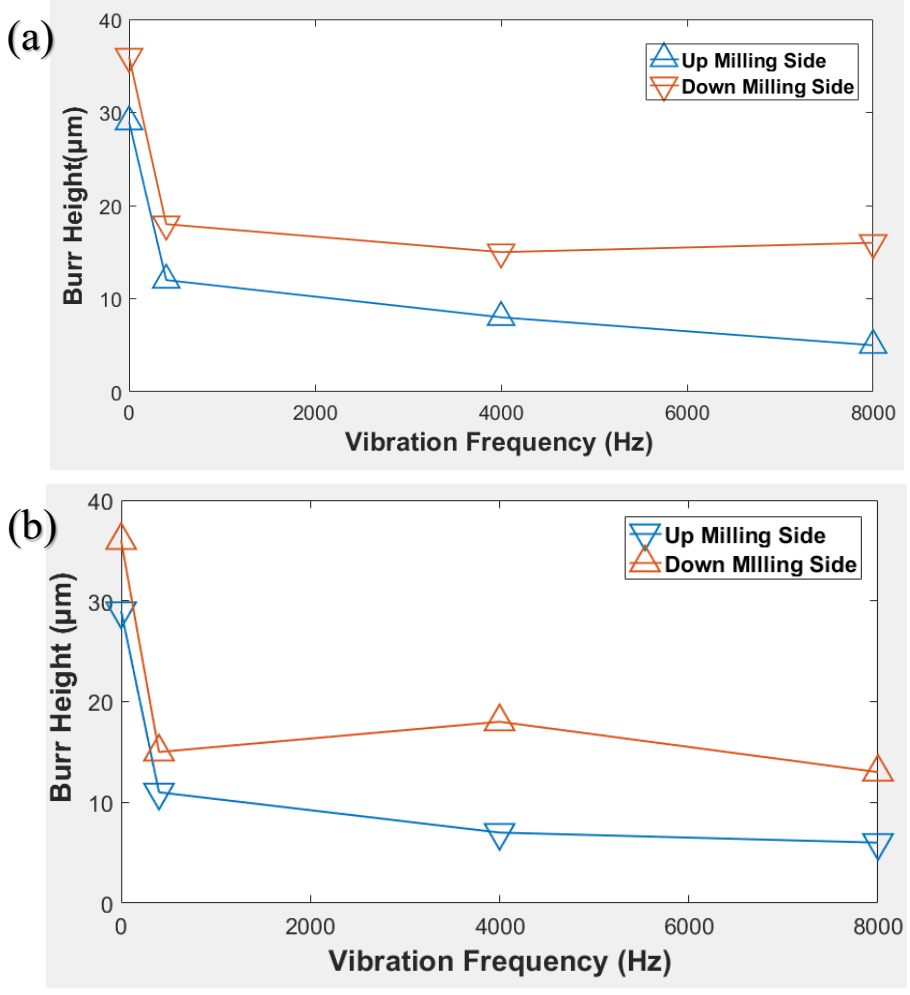

Figure 6-7 Burr height measurement results, (a) Feed direction vibration assisted micro milling, (b) Feed and cross feed direction vibration assisted micro milling

6.4 Relationship between vibration parameters and burr height

To further study the relationship between each vibration parameter and burr height, a full factor slot milling orthogonal experiment on titanium alloy is carried out and all cutting and vibration parameters are listed in table 6-2. Four variation factors, *x* direction vibration frequency and amplitude, and y direction vibration frequency and amplitude with 3 changing levels are set in the experiments. Moreover, the tool and workpiece will not be separated during processing in all these 81 sets of experiments to eliminate the influence of tool-workpiece separation on burr generation. The measurement of burr height is shown in Fig. 6-6.

Table 6-2 Cutting and vibration parameters for orthogonal experiments

level	Spindle speed (rpm)	Cutting depth (μm)	Feed per tooth (μm)	*x*-direction(feed)		*y*-direction	
				vibration amplitude (μm)	vibration frequency (Hz)	vibration amplitude (μm)	vibration frequency (Hz)
1	30000	50	2	500	0.4	500	0.4
2	30000	50	2	2000	0.8	2000	0.8
3	30000	50	2	5000	1.2	5000	1.2

Table 6-3 shows the results of burr height of all 81 sets of experiments. And ANOVA is carried out on the burr height to isolate the main effects of each source of variations (Table 6-4). It can be concluded that the vibration frequency in *x* direction and vibration amplitude in *y* direction have a significant influence on burr height. The contribution ratio for the vibration frequency in *x* direction and vibration amplitude in *y* direction is 61.10% and 28.40%, respectively.

Table 6-3 Burr height results

x-direction		*y*-direction		Burr height (μm)
vibration frequency (Hz)	vibration amplitude (μm)	vibration frequency (Hz)	vibration amplitude (μm)	
500	0.4	500	0.4	4.6
500	0.4	500	0.8	11
500	0.4	500	1.2	28.05
500	0.4	2000	0.4	12.65
500	0.4	2000	0.8	12.85
500	0.4	2000	1.2	28.75
500	0.4	5000	0.4	9.3
500	0.4	5000	0.8	6
500	0.4	5000	1.2	17.55
500	0.8	500	0.4	6.75

500	0.8	500	0.8	18.45
500	0.8	500	1.2	14.1
500	0.8	2000	0.4	28.05
500	0.8	2000	0.8	30.15
500	0.8	2000	1.2	8.4
500	0.8	5000	0.4	17.9
500	0.8	5000	0.8	20.15
500	0.8	5000	1.2	14.4
500	1.2	500	0.4	20.95
500	1.2	500	0.8	14.9
500	1.2	500	1.2	13.75
500	1.2	2000	0.4	23.2
500	1.2	2000	0.8	22.85
500	1.2	2000	1.2	16.15
500	1.2	5000	0.4	29.5
500	1.2	5000	0.8	8.45
500	1.2	5000	1.2	16.4
2000	0.4	500	0.4	40.4
2000	0.4	500	0.8	7.45
2000	0.4	500	1.2	24.6
2000	0.4	2000	0.4	37.95
2000	0.4	2000	0.8	7.1
2000	0.4	2000	1.2	33.8
2000	0.4	5000	0.4	17.7
2000	0.4	5000	0.8	8.45
2000	0.4	5000	1.2	10.15
2000	0.8	500	0.4	12.6
2000	0.8	500	0.8	11.25
2000	0.8	500	1.2	11.25
2000	0.8	2000	0.4	7.65
2000	0.8	2000	0.8	13.8
2000	0.8	2000	1.2	11.15
2000	0.8	5000	0.4	27.4
2000	0.8	5000	0.8	42.85
2000	0.8	5000	1.2	8.15
2000	1.2	500	0.4	19.85
2000	1.2	500	0.8	29.25
2000	1.2	500	1.2	17
2000	1.2	2000	0.4	41.1
2000	1.2	2000	0.8	19.25
2000	1.2	2000	1.2	8.65
2000	1.2	5000	0.4	59.5
2000	1.2	5000	0.8	45.25
2000	1.2	5000	1.2	17.7
5000	0.4	500	0.4	60
5000	0.4	500	0.8	32.9
5000	0.4	500	1.2	9.75
5000	0.4	2000	0.4	54.85

5000	0.4	2000	0.8	49.65
5000	0.4	2000	1.2	20.2
5000	0.4	5000	0.4	57.9
5000	0.4	5000	0.8	18.55
5000	0.4	5000	1.2	24.6
5000	0.8	500	0.4	39.05
5000	0.8	500	0.8	45.6
5000	0.8	500	1.2	23.65
5000	0.8	2000	0.4	23.35
5000	0.8	2000	0.8	22.15
5000	0.8	2000	1.2	24.6
5000	0.8	5000	0.4	23.65
5000	0.8	5000	0.8	43.2
5000	0.8	5000	1.2	10.55
5000	1.2	500	0.4	17.1
5000	1.2	500	0.8	33.3
5000	1.2	500	1.2	28.8
5000	1.2	2000	0.4	32.05
5000	1.2	2000	0.8	57.2
5000	1.2	2000	1.2	41.6
5000	1.2	5000	0.4	51.5
5000	1.2	5000	0.8	13.2
5000	1.2	5000	1.2	7.65

Table 6-4 ANOVA for burr height

Source of variation	Degree of freedom	Sum of square	Mean of square	F Value	P Value	Contribution
f_x	2	3253.4	1626.7	10.15	0.000	61.10%
A_x	2	398.5	199.2	1.24	0.295	7.40%
f_y	2	165.1	82.6	0.52	0.6	3.10%
A_y	2	1508.3	754.2	4.7	0.012	28.40%
Error	72	11542	160.3			
Total	80	16867.3				

6.5 Conclusion

In this section, vibration assisted micro milling experiments are performed on Ti-6Al-4V workpiece using a two-dimensional vibration stage developed. The following conclusions can be drawn:

1) With appropriate machining and vibration parameters, vibration assisted micro milling can reduce tearing burr formation, especially on the down milling side. In the micro

milling with vibration assistance, up milling and down milling can occur in both sides of the slot.

2) Vibration assisted milling produces very small top burr size compared with conventional micro milling, this is due to the former can reduce average cutting force and decrease the ploughing/rubbing between workpiece and cutter.
3) The vibration direction has significant influence on the burr reduction, and the vibration applied in feed direction has better effect than cross-feed direction.
4) Both frequency and vibration directions affect the top burr height. Generally higher vibration frequency helps minimize burr formation, although more systematic investigation will be carried on optimizing the machining/vibration parameter.
5) Relationship between vibration parameters and burr height is investigated through a full factor orthogonal experiment and analyzed using ANOVA, the results show that vibration frequency in *x* direction (feed direction) and vibration amplitude in *y* direction (cross-feed direction) have a significant influence on burr height.

Chapter 7 Conclusions and recommendations for future work

7.1 Summary and conclusions

As an unconventional machining technology, vibration assisted machining adds high frequency vibration on cutting tool or workpiece to enhance cutting performance. This research is proposed a systematic investigation on vibration assisted micro milling technology, And the main contribution of this research is:

1. Establish a motion decoupled two-dimensional piezoelectric actuator driven vibration stage. For the mechanical design, a double parallel four-bar linkage structure with double layer flexible hinges is first proposed, which can guide the motion and reduce the displacement coupling effect between the two directions. Matrix-based compliance modelling (MCM) method is developed to enhance the accuracy of the analytical model. For the control system design, a fuzzy adaptive PID control system is developed to further increase the motion accuracy.

2. Investigate the cutting mechanisms in vibration assisted micro milling systematically. The condition of tool-workpiece separation is theoretically studied, as well as the cutting tool tip trajectories. A textured surface formation model is developed based on the results of tool tip kinematic analysis and tool tip 3D geometry. Burr reduction and tool wear suppression mechanism is studied using both theoretical and FEA methods.

3. Study the relevant applications in vibration assisted micro milling. A new contact model is developed based on the manufactured fish scale surface textures by considering the effects of trapped air pressure in the surface microstructure, infiltration area and the percentage of area occupied by solids. A new strategy on liquid flow controlling in microfluidic chips is proposed by arranging the designed textured surfaces on different locations of the channels of the microfluidic chips.

Based on the results and discussion from this research, the conclusions can be drawn as following:

1. A new 2D non-resonant vibration stage with high motion accuracy and motion decoupling is developed by using double parallel four-bar linkages with double layer flexible hinges structure. The compliance and dynamic characteristics of the stage are conducted by using

matrix-based compliance modelling method and the Lagrangian principle, respectively. Acceptable deviations (4.3% and 2.2%) can be obtained by comparing the analytical results with the FEA results, which indicate the feasibility of the proposed analytical model. A close-loop control system is developed by using fuzzy adaptive PID control method based on LabVIEW program. The stage frequency-response tests confirm the resonant vibration frequencies and a relatively low tool tip coupling error (2.6% of the vibration amplitude).

2. A surface generation model is proposed by considering tool tip geometry and tool trajectories. Fish scales surface textures are produced according to the established surface generation model. A contact model is developed to predict the hydrophilicity of fish scales textured surfaces by considering the effects of trapped air pressure in the surface microstructure, infiltration area and the percentage of area occupied by solids on a rough surface. The wettability testing results on the machined surface show that the proposed contact model can predict the contact angle accurately. The results also indicate that the fish scales textured surface turns to more hydrophilic and a surface with controllable wettability can be obtained by optimizing the machining and vibration parameters. The following surface textures are also used for microfluidic chips manufacturing. One-way flow function can be obtained in T-shaped microchannels due to the liquid driving force is smaller than the surface tension difference between the two outlets, which is caused by differences in surface microstructure and wettability of the two outlets. Micro-mixers in the Y-shaped microchannel are developed by setting different fish scales surface textures in the mixing channel. The liquid flow results show that chaotic convection can be obtained by the fish scales surface textures and the strength of chaotic convection varies with the wettability and characteristic dimensions of the fish scales.

3. Tool wear suppression mechanism in vibration assisted micro milling is investigated through both theorical and experimental method. Coating layer loss initiates wear mechanism for coated tool, and adhesive and mechanical wear are the main wear mechanisms for the substrate wear of the cutting tools. These wears can be suppressed effectively when tool-workpiece separation occurs due to lower cutting temperature and cutting force, smaller built-up edge and the suppression on the tool ploughing effect. The relationship between tool wear and cutting performance is also studied. Compared with conventional micro milling, the cutting performance in vibration assisted micro milling

can be improved. The machining results also indicate that better surface finish, smaller burr and lesser surface crack can be obtained by increasing vibration frequency and satisfying tool-workpiece separation condition due to the low tool wear and the unique cutting mechanism.

4. Burr formation mechanism in vibration assisted micro milling is studied. With appropriate machining and vibration parameters, vibration assisted micro milling can reduce tearing burr formation, especially on the down milling side. In the micro milling with vibration assistance, up milling and down milling can occur in both sides of the slot. Vibration assisted milling produces very small top burr size compared with conventional micro milling, this is due to the former can reduce average cutting force and decrease the ploughing/rubbing between workpiece and cutter. The vibration direction has significant influence on the burr reduction, and the vibration applied in feed direction has better effect than cross-feed direction. Both frequency and vibration directions affect the top burr height. Generally higher vibration frequency helps minimize burr formation, although more systematic investigation will be carried on optimizing the machining/vibration parameter.

7.2 Recommendations for future work

7.2.1 Future trends of vibration assisted machining technology

With the development of processing technology, the application of vibration assisted machining is becoming increasingly widespread, and research into vibration assisted machining is becoming more and more intensive, mainly in the following main aspects:

(1) Development and adoption of new tool materials

The proportion of difficult-to-machine materials in modern products is increasing, as well as a higher processing quality of these parts. In order to achieve better cutting performance, in addition to the optimization of tool geometry parameters, more attention has been focused on the development and application of tool materials in vibration assisted machining and main research focus is on natural and synthetic diamond and ultra-fine grained carbide materials.

(2) Ultra-high frequency vibration assisted machining

Ultra-high frequency vibration assisted machining will continue to be a research focus in vibration assisted machining in the future. Recent research indicates that the possibility of grinding wheel ablation can be effectively reduced by adding high-frequency vibration, which also improves the grinding wheel's life and the surface quality of the workpiece. In recent years, research into ultra-high frequency vibration equipment has made it possible to reach a maximum vibration frequency of 100 kHz, and at the same time its processing performance for brittle and hard materials has also been significantly improved.

(3) Precision/ultra-precision application

It has been reported that the dimensional and geometric accuracy and wear resistance as well as corrosion resistance of the workpiece can be improved dramatically when low frequency vibration is applied. However, only high frequency vibration assisted machining, such as ultrasonic vibration assisted machining can currently achieve a precision machining process. For example, a surface roughness of Ra 0.02~0.04 μm can be obtained by vibration assisted honing and surface quality improves by an order of magnitude in the ultrasonic vibration extrusion process compared to conventional extrusion. Ultrasonic vibration machining can not only guarantee the quality of ultra-precision machining but also allows for higher cutting rates, leading to higher productivity.

(4) In-depth study of vibration assisted machining mechanism

Although the cutting mechanism of the vibration assisted machining has been investigated by several researchers, it is still not fully understood. Current and future research on vibration assisted machining will focus on several area, including the effect of the separation and non-separation of the workpiece and cutting tool on chip formation, mechanical analysis of the interaction between the cutting tool and workpiece, microscopic studies and mathematical descriptions of vibration assisted machining mechanisms, to name a few.

7.2.2 Further work of this study

This research has achieved the expected aims and objectives, the recommendations in which topics in further research would be beneficial are summarised as follows:

1. The current results show that vibration frequency has a great influence on cutting performance. Therefore, it is desired to develop an ultra-high frequency (up to 100 kHz) vibration device and study its cutting mechanism.

2. The demand for composite material components is increasing due to its wide range of applications and excellent mechanical properties. However, processing these materials is a challenging task because serious defeats, such as tearing, burring and delamination, are easy to occur in the conventional machining process, leading to poor processing quality. Therefore, research on vibration-assisted processing technology for processing composite materials shows a great potential to improve the processing quality.

3. Microfluidic chips have received extensive attention in the cell biology field due to their high precision and controllable characteristics. Meanwhile, cell culture process also can be influenced by textured surface. Therefore, it is very promising to develop microfluidic chips for biological cell culture based on the results of current research on textured surface and microfluidic chips manufacturing.

4. Through studying the relationship between the machined titanium alloy surface characteristics and biocompatibility, this proposed study may also help to address the current limitations of titanium alloy implants in the biomedical field.

References

Lenkiewicz, W., 1969. The sliding friction process—effect of external vibrations. *Wear*, 13(2), pp.99-108.

Adnan, A.S. and Subbiah, S., 2010. Experimental investigation of transverse vibration-assisted orthogonal cutting of AL-2024. I*nternational Journal of machine tools and manufacture*, 50(3), pp.294-302. doi:10.1016/j.ijmachtools.2009.11.004.

Ahn, J.H., Lim, H.S. and Son, S.M., 1999, October. Improvement of micro-machining accuracy by 2-dimensional vibration cutting. *In Proc ASPE*. Vol. 20, pp. 150-153.

Al-Bender, F., Lampaert, V. and Swevers, J., 2005. The generalized Maxwell-slip model: a novel model for friction simulation and compensation. *IEEE Transactions on automatic control*, 50(11), pp.1883-1887.

Alam, K., Mitrofanov, A.V. and Silberschmidt, V.V., 2011. Experimental investigations of forces and torque in conventional and ultrasonically-assisted drilling of cortical bone. *Medical engineering & physics*, 33(2), pp.234-239. doi: 10.1016/j.medengphy.2010.10.003.

Alpas, A.T. and Zhang, J., 1994. Effect of microstructure (particulate size and volume fraction) and counterface material on the sliding wear resistance of particulate-reinforced aluminum matrix composites. *Metallurgical and Materials Transactions A*, 25(5), pp.969-983. doi: 10.1007/BF02652272.

Amin, S.G., Ahmed, M.H.M. and Youssef, H.A., 1995. Computer-aided design of acoustic horns for ultrasonic machining using finite-element analysis. *Journal of Materials Processing Technology*, 55(3-4), pp.254-260. doi: 10.1016/0924-0136(95)02015-2.

Aramcharoen, A. and Mativenga, P.T., 2009. Size effect and tool geometry in micromilling of tool steel. *Precision Engineering*, 33(4), pp.402-407. doi:10.1016/j.precisioneng.2008.11.002.

Ashley, C. and Mills, B., 1966. Frequency response of an electro-hydraulic vibrator with inertial load. *Journal of Mechanical Engineering Science*, 8(1), pp.27-35.

Asumi, K., Fukunaga, R., Fujimura, T. and Kurosawa, M.K., 2009. Miniaturization of a V-shape transducer ultrasonic motor. *Japanese Journal of Applied Physics*, 48(7S), p.07GM02. doi: 10.1143/JJAP.48.07GM02.

Babitsky, V.I., Astashev, V.K. and Meadows, A., 2007. Vibration excitation and energy transfer during ultrasonically assisted drilling. *Journal of sound and vibration*, 308(3-5), pp.805-814. doi: 10.1016/j.jsv.2007.03.064.

Babitsky, V.I., Mitrofanov, A.V. and Silberschmidt, V.V., 2004. Ultrasonically assisted turning of aviation materials: simulations and experimental study. *Ultrasonics*, 42(1-9), pp.81-86. doi: 10.1016/j.ultras.2004.02.001.

Bae, W.G., Kim, S.M., Choi, S.J., Oh, S.G., Yoon, H., Char, K. and Suh, K.Y., 2014. In Situ Realization of Asymmetric Ratchet Structures within Microchannels by Directionally Guided Light Transmission and Their Directional Flow Behavior. *Advanced Materials*, 26(17), pp.2665-2670. doi: 10.1002/adma.201305001.

Baghlani, V., Mehbudi, P., Akbari, J., Nezhad, E.Z., Sarhan, A.A. and Hamouda, A.M.S., 2016. An optimization technique on ultrasonic and cutting parameters for drilling and deep drilling of nickel-based high-strength Inconel 738LC superalloy with deeper and higher hole quality. *The International Journal of Advanced Manufacturing Technology*, 82(5-8), pp.877-888. doi: 10.1007/s00170-015-7414-6.

Balamuth, L., 1964. Recent developments in ultrasonic metalworking processes (No. 640149). SAE Technical Paper.

Bamshad, A., Nikfarjam, A. and Khaleghi, H., 2016. A new simple and fast thermally-solvent assisted method to bond PMMA–PMMA in micro-fluidics devices. *Journal of Micromechanics and Microengineering*, 26(6), p.065017. doi: 10.1088/09601317/26/6/065017.

Bansevicius, R. and Tolocka, R.T., 2002. Piezoelectric actuators. *Mechatronics Handbook by Bishop*.

Barani, A., Amini, S., Paktinat, H. and Tehrani, A.F., 2014. Built-up edge investigation in vibration drilling of Al2024-T6. *Ultrasonics*, 54(5), pp.1300-1310. doi: 10.1016/j.ultras.2014.01.003.

Basturk, S., Senbabaoglu, F., Islam, C., Erten, M., Lazoglu, I. and Gulmez, T., 2010. Titanium machining with new plasma boronized cutting tools. *CIRP annals*, 59(1), pp.101-104. doi: 10.1016/j.cirp.2010.03.095.

Börner, R., Winkler, S., Junge, T., Titsch, C., Schubert, A. and Drossel, W.G., 2018. Generation of functional surfaces by using a simulation tool for surface prediction and micro structuring of cold-working steel with ultrasonic vibration assisted face milling. *Journal of Materials Processing Technology*, 255, pp.749-759. doi: 10.1016/j.jmatprotec.2018.01.027.

Borruto, A., Crivellone, G. and Marani, F., 1998. Influence of surface wettability on friction and wear tests. *Wear*, 222(1), pp.57-65. doi: 10.1016/S0043-1648(98)00256-7.

Brehl, D.E., Dow, T.A., Garrard, K. and Sohn, A., 1999. Micro-structure fabrication using elliptical vibration-assisted machining (EVAM). *Aspe Proceedings*.

Brehl, D.E. and Dow, T.A., 2008. Review of vibration-assisted machining. *Precision engineering*, 32(3), pp.153-172. doi: 10.1016/j.precisioneng.2007.08.003.

Buckley, J.S., Takamura, K. and Morrow, N.R., 1989. Influence of electrical surface charges on the wetting properties of crude oils. *SPE Reservoir Engineering*, 4(03), pp.332-340. doi: 10.2118/16964-PA.

Burgers, A.R., Bultman, J.H., Beneking, C., Nositschka, W.A., Voigt, O. and Kurz, H., 2000. Silicon solar cells textured by reactive ion etching with natural lithography. *16th European Photovoltaic Solar Energy Coriference*.

Stroock, A.D., Dertinger, S.K., Ajdari, A., Mezić, I., Stone, H.A. and Whitesides, G.M., 2002. Chaotic mixer for microchannels. *Science*, 295(5555), pp.647-651. doi: 10.1126/science.282.5388.484.

Capretto, L., Cheng, W., Hill, M. and Zhang, X., 2011. Micromixing within microfluidic devices. In Microfluidics (pp. 27-68). *Springer,* Berlin, Heidelberg. doi: 10.1007/128_2011_150.

Cassie, A.B.D. and Baxter, S., 1944. Wettability of porous surfaces. *Transactions of the Faraday society*, 40, pp.546-551. doi: 10.1039/tf9444000546.

Chang, S.S. and Bone, G.M., 2005. Burr size reduction in drilling by ultrasonic assistance. Robotics and computer-integrated manufacturing, 21(4-5), pp.442-450. doi: 10.1016/j.rcim.2004.11.005.

Chang, S.S. and Bone, G.M., 2010. Burr height model for vibration assisted drilling of aluminum 6061-T6. *Precision Engineering*, 34(3), pp.369-375. doi: 10.1016/j.precisioneng.2009.09.002.

Chee, S.K., Suzuki, H., Okada, M., Yano, T., Higuchi, T. and Lin, W.M., 2011. Precision polishing of micro mold by using piezoelectric actuator incorporated with mechanical amplitude magnified mechanism. *In Advanced Materials Research* (Vol. 325, pp. 470-475). Trans Tech Publications Ltd. doi: 10.4028/www.scientific.net/AMR.325.470.

Chee, S.K., Suzuki, H., Uehara, J., Yano, T., Higuchi, T. and Lin, W., 2013. A Low Contact Force Polishing System for Micro Molds that Utilizes 2-Dimensional Low Frequency Vibrations (2DLFV) with Piezoelectric Actuators (PZT) and a Mechanical Transformer Mechanism. IJAT, 7(1), pp.71-82.

Chen, G. and Howell, L.L., 2009. Two general solutions of torsional compliance for variable rectangular cross-section hinges in compliant mechanisms. *Precision Engineering*, 33(3), pp.268-274. doi: 10.1016/j.precisioneng.2008.08.001.

Chen, J.B., Fang, Q.H., Wang, C.C., Du, J.K. and Liu, F., 2016. Theoretical study on brittle–ductile transition behavior in elliptical ultrasonic assisted grinding of hard brittle materials. *Precision Engineering*, 46, pp.104-117. doi: 10.1016/j.precisioneng.2016.04.005.

Chen, S., Zou, P., Tian, Y., Duan, J. and Wang, W., 2019. Study on modal analysis and chip breaking mechanism of Inconel 718 by ultrasonic vibration-assisted drilling. *The International Journal of Advanced Manufacturing Technology*, 105(1-4), pp.177-191. doi: 10.1007/s00170-019-04155-6.

Chen, W., Teng, X., Zheng, L., Xie, W. and Huo, D., 2018. Burr reduction mechanism in vibration-assisted micro milling. *Manufacturing letters*, 16, pp.6-9. doi: 10.1016/j.mfglet.2018.02.015.

Chen, W., Zheng, L., Teng, X., Yang, K. and Huo, D., 2018. Cutting mechanism investigation in vibration-assisted machining. *Nanomanufacturing and Metrology*, 1(4), pp.268-276. doi: 10.1007/s41871-018-0031-x.

Chen, W., Zheng, L., Huo, D. and Chen, Y., 2018. Surface texture formation by non-resonant vibration assisted micro milling. *Journal of Micromechanics and Microengineering*, 28(2), p.025006. doi: 10.1088/1361-6439/aaa06f.

Chern, G.L. and Chang, Y.C., 2006. Using two-dimensional vibration cutting for micro-milling. *International Journal of Machine Tools and Manufacture*, 46(6), pp.659-666. doi: 10.1016/j.ijmachtools.2005.07.006.

Cowper, G.R., 1966. The shear coefficient in Timoshenko's beam theory. *Journal of Applied Mechanics*, 33(2), p. 335. doi: 10.1115/1.3625046.

Crawley, E.F. and De Luis, J., 1987. Use of piezoelectric actuators as elements of intelligent structures. *AIAA journal*, 25(10), pp.1373-1385. doi: 10.2514/3.9792.

Dadgari, A., Huo, D. and Swailes, D., 2018. Investigation on tool wear and tool life prediction in micro-milling of Ti-6Al-4V. *Nanotechnology and Precision Engineering*, 1(4), pp.218-225. doi: 10.1016/j.npe.2018.12.005.

Dautzenberg, J.H., Hijink, J.A.W. and van der Wolf, A.C.H., 1982. The minimum energy principle applied to the cutting process of various workpiece materials and tool rake angles. *CIRP annals,* 31(1), pp.91-96. doi: 10.1016/S0007-8506(07)63275-2.

Deshmukh, A.A., Liepmann, D. and Pisano, A.P., 2000, June. Continuous micromixer with pulsatile micropumps. *In Technical Digest of the IEEE Solid State Sensor and Actuator Workshop* (Hilton Head Island, SC) (Vol. 736).

Ding, H., Ibrahim, R., Cheng, K. and Chen, S.J., 2010. Experimental study on machinability improvement of hardened tool steel using two dimensional vibration-assisted micro-end-milling. *International Journal of Machine Tools and Manufacture*, 50(12), pp.1115-1118. doi: 10.1016/j.ijmachtools.2010.08.010.

Ding, H., Chen, S.J., Ibrahim, R. and Cheng, K., 2011. Investigation of the size effect on burr formation in two-dimensional vibration-assisted micro end milling. *Proceedings of the*

Institution of Mechanical Engineers, Part B: Journal of Engineering Manufacture, 225(11), pp.2032-2039. doi: 10.1177/0954405411400820.

Ding, H., Chen, S.J. and Cheng, K., 2010. Two-dimensional vibration-assisted micro end milling: cutting force modelling and machining process dynamics. *Proceedings of the Institution of Mechanical Engineers, Part B: Journal of Engineering Manufacture*, 224(12), pp.1775-1783. doi: 10.1243/09544054JEM1984.

Ding, H., Chen, S.J. and Cheng, K., 2011. Dynamic surface generation modeling of two-dimensional vibration-assisted micro-end-milling. *The International Journal of Advanced Manufacturing Technology*, 53(9-12), pp.1075-1079. doi: 10.1007/s00170-010-2903-0.

Ding, K., Fu, Y., Su, H., Chen, Y., Yu, X. and Ding, G., 2014. Experimental studies on drilling tool load and machining quality of C/SiC composites in rotary ultrasonic machining. *Journal of Materials Processing Technology*, 214(12), pp.2900-2907. doi: 10.1016/j.jmatprotec.2014.06.015.

Dong, G., Zhang, H., Zhou, M. and Zhang, Y., 2013. Experimental investigation on ultrasonic vibration-assisted turning of SiCp/Al composites. *Materials and manufacturing processes*, 28(9), pp.999-1002. doi: 10.1080/10426914.2012.709338.

Dvivedi, A. and Kumar, P., 2007. Surface quality evaluation in ultrasonic drilling through the Taguchi technique. *The International Journal of Advanced Manufacturing Technology*, 34(1-2), pp.131-140. doi: 10.1007/s00170-006-0586-3.

Ezugwu, E.O., Bonney, J. and Yamane, Y., 2003. An overview of the machinability of aeroengine alloys. J*ournal of materials processing technology*, 134(2), pp.233-253. doi: 10.1016/S0924-0136(02)01042-7.

Feng, X.J. and Jiang, L., 2006. Design and creation of superwetting/antiwetting surfaces. *Advanced Materials*, 18(23), pp.3063-3078. doi: 10.1002/adma.200501961.

Firincioglu, T., Blunt, M.J. and Zhou, D., 1999. Three-phase flow and wetability effects in triangular capillaries. *Colloids and Surfaces A: Physicochemical and Engineering Aspects,* 155(2-3), pp.259-276. doi: 10.1016/S0927-7757(99)00039-4.

Fleming, A.J., 2009. Nanopositioning system with force feedback for high-performance tracking and vibration control. *IEEE/Asme Transactions on Mechatronics*, 15(3), pp.433-447. doi: 10.1109/TMECH.2009.2028422.

F Fujii, T., Sando, Y., Higashino, K. and Fujii, Y., 2003. A plug and play microfluidic device. *Lab on a Chip*, 3(3), pp.193-197. doi: 10.1039/b301410j.

Li, G., 2012. Non-resonant vibration auxiliary table development and study on micro-milling technology experiment [D]. *Harbin institute of technology*.

Geng, D., Zhang, D., Xu, Y., He, F., Liu, D. and Duan, Z., 2015. Rotary ultrasonic elliptical machining for side milling of CFRP: Tool performance and surface integrity. *Ultrasonics*, 59, pp.128-137. doi: 10.1016/j.ultras.2015.02.006.

Geoffrey, B. and Winston, A. K., 1989. Fundamentals of Machining and Machine Tools, *Machining: Fundamentals and Recent Advances*. doi: 10.1007/978-1-84800-213-5.

Gillespie, L. K. and Blotter, P. T., 1976. The Formation and Properties of Machining Burrs, *Journal of Engineering for Industry*, 98(1), p. 66. doi: 10.1115/1.3438875.

Greco, A., Raphaelson, S., Ehmann, K., Wang, Q.J. and Lin, C., 2009. Surface texturing of tribological interfaces using the vibromechanical texturing method. *Journal of manufacturing science and engineering*, 131(6). doi: 10.1115/1.4000418.

Grover, W.H., Ivester, R.H., Jensen, E.C. and Mathies, R.A., 2006. Development and multiplexed control of latching pneumatic valves using microfluidic logical structures. *Lab on a Chip*, 6(5), pp.623-631. doi: 10.1039/b518362f.

Guckenberger, D.J., de Groot, T.E., Wan, A.M., Beebe, D.J. and Young, E.W., 2015. Micromilling: a method for ultra-rapid prototyping of plastic microfluidic devices. *Lab on a Chip*, 15(11), pp.2364-2378. doi: 10.1039/c5lc00234f.

Gui, L. and Liu, J., 2004. Ice valve for a mini/micro flow channel. *Journal of Micromechanics and Microengineering*, 14(2), p.242. doi: 10.1088/0960-1317/14/2/011.

Guo, J., Suzuki, H., MORITA, S., Yamagata, Y. and Higuchi, T., 2012. Micro polishing of tungsten carbide using magnetostrictive vibrating polisher. In *Key Engineering Materials* (Vol.

516, pp. 569-574). Trans Tech Publications Ltd. doi: 10.4028/www.scientific.net/KEM.516.569.

Guo, J., Morita, S.Y., Hara, M., Yamagata, Y. and Higuchi, T., 2012. Ultra-precision finishing of micro-aspheric mold using a magnetostrictive vibrating polisher. *CIRP annals*, *61*(1), pp.371-374.. 371–374. doi: 10.1016/j.cirp.2012.03.141.

Guo, J., Suzuki, H. and Higuchi, T., 2013. Development of micro polishing system using a magnetostrictive vibrating polisher. *Precision Engineering*, *37*(1), pp.81-87. doi: 10.1016/j.precisioneng.2012.07.003.

Guo, P., Lu, Y., Ehmann, K.F. and Cao, J., 2014. Generation of hierarchical micro-structures for anisotropic wetting by elliptical vibration cutting. *CIRP Annals*, *63*(1), pp.553-556. doi: 10.1016/j.cirp.2014.03.048.

Guo, P. and Ehmann, K.F., 2013. An analysis of the surface generation mechanics of the elliptical vibration texturing process. *International Journal of Machine Tools and Manufacture*, *64*, pp.85-95. doi: 10.1016/j.ijmachtools.2012.08.003.

Guo, P. and Ehmann, K.F., 2013. Development of a tertiary motion generator for elliptical vibration texturing. *Precision Engineering*, *37*(2), pp.364-371. doi: 10.1016/j.precisioneng.2012.10.005.

Hadad, M. and Ramezani, M., 2016. Modeling and analysis of a novel approach in machining and structuring of flat surfaces using face milling process. *International Journal of Machine Tools and Manufacture*, *105*, pp.32-44. doi: 10.1016/j.ijmachtools.2016.03.005.

Haidong, Z., Ping, Z., Wenbin, M. and Zhongming, Z., 2016. A study on ultrasonic elliptical vibration cutting of Inconel 718. *Shock and Vibration*, *2016*. doi: 10.1155/2016/3638574.

Hartshorne, H., Backhouse, C.J. and Lee, W.E., 2004. Ferrofluid-based microchip pump and valve. *Sensors and Actuators B: Chemical*, *99*(2-3), pp.592-600. doi: 10.1016/j.snb.2004.01.016.

Hatt, O., Crawforth, P. and Jackson, M., 2017. On the mechanism of tool crater wear during titanium alloy machining. *Wear*, *374*, pp.15-20. doi: 10.1016/j.wear.2016.12.036.

Hessel, V., Löwe, H. and Schönfeld, F., 2005. Micromixers—a review on passive and active mixing principles. *Chemical Engineering Science*, *60*(8-9), pp.2479-2501. doi: 10.1016/j.ces.2004.11.033.

Hong, M.S. and Ehmann, K.F., 1995. Generation of engineered surfaces by the surface-shaping system. *International Journal of Machine Tools and Manufacture*, *35*(9), pp.1269-1290. doi: 10.1016/0890-6955(94)00114-Y.

Hsu, C.Y., Huang, C.K. and Wu, C.Y., 2007. Milling of MAR-M247 nickel-based superalloy with high temperature and ultrasonic aiding. *The International Journal of Advanced Manufacturing Technology*, *34*(9-10), pp.857-866. pp. 857–866. doi: 10.1007/s00170-006-0657-5.

Hsu, I. and Tsao, C.C., 2009. Study on the effect of frequency tracing in ultrasonic-assisted drilling of titanium alloy. *The International Journal of Advanced Manufacturing Technology*, *43*(1-2), p.127. doi: 10.1007/s00170-008-1696-x.

Huo, D., Lin, C., Choong, Z.J., Pancholi, K. and Degenaar, P., 2015. Surface and subsurface characterisation in micro-milling of monocrystalline silicon. *The International Journal of Advanced Manufacturing Technology*, *81*(5-8), pp.1319-1331. doi: 10.1007/s00170-015-7308-7.

Huo, D., Lin, C. and Dalgarno, K., 2014. An experimental investigation on micro machining of fine-grained graphite. *The International Journal of Advanced Manufacturing Technology*, *72*(5-8), pp.943-953. doi: 10.1007/s00170-014-5730-x.

I Ibrahim, R., 2010. *Vibration assisted machining: Modelling, simulation, optimization, control and applications* (Doctoral dissertation, Brunel University School of Engineering and Design PhD Theses).

Janghorbanian, J., Razfar, M.R. and Abootorabi Zarchi, M.M., 2013. Effect of cutting speed on tool life in ultrasonic-assisted milling process. *Proceedings of the Institution of Mechanical Engineers, Part B: Journal of Engineering Manufacture*, *227*(8), pp.1157-1164. doi: 10.1177/0954405413483722.

Janghorbanian, J., Razfar, M.R. and Abootorabi Zarchi, M.M., 2013. Effect of cutting speed on tool life in ultrasonic-assisted milling process. *Proceedings of the Institution of Mechanical*

Engineers, Part B: Journal of Engineering Manufacture, *227*(8), pp.1157-1164. doi: 10.1177/0954405413483722.

Jawaid, A., Sharif, S. and Koksal, S., 2000. Evaluation of wear mechanisms of coated carbide tools when face milling titanium alloy. *Journal of Materials Processing Technology*, *99*(1-3), pp.266-274. doi: 10.1016/S0924-0136(99)00438-0.

J Jen, C.P., Wu, C.Y., Lin, Y.C. and Wu, C.Y., 2003. Design and simulation of the micromixer with chaotic advection in twisted microchannels. *Lab on a Chip*, *3*(2), pp.77-81. doi: 10.1039/b211091a.

Jieqiong, L., Yingchun, L. and Xiaoqin, Z., 2014. Tool path generation for fabricating optical freeform surfaces by non-resonant three-dimensional elliptical vibration cutting. *Proceedings of the Institution of Mechanical Engineers, Part C: Journal of Mechanical Engineering Science*, *228*(7), pp.1208-1222. doi: 10.1177/0954406213502448.

Jin, X. and Xie, B., 2015. Experimental study on surface generation in vibration-assisted micro-milling of glass. *The International Journal of Advanced Manufacturing Technology*, *81*(1-4), pp.507-512. doi: 10.1007/s00170-015-7211-2.

Johnson, T.J., Ross, D. and Locascio, L.E., 2002. Rapid microfluidic mixing. *Analytical chemistry*, *74*(1), pp.45-51. doi: 10.1021/ac010895d.

Jung, Y.C. and Bhushan, B., 2006. Contact angle, adhesion and friction properties of micro- and nanopatterned polymers for superhydrophobicity. *Nanotechnology*, *17*(19), p.4970. doi: 10.1088/0957-4484/17/19/033.

Kanemitsu, Y., Uto, H., Masumoto, Y., Matsumoto, T., Futagi, T. and Mimura, H., 1993. Microstructure and optical properties of free-standing porous silicon films: Size dependence of absorption spectra in Si nanometer-sized crystallites. *Physical review B*, *48*(4), p.2827. doi: 10.1103/PhysRevB.48.2827.

Kim, G.D. and Loh, B.G., 2007. An ultrasonic elliptical vibration cutting device for micro V-groove machining: Kinematical analysis and micro V-groove machining characteristics. *Journal of materials processing technology*, *190*(1-3), pp.181-188. doi: 10.1016/j.jmatprotec.2007.02.047.

Kim, G.D. and Loh, B.G., 2007. Characteristics of chip formation in micro V-grooving using elliptical vibration cutting. *Journal of micromechanics and microengineering*, *17*(8), p.1458. doi: 10.1088/0960-1317/17/8/007.

Kim, G.D. and Loh, B.G., 2010. Machining of micro-channels and pyramid patterns using elliptical vibration cutting. *The International Journal of Advanced Manufacturing Technology*, *49*(9-12), pp.961-968. doi: 10.1007/s00170-009-2451-7.

Kim, H.S., Kim, S.I., Lee, K.I., Lee, D.H., Bang, Y.B. and Lee, K.I., 2009. Development of a programmable vibration cutting tool for diamond turning of hardened mold steels. *The International Journal of Advanced Manufacturing Technology*, *40*(1-2), pp.26-40. doi: 10.1007/s00170-007-1311-6.

Kim, J.D. and Choi, I.H., 1997. Micro surface phenomenon of ductile cutting in the ultrasonic vibration cutting of optical plastics. *Journal of materials processing technology*, *68*(1), pp.89-98. doi: 10.1016/S0924-0136(96)02546-0.

Kim, T.I. and Suh, K.Y., 2009. Unidirectional wetting and spreading on stooped polymer nanohairs. *Soft Matter*, *5*(21), pp.4131-4135. doi: 10.1039/b915079j.

Klimant, P., Witt, M. and Kuhl, M., 2014. CAD kernel based simulation of milling processes. *Procedia CIRP*, *17*, pp.710-715. doi: 10.1016/j.procir.2014.01.042.

Kong, X., Zhang, L., Dong, J. and Cohen, P.H., 2015, June. Machining force modeling of vibration-assisted nano-machining process. In *International Manufacturing Science and Engineering Conference* (Vol. 56833, p. V002T01A005). American Society of Mechanical Engineers. doi: 10.1115/MSEC20159423.

Kong, X., Dong, J. and Cohen, P.H., 2017. Modeling of the dynamic machining force of vibration-assisted nanomachining process. *Journal of Manufacturing Processes*, *28*, pp.101-108. doi: 10.1016/j.jmapro.2017.05.028.

Koseki, Y., Tanikawa, T., Koyachi, N. and Arai, T., 2002. Kinematic analysis of a translational 3-dof micro-parallel mechanism using the matrix method. *Advanced Robotics*, *16*(3), pp.251-264. doi: 10.1163/156855302760121927.

Kuhnen, K., 2003. Modeling, identification and compensation of complex hysteretic nonlinearities: A modified Prandtl-Ishlinskii approach. *European journal of control*, *9*(4), pp.407-418. doi: 10.3166/ejc.9.407-418.

Kumar, M.N., Subbu, S.K., Krishna, P.V. and Venugopal, A., 2014. Vibration assisted conventional and advanced machining: A review. *Procedia Engineering*, *97*, pp.1577-1586. doi: 10.1016/j.proeng.2014.12.441.

Kumar, S., Wu, C.S., Padhy, G.K. and Ding, W., 2017. Application of ultrasonic vibrations in welding and metal processing: a status review. *Journal of Manufacturing Processes*, *26*, pp.295-322. doi: 10.1016/j.jmapro.2017.02.027.

Kuo, K.L., 2008. Design of rotary ultrasonic milling tool using FEM simulation. *Journal of Materials Processing Technology*, *201*(1-3), pp.48-52. doi: 10.1016/j.jmatprotec.2007.11.289.

Kurniawan, R., Ko, T.J., Ping, L.C., Kumaran, S.T., Kiswanto, G., Guo, P. and Ehmann, K.F., 2017. Development of a two-frequency, elliptical-vibration texturing device for surface texturing. *Journal of Mechanical Science and Technology*, *31*(7), pp.3465-3473. doi: 10.1007/s12206-017-0635-x.

Kurosawa, M.K., Kodaira, O., Tsuchitoi, Y. and Higuchi, T., 1998. Transducer for high speed and large thrust ultrasonic linear motor using two sandwich-type vibrators. *IEEE transactions on ultrasonics, ferroelectrics, and frequency control*, *45*(5), pp.1188-1195. doi: 10.1109/58.726442.

Leang, K.K. and Devasia, S., 2007. Feedback-linearized inverse feedforward for creep, hysteresis, and vibration compensation in AFM piezoactuators. *IEEE Transactions on Control Systems Technology*, *15*(5), pp.927-935. doi: 10.1109/TCST.2007.902956.

Lee, D.Y., Kim, D.M., Gweon, D.G. and Park, J., 2007. A calibrated atomic force microscope using an orthogonal scanner and a calibrated laser interferometer. *Applied surface science*, *253*(8), pp.3945-3951. doi: 10.1016/j.apsusc.2006.08.027.

Lee, J.B., Gwon, H.R., Lee, S.H. and Cho, M., 2010. Wetting transition characteristics on microstructured hydrophobic surfaces. *Materials transactions*, pp.1007121122-1007121122. doi: 10.2320/matertrans.M2010118.

Li, G., Wang, B., Xue, J., Qu, D. and Zhang, P., 2019. Development of vibration-assisted micro-milling device and effect of vibration parameters on surface quality and exit-burr. *Proceedings of the Institution of Mechanical Engineers, Part B: Journal of Engineering Manufacture*, *233*(6), pp.1723-1729. doi: 10.1177/0954405418774592.

Li, K.M. and Wang, S.L., 2014. Effect of tool wear in ultrasonic vibration-assisted micro-milling. *Proceedings of the Institution of Mechanical Engineers, Part B: Journal of Engineering Manufacture*, *228*(6), pp.847-855. doi: 10.1177/0954405413510514.

Ru, L. and Jierong, C., 2006. Studies of wettability of medical PVC by remote nitrogen plasma. *Plasma Science and Technology*, *8*(3), p.325. doi: 10.1088/1009-0630/8/3/17.

Li, W. and Amirfazli, A., 2005. A thermodynamic approach for determining the contact angle hysteresis for superhydrophobic surfaces. *Journal of colloid and interface science*, *292*(1), pp.195-201. doi: 10.1016/j.jcis.2005.05.062.

Li, X. and Zhang, D., 2006. Ultrasonic elliptical vibration transducer driven by single actuator and its application in precision cutting. *Journal of materials processing technology*, *180*(1-3), pp.91-95. doi: 10.1016/j.jmatprotec.2006.05.007.

Li, Y. and Xu, Q., 2009. Design and analysis of a totally decoupled flexure-based XY parallel micromanipulator. *IEEE transactions on robotics*, *25*(3), pp.645-657. doi: 10.1109/TRO.2009.2014130.

Li, Y. and Xu, Q., 2010. A totally decoupled piezo-driven XYZ flexure parallel micropositioning stage for micro/nanomanipulation. *IEEE Transactions on Automation Science and Engineering*, *8*(2), pp.265-279. doi: 10.1109/TASE.2010.2077675.

Lian, H., Guo, Z., Huang, Z., Tang, Y. and Song, J., 2013. Experimental research of Al6061 on ultrasonic vibration assisted micro-milling. *Procedia CIRP*, *6*, pp.561-564. doi: 10.1016/j.procir.2013.03.056.

Liang, Z., Wang, X., Zhao, W., Wu, Y., Sato, T. and Lin, W., 2010. A feasibility study on elliptical ultrasonic assisted grinding of sapphire substrate. *International Journal of Abrasive Technology*, *3*(3), pp.190-202. doi: 10.1504/IJAT.2010.03405.

Liang, Z., Wang, X., Wu, Y., Xie, L., Jiao, L. and Zhao, W., 2013. Experimental study on brittle–ductile transition in elliptical ultrasonic assisted grinding (EUAG) of monocrystal sapphire using single diamond abrasive grain. *International Journal of Machine Tools and Manufacture*, *71*, pp.41-51. doi: 10.1016/j.ijmachtools.2013.04.004.

Liao, H., Normand, B. and Coddet, C., 2000. Influence of coating microstructure on the abrasive wear resistance of WC/Co cermet coatings. *Surface and Coatings Technology*, *124*(2-3), pp.235-242. doi: 10.1016/S0257-8972(99)00653-2.

Lin, J., Han, J., Lu, M., Yu, B. and Gu, Y., 2017. Design, analysis and testing of a new piezoelectric tool actuator for elliptical vibration turning. *Smart Materials and Structures*, *26*(8), p.085008. doi: 10.1088/1361-665X/aa71f0.

Lin, J., Lu, M. and Zhou, X., 2016. Development of a non-resonant 3D elliptical vibration cutting apparatus for diamond turning. *Experimental techniques*, *40*(1), pp.173-183. doi: 10.1007/s40799-016-0021-0.

Liu, J., Zhang, D., Qin, L. and Yan, L., 2012. Feasibility study of the rotary ultrasonic elliptical machining of carbon fiber reinforced plastics (CFRP). *International Journal of Machine Tools and Manufacture*, *53*(1), pp.141-150. doi: 10.1016/j.ijmachtools.2011.10.007.

Liu, K., Li, X.P., Rahman, M. and Liu, X.D., 2004. A study of the cutting modes in the grooving of tungsten carbide. *The International Journal of Advanced Manufacturing Technology*, *24*(5-6), pp.321-326. doi: 10.1007/s00170-003-1565-6.

Liu, P. (2013) *Development of a new apparatus for three-dimensional elliptical vibration cutting*. Jilin University.

Liu, Y. (2015) *The Non-resonant Elliptical Vibration turning of Microstructure surface*. Jilin University.

Lobontiu, N., Paine, J.S., Garcia, E. and Goldfarb, M., 2001. Corner-filleted flexure hinges. *J. Mech. Des.*, *123*(3), pp.346-352. doi: 10.1115/1.1372190.

L Loh, B.G. and Kim, G.D., 2012. Correcting distortion and rotation direction of an elliptical trajectory in elliptical vibration cutting by modulating phase and relative magnitude of the

sinusoidal excitation voltages. *Proceedings of the Institution of Mechanical Engineers, Part B: Journal of Engineering Manufacture*, *226*(5), pp.813-823. doi: 10.1177/0954405411431375.

Lu, D., Wang, Q., Wu, Y., Cao, J. and Guo, H., 2015. Fundamental turning characteristics of Inconel 718 by applying ultrasonic elliptical vibration on the base plane. *Materials and Manufacturing Processes*, *30*(8), pp.1010-1017. doi: 10.1080/10426914.2014.973588.

Lu, M. (2014) *Development of 3D Elliptical vibration assisted cutting appratus and its control*. Jilin University.

Lu, Y., Guo, P., Pei, P. and Ehmann, K.F., 2015. Experimental studies of wettability control on cylindrical surfaces by elliptical vibration texturing. *The International Journal of Advanced Manufacturing Technology*, *76*(9-12), pp.1807-1817. doi: 10.1007/s00170-014-6384-4.

Maboudian, R. and Howe, R.T., 1997. Critical review: Adhesion in surface micromechanical structures. *Journal of Vacuum Science & Technology B: Microelectronics and Nanometer Structures Processing, Measurement, and Phenomena*, *15*(1), pp.1-20. doi: 10.1116/1.589247.

Machai, C. and Biermann, D., 2011. Machining of β-titanium-alloy Ti–10V–2Fe–3Al under cryogenic conditions: Cooling with carbon dioxide snow. *Journal of Materials Processing Technology*, *211*(6), pp.1175-1183. doi: 10.1016/j.jmatprotec.2011.01.022.

Moheimani, S. O. R. and Vautier, B. J. G. (2005) 'Resonant control of structural vibration using charge-driven piezoelectric actuators', *IEEE Transactions on Control Systems Technology*. doi: 10.1109/TCST.2005.857407.

Moheimani, S.R. and Vautier, B.J., 2005. Resonant control of structural vibration using charge-driven piezoelectric actuators. *IEEE Transactions on control systems technology*, *13*(6), pp.1021-1035. doi: 10.1115/DETC2007-35043.

Moriwaki, T. and Shamoto, E., 1995. Ultrasonic elliptical vibration cutting. *CIRP annals*, *44*(1), pp.31-34. doi: 10.1016/S0007-8506(07)62269-0.

Nakayama, K., Arai, M. and Kanda, T., 1988. Machining characteristics of hard materials. *CIRP Annals*, *37*(1), pp.89-92. doi: 10.1016/S0007-8506(07)61592-3.

Nath, C. and Rahman, M., 2008. Effect of machining parameters in ultrasonic vibration cutting. *International Journal of Machine Tools and Manufacture*, *48*(9), pp.965-974. doi: 10.1016/j.ijmachtools.2008.01.013.

Negishi, N., 2003. *Elliptical Vibration Assisted Machining with Single Crystal Diamond Tools*. North Carolina State University.

Nam-Trung, N. and Zhigang, W., 2005. Micromixers—a review. *J Micromech Microeng*, *15*(2), p.R1. doi: 10.1088/0960-1317/15/2/R01.

Ni, C. *et al.,* 2019. Research on the Characteristics of Cutting Force Signal and Chip in Ultrasonic Vibration-assisted Milling of Titanium Alloys, *Jixie Gongcheng Xuebao/Journal of Mechanical Engineering*, 55(7), pp. 207–216. doi: 10.3901/JME.2019.07.207.

Nik, M.G., Movahhedy, M.R. and Akbari, J., 2012. Ultrasonic-assisted grinding of Ti6Al4V alloy. *Procedia Cirp*, *1*(1), pp.353-358. doi: 10.1016/j.procir.2012.04.063.

Niu, X. and Lee, Y.K., 2003. Efficient spatial-temporal chaotic mixing in microchannels. *Journal of Micromechanics and microengineering*, *13*(3), p.454. doi: 10.1088/0960-1317/13/3/316.

Oh, K.W., Park, C., Namkoong, K., Kim, J., Ock, K.S., Kim, S., Kim, Y.A., Cho, Y.K. and Ko, C., 2005. World-to-chip microfluidic interface with built-in valves for multichamber chip-based PCR assays. *Lab on a Chip*, *5*(8), pp.845-850. doi: 10.1039/b503437j.

Oh, K.W., Lee, K., Ahn, B. and Furlani, E.P., 2012. Design of pressure-driven microfluidic networks using electric circuit analogy. *Lab on a Chip*, *12*(3), pp.515-545. doi: 10.1039/c2lc20799k.

Ostasevicius, V., Gaidys, R., Dauksevicius, R. and Mikuckyte, S., 2013. Study of vibration milling for improving surface finish of difficult-to-cut materials. *Strojniški vestnik-Journal of Mechanical Engineering*, *59*(6), pp.351-357. doi: 10.5545/sv-jme.2012.856.

El Moctar, A.O., Aubry, N. and Batton, J., 2003. Electro-hydrodynamic micro-fluidic mixer. *Lab on a Chip*, *3*(4), pp.273-280. doi: 10.1039/b306868b.

Ouyang, J.H., Sasaki, S. and Umeda, K., 2002. The friction and wear characteristics of low-pressure plasma-sprayed ZrO2-BaCrO4 composite coating at elevated temperatures. *Surface and Coatings Technology*, *154*(2-3), pp.131-139. doi: 10.1016/S0257-8972(02)00024-5.

Pal, R., Yang, M., Johnson, B.N., Burke, D.T. and Burns, M.A., 2004. Phase change microvalve for integrated devices. *Analytical chemistry*, *76*(13), pp.3740-3748. doi: 10.1021/ac0352934.

Park, C.I., Jeong, H.E., Lee, S.H., Cho, H.S. and Suh, K.Y., 2009. Wetting transition and optimal design for microstructured surfaces with hydrophobic and hydrophilic materials. *Journal of colloid and interface science*, *336*(1), pp.298-303. doi: 10.1016/j.jcis.2009.04.022.

Pecat, O. and Brinksmeier, E., 2014. Tool wear analyses in low frequency vibration assisted drilling of CFRP/Ti6Al4V stack material. *Procedia Cirp*, *14*(14), pp.142-147. doi: 10.1016/j.procir.2014.03.050.

Peng, Y., Liang, Z., Wu, Y., Guo, Y. and Wang, C., 2012. Characteristics of chip generation by vertical elliptic ultrasonic vibration-assisted grinding of brittle materials. *The International Journal of Advanced Manufacturing Technology*, *62*(5-8), pp.563-568. doi: 10.1007/s00170-011-3839-8.

Pham, H.H. and Chen, I.M., 2005. Stiffness modeling of flexure parallel mechanism. *Precision Engineering*, *29*(4), pp.467-478. doi: 10.1016/j.precisioneng.2004.12.006.

P Piquard, R., d'Acunto, A., Laheurte, P. and Dudzinski, D., 2014. Micro-end milling of NiTi biomedical alloys, burr formation and phase transformation. *Precision Engineering*, *38*(2), pp.356-364. doi: 10.1016/j.precisioneng.2013.11.006.

Pit, R., Hervet, H. and Leger, L., 2000. Direct experimental evidence of slip in hexadecane: solid interfaces. *Physical review letters*, *85*(5), p.980. doi: 10.1103/PhysRevLett.85.980.

Qin, N., Pei, Z.J. and Guo, D.M., 2009, January. Ultrasonic-Vibration-Assisted Grinding of Titanium: Cutting Force Modeling With Design of Experiments. In *International Manufacturing Science and Engineering Conference* (Vol. 43628, pp. 619-624). doi: 10.1115/MSEC2009-84325.

Razi, S., Mollabashi, M. and Madanipour, K., 2015. Laser processing of metallic biomaterials: An approach for surface patterning and wettability control. *The European Physical Journal Plus*, *130*(12), p.247. doi: 10.1140/epjp/i2015-15247-5.

Ribeiro, M.V., Moreira, M.R.V. and Ferreira, J.R., 2003. Optimization of titanium alloy (6Al–4V) machining. *Journal of materials processing technology*, *143*, pp.458-463. doi: 10.1016/S0924-0136(03)00457-6.

Yan, J., Murakami, Y. and Davim, J.P., 2009. Tool design, tool wear and tool life. In *Machining dynamics* (pp. 117-149). Springer, London.

R Roy, S., 2017. Design of a circular hollow ultrasonic horn for USM using finite element analysis. *The International Journal of Advanced Manufacturing Technology*, *93*(1-4), pp.319-328. doi: 10.1007/s00170-016-8985-6.

Rukosuyev, M.V., Lee, J., Cho, S.J., Lim, G. and Jun, M.B., 2014. One-step fabrication of superhydrophobic hierarchical structures by femtosecond laser ablation. *Applied surface science*, *313*, pp.411-417. doi: 10.1016/j.apsusc.2014.05.224.

Ryu, J.W., Lee, S.Q., Gweon, D.G. and Moon, K.S., 1999. Inverse kinematic modeling of a coupled flexure hinge mechanism. *Mechatronics*, *9*(6), pp.657-674. doi: 10.1016/S0957-4158(99)00006-9.

Sadik, M.I., Isakson, S., Malakizadi, A. and Nyborg, L., 2016. Influence of coolant flow rate on tool life and wear development in cryogenic and wet milling of Ti-6Al-4V. *Procedia CIRP*, *46*(1), pp.91-94. doi: 10.1016/j.procir.2016.02.014.

Satarkar, N.S., Zhang, W., Eitel, R.E. and Hilt, J.Z., 2009. Magnetic hydrogel nanocomposites as remote controlled microfluidic valves. *Lab on a Chip*, *9*(12), pp.1773-1779. doi: 10.1039/b822694f.

Shabgard, M.R., Badamchizadeh, M.A., Ranjbary, G. and Amini, K., 2013. Fuzzy approach to select machining parameters in electrical discharge machining (EDM) and ultrasonic-assisted EDM processes. *Journal of Manufacturing Systems*, *32*(1), pp.32-39. doi: 10.1016/j.jmsy.2012.09.002.

Shamoto, E., Suzuki, N., Moriwaki, T. and Naoi, Y., 2002. Development of ultrasonic elliptical vibration controller for elliptical vibration cutting. *CIRP Annals*, *51*(1), pp.327-330. doi: 10.1016/S0007-8506(07)61528-5.

Shamoto, E., Suzuki, N., Hino, R., Tsuchiya, E., Hori, Y., Inagaki, H. and Yoshino, K., 2005, November. A new method to machine sculptured surfaces by applying ultrasonic elliptical vibration cutting. In *IEEE International Symposium on Micro-NanoMechatronics and Human Science, 2005* (pp. 91-96). IEEE. doi: 10.1109/MHS.2005.1589969.

Shamoto, E., Suzuki, N., Tsuchiya, E., Hori, Y., Inagaki, H. and Yoshino, K., 2005. Development of 3 DOF ultrasonic vibration tool for elliptical vibration cutting of sculptured surfaces. *CIRP annals*, *54*(1), pp.321-324. doi: 10.1016/S0007-8506(07)60113-9.

Shamoto, E. and Moriwaki, T., 1994. Study on elliptical vibration cutting. *CIRP annals*, *43*(1), pp.35-38. doi: 10.1016/S0007-8506(07)62158-1.

Shamoto, E. and Moriwaki, T., 1999. Ultaprecision diamond cutting of hardened steel by applying elliptical vibration cutting. *CIRP Annals*, *48*(1), pp.441-444. doi: 10.1016/S0007-8506(07)63222-3.

Shamoto, E., Suzuki, N. and Hino, R., 2008. Analysis of 3D elliptical vibration cutting with thin shear plane model. *CIRP annals*, *57*(1), pp.57-60. doi: 10.1016/j.cirp.2008.03.073.

Sharman, A.R.C., Hughes, J.I. and Ridgway, K., 2015. The effect of tool nose radius on surface integrity and residual stresses when turning Inconel 718™. *Journal of Materials Processing Technology*, *216*, pp.123-132. doi: 10.1016/j.jmatprotec.2014.09.002.

Shen, J.Y., Wang, J.Q., Jiang, B. and Xu, X.P., 2015. Study on wear of diamond wheel in ultrasonic vibration-assisted grinding ceramic. *Wear*, *332*, pp.788-793. doi: 10.1016/j.wear.2015.02.047.

Shen, X.H., Zhang, J.H., Yin, T.J. and Dong, C.J., 2010. A study on cutting force in micro end milling with ultrasonic vibration. In *Advanced Materials Research* (Vol. 97, pp. 1910-1914). Trans Tech Publications Ltd. doi: 10.4028/www.scientific.net/AMR.97-101.1910.

Shen, X.H., Zhang, J., Xing, D.X. and Zhao, Y., 2012. A study of surface roughness variation in ultrasonic vibration-assisted milling. *The International Journal of Advanced Manufacturing Technology*, *58*(5-8), pp.553-561. doi: 10.1007/s00170-011-3399-y.

Shen, X.H., Zhang, J.H., Li, H., Wang, J.J. and Wang, X.C., 2012. Ultrasonic vibration-assisted milling of aluminum alloy. *The International Journal of Advanced Manufacturing Technology*, *63*(1-4), pp.41-49. doi: 10.1007/s00170-011-3882-5.

Shiou, F.J. and Ciou, H.S., 2008. Ultra-precision surface finish of the hardened stainless mold steel using vibration-assisted ball polishing process. *International Journal of Machine Tools and Manufacture*, *48*(7-8), pp.721-732. doi: 10.1016/j.ijmachtools.2008.01.001.

da Silva, L.C., da Mota, P.R., da Silva, M.B., Ezugwu, E.O. and Machado, Á.R., 2015. Study of burr behavior in face milling of PH 13-8 Mo stainless steel. *CIRP Journal of Manufacturing Science and Technology*, *8*, pp.34-42. doi: 10.1016/j.cirpj.2014.10.003.

da Silva, R.B., Machado, Á.R., Ezugwu, E.O., Bonney, J. and Sales, W.F., 2013. Tool life and wear mechanisms in high speed machining of Ti–6Al–4V alloy with PCD tools under various coolant pressures. *Journal of Materials Processing Technology*, *213*(8), pp.1459-1464. doi: 10.1016/j.jmatprotec.2013.03.008.

Sinn, G., Zettl, B., Mayer, H. and Stanzl-Tschegg, S., 2005. Ultrasonic-assisted cutting of wood. *Journal of Materials Processing Technology*, *170*(1-2), pp.42-49. doi: 10.1016/j.jmatprotec.2005.04.076.

Sommers, A.D. and Jacobi, A.M., 2006. Creating micro-scale surface topology to achieve anisotropic wettability on an aluminum surface. *Journal of Micromechanics and Microengineering*, *16*(8), p.1571. doi: 10.1088/0960-1317/16/8/018.

Song, D., Zhao, J., Ji, S. and Zhou, X., 2016. Development of a novel two-dimensional ultrasonically actuated polishing process. *AIP Advances*, *6*(11), p.115105. doi: 10.1063/1.4967292.

Stroock, A.D., Dertinger, S.K., Ajdari, A., Mezić, I., Stone, H.A. and Whitesides, G.M., 2002. Chaotic mixer for microchannels. *Science*, *295*(5555), pp.647-651. doi: 10.1126/science.1066238.

Studer, V., Hang, G., Pandolfi, A., Ortiz, M., French Anderson, W. and Quake, S.R., 2004. Scaling properties of a low-actuation pressure microfluidic valve. *Journal of applied physics*, *95*(1), pp.393-398. doi: 10.1063/1.1629781.

Suárez, A., Veiga, F., de Lacalle, L.N.L., Polvorosa, R., Lutze, S. and Wretland, A., 2016. Effects of ultrasonics-assisted face milling on surface integrity and fatigue life of Ni-Alloy 718. *Journal of Materials Engineering and Performance*, *25*(11), pp.5076-5086. doi: 10.1007/s11665-016-2343-6.

Sutter, G. and List, G., 2013. Very high speed cutting of Ti–6Al–4V titanium alloy–change in morphology and mechanism of chip formation. *International Journal of Machine Tools and Manufacture*, *66*, pp.37-43. doi: 10.1016/j.ijmachtools.2012.11.004.

Suzuki, H., Moriwaki, T., Okino, T. and Ando, Y., 2006. Development of ultrasonic vibration assisted polishing machine for micro aspheric die and mold. *CIRP annals*, *55*(1), pp.385-388. doi: 10.1016/S0007-8506(07)60441-7.

Suzuki, H., Hamada, S., Okino, T., Kondo, M., Yamagata, Y. and Higuchi, T., 2010. Ultraprecision finishing of micro-aspheric surface by ultrasonic two-axis vibration assisted polishing. *CIRP annals*, *59*(1), pp.347-350. doi: 10.1016/j.cirp.2010.03.117.

Suzuki, H., Marshall, M.B., Sims, N.D. and Dwyer-Joyce, R.S., 2017. Design and implementation of a non-resonant vibration-assisted machining device to create bespoke surface textures. *Proceedings of the Institution of Mechanical Engineers, Part C: Journal of Mechanical Engineering Science*, *231*(5), pp.860-875. doi: 10.1177/0954406215625087.

Suzuki, N., Yan, Z., Hino, R., Shamoto, E., Hirahara, Y. and Imasuda, T., 2006, November. Ultraprecision micro-machining of single crystal germanium by applying elliptical vibratlon cutting. In *2006 IEEE International Symposium on MicroNanoMechanical and Human Science* (pp. 1-6). IEEE. doi: 10.1109/MHS.2006.320323.

Suzuki, N., Haritani, M., Yang, J.B., Hino, R. and Shamoto, E., 2007. Elliptical vibration cutting of tungsten alloy molds for optical glass parts. *CIRP annals*, *56*(1), pp.127-130. doi: 10.1016/j.cirp.2007.05.032.

Suzuki, N., Hino, R. and Shamoto, E., 2007, April. Development of 3 DOF ultrasonic elliptical vibration system for elliptical vibration cutting. In *Proceedings of ASPE Spring Topical Meeting on Vibration Assisted Machining Technology* (pp. 15-20).

Syahputra, H.P., Ko, T.J. and Chung, B.M., 2014. Development of 2-axis hybrid positioning system for precision contouring on micro-milling operation. *Journal of Mechanical Science and Technology*, *28*(2), pp.691-697. doi: 10.1007/s12206-013-1132-5.

Tan, R., Zhao, X., Zou, X. and Sun, T., 2018. A novel ultrasonic elliptical vibration cutting device based on a sandwiched and symmetrical structure. *The International Journal of Advanced Manufacturing Technology*, *97*(1-4), pp.1397-1406. doi: 10.1007/s00170-018-2015-9.

Tang, H. and Li, Y., 2013. Design, analysis, and test of a novel 2-DOF nanopositioning system driven by dual mode. *IEEE Transactions on Robotics*, *29*(3), pp.650-662. doi: 10.1109/TRO.2013.2248536.

Tao, G., Ma, C., Bai, L., Shen, X. and Zhang, J., 2017. Feed-direction ultrasonic vibration−assisted milling surface texture formation. *Materials and Manufacturing Processes*, *32*(2), pp.193-198. doi: 10.1080/10426914.2016.1198029.

Teng, X., Huo, D., Shyha, I., Chen, W. and Wong, E., 2018. An experimental study on tool wear behaviour in micro milling of nano Mg/Ti metal matrix composites. *The International Journal of Advanced Manufacturing Technology*, *96*(5-8), pp.2127-2140. doi: 10.1007/s00170-018-1672-z.

Thoe, T.B., Aspinwall, D.K. and Wise, M.L.H., 1998. Review on ultrasonic machining. *International journal of machine tools and manufacture*, *38*(4), pp.239-255.

Ton, T.P., Park, H.Y. and Ko, S.L., 2011. Experimental analysis of deburring process on inclined exit surface by new deburring tool. *CIRP annals*, *60*(1), pp.129-132. doi: 10.1016/j.cirp.2011.03.124.

Topuz, F., Möller, M. and Groll, J., 2015. Covalently layer-by-layer assembled homogeneous nanolayers with switchable wettability. *Polymer Chemistry*, *6*(25), pp.4690-4697. doi: 10.1039/C5PY00515A.

Tretheway, D.C. and Meinhart, C.D., 2004. A generating mechanism for apparent fluid slip in hydrophobic microchannels. *Physics of Fluids*, *16*(5), pp.1509-1515. doi: 10.1063/1.1669400.

Uhlmanna, E. and Domingosa, D.C., 2016. Investigations on vibration-assisted EDM-machining of seal slots in high-temperature resistant materials for turbine components–part II. *Energy*, *1000*, p.0. doi: 10.1016/j.procir.2016.02.179.

Ulutan, D. and Ozel, T., 2011. Machining induced surface integrity in titanium and nickel alloys: A review. *International Journal of Machine Tools and Manufacture*, *51*(3), pp.250-280. doi: 10.1016/j.ijmachtools.2010.11.003.

Hessel, V., Löwe, H. and Schönfeld, F., 2005. Micromixers—a review on passive and active mixing principles. *Chemical Engineering Science*, *60*(8-9), pp.2479-2501.

Wang, G., 2012. *Development of a Three-dimentional elliptical vibration assisted Diamond Cutting Apparatus*. Harbin Institute of Technology.

Wang, G., Zhou, X., Ma, P., Wang, R., Meng, G. and Yang, X., 2018. A novel vibration assisted polishing device based on the flexural mechanism driven by the piezoelectric actuators. *AIP Advances*, *8*(1), p.015012. doi: 10.1063/1.5009027.

Wang, J., Chen, Z., Mauk, M., Hong, K.S., Li, M., Yang, S. and Bau, H.H., 2005. Self-actuated, thermo-responsive hydrogel valves for lab on a chip. *Biomedical microdevices*, *7*(4), pp.313-322. doi: 10.1007/s10544-005-6073-z.

Wang, S., Wang, T., Ge, P., Xue, P., Ye, S., Chen, H., Li, Z., Zhang, J. and Yang, B., 2015. Controlling flow behavior of water in microfluidics with a chemically patterned anisotropic wetting surface. *Langmuir*, *31*(13), pp.4032-4039. doi: 10.1021/acs.langmuir.5b00328.

Wang, T., Chen, H., Liu, K., Li, Y., Xue, P., Yu, Y., Wang, S., Zhang, J., Kumacheva, E. and Yang, B., 2014. Anisotropic Janus Si nanopillar arrays as a microfluidic one-way valve for gas–liquid separation. *Nanoscale*, *6*(7), pp.3846-3853. doi: 10.1039/c3nr05865d.

Weinert, K., Kersting, P., Surmann, T. and Biermann, D., 2008. Modeling regenerative workpiece vibrations in five-axis milling. *Production Engineering*, *2*(3), p.255. doi: 10.1007/s11740-008-0113-5.

Wenzel, R.N., 1936. Resistance of solid surfaces to wetting by water. *Industrial & Engineering Chemistry*, *28*(8), pp.988-994. doi: 10.1021/ie50320a024.

Xu, C.N., Akiyama, M., Nonaka, K. and Watanabe, T., 1998. Electrical power generation characteristics of PZT piezoelectric ceramics. *IEEE transactions on ultrasonics, ferroelectrics, and frequency control*, *45*(4), pp.1065-1070.

Xu, M.G., Zhang, J.H., Li, Y., Zhang, Q.H. and Ren, S.F., 2009. Material removal mechanisms of cemented carbides machined by ultrasonic vibration assisted EDM in gas medium. *Journal of materials processing technology*, *209*(4), pp.1742-1746. doi: 10.1016/j.jmatprotec.2008.04.031.

Xu, W.X. and Zhang, L.C., 2015. Ultrasonic vibration-assisted machining: principle, design and application. *Advances in Manufacturing*, *3*(3), pp.173-192. doi: 10.1007/s40436-015-0115-4.

Yadav, A.K., Bajpai, V., Singh, N.K. and Singh, R.K., 2017. FE modeling of burr size in high-speed micro-milling of Ti6Al4V. *Precision Engineering*, *49*, pp.287-292. doi: 10.1016/j.precisioneng.2017.02.017.

Yamahata, C., Chastellain, M., Parashar, V.K., Petri, A., Hofmann, H. and Gijs, M.A., 2005. Plastic micropump with ferrofluidic actuation. *Journal of microelectromechanical systems*, *14*(1), pp.96-102. doi: 10.1109/JMEMS.2004.839007.

ISO/TC 29/SC 9 Tools with defined cutting edges, holding tools, cutting items, adaptive items and interfaces, 2013. ISO 7755-1:2013 Hardmetal burrs - Part 1: General specifications. *International Organization for Standardization*. Geneva, Switzerland.

Yang, H.C., Chen, Y.F., Ye, C., Jin, Y.N., Li, H. and Xu, Z.K., 2015. Polymer membrane with a mineral coating for enhanced curling resistance and surface wettability. *Chemical Communications*, *51*(64), pp.12779-12782. doi: 10.1039/C5CC03216D.

Li, Y. and Xu, Q., 2009. Design and analysis of a totally decoupled flexure-based XY parallel micromanipulator. *IEEE transactions on robotics*, *25*(3), pp.645-657. doi: 10.1109/tro.2009.2014130.

Yanyan, Y., Bo, Z. and Junli, L., 2009. Ultraprecision surface finishing of nano-ZrO 2 ceramics using two-dimensional ultrasonic assisted grinding. *The International Journal of Advanced Manufacturing Technology*, *43*(5-6), p.462. doi: 10.1007/s00170-008-1732-x.

Yen, D.P., Ando, Y. and Shen, K., 2016. A cost-effective micromilling platform for rapid prototyping of microdevices. *Technology*, *4*(04), pp.234-239. doi: 10.1142/s2339547816200041.

Yin, S. and Shinmura, T., 2004. A comparative study: polishing characteristics and its mechanisms of three vibration modes in vibration-assisted magnetic abrasive polishing. *International Journal of Machine Tools and Manufacture*, *44*(4), pp.383-390. doi: 10.1016/j.ijmachtools.2003.10.002.

Yin, Z., Fu, Y., Xu, J., Li, H., Cao, Z. and Chen, Y., 2017. A novel single driven ultrasonic elliptical vibration cutting device. *The International Journal of Advanced Manufacturing Technology*, *90*(9-12), pp.3289-3300. doi: 10.1007/s00170-016-9641-x.

Yin, Z., Fu, Y., Li, H., Cao, Z. and Chen, Y., 2017. Mathematical modeling and experimental verification of a novel single-actuated ultrasonic elliptical vibrator. *Advances in Mechanical Engineering*, *9*(12), p.1687814017745413. doi: 10.1177/1687814017745413.

Young, T., 1805. III. An essay on the cohesion of fluids. *Philosophical transactions of the royal society of London*, (95), pp.65-87. doi: 10.1098/rstl.1805.0005.

Z Zhang, C., Ehmann, K. and Li, Y., 2015. Analysis of cutting forces in the ultrasonic elliptical vibration-assisted micro-groove turning process. *The International Journal of Advanced Manufacturing Technology*, *78*(1-4), pp.139-152. doi: 10.1007/s00170-014-6628-3.

Zhang, F., Chen, W., Lin, J. and Wang, Z., 2005. Bidirectional linear ultrasonic motor using longitudinal vibrating transducers. *IEEE transactions on ultrasonics, ferroelectrics, and frequency control*, *52*(1), pp.134-138. doi: 10.1109/TUFFC.2005.1397358.

Zhang, J., Suzuki, N., Wang, Y. and Shamoto, E., 2014. Fundamental investigation of ultra-precision ductile machining of tungsten carbide by applying elliptical vibration cutting with single crystal diamond. *Journal of Materials Processing Technology*, *214*(11), pp.2644-2659. doi: 10.1016/j.jmatprotec.2014.05.024.

Zhang, J.X. and Sun, B.Y., 2006. Design and analysis of 2-DOF nanopositioning stage based on dual flexure hinges. *Piezoelectrics and Acoustooptics*, *28*, pp.624-626.

Zhang, X., Nath, C., Kumar, A.S., Rahman, M. and Liu, K., 2010, January. A study on ultrasonic elliptical vibration cutting of hardened steel using PCD tools. In *International Manufacturing Science and Engineering Conference* (Vol. 49460, pp. 163-169). doi: 10.1115/MSEC2010-34239.

Zhang, X., Liu, K., Kumar, A.S. and Rahman, M., 2014. A study of the diamond tool wear suppression mechanism in vibration-assisted machining of steel. *Journal of Materials Processing Technology*, *214*(2), pp.496-506. doi: 10.1016/j.jmatprotec.2013.10.002.

Zhang, X. *et al.*, 2017. The Improvement of Deep-hole Boring Machining Quality Assisted with Ultrasonic Vibration, *Jixie Gongcheng Xuebao/Journal of Mechanical Engineering*. doi: 10.3901/JME.2017.19.143.

Z Zhang, X., Kumar, A.S. and Rahman, M., 2012, November. Effects of cutting and vibration parameters on transient cutting force in elliptical vibration cutting. In *International Conference on Intelligent Robotics, Automation, and Manufacturing* (pp. 483-490). Springer, Berlin, Heidelberg. doi: 10.1007/978-3-642-35197-6_54.

Zhang, Y., Kang, R., Liu, J., Zhang, Y., Zheng, W. and Dong, Z., 2017. Review of ultrasonic vibration assisted drilling. *J Mech Eng*, *53*. doi: 10.3901/JME.2017.19.033.

Zheng, L., Chen, W. and Huo, D., 2019. Experimental investigation on burr formation in vibration-assisted micro-milling of Ti-6Al-4V. *Proceedings of the Institution of Mechanical Engineers, Part C: Journal of Mechanical Engineering Science*, *233*(12), pp.4112-4119. doi: 10.1177/0954406218792360.

Zhenyu, S., Zhanqiang, L., Hao, S. and Xianzhi, Z., 2016. Prediction of contact angle for hydrophobic surface fabricated with micro-machining based on minimum Gibbs free energy. *Applied Surface Science*, *364*, pp.597-603. doi: 10.1016/j.apsusc.2015.12.199.

Zhong, Z.W. and Lin, G., 2006. Ultrasonic assisted turning of an aluminium-based metal matrix composite reinforced with SiC particles. *The International Journal of Advanced Manufacturing Technology*, *27*(11-12), pp.1077-1081. doi: 10.1007/s00170-004-2320-3.

Zhou, M., Wang, X.J., Ngoi, B.K.A. and Gan, J.G.K., 2002. Brittle–ductile transition in the diamond cutting of glasses with the aid of ultrasonic vibration. *Journal of Materials Processing Technology*, *121*(2-3), pp.243-251. doi: 10.1016/S0924-0136(01)01262-6.

Zhou, M., Eow, Y.T., Ngoi, B.K.A. and Lim, E.N., 2003. Vibration-assisted precision machining of steel with PCD tools. *Materials and manufacturing processes*, *18*(5), pp.825-834. doi: 10.1081/AMP-120024978.

Zhou, X., Morrow, N.R. and Ma, S., 1996, January. Interrelationship of wettability, initial water saturation, aging time, and oil recovery by spontaneous imbibition and waterflooding. In *SPE/DOE Improved Oil Recovery Symposium*. Society of Petroleum Engineers. doi: 10.2118/62507-PA.

Zhu, Z., To, S., Ehmann, K.F. and Zhou, X., 2017. Design, analysis, and realization of a novel piezoelectrically actuated rotary spatial vibration system for micro-/nanomachining. *IEEE/ASME transactions on mechatronics*, *22*(3), pp.1227-1237. doi: 10.1109/TMECH.2017.2682983.

Zhu, Z., Zhou, X., Wang, R. and Liu, Q., 2015. A simple compliance modeling method for flexure hinges. *Science China Technological Sciences*, *58*(1), pp.56-63. doi: 10.1007/s11431-014-5667-1.

Appendixs

I Relationship data between input signal voltage and vibration displacement

Signal Voltage(V) \ Frequency(Hz)	200	400	600	800	1000	1200	1400	1600	1800	2000	2500	2700	3000	3500	4000	4500	5000	5500	6000	6500	7000	7500	8000	8500	9000	9500
0	0	0	0	0	0	0	0	0	0	0	0		0	0	0	0	0	0	0	0	0	0	0	0	0	0
0.03											1		0.6							unstable	unstable					
0.05											1.5									unstable	unstable					
0.08																				unstable	unstable					
0.1	0.4	0.5		0.5	0.6	0.6	1	0.5	0.4	0.6	2	0.55	1							unstable	unstable					
0.2	0.9	1		1	1.1	1.2	1.9	1	0.9	1.4	4	1.1	2	0.6						unstable	unstable					
0.3	1.4	1.5		1.5	1.7	1.9	2.6	1.5	1.5	2.2	6	1.6	2.6	1	0.5					unstable	unstable	0.4		0.65	0.4	0.5
0.4	2	2	0.5	2	2.2	2.6	3.3	2	2.2	3.1	8	2.2	3.4	1.8	0.7	0.55	0.5	0.4		unstable	unstable	0.7	0.4	0.7	0.45	0.8
0.5	2.4	2.6	1.1	2.5	2.9	3.3	4	2.6	2.8	4	10.2	2.6	4.2	3	0.9	0.7	0.8	0.7	0.4	unstable	unstable	0.75	0.5	0.8	0.5	0.8
0.6	3	3.2	1.6	3	3.4	4	4.6	3.1	3.5	5	12.4	3.1	5	3.8	1.1	1	0.88	0.8	0.5	unstable	unstable	0.8	0.55	0.9	0.51	1
0.7	3.6	4	2.3	3.6	4	4.6	5.4	3.7	4.3	6.1	14.6	3.7	6	4.8	1.6	1.3	1	0.9	0.5	unstable	unstable	0.85	0.55	0.95	0.5	1
0.8	4.1	4.5	3	4.3	4.5	5.4	6.2	4.4	7	7.4	16.8	4.1	6.6	5.7	1.8	1.4	1.1	1	0.6	unstable	unstable	0.9	0.55	0.98	0.55	1
1	5.6	5.6	4.2	5.4	5.8	7	8	5.8	6.6	9.6	21.6	5.2	8	8	2	1.6	1.2	1.1	0.6	unstable	unstable	0.95	0.55	1	0.5	1
1.2	6.8	7	5.7	6.8	7.1	7.6	10	7	8.2	11		6.8	10.4	8.8	2.6	1.7	1.25	1.1	0.6			0.9	0.55	1.1	0.5	
1.5	8.8	9.1	7.8	8.8	9.1	9.8	13.3	9	10.8	15		8	11.5	9.6	2.7	1.8	1.25	1.1	0.6			1	0.55	1.1	0.5	
1.8	11	11.2	9.9	11	11.3	12.2	17	11	14	18		8.4	12	10.2	2.8	2	1.25	1.1	0.6			1.05		1.1	0.5	

II LabVIEW program block diagram

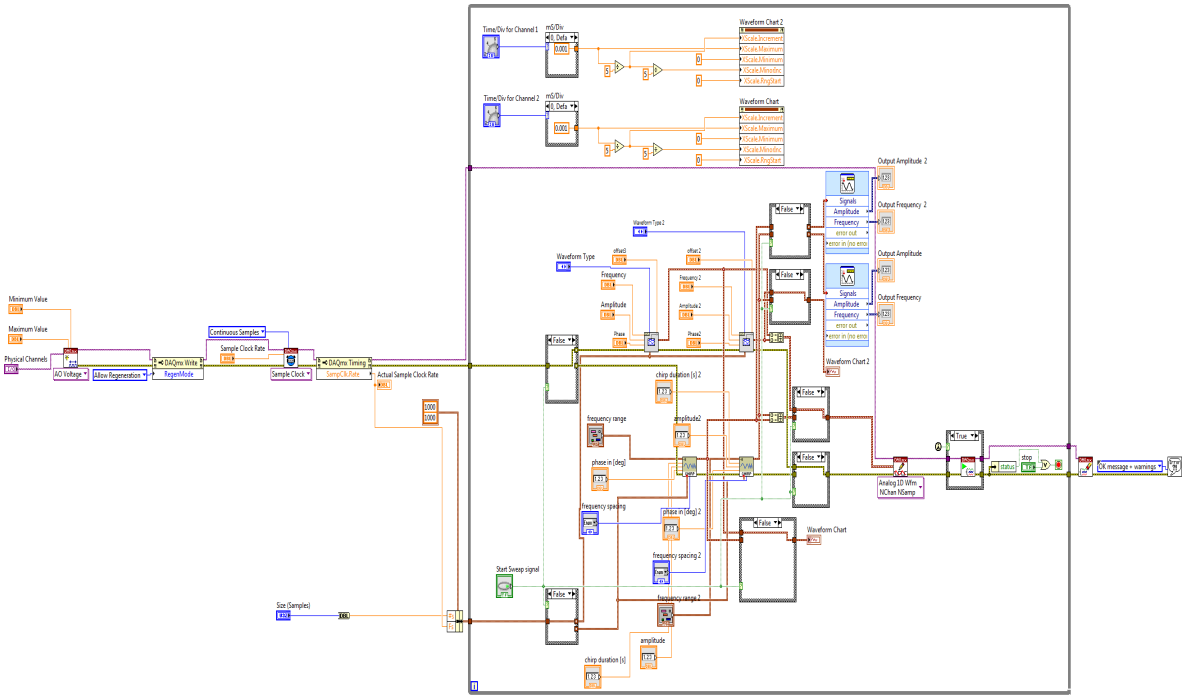

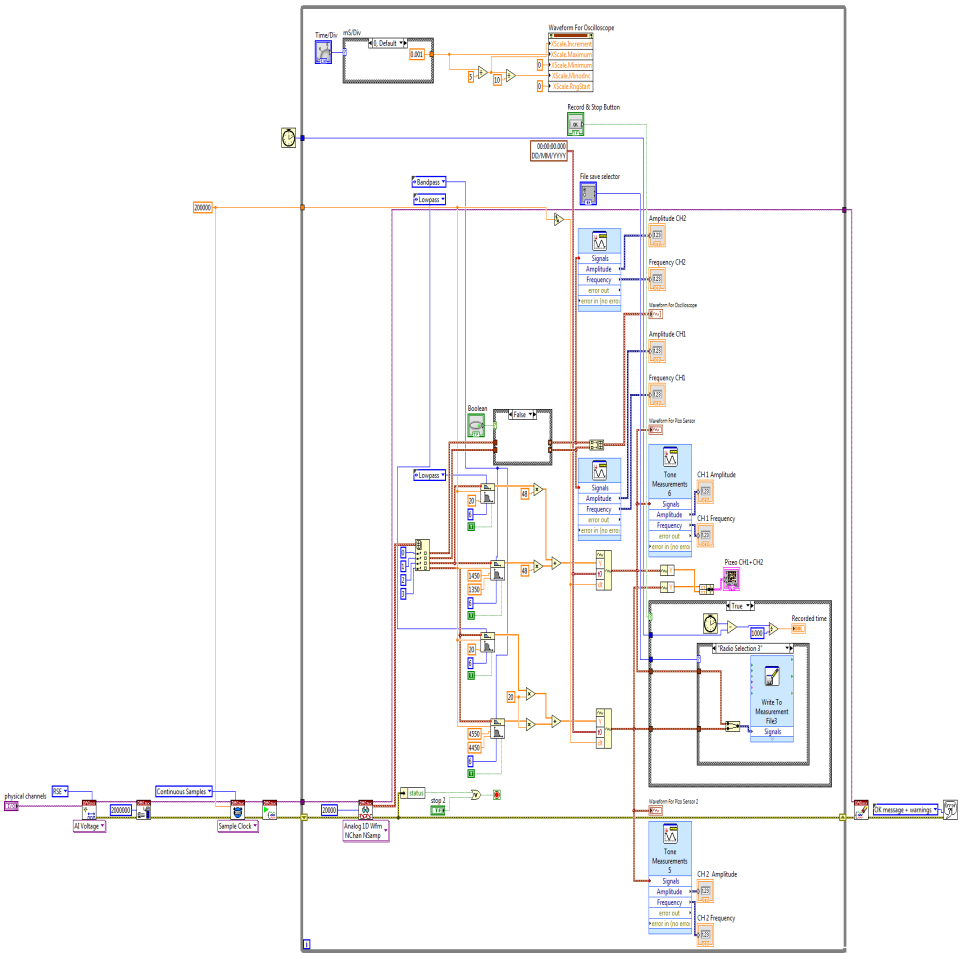

III Ansys APDL simulation code for the static FE model

```
**General Preprocessing**

/PREP7

ET, 1, SOLID98,3                ! 3-D COUPLED-FIELD SOLID !

ET, 2, SOLID95,                 !DEFINE ELEMENT TYPE FOR THE BACK COVER BOARD OR POLE

**matrial properties for steel**

MP, DENS, 1, 7800                          ! STEEL DENSITY, KG/M**3

MP, EX, 1, 2.1E11                           ! ELASTIC MODULI, N/M^2

MP, PRXY, 1, 0.3                            ! POISSON'S RATIO

**matrial properties for aluminum**

!MP, DENS, 2, 2700                                  ! ALUMINUM DENSITY

!MP, EX, 2, 7.1E10                                   ! ALUMINUM ELASTIC MODULI

!MP, PRXY, 2, 0.345                                  ! ALUMINUM POISSON'S RATIO

**matrial properties for piezoceramic1**

mp,dens,2,7500    !desity, kg/m^3

mp,perx,2,6.74565e-9    !permittivity at constant strain, F/m

mp,pery,2,6.74565e-9

mp,perz,2,5.86687e-9

tb,anel,2,6,,0,      !anisotropic elastic stiffness, N/m^2

tbdata,1,1.39e11,7.78e10,7.43e10    !c11,c12,c13

tbdata,7,1.39e11,7.43e10              !c11,c13

tbdata,12,1.15e11                      !c33

tbdata,16,3.06e10                      !c44

tbdata,19,2.56e10                      !c55
```

```
tbdata,21,2.56e10                    !c66

tb,piez,2    !piezoceramic stress coefficients, C/m^2

tbdata,3,-5.20279        !e13

tbdata,6,-5.20279        !e23

tbdata,9,15.08041        !e33

tbdata,14,12.71795       !e42

tbdata,16,12.71795       !e51

CYLIND, 0.025, 0.01, 0, 0.005, 0, 360                    ! THE BACK COVER BOARD

WPOFFS, 0, 0, 0.005

CYLIND, 0.025, 0.01, 0, 0.005, 0, 360                    ! PIEZOELECTRIC CERAMIC

WPOFFS, 0, 0, 0.005

CYLIND, 0.025, 0.01, 0, 0.005, 0, 360                    ! PIEZOELECTRIC CERAMIC

WPOFFS, 0, 0, 0.005

CYLIND, 0.025, 0.01, 0, 0.005, 0, 360                    ! PIEZOELECTRIC CERAMIC

WPOFFS, 0, 0, 0.005

CYLIND, 0.025, 0.01, 0, 0.005, 0, 360                    ! PIEZOELECTRIC CERAMIC

WPOFFS, 0, 0, 0.005

CYLIND, 0.035, 0.01,0, 0.005, 0, 360                     ! THE FROND COVER
BOARD

WPOFFS, 0, 0, 0.005

CONE,0.025,0.01,0,0.015,0,360,

WPOFFS, 0, 0, 0.015

!CYLIND, 0.025, 0,0, 0.003, 0, 360                       ! THE FROND COVER BOARD

!WPOFFS, 0, 0, 0.003
```

```
CYLIND, 0.01, 0,0, 0.03, 0, 360

VGLUE,ALL

NUMCMP, ALL

!DESTINATION ENTITY ATTRIBUTE

VSEL,S, , ,            1

VATT, 1 , , 2, ,

VSEL,S, , ,            4

VATT, 2 , , 1, ,

VSEL,S, , ,            5

VATT, 2 , , 1, ,

VSEL,S, , ,            6

VATT, 2 , , 1, ,

VSEL,S, , ,            7

VATT, 2 , , 1, ,

VSEL,S, , ,            2

VATT, 1 , , 2, ,

VSEL,S, , ,            3

VATT, 1 , , 2, ,

VSEL,S, , ,            8

VATT, 1 , , 2, ,

VSEL,ALL

SMRTSIZE, 6

MSHAPE, 1,3D

MSHKEY, 0
```

```
VMESH, ALL

NUMMRG, ALL, , , , LOW

NUMCMP, ALL

CSYS, 0

WPCSYS, 0

ALLSEL, ALL, ALL

FINI

/SOL

!*

ANTYPE,2

!*

MODOPT,LANB,20

EQSLV,SPAR

MXPAND,20, , ,0

LUMPM,0

PSTRES,0

!*

MODOPT,LANB,20,200,40000, ,OFF

FLST,2,2,5,ORDE,2

FITEM,2,11

FITEM,2,-12

!*

/GO

DA,P51X,ALL,
```

```
    SOLVE

FINI
```

IV List of publications arising from this PhD research

- 1. ***Lu Zheng***, Wanqun Chen, Dehong Huo. <Vibration Assisted Machining: Theory, Modelling and Applications>, Wiley, Will be published in 7. 2020 — Book
- 2. ***Lu Zheng***, Wanqun Chen, Dehong Huo and X. Lyu, "Design, analysis and control of a 2D vibration device for vibration assisted micro milling," IEEE/ASME Transactions on Mechatronics. — IF:4.943 JCR Q1
- 3. ***Lu Zheng***, Wanqun Chen, Michele Pozzi, Xiangyu Teng, and Dehong Huo. "Modulation of surface wettability by vibration assisted milling." Precision Engineering 55 (2019): 179-188. — IF: 2.582 JCR Q2
- 4. ***Lu Zheng,*** Wanqun Chen, Dehong Huo. "Experimental investigation on burr formation in vibration-assisted micro-milling of Ti-6Al-4V." Proc. Inst. Mech. Eng. Part C J. Mech. Eng. Sci.(2018). — IF: 1.359 JCR Q4
- 5. ***Lu Zheng***, Wanqun Chen, Dehong Huo. "Review of vibration devices for vibration-assisted machining" Int J Adv Manuf Technol. — IF: 2.496 JCR Q3
- 6. ***Lu Zheng***, Wanqun Chen, Dehong Huo. "Investigation on tool wear suppression mechanism in non-resonant vibration assisted micro milling." Micromachines. — IF: 2.426 JCR Q3
- 7. Wanqun Chen, ***Lu Zheng***, Wenkun Xie, Kai Yang, Dehong Huo. Modelling and experimental investigation on textured surface generation in vibration-assisted micro-milling. Journal of Materials Processing Technology 266 (2019): 339-350. — IF:4.943 JCR Q1
- 8. Wanqun Chen, ***Lu Zheng***, Xiangyu Teng, Kai Yang, and Dehong Huo. Finite element simulation and experimental investigation on cutting mechanism in vibration-assisted micro-milling. The International Journal of Advanced Manufacturing Technology (2019) — IF:2.496 JCR Q3
- 9. Wanqun Chen, ***Lu Zheng*****,** Dehong Huo. "Surface texture formation by non-resonant vibration assisted micro milling." Journal of Micromechanics and Microengineering (2017). — IF:1.888 JCR Q4
- 10. Wanqun Chen, ***Lu Zheng***, Xiangyu Teng, Kai Yang, and Dehong Huo. "Cutting Mechanism Investigation in Vibration-Assisted Machining." Nanomanufacturing and Metrology 1, no. 4 (2018): 268-276. — Journal paper
- 11. Wanqun Chen, Xiangyu Teng, ***Lu Zheng***, Wenkun Xie, and Dehong Huo. "Burr reduction mechanism in vibration-assisted micro milling." Manufacturing letters 16 (2018) — Journal paper
- 12. Teng, Xiangyu, Dehong Huo, Wanqun Chen, Eugene Wong, ***Lu Zheng***, and Islam Shyha. "Finite element modelling on cutting mechanism of nano Mg/SiC metal matrix composites considering cutting edge radius." Journal of Manufacturing Processes 32 (2018): 116-126. — IF: 2.809 JCR Q3
- 13. **Lu Zheng**, Wanqun Chen, Dehong Huo. "Wettability and liquid flow control in microfluidic channels by vibration assisted micro milling" 19th International Conference of the European Society for Precision Engineering and Nanotechnology, EUSPEN 2019 — Conference paper